Michael J. Unterberger

Microstructurally-Motivated Constitutive Modeling of Cross-Linked Filamentous Actin Networks

Monographic Series TU Graz

Computation in Engineering and Science

Series Editors

Monographic Series TU Graz

Computation in Engineering and Science Volume 21

Michael J. Unterberger

Microstructurally-Motivated Constitutive Modeling of Cross-Linked Filamentous Actin Networks

---

This work is based on the dissertation *"Microstructurally-Motivated Constitutive Modeling of Cross-Linked Filamentous Actin Networks"*, presented by Michael J. Unterberger at Graz University of Technology, Institute of Biomechanics in September 2013.
Supervisor: G. A. Holzapfel (Graz University of Technology)
Reviewer: R. W. Ogden (University of Glasgow)

Cover photo	Vier-Spezies-Rechenmaschine by courtesy of the Gottfried Wilhelm Leibniz Bibliothek – Niedersächsische Landesbibliothek Hannover
Layout	Wolfgang Karl, TU Graz / Universitätsbibliothek Christina Fraueneder, TU Graz / Büro des Rektorates
Printed	by TU Graz / Büroservice

Verlag der Technischen Universität Graz

www.ub.tugraz.at/Verlag

ISBN: 978-3-85125-303-0 (print)
ISBN: 978-3-85125-306-1 (e-book)

DOI: 10.3217/978-3-85125-303-0

MICHAEL J. UNTERBERGER

Michael J. Unterberger holds a Master's degree from the Vienna University of Technology, from where he received a background in industrial engineering. During the late period of his studies his attention was drawn to numerical methods in applied mechanics and he focused on multi-body simulation. In cooperation with Magna Steyr AG & Co KG he investigated the dynamics of an all-wheel drive vehicle with a special interest in the interactions between the vehicle and the road handling control during his Master's thesis. After completing his Master's degree with distinction, Michael started his PhD in Biomedical Engineering in April 2009 at the Institute of Biomechanics, Graz University of Technology, Austria, under the direction of Professor Gerhard A. Holzapfel where his research interest shifted to constitutive mechanical modeling and the finite element method.

His work aims to study the mechanical properties of cross-linked filamentous actin networks, an immensely important system in cells which provides their structural integrity and ability for movement. He develops multiscale models in order to describe and predict the mechanical behavior of such networks and seeks to efficiently implement these into finite element programs. Towards this end Michael actively collaborates with international researchers from various fields. Recently he started to transfer the insights gained from his work on actin networks to biological tissues where similarities in the structure allow adapted assumptions for new constitutive models. Michael's scientific findings have resulted in four original papers and have been presented at several international conferences. He has completed his PhD with distinction in September 2013.

ABSTRACT

The mechanical properties of cells are related to several diseases, such as malaria, asthma, arthritis, atherosclerosis, glaucoma and cancer. The cytoskeleton is the primary contributor to the stiffness of cells. It consists of many different filamentous proteins, such as actin, which are cross-linked into networks. This thesis focuses on the mechanical properties of cross-linked actin networks. Starting from the single molecule all the way up to the final structure, actin creates a hierarchy of several levels exhibiting remarkable behavior. The hierarchy spans several length scales with complex behavior on each level. Therefore, limitations in computational power call for different modeling approaches for the different scales. On the filament level, we use worm-like chain models to obtain a force-extension relationship. Assemblies of actin filaments are connected with cross-linker proteins. Microstructurally-motivated continuum models of the networks provide insights into larger systems containing cross-linked actin networks. The modeling of such systems also helps to gain insight into the processes on smaller scales. At the same time, however, the models call for verification, and, hence, trigger the improvement of established experiments and the development of new methods.

In this dissertation we provide a comprehensive review of the existing literature on the multiscale modeling of actin. In the second chapter we introduce a network model using a non-affine homogenization method to obtain a continuum mechanical model for reconstituted actin gels. We present stress-strain data obtained from rotational rheometry and use them to fit the non-affine network model. Most material parameters are physically interpretable and their values are determined to be in a reasonable range. In the third chapter, we extend the non-affine network model to also capture the viscoelastic properties of actin gels. We provide data from large amplitude oscillation experiments, together with storage and loss moduli over a large range of amplitudes and frequencies. The model is able to fit all three experiments simultaneously. In the fourth chapter, we introduce an affine network model and show that like the non-affine model, it is able to capture the exceptional normal stress behavior of semiflexible filament gels. Within this framework we are able to consider the finite stiffness of cross-linking proteins, which cause a softening in bulk behavior. All of these continuum models are formulated to allow straightforward finite element implementation. We performed analyses of problems which resemble the indentation of a spherical tip mounted on an atomic force microscope as well as the aspiration of a droplet into a micropipette. When analyzing the data obtained from rotational rheometry, we assume simple shear as the governing deformation mode, which is common in the literature. In the final chapter we examine this assumption and highlight the errors made using several examples for material models.

CONTENTS

1 INTRODUCTION

This introductory chapter is intended to give an overview of the recent research on actin with a focus on modeling. It presents the state of the art biomechanics concerned with actin and puts our contributions in the context of the existing literature.

1.1 Motivation

The cytoskeleton is the main promoter of cell stiffness and plays a crucial role in maintaining the cell shape. It is involved in cell migration, cell division and active contraction. Interactions are not limited to the mechanical transmission of forces, interactions include the conversion of mechanical stimuli to biochemical signals, i.e. mechanotransduction. It includes cell force transmission from the extracellular matrix to the cytoskeleton [1]. Experiments show that the orientation of the cytoskeleton is a function of the interplay between the biochemical activity and the magnitude of stretching [2]. Cell mechanics and thus the mechanics of the cytoskeleton are also important in a large number of diseases, e.g., malaria [3], asthma [4], arthritis [5], atherosclerosis [6], glaucoma [7] and cancer [8, 9], where the considered cells show different stiffness properties compared to their healthy counterparts. Knowledge of the mechanics may help to understand and improve diagnosis [10].

Improvements to this existing knowledge are made possible through experiments. However, models are necessary to gain a deeper understanding of cell mechanics. Suitable hypotheses, which are inferred from material models, allow us to relate the mechanics of the microscopic structures to the overall cell behavior and serve as a driver for improved experimental techniques. A similar issue was addressed when Albert Einstein said to Werner Heisenberg:

> Erst die Theorie entscheidet, was beobachtbar ist. Ehe Sie die Theorie haben, wissen Sie gar nicht, welche Größen die beobachtbaren sind.

The theory decides what we measure in an experiment. In other words, without a proper model, we do not know which quantities to measure in an experiment.

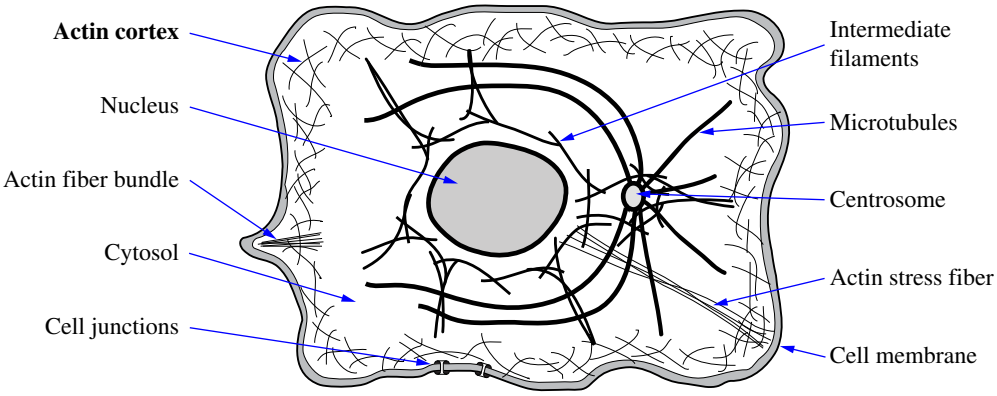

Figure 1.1: Mechanically important components of the eukaryotic cell. Microtubules extend from the centrosome and intermediate filaments surround the nucleus. Actin appears in three morphologies: stress fibers, fiber bundles and a network concentrated in the cortex. Cell junctions transmit external mechanical signals to the cytoskeleton. Adapted from [11].

1.2 Cytoskeleton

The cytoskeleton consists of multiple proteins which are arranged in various different structures. The three most important components are microtubules, intermediate filaments, and filamentous (F-)actin, see Fig. 1.1, which are complemented by cross-linker and motor proteins. The cytoskeleton is connected to the environment, i.e. neighboring cells or the extracellular matrix, via cell junctions.

1.2.1 Cytoskeletal proteins

Generally accepted knowledge about the biology of the cytoskeletal proteins is compiled by Alberts et al. [12]. The various filaments differ strongly in structure and function and are important contributors to biological processes.

Microtubules are hollow cylinders with a diameter of 25 nm; Fig. 1.2(a) shows a schematic representation. They are built from tubulin dimers which constantly assemble and disassemble and thereby reorganizing the microtubule network. The geometry allows only for slight bending; recall in this context the area moment of inertia of hollow profiles. With one end microtubules are attached to the centrosome, which acts as organization center (Fig. 1.1). Microtubules serve as pathways for transport of substances inside cells by allowing motor proteins to move along the strands [13]. They are essential in cell division by creating the spindle apparatus.

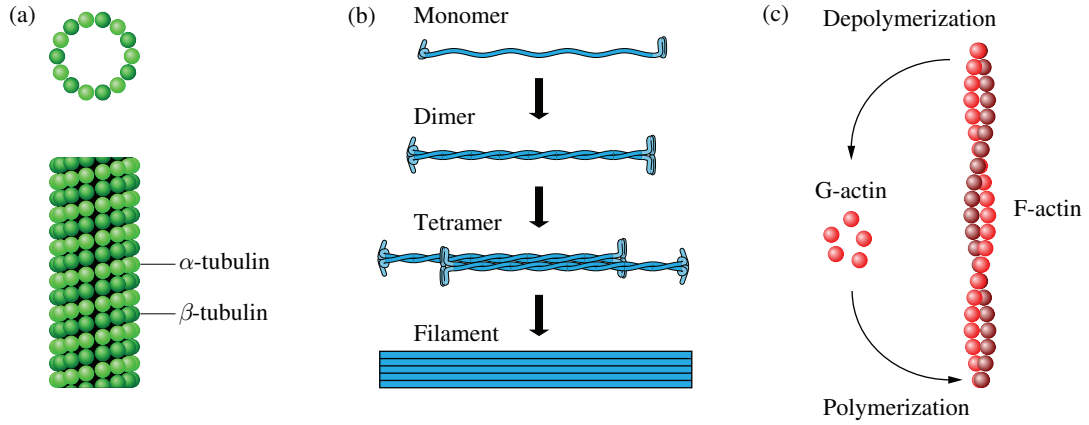

Figure 1.2: Structure of cytoskeletal filaments: (a) microtubule, (b) intermediate filament, (c) actin. Modified from [12].

Intermediate filaments are a family of fibrous protein polymers with a diameter of $\sim 10\,\mathrm{nm}$. This value lies between that of microtubules and actin, hence the name. They comprise a heterogeneous group of proteins which can be categorized into, e.g., keratins, desmins, lamins or neurofilaments. They possess differing function, for instance, one intermediate filament builds the nuclear lamina providing stiffness for the cell nucleus. Others extend over the cytoplasm increasing the overall stiffness of the whole cell. The monomers combine into a coiled coil dimer, see Fig. 1.2(b). Subsequently the dimers assemble into tetramers and eventually pack into filaments.

Actin is a globular protein, G-actin, built up from four subdomains, arranged in a U-shape. Several G-actin molecules assemble into filaments, i.e. a protein polymer with a two-stranded helical structure and diameter 5–9 nm called F-actin. This filament appears in various morphologies each fulfilling another function. For instance, they create a two-dimensional network in the moving front of adherent cells to facilitate locomotion. Actin filaments are also a key component during active contraction of cells [14]. Their in vivo contour length is around $\sim 1\,\mu\mathrm{m}$ [15].

1.2.2 Actin on multiple scales

The cytoskeletal protein which is most extensively studied is F-actin. Under closer examination, this filament and its networks exhibit a hierarchical structure on multiple length scales, see Fig. 1.3. The filaments may be connected to each other by cross-linker proteins and form various structures namely fiber bundles (filopodia), actively contractible stress fibers and a fairly isotropic and homogeneous network

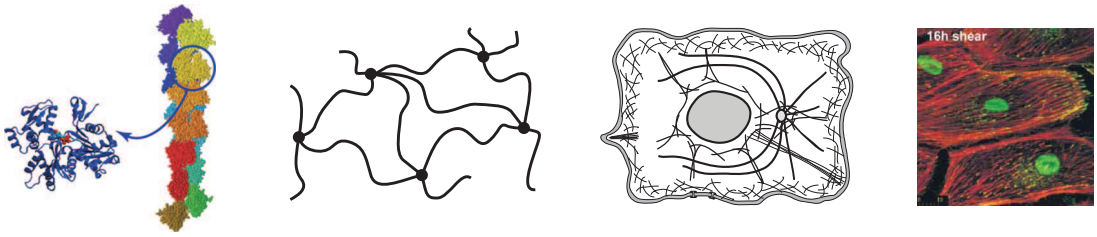

Actin molecule		Actin filament		Actin network		Whole cell		Multiple cells
1 nm	<	10 nm	<	1 μm	<	10 μm	<	1 mm

Figure 1.3: Different spatial scales from the actin molecule, over the filament and network to whole cells and compounds of cells. Pictures of the molecule and filament are modified from [16], the depiction of the cell compound is from [17].

dispersed throughout the cell and concentrated in the cortex beneath the cell membrane, see Fig. 1.1. While the latter structure is found in adherent and suspended cells, fiber bundles and stress fibers are only present in adherent cells such as endothelial cells and absent in suspended cells, e.g., fibroblasts [18]. The cross-links in actin networks can transiently form and unbind. For example, shear stress acting on endothelial cells causes reorganization of the actin cytoskeleton [17] and the filaments are subject to constant remodeling [19, 20].

Actin binding proteins. The various morphologies of actin networks are created through cross-linking via actin binding proteins (ABP). Over 60 different ABP are known [21] and the angle between two connected filaments determines the function of the cross-link. Small angles, binding two adjacent filaments in parallel, create actin bundles such as stress fibers with α-actinin [22], and filopodia and lamellopodia with fascin [23]. When large angles are realized by linker proteins such as filamin-A [24], scruin [25] or heavy meromyosin [26], the filaments build a soft gel as it is found in the cell cortex.

Multiscale modeling for actin. In a multiscale approach of modeling we consider the smaller length scales first and delineate, subsequently, properties of the material on the next higher scale. In the case of actin, see Fig. 1.3, one may investigate the properties of multiple G-actin molecules to obtain a force-extension relationship of F-actin. This knowledge can then be used in turn to inform its cross-linked network. The actin network is a constituent of the cytoskeleton and hence may be considered when modeling a whole cell. This method may be transferred to an even larger length scale, where arrangements of multiple cells are informed by the properties of a single cell.

1.2.3 Experimental methods and important properties

In the sense of Humphrey [27] we base our modeling hypotheses on existing observations. We must then verify the model by performing experiments, which in turn may lead to a refined theory. Hence, experimentation is a crucial task in the process of deriving material models. Therefore, we provide here a short introduction to some important experimental techniques to characterize the mechanical properties of F-actin.

Single filament. The thermal fluctuations of single actin filaments are observed with fluorescence light microscopy. For instance, from such observations, Isambert et al. [28] calculated the persistence length L_p, a characteristic length of a filament over which a bend can be made with energy cost $k_\mathrm{B}T$ [29]. The persistence length of actin was determined by various measurements with differing experimental approaches as 9–17 μm, see, e.g., [28, 30–34]. A commonly accepted value is $L_\mathrm{p} = 16\,\mu\mathrm{m}$ [35]. We also want to relate the tensile force pulling on the ends of a filament to the resulting extension. These measurements can be achieved by attaching a filament to elastic beams and measuring their deflection, see, e.g., [36]. Such a beam element may also be the tip of an atomic force microscope (AFM). The contour length of F-actin is on the same order of magnitude as the persistence length. Hence, these filaments are called semiflexible, meaning that the chains are too stiff to form loops but are flexible enough to exhibit considerable thermal bending [37].

Networks. Networks of cross-linked F-actin can be reconstituted in vitro and serve as model system for the in vivo networks. Rheometry with parallel plate geometry as, e.g., performed by [38], evolved into the state of the art technique to characterize these networks. Figure 1.4(a) and (b) shows a picture of a rheometer and a schematic of the sample inside the measuring chamber. In such an experiment, the upper plate is rotated with respect to the lower plate while the distance between the plates is kept constant. The deformation can then be related to the torsion couple and normal force. The resulting stress-strain diagrams, see, e.g., Fig. 1.4(c), may be interpreted by means of elastic models. The viscoelastic properties are characterized by applying oscillatory deformation which may be broken down into an elastic (storage modulus G') and a viscous (loss modulus G'') part. The mechanics of cross-linked actin networks depend strongly on the type of cross-linker protein. Wagner et al. [40] showed experimentally that the structure of the cross-linkers plays an important role for the mechanical response of the network. The different morphologies due to cross-linking proteins are also influential on the mechanics [26]. The typical nonlinear strain-stiffening of cross-linked F-actin samples, characterized by the increasing slope of the shear stress curve in Fig. 1.4(c), was systematically investigated by [41].

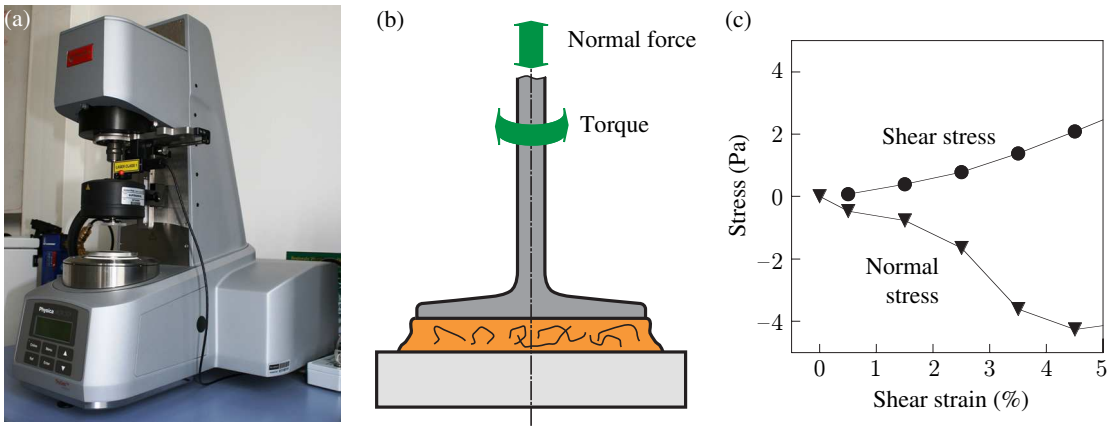

Figure 1.4: Rheometry. (a) Picture of a commonly used commercial device. (b) Schematic of a rotational rheometer with parallel plate geometry. (c) Typical elastic response of cross-linked actin gels and their exceptional normal stress behavior, modified from [39].

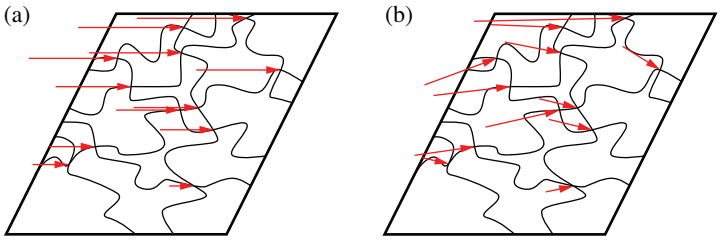

Figure 1.5: Elastic deformation regimes. (a) During affine deformation the movement of material points (red arrows) follows the macroscopic deformation. (b) The movement of material points is only loosely related to the macroscopic deformation in the non-affine regime.

Affinity. When all subregions of a filament network, e.g., the neighborhood of the cross-links, deform according to the macroscopic deformation during an experiment, the deformation is affine. In contrast, when the positions of such subregions deviate from the predicted positions, the deformation is non-affine. This phenomenon is investigated both experimentally [42] and theoretically, e.g., [43]. For quantification purposes, several non-affinity measures are introduced in the literature. One particular definition for the degree of non-affinity A is

$$A = \langle (\mathbf{u} - \mathbf{u}_{\text{affine}})^2 \rangle, \tag{1.1}$$

where $\mathbf{u}$ is the displacement of a point and $\mathbf{u}_{\text{affine}}$ is the (theoretical) affine displacement of the same point. The angle brackets mark the average over all considered points. Figure 1.5 depicts the difference between affine and non-affine deformation for simple shear. The red arrows start from the reference location and represent the displacement vector with the arrowhead at the current location. In the affine case,

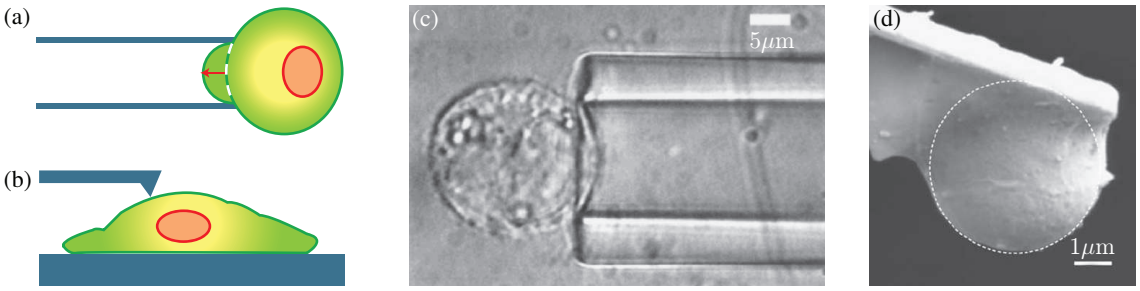

Figure 1.6: Experiments on cells. Schematics of (a) micropipette aspiration and (b) AFM indentation, modified from [51]. (c) Micropipette aspiration of a chondrocyte, modified from [52]. (d) Spherical tip on an AFM cantilever, modified from [53].

all points move parallel to the base. The length of the vector is proportional to the vertical position, see Fig. 1.5(a). These strict rules are violated when the material deforms non-affinely as in Fig. 1.5(a) Non-affine deformation is always dependent on the considered length scale, i.e. the size of the considered subregions. The more one zooms into the microstructure, the more non-affine the deformation appears. Hatami-Marbini and Picu [44] found that no characteristic length scale separates the affine from the non-affine response.

Exceptional normal stress. Another important observation made in rheological experiments is related to the Poynting effect. Poynting [45] observed that metal wires elongate when twisted and this behavior was seen for rubber as well [46]. In rheometry, this effect results in a compressive force when the gap between the two plates is held constant. A force in the opposite direction is observed for various biological network materials, i.e. cross-linked F-actin, collagen, fibrin and neurofilaments [39]. Hence, the rheometer needs to apply a tensile force on the sample in order to keep the measuring gap. Janmey et al. [39] called this property 'negative normal stress' which refers to the readout of commercial rheometers, see Fig. 1.4(c). Conti and MacKintosh [47] confirm this effect theoretically using discrete filament models. In continuum mechanics, however, a *tensile* force is defined to be *positive*. Therefore, Unterberger et al. [48] suggest the term 'exceptional normal stress' instead. This exceptional normal stress response is also present in nanotube suspensions [49].

Experiments on cells. The mechanical properties of whole cells can be characterized with a variety of experimental methods, see, e.g. [50] for a review including modeling techniques. Two widely used methods are micropipette aspiration and cell poking with AFM, see Fig. 1.6 for schematics and microscopic images. These techniques are two striking examples highlighting the need for improved models. The most commonly used model for interpreting micropipette aspiration experiments is

a thin-walled pressure vessel combined with Laplace's law [54]. On the other hand, AFM is often evaluated using the Hertzian contact model, e.g., [55]. Both models require indefensible assumptions such as small strains and linear material properties. This fact calls for improved models of the cell, especially of the cytoskeleton. Multiscale models of cross-linked actin networks may help in this sense.

1.3 Models for actin on different scales

In this part we focus on the modeling techniques available for the lower scales, as shown in Fig. 1.3. Specifically, we are concerned with models for G-actin using the molecular dynamics (MD) method. By means of coarse-graining (CG) we transfer the knowledge of the molecular level to filaments. A further step of simplification results in continuum models for F-actin.

In the subsequent sections we want to move our considerations to the next higher length scale, i.e. the network level. MacKintosh et al. [56] depart from their filament model to derive scaling arguments to predict dependence of the storage modulus from the actin concentration. For deeper insights into the mechanics of actin gels, network models are developed. Two approaches are proposed in the literature: (i) cross-linked networks of discrete filaments and (ii) homogenization within the framework of continuum mechanics. In the following parts we discuss both approaches and their respective implications.

1.3.1 Molecular level

Molecular dynamics is a method proposed by Alder and Wainwright [57] which enables to simulate the interactions of particles on the atomic length scale. Powerful computers allow to apply this method to very large groups of atoms, which build several actin molecules and thus short filaments. Matsushita et al. [58] obtain the molecular structure of F-actin from the Protein Data Bank, see Fig. 1.7(a), and surround it with water molecules, sodium and chlorine ions. By performing simulations in the thermal equilibrium, the authors measure thermal fluctuations of filamentous actin and infer stiffness parameters through the equipartition of energy. The apparent extensional stiffness decreases with increasing sampling size and converges to a value, comparable to experimental data, see Fig. 1.7(b). Matsushita et al. [58] conclude that a large enough size of the sampling time window is crucial to obtain reliable results leading to a tradeoff between predictive reliability and computational cost. The influence of a tensile force on this model is reported the follow-up study [60], which applies an external force to the subunits G_1, G_2 and G_{13}, G_{14} using the steered

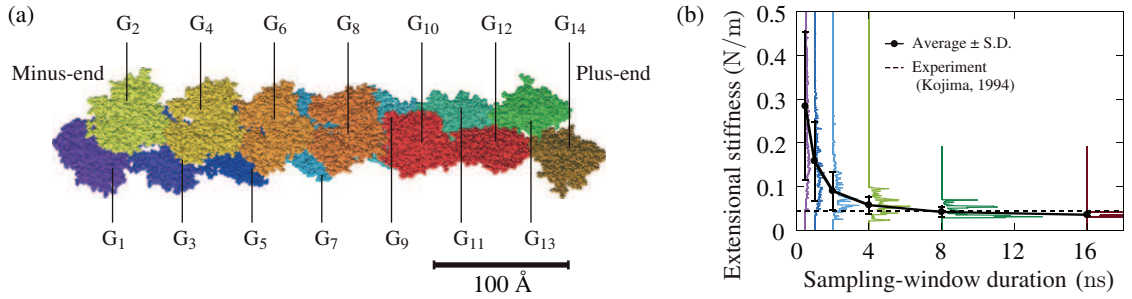

Figure 1.7: Molecular dynamics simulation. (a) Model of a filament consisting of $i = 1, \ldots, 14$ monomers G_i. (b) Distribution of extensional stiffness of a fluctuating actin filament as a function of a sampling time window, compared with experimental data [59]. Modified from [58].

molecular dynamics (SMD) method. While, under force, the filament extends, the apparent stiffness increases indicating a nonlinear force-stretch relationship.

The large number of atoms involved in MD simulations limit the numerically accessible system size to relatively short filaments. This limit may be raised using a coarse-grained molecular dynamics (CG-MD) method [e.g., 61] to investigate long filaments. In this method, the atoms of a G-actin molecule are substituted by an elastic network consisting of the four G-actin subdomains. The interactions between the entities of the coarse-grained model are informed by (fine-grained) MD simulations by means of the fluctuation-matching method. From normal mode analysis, the persistence length can be extracted which is in good agreement with experimental measurements of Isambert et al. [28]. Deriu et al. [62] use a similar CG-MD method, however, with additional shearing interactions, where the authors achieve an equilibrium configuration for G-actin before coarse-graining. They compare it to an F-actin model which is not refined by MD simulations. It turns out that the nonrefined model is always stiffer than the CG-MD model. The subunits of the G-actin molecule can attain different conformations due to variations in the biochemical state. These variations lead to different interactions between G-actin subunits and other molecules in the filament, and hence cause heterogeneous mechanical properties of F-actin. Recent developments of CG models account for this fact, e.g., [63], in some cases also based on MD simulations [64, 65].

The CG method may serve as a bridge between modeling on the molecular level and continuum mechanical models through normal mode analysis. For example, Ming et al. [66] proposed the substructure synthesis method which allows a scaling up of the dynamic information obtained from atomistic simulations. The method uses the kinetic and the potential energies resulting in mass and stiffness matrices. The stationary Rayleigh quotient leads to an eigenvalue problem allowing the extraction of bending, twisting and stretching modes. When applied to large actin filaments,

i.e. 4.6 μm, the comparison to a continuum model is in good agreement [67]. Wu and Ma [68] use this model to refine the atomic model against fiber diffraction data.

Figure 1.7(a) shows the helical structure of F-actin. This geometry causes coupling between axial stretch, bending and twisting deformation. For this reason, Yamaoka and Adachi [69] model a filament as an extensible Cosserat rod with a mismatched centroid. These couplings have local impact on the deformation of the filament and may affect molecular events such as binding with cross-linkers. Modeling of couplings due to a mismatched centroid may also be achieved with MD simulations [70]. Unfortunately, there is no direct comparison available between the two modeling strategies, continuum model versus MD. On the macroscopic scale, i.e. when considering force-extension relations of filaments, the influence of the mismatched centroid is negligible [69] and is, therefore, excluded in the studies of the following section.

1.3.2 Continuum models for single actin filaments

Despite the mismatched centroid, F-actin is a relatively homogeneous chain which is suitable for the application of continuum mechanics. It is regularly regarded as a worm-like chain, based on the work of Kratky and Porod [71], where the bending stiffness of the filament is related to the persistence length L_p. A first numerical treatment of the theory was accomplished by Fixman and Kovac [72], where in general, we are interested in the derivation of a force-extension relation. Most authors achieve this goal through statistical mechanics. A fully mechanical approach for extensible filaments was presented recently by Holzapfel and Ogden [73] which we want to sketch in the following.

In an extensible filament, see Fig. 1.8, the arc length in the reference configuration S and in the current configuration s are different from each other and characterized by the stretch $\lambda(S) = s'(S)$, where in this section the prime denotes the derivative with respect to S. Subsequently, *all* quantities are given in terms of the *reference* arc-length S. The total length of the filament in the reference configuration, i.e. the contour length is L. A point on the filament backbone is located at the position vector $\mathbf{x}$. Its derivative with respect to S gives the tangent to the filament backbone $\boldsymbol{\tau} = \lambda^{-1}\mathbf{x}'$. This tangent is inclined to the $\mathbf{e}_1$-axis by the angle θ. The curvature is $\kappa = \theta'$.

The force $\mathbf{p}$ in the cross section at position S is $\mathbf{p} = t\boldsymbol{\tau} + n\boldsymbol{\nu}$, where t is the tension in tangential direction, n is the normal component and $\boldsymbol{\nu}$ is the normal vector. The moment of the force about the origin is $\mathbf{x} \times \mathbf{p}$ and the resulting contact couple is $\mathbf{m} = m\boldsymbol{\tau} \times \boldsymbol{\nu}$. The equilibrium equations are a simplified form of special Cosserat rods [see, e.g., 75]. By neglecting body couples they become

$$\mathbf{p}' + \mathbf{b} = \mathbf{0}, \qquad \mathbf{m}' + \mathbf{x}' \times \mathbf{p} = \mathbf{0}, \tag{1.2}$$

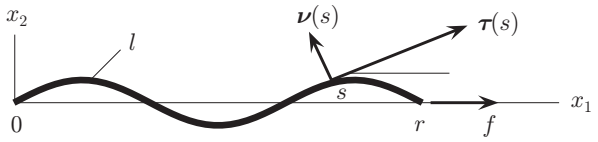

Figure 1.8: Biopolymer subject to thermal fluctuations and a tensile force f in the current configuration. The tangent to the filament backbone at the current arc length s is $\boldsymbol{\tau}(s)$ with the normal vector $\boldsymbol{\nu}(s)$. Modified from [74].

where $\mathbf{b}$ is the body force per unit reference length. It is convenient to introduce $\mathbf{c} = c\,\mathbf{e}_2$ such that $\mathbf{c}' = \mathbf{b}$. Then, with the equilibrium we can express

$$t = f\cos\theta - c\sin\theta, \qquad n = -f\sin\theta - c\cos\theta, \qquad m' = \lambda n, \tag{1.3}$$

where f is the prescribed tension in axial direction at the end of the filament.

Next, we use a decoupled quadratic stored energy $U(\lambda, \kappa)$ as constitutive model for the filament

$$U(\lambda, \kappa) = \frac{1}{2}\mu_0(\lambda - 1)^2 + \frac{1}{2}B_0\kappa^2, \tag{1.4}$$

where the bending stiffness $B_0 = k_\mathrm{B}TL_\mathrm{p}$ and the stretch modulus μ_0 are material parameters. Note, that the Boltzmann constant k_B and the temperature T relate the bending stiffness to the persistence length. The tensile force t and bending moment m are given by $t = U_\lambda$ and $m = U_\kappa$, respectively, where the subscripts denote the partial derivative with respect to the variable. Therefore, we obtain $t = \mu_0(\lambda - 1)$ and $m' = B_0\theta''$. Assume now that the filament undergoes only small undulations to approximate $\sin\theta \sim \theta$ and $\cos\theta \sim 1$ and rewrite $(1.3)_1$ as $\mu_0(\lambda - 1) = f - c\theta$. By noting that c is linear in θ we can approximate the stretch as $\lambda = \lambda^{(0)} + \lambda^{(2)}$, correct to the second order, with

$$\lambda^{(0)} = 1 + f/\mu_0, \qquad \lambda^{(2)} = -\frac{1}{2\mu_0}(f\theta^2 + 2c\theta). \tag{1.5}$$

By combining $(1.3)_2$ and $(1.3)_3$ we get

$$B\theta'' - f\theta = c, \tag{1.6}$$

where we used the short hand notation $B = B_0/\lambda^{(0)}$. Notice the similarity to the Euler buckling problem, for which the right hand side of (1.6) is zero. Recall that f is a tensile force so that c is required to obtain non-trivial solutions for θ from (1.6). Holzapfel and Ogden [73] concluded that in order to fulfill the governing equations of mechanics, a body force term represented by c is required to allow for thermal fluctuations.

In order to solve the differential equation (1.6) we write

$$c = \sum_{n=1}^{\infty} c_n \sin(q_n S), \qquad \theta = \sum_{n=1}^{\infty} a_n \sin(q_n S) \tag{1.7}$$

as Fourier series with $q_n = n\pi/L$. Using the approximation for λ on $x' = \lambda\cos\theta \sim \lambda^{(0)}(1-\theta^2/2) + \lambda^{(2)}$ and integration from $S = 0$ to $S = L$ gives

$$r^\star = \lambda^{(0)} - \frac{1}{4}\sum_{n=1}^{\infty} \frac{c_n^2}{(Bq_n^2 + f)^2} + \frac{1}{2\mu_0}\sum_{n=1}^{\infty} \frac{c_n^2}{Bq_n^2 + f} \tag{1.8}$$

as solution for (1.6), where $r^\star = r/L$ and r is the end-to-end distance. We introduce the shorthand notations

$$f^\star = fL^2/(\pi^2 B_0), \qquad \alpha = \pi^2 B_0/(\mu_0 L^2) \tag{1.9}$$

and consider the single term version of (1.8). With the relation at zero force, they can determine c_1 and obtain

$$r^\star = 1 + \alpha f^\star - \frac{(1+2\alpha f^\star)(1+\alpha f^\star)^2}{(1+f^\star+\alpha f^{\star 2})^2}(1 - r_0/L), \tag{1.10}$$

where r_0 is the end-to-end distance at zero force. The inextensible case is included in (1.8) and (1.10) for $\mu_0 \to \infty$ (or $\alpha = 0$) and $\lambda = 1$, i.e.

$$r^\star = 1 - \frac{1}{4}\sum_{n=1}^{\infty} \frac{c_n^2}{(B_0 q_n^2 + f)^2}, \qquad r^\star = 1 - \frac{1}{(1+f^\star)^2}(1 - r_0/L), \tag{1.11}$$

respectively. If we express now $f^\star$ as a function of $r^\star = r/L$, we see that the dimensionless force approaches infinity when $r \to L$. Physically, this means that the maximum end-to-end distance r of an inextensible filament can be measured when the filament is straightened out.

Similar relations for inextensible filaments are obtained by means of statistical mechanics. The force-stretch relationship is then based on the Hamiltonian of the system, see, e.g., [73]:

$$\mathcal{H} = \mathcal{H}_{\text{bend}} + \frac{1}{2}\int_0^L f\theta^2 \,\mathrm{d}s - f(L - r_0), \qquad \mathcal{H}_{\text{bend}} = \frac{1}{2}B_0 \int_0^L \kappa^2 \,\mathrm{d}s, \tag{1.12}$$

where $\mathcal{H}_{\text{bend}}$ is the bending energy. Bustamante et al. [76] and Marko and Siggia [29] derived a closed form approximation by means of the equipartition theorem

$$f^\star = \left(\frac{L}{\pi L_{\text{p}}}\right)^2 \left(r^\star + \frac{1}{4(1-r^\star)^2} - \frac{1}{4}\right). \tag{1.13}$$

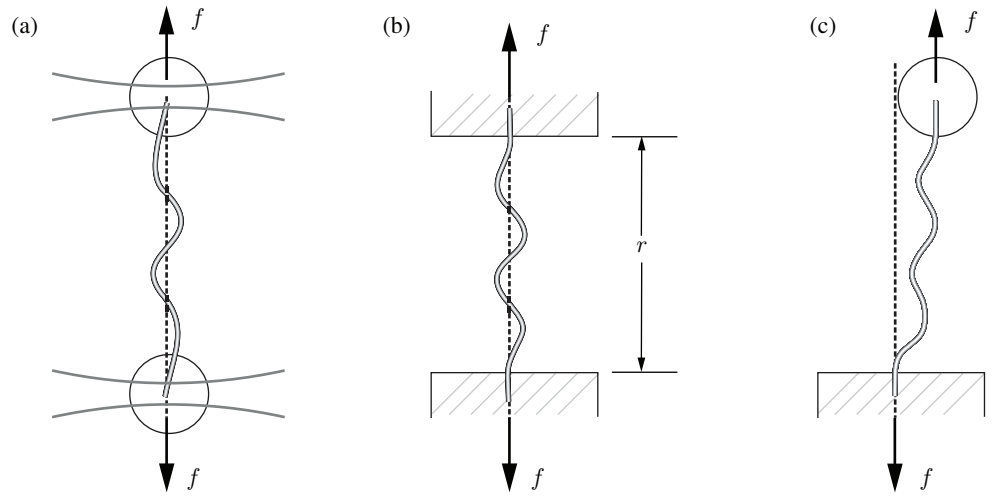

Figure 1.9: Boundary conditions for measuring the force-extension relation of actin filaments depending on the experimental method. (a) Pinned end conditions where both ends of the filament are attached to beads moved by optical tweezers. (b) Clamped-clamped conditions in a flow chamber, where filaments are sandwiched between two coverslips. (c) Partially clamped condition with one end of the filament attached to a coverslip while the other end is moved by a bead in an optical or magnetic trap. Adapted from [79].

Improved predictions may be made by adding correction terms of the form $k_i(r^\star)^i$ with $i = 2, 3, \ldots, 7$ according to [77]. MacKintosh et al. [56] use similar arguments and a series expansion of the transverse fluctuations resulting in

$$r^\star = 1 - \frac{k_\mathrm{B}TL}{\pi^2 B_0} \sum_{n=1}^{\infty} \frac{1}{1+f^\star} \tag{1.14}$$

(see [78] for a more detailed derivation). Purohit et al. [79] generalize this approach from the pinned ends boundary condition to other boundary conditions, see Fig. 1.9. Considering that the infinite series in (1.14) has a finite value, for the pinned ends the authors obtain

$$r^\star = 1 - \frac{k_\mathrm{B}TL}{2B_0\pi\sqrt{f^\star}} \mathcal{L}(\pi\sqrt{f^\star}), \tag{1.15}$$

where the Langevin function $\mathcal{L}(\xi) = \coth\xi - 1/\xi$ is used. This equation appeared already earlier, however, without derivation [80]. Hori et al. [81] obtained this equation for other boundary conditions, i.e. the partially clamped case in Fig. 1.9(c). Palmer and Boyce [82] derived (1.15) independently and used Cohen's Padé approximation [83] for the inverse Langevin function to obtain an explicit force-extension relation

$$f^\star = \frac{L}{4\pi L_\mathrm{p}(1-r^\star)^2} \left[\frac{L/L_\mathrm{p} - 6(1-r^\star)}{L/L_\mathrm{p} - 2(1-r^\star)} \right], \tag{1.16}$$

which is exact to the sixth order. For a freely fluctuating filament, i.e. $f^\star = 0$, (1.15) reduces to $r_0/L = 1 - L/(6L_\mathrm{p})$, which is in agreement with an earlier prediction [84]. Additionally to the force-extension relation, Purohit et al. [79] obtain such relations for the other boundary conditions depicted in Fig. 1.9, however, without being able to eliminate the infinite series. Furthermore they provide predictions for the transverse fluctuations which may be validated by the observation of actin filaments in a fluorescence microscope.

Blundell and Terentjev [85] assume in their alternative approach global inextensibility, i.e. they develop a mean field theory. Based on the Hamiltonian for bending $\mathcal{H}_\mathrm{bend}$, they derive the probability density P for the end-to-end distance r by means of Boltzmann statistics. The free energy of the filament is then $E = -k_\mathrm{B}T \ln P$. With $f = \partial E/\partial r$, the approximation for semiflexible filaments yields

$$r^\star = 1 - \frac{k_\mathrm{B}TL}{B_0\pi^{3/2}} \frac{1}{(1+f^\star)^{1/2}}. \tag{1.17}$$

When comparing the results of [73], the single term version of [56] and [85], i.e. (1.11), (1.14) and (1.17), respectively, a common pattern can be deduced, i.e.

$$r^\star = 1 - \frac{\alpha_\beta}{(1+f^\star)^\beta}, \tag{1.18}$$

as it is pointed out by [74]. This generalization reveals that the proportional factor α_β is different for the models. However, the fundamental difference between the models is the exponent: $\beta = 2$ [73], $\beta = 1$ [56] and $\beta = 1/2$ [85]. Unterberger et al. [48] apply this generalization to the relation for extensible filaments (1.10), i.e.

$$r^\star = 1 + \alpha f^\star - \frac{(1+2\alpha f^\star)(1+\alpha f^\star)^\beta}{(1+f^\star+\alpha f^{\star 2})^\beta}(1 - r_0/L). \tag{1.19}$$

A fit of this model to experimental data [36] is depicted in Fig. 1.10. The diagram illustrates that inextensible filament models can capture the low force regime only and extensible models must be applied for large forces. All physically interpretable parameters are within a reasonable range.

For the models suggested in [56, 85] an ad hoc enhancement to consider extensibility is proposed. Starting with the inextensible force-extension relation $r(f; L)$ we may include the stretch modulus μ_0 according to [37]

$$r_\mathrm{e}(f; L) = \left(1 + \frac{f}{\mu_0}\right) r\left(f\left(1 + \frac{f}{\mu_0}\right); L\right), \tag{1.20}$$

where $r_\mathrm{e}(f; L)$ is the extensible end-to-end distance. Note, however, that this approach is not based on a rigorous derivation beginning with correct kinematics.

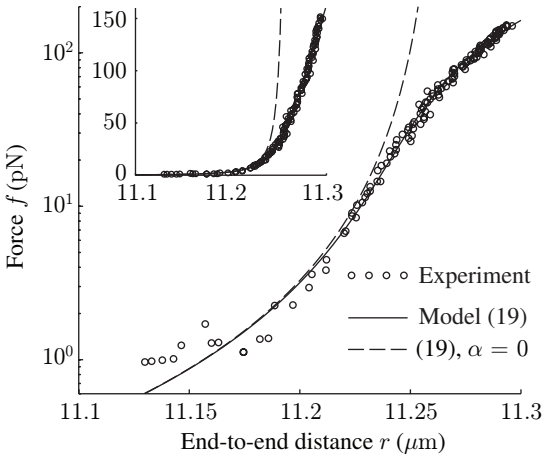

Figure 1.10: Fit of (1.19), solid curve, and its inextensible limit, dashed curve, to experimental data [36]. The contour length was measured as $L = 11.26\,\mu$m. Inset: linear axes show the deviation more pronounced. Adapted from [48].

In a recent development Blundell and Terentjev [86] use the Metropolis Monte Carlo method for modeling actin filaments. In contrast to all analytic approaches they require no linearization of the governing equations. Furthermore, they are able to subject the filament to arbitrary forces. As special cases, the authors show good agreement of the simulations with analytic solutions. The method can be extended to investigate external forces acting on any part of the filament or to explore the influence of steric constraints.

1.3.3 Discrete filaments networks: Mikado models

Two research groups published simultaneously two-dimensional discrete network models for cross-linked actin networks: Wilhelm and Frey [87] and Head et al. [88, 89]. While the former base their model on linear beams and concentrate on the scaling of the shear modulus, the latter investigate distinct elastic regimes of non-affine and affine deformation. Head et al. [88] consider bending (with modulus B_0) and stretching (with modulus μ_0) of filaments in two-dimensional representative area elements but neglect entropic contributions. The external force is balanced by the Hamiltonian of the worm-like chain model $\mathcal{H} = \mathcal{H}_{\text{bend}} + \mathcal{H}_{\text{stretch}}$, with the bending contribution defined in $(1.12)_2$ and the stretching contribution is [88]

$$\mathcal{H}_{\text{stretch}} = \frac{1}{2}\mu_0 \int \lambda^2 \,\mathrm{d}s. \tag{1.21}$$

Stiff cross-links allow free relative rotation of the filaments. The solution is obtained through linearization and minimization of the total energy. The dependence of the

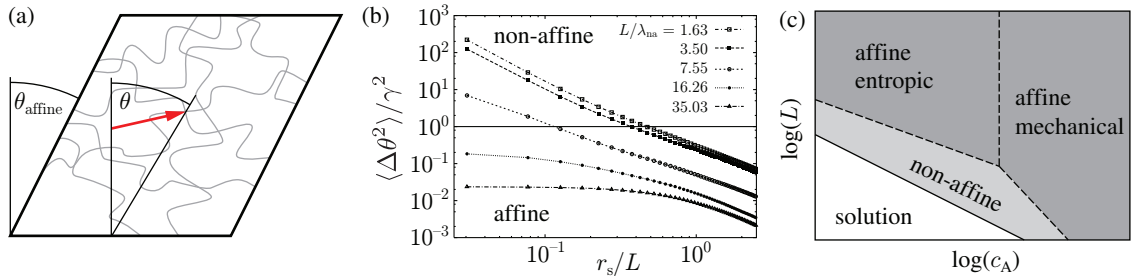

Figure 1.11: Non-affine deformations in actin networks. (a) Non-affine displacement of a cross-link in a network under simple shear denoted by the red arrow. The shear angle θ is not equal to the affine shear angle θ_{affine}. (b) Normalized affinity measure $\langle \Delta\theta^2 \rangle / \gamma^2$ versus normalized distance of two points r/L for varying L/λ_{na}. The solid line separates the non-affine from the affine deformation regime. (c) Elastic regimes depending on contour length L and actin concentration c_A. (b) and (c) are modified from [88].

results on the system size vanishes for very large systems. Head et al. determine the scaling of the bulk shear moduli for the non-affine and affine mechanical regime and support their arguments with numerical experiments. A network deforms in an affine or non-affine manner depending on the material properties of the filaments and the mesh size. The fundamental length scale for non-affine deformations λ_{na} is empirically determined as $\lambda_{\text{na}} = l_c^{4/3}(\mu_0/B_0)^{1/6}$, where l_c is the distance between two cross-links for a filament of contour length L. When $\lambda_{\text{na}} \ll L$ the network is observed to deform affinely while $\lambda_{\text{na}} \gg L$ corresponds to the non-affine regime. The degree of affinity depends also on the length scale r_s which is considered. In the numerical experiment, the macroscopic deformation is simple shear characterized by a shear strain γ which results in an affine shear angle θ_{affine}, where $\gamma = \tan\theta_{\text{affine}}$, see Fig. 1.11(a). By means of the actual shear angle θ the authors define an affinity measure on length scale r_s

$$\langle \Delta\theta^2(r_s) \rangle = \langle (\theta - \theta_{\text{affine}})^2 \rangle, \tag{1.22}$$

where the angled brackets denote an averaging. The monotonically decreasing curves in Fig. 1.11(b) suggest that the deformation is more affine, the larger the length of interest r_s is. Values for the normalized non-affinity measure $\langle \Delta\theta^2(r) \rangle / \gamma^2$ smaller than one, i.e. underneath the solid line, are considered affine. Depending on the actin concentration c_A in the sample and the contour length L of the filaments, Head et al. [88] are able to identify distinct regimes non-affine and affine deformation at a fixed length scale r_s. For very low c_A and L, there are not enough or too short filaments in the sample to build a network. Hence, the actin is in solution. For medium c_A and L, we observe a phase change to a loose network which deforms non-affinely. In the case of large contour lengths, the network deforms affinely with a dominating entropic contribution to the filament elasticity, i.e. straightening out the thermal

fluctuations requires the major amount of work. For dense networks with large actin concentrations c_A, the affine deformation is dominated by stretching. The elongation of the filaments stores energy in a mechanical manner. Onck et al. [90] investigated network properties for large macroscopic shear strains. They use the finite element method on simpler 2D randomly oriented Euler-Bernoulli beam elements accounting for stretching and bending. They also assume stiff cross-links in networks with small filament density. The small strain response is dominated by bending of filaments resulting in a soft response and non-affine network reorientation. After a transition to stretching dominated deformations at higher shear strains the deformation mode is more affine. Missel et al. [91] develop a 2D model with bending and stretching elasticity and Poisson distributed filaments. The nematic order parameter $S \in [0, 1]$ is a measure for the anisotropy with $S = 0$ meaning isotropy and $S = 1$ corresponds to perfectly aligned filaments. The floppy modes model [92], which explains the small strain shear modulus for materials with increasing anisotropy very well, is confirmed by numerical experiments. A higher degree of filament alignment results in a higher chance of filaments to buckle and thereby lowering the current shear modulus. It is worth noting that the geometric measure of nonaffinity (1.22) is independent of anisotropy. Unfortunately, Missel et al. [91] restrict themselves to the small strain regime.

Additional properties may be investigated with 2D discrete network models. Conti and MacKintosh [47] use the same network technology to investigate the normal stress response in simple shear. Their findings are in qualitative agreement with experimental results [39]. Interestingly, a smaller bending modulus B_0 results in a more pronounced normal stress response. They conclude that an asymmetric force-extension relation of filaments are the reason for the exceptional normal stress. Head et al. [93] apply local perturbations to filament networks similar to the experimental method of Mizuno et al. [94]. Their results indicate the importance of modeling the active behavior of motor proteins. DiDonna and Levine [95] present a mean-field theory for cross-linker unfolding in discrete networks. The filaments are linear springs while the cross-linkers are subjected to a sawtooth-shaped force-extension relationship. Although the model is oversimplified we can learn about the unfolding mechanisms influencing the softening of cross-linked actin networks in the very large strain regime. A second mechanism related to the cross-linking proteins causes softening of actin networks. When the force in a bond exceeds a critical value F_cr, these bonds may rupture. Abhilash et al. [96] investigated forced bond dissociation by modeling 2D Euler-Bernoulli beams connected though spring elements. The cross-link dissociation is not determined but decided through a kinetic Monte Carlo algorithm. Representative networks under shear are depicted in Fig. 1.12(a) for varying shear rates $\dot{\gamma}$. The normalized stiffness G/G_0 increases independently of the shear rate. The ultimate strain, and hence the ultimate normalized stiffness, increases notably with increasing deformation speed.

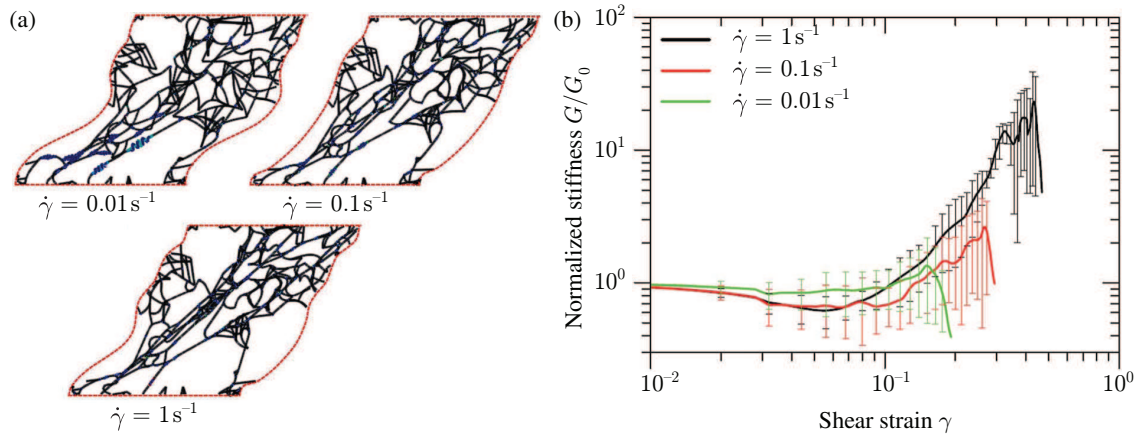

Figure 1.12: Influence of the shear rate ($\dot{\gamma} = 0.01, 0.1, 1\,\mathrm{s}^{-1}$) on cross-link rupture. (a) Deformed network configurations at $\gamma = 0.5$. (b) Shear modulus G normalized by the initial shear modulus G_0 versus shear strain γ for 25 network realizations and stochastic bond dissociation. Adapted from [96].

The 2D networks are relatively simple to generate, however, they have only a limited predictive capability. Therefore, the efforts in modeling discrete filament networks shifted towards the analysis of 3D models. Common to all 3D models is the problem of cross-linking. In 2D systems, the randomly generated filaments are simply linked at the locations where they cross each other. The additional dimension makes it very unlikely that two filaments meet at one position. There are currently two solution to this problem. First, filaments are randomly generated and subsequently moved by an attractive force or the Monte-Carlo method is employed to bring two neighbors in close proximity to each other. Then cross-links are established at the points of the smallest distance. This method is used by, e.g., Huisman et al. [97]. In the second approach, an initial network topology is generated by connecting points in a volume element. Then the free energy of the network is minimized by means of the Monte Carlo minimization scheme, see, e.g., [98].

The two-dimensional approach [90] was transferred to three-dimensional representative volume elements by Huisman et al. [97], where Euler-Bernoulli beams with bending and stretching and adding an additional twisting mode include static undulations to mimic the filament shape due to thermal activity. These undulations soften the networks in the case of semiflexible filaments but not for stiff filaments. Figure 1.13(a) relates the stored energies associated with bending and stretching and color codes the filaments accordingly, red representing bending dominated and blue representing stretching dominated deformation. For a shear strain of $\gamma = 0.5$, several (blue) filaments oriented in the principal strain direction are highly stretched. The non-affine reorientation of filaments can be observed by following a filament over several time steps as in Fig. 1.13(b). Figure 1.13(c) shows a visualization of non-affinity

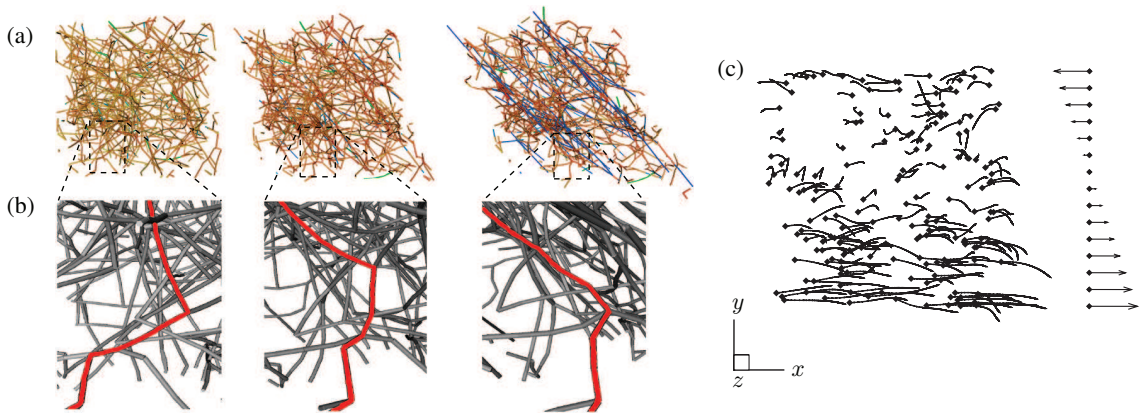

Figure 1.13: Three-dimensional network of Euler-Bernoulli beams. (a) Snapshots for shear strains of $\gamma = 0.1$, 0.3 and 0.5. Bending dominated filaments are marked in red, while blue marks the stretching dominated filaments. (b) Enlarged section of (a) following one filament in its reorientation and stretching. (c) Displacement map of cross-links with diamonds indicating the reference position. The arrows show the affine deformation. Modified from [97]

through the trajectories of 20% of the cross-links in the x-y-plane. The diamonds mark the reference position and the arrows show the affine deformation. Huisman et al. [98, 99] create 3D networks based on the inextensible worm-like chain with the energy defined by $(1.12)_2$. This model is able to replicate the typical nonlinear strain stiffening response of cross-linked actin networks. Conversely to the conclusions in [90] obtained from 2D networks, Huisman et al. [98] observe that non-affinity increases with increasing macroscopic strain γ. They observe collective reorientations, i.e. large local displacements during a small strain increment.

The authors plot the incremental shear modulus $G = \partial\sigma_{xy}/\partial\gamma$ normalized by the initial shear modulus $G_0 = G(\gamma = 0)$ versus the shear stress σ_{xy} normalized by the critical shear stress $\sigma_{xy,\mathrm{c}}$, i.e. the shear stress at which strain-stiffening starts [98]. They obtain a master curve, for various degrees of network connectivity, described by

$$\frac{G}{G_0} \propto \begin{cases} 1 & \text{if } \sigma_{xy}/\sigma_{xy,\mathrm{c}} < 1, \\ \left(\dfrac{\sigma_{xy}}{\sigma_{xy,\mathrm{c}}}\right)^{3/2} & \text{if } \sigma_{xy}/\sigma_{xy,\mathrm{c}} \geq 1, \end{cases} \tag{1.23}$$

where the power law exponent 3/2 for the supercritical regime is observed experimentally for actin networks with rigid cross-links [41].

In their following study, Huisman et al. [99] examine dynamic experiments. They model the influence of the fluid surrounding the filaments by means of axial, perpendicular and rotational drag. Hence, they build a network as a viscoelastic solid while

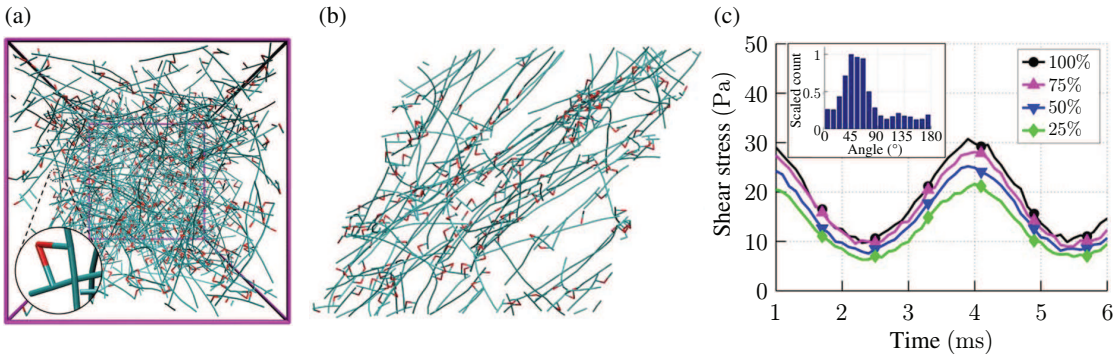

Figure 1.14: Discrete fiber network in 3D. (a) Example of a representative volume element. (b) Reduced network with the most strained cross-links. (c) Results of a computational oscillation shear experiment with the fraction of remaining cross-links. Inset: angular distribution of the remaining fibers. Adapted from [102].

the filaments are purely elastic. The model reproduces the power law relationship of the storage modulus G' and the loss modulus G'' with the frequency f at high frequencies with an exponent of 3/4, which was predicted theoretically [100]. Kim et al. [101] introduce a computational method for actin polymerization and cross-linking kinetics by means of Brownian dynamics, see Fig. 1.14(a) for an example of a representative volume element. In their follow-up study, Kim et al. [102] examine the viscoelastic properties of these networks under simple shear by coarse graining the individual actin monomers to cylindrical segments. They show that these structures possess a supportive framework, i.e. only relatively few filaments bear a majority of the applied load, see Fig. 1.14(b) and (c). The inset shows that the remaining fibers are mainly oriented in the direction of the first principal strain. In this context, recall the stretched filaments in Fig. 1.13(a). They find the power law dependence of G' and G'' from f with an exponent of 3/4.

Žagar et al. [103] use the same network assembly procedure as in [97] to obtain a 3D topology. They find a low number of cross-links in the network, i.e. a low network connectivity. This is a crucial parameter for the initial stiffness while for high connectivity the influence on the initial stiffness diminishes. The authors confirm the findings of [98] and obtain a similar master curve for the G/G_0-$\sigma_{xy}/\sigma_{xy,\mathrm{c}}$-relation with a power law exponent of 3/2 for the supercritical regime. Žagar et al. [103] attribute the linear regime at small strains to bending and reorientation of filament sections. The large strain region with the nonlinear stiffening is dominated by axial stretching of filaments, cf. [97]. They find, similar to [101], a supportive network evolving for large strains. From the supportive network concept they conclude that the large strain network response must be proportional to the straightening of a single, very long percolated and undulated chain. Indeed, Žagar et al. find the power law exponent in a very simple fashion under reference to the filament model of [104].

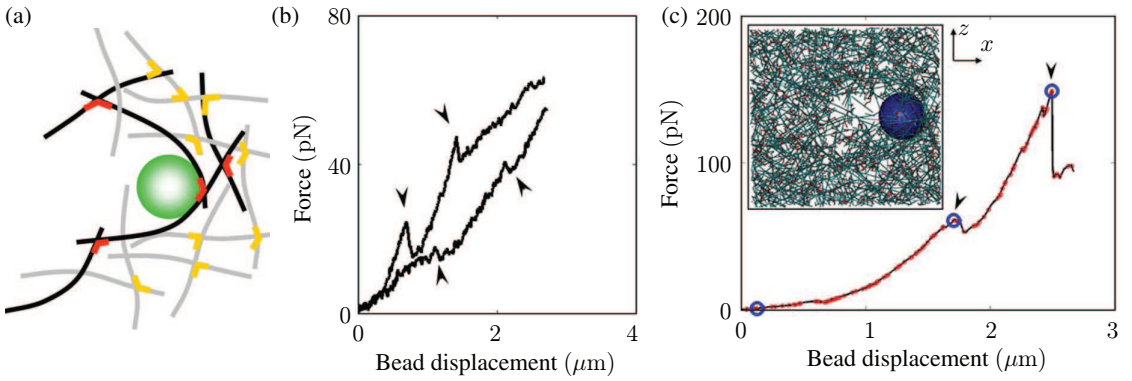

Figure 1.15: Discrete fiber network in 3D. (a) Schematic of the micro-bead experiment with (b) experimental and (c) numerical results. The arrows indicate forced unbinding of cross-links. Inset: setup of the numerical model. Adapted from [105].

Lee et al. [105] use a micrometer sized polystyrene bead inside a cross-linked actin network and and attach it to a filament. Then, they pull on the filament by optically trapping the bead and thus induce a local deformation. The authors model the experiment by means of modified networks taken from [102]. Figure 1.15(a) shows a schematic of the experiment with filaments (gray) and cross-linkers (yellow). The filaments with the largest stress (black) are likely to cause rupture of their cross-linkers (red). By comparing experimental results, see Figure 1.15(b), with computational data, see Figure 1.15(c), we observe a qualitative agreement. Sudden drops of the curves are due to spontaneous cross-linker unbinding in the proximity of the micro-bead and, therefore, indicate the damage mechanism.

Cyron et al. [106] include the stochastic features of actin filaments, expressed through random thermal undulations. They separate the governing forces and moments into viscous, stochastic and external parts comprising the equilibrium equation. The viscous parts account for the damping by the surrounding fluid. Brownian dynamics is captured through the stochastic parts. The external parts represent deterministic interactions between filaments, cross-linkers and the surrounding fluid. The equilibrium equation becomes a stochastic partial differential equation. The cross-links are considered as flexible with stretching, shear, torsion and bending stiffness. They cannot actively produce force, i.e. they are not motor proteins. The cross-linker proteins are included as entities and their binding kinetics is modeled similar to [101]. The cross-linkers bind under a preferred angle with a tolerance around it. Solutions for the model are obtained by means of the finite element method. Cyron et al. reproduce correctly the high frequency power law between G', G'' and f with exponent 3/4. Depending on the preferred binding angle and tolerance of the cross-linkers they achieve to reconstruct different morphologies for their networks, see Fig. 1.16.

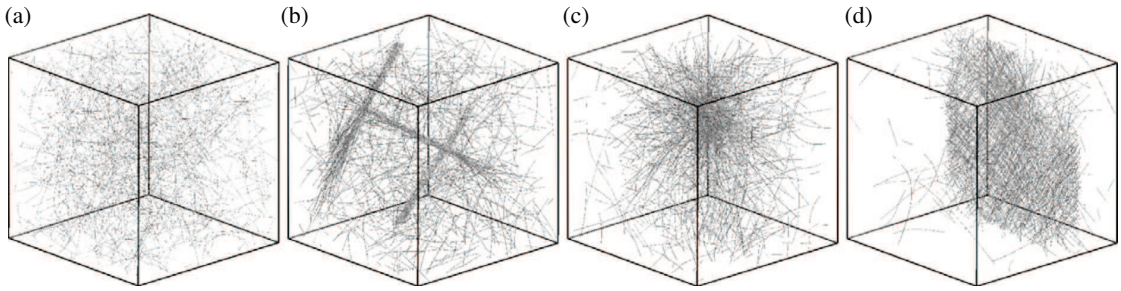

Figure 1.16: Network polymorphism with (a) isotropic, (b) bundle, (c) cluster and (d) layer network phases. Adapted from [106].

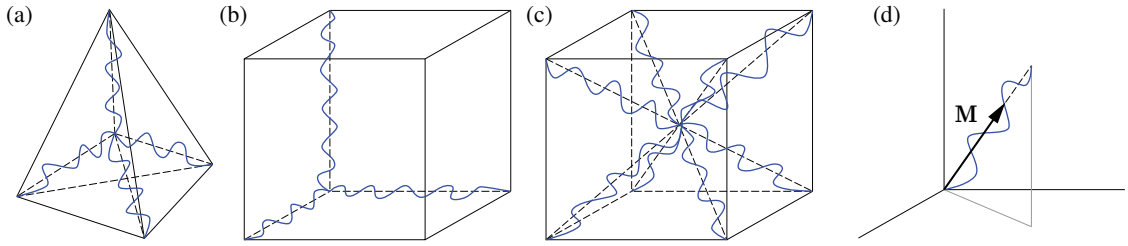

Figure 1.17: Spatial arrangement of chains in network models: (a) 4-chain model, (b) 3-chain model, (c) 8-chain model and (d) full network model with direction vector $\mathbf{M}$ in the reference configuration.

1.3.4 Micro-structurally motivated continuum mechanical models

The discrete filament networks are limited in their size by the current computational possibilities. Larger systems may be investigated using continuum mechanics. Two-scale models for cross-linked actin networks within the continuum mechanical framework are, in general, based on developments in rubber elasticity. In continuum mechanics we describe a deformation with the deformation gradient $\mathbf{F} = \operatorname{Grad} \mathbf{x}(\mathbf{X})$, where $\mathbf{X}$ and $\mathbf{x}$ describe a curve in the reference and the current configuration, respectively. The high water content in actin networks leads to the assumption of incompressibility, where the Jacobian $J = \det \mathbf{F} = 1$. The right Cauchy-Green tensor $\mathbf{C} = \mathbf{F}^\top \mathbf{F}$ and the left Cauchy-Green tensor $\mathbf{b} = \mathbf{F}\mathbf{F}^\top$ are commonly used kinematic measures which are independent of rigid body motions.

The basic idea, common to all two-scale continuum models, is to use a force-extension relationship, as in Section 1.3.2, for actin filaments in a three-dimensional ensemble and a subsequent homogenization. This is achieved using network models for polymers. The earliest of these models is the 4-chain model [107] which was later extended [108], see, Fig. 1.17(a). Four filaments are arranged in a tetrahedron and are connected at the center point. The center point displaces non-affinely and its position needs to be determined by solving the equilibrium equations iteratively. The 3-chain

model [109] is a simplified network, shown in Fig. 1.17(b). In this case the chains need to be oriented in the principal strain directions. Both models are dependent on the orientation of the volume element with respect to the principal stretch axes [110]. Arruda and Boyce [111] developed the eight-chain model, which eliminates this 'anisotropy' by adding cubic symmetry, see, Fig. 1.17(c). The root-mean square of the principal stretches is

$$\lambda_{\mathrm{AB}} = \sqrt{I_1/3}, \tag{1.24}$$

where $I_1 = \operatorname{tr}\mathbf{C} = \operatorname{tr}\mathbf{b}$ is the first invariant of the right or left Cauchy-Green tensor. The strain-energy function Ψ for the eight-chain network is then given as $\Psi = nw(\lambda_{\mathrm{AB}})$, where n is the number of filaments per unit reference volume (filament density) and $w(\lambda_{\mathrm{AB}})$ is the strain energy of a single filament. Palmer and Boyce [82] apply the eight-chain model to cross-linked actin networks. They define the current end-to-end distance of a filament as $r = \lambda_0\lambda_{\mathrm{AB}}r_0$, where λ_0 is a pre-stretch. The Cauchy stress tensor is calculated according to $\boldsymbol{\sigma} = -p\mathbf{I} + 2\mathbf{F}(\partial\Psi/\partial\mathbf{C})\mathbf{F}^{\top}$, see, e.g., [112], where p is the Lagrange multiplier associated with incompressibility, and thus,

$$\boldsymbol{\sigma} = -p\mathbf{I} + \frac{n\lambda_0 w'}{3\lambda_{\mathrm{AB}}}\mathbf{b}. \tag{1.25}$$

The single filament is represented by (1.16) with $w'(\lambda_{\mathrm{AB}}) = f(\lambda_{\mathrm{AB}})r_0$, where the prime denotes the derivative with respect to λ_{AB}. When the shear stress is fitted against the experimental data in [41], this model gives plausible scaling for the involved material parameters. It may also be applied to networks with filament bundles. Palmer and Boyce relate a bundle of m filaments to an effective filament with a larger radius. By means of the area moment of inertia they determine an effective persistence length $L_{\mathrm{p},m}$ which is related to the persistence length of a single filament L_{p} through $L_{\mathrm{p},m}/L_{\mathrm{p}} = m^2$. While this model appeals through its simplicity, it fails to describe the normal stress response correctly. In fact, when using the plane stress condition the normal stress is zero.

Finally, the full network model, introduced by Treloar and Riding [113] and extensively discussed in [114], suggests to consider filaments in all steric directions, see, Fig. 1.17(d). These directions are denoted as $\mathbf{M}$ in the reference configuration, creating a (micro-)sphere Ω with their arrowheads, and map according to $\mathbf{m} = \mathbf{FM}$ to the current configuration. The calculation of the stress tensors requires the solution of integrals over the surface of this sphere. The full network model can be applied to cross-linked actin networks, reflecting affine deformation of the filaments [37, 115]. Therefore it is referred to as affine network model. A filament which was initially oriented in the direction $\mathbf{M}$ attains a stretch of $\lambda_{\mathrm{AN}} = (\mathbf{m}\cdot\mathbf{m})^{1/2}$. The end-to-end distance of the filament is thus changed to $r = \lambda_{\mathrm{AN}}r_0$. The filaments may have an

angular distribution $\rho(\mathbf{M})$ over the micro-sphere Ω, so that

$$\frac{1}{4\pi}\int_{\Omega}\rho(\mathbf{M})\,\mathrm{d}\Omega = 1. \tag{1.26}$$

The strain-energy function is then the sum of the strain energies of the single filaments, i.e.

$$\Psi = n\int_{\Omega}\rho(\mathbf{M})w(\lambda_{\mathrm{AN}})\,\mathrm{d}\Omega. \tag{1.27}$$

Note that λ_{AN} and thus the strain energy of the filament is a function of the right Cauchy-Green tensor $\mathbf{C}$. The Cauchy stress tensor is then given as [115]

$$\boldsymbol{\sigma} = -p\mathbf{I} + n\int_{\Omega}\rho(\mathbf{M})\frac{w'}{\lambda_{\mathrm{AN}}}\mathbf{m}\otimes\mathbf{m}\,\mathrm{d}\Omega, \tag{1.28}$$

where $\otimes$ denotes the dyadic product. The prime denotes the partial derivative with respect to the affine stretch λ_{AN} and is connected to the force extension relationship, e.g., equation (1.19), through $w'(\lambda_{\mathrm{AN}}) = f(\lambda_{\mathrm{AN}})r_0$. When modeling experiments conducted on reconstituted cross-linked actin networks, the samples are thought to be isotropic and thus $\rho(\mathbf{M}) = 1$.

Storm et al. [37] model a large variety of biopolymer networks by means of the affine network with the extensible version of the model by MacKintosh et al., i.e. (1.14) enhanced with (1.20). Additionally they assume that the end-to-end distance of the filaments of equal contour length is distributed according to [116]. This leads to a network where the stress tensor does not vanish when $\mathbf{F} = \mathbf{I}$. The deformation gradient at zero stress may be determined by solving the equilibrium equations. With this extended theory Storm et al. obtain insight into the scaling of the incremental shear modulus and show a good agreement with experimental data of fibrin networks (a protein associated with blood coagulation) at different protein concentrations.

Van Oosterwyck et al. [117] use an inextensible filament model (1.16) with the affine network and observe locking of the model as the end-to-end distance r reaches the contour length L in the principal strain direction. This limitation of the affine network is pointed out earlier [111]. They overcome this phenomenon by allowing for junctional sliding. This is implemented with a variable contour length, which increases when the filament stretch λ_{AN} exceeds a critical value making larger values for r possible. The parameter identification for this model is very challenging as it requires a nested optimization to determine the sliding function as well as the parameters in model (1.16).

The study of Holzapfel et al. [115] enhances the affine network model by considering the finite stiffness of cross-linkers. The model adds a part of a cross-linker to the end of a filament resulting in two nonlinear springs connected in series. The actin

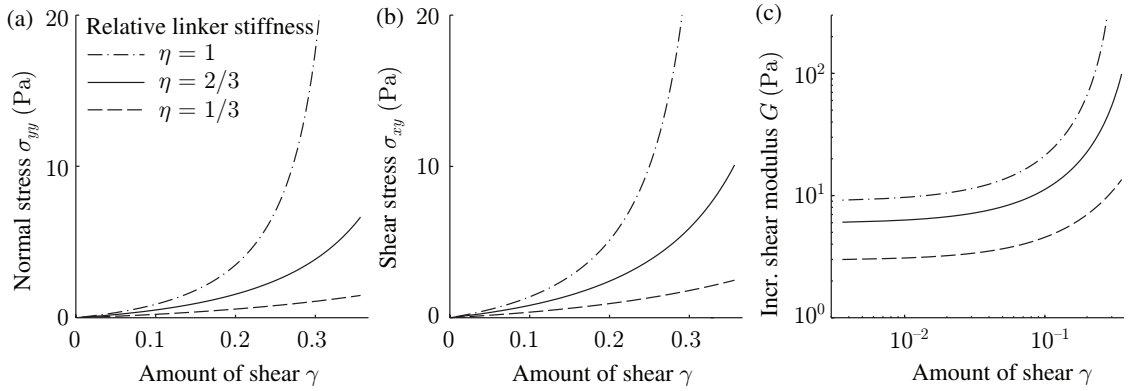

Figure 1.18: Effect of the relative linker stiffness η on the Cauchy normal stress σ_{yy}, the shear stress σ_{xy} and the incremental shear modulus G. Adapted from [115].

filament is represented through the inextensible model $(1.11)_2$. The relative linker stiffness $\eta \in (0, 1]$ relates the elongation Δr_f of the actin filament to the total elongation Δr, i.e. $\Delta r_\mathrm{f} = \eta \Delta r$. Consequently $\eta = 1$ denotes a perfectly rigid cross-link which becomes softer as $\eta \to 0$. By means of the force equilibrium between the filament and the cross-linker we can determine the strain energy $w(\lambda_\mathrm{AN})$ stored in both constituents which may be used in (1.28). Figure 1.18 shows the influence of η on the Cauchy normal stress σ_{yy} and shear stress σ_{xy} in the simple shear experiment. Additionally the figure depicts the incremental shear modulus $G = \partial \sigma_{xy} / \partial \gamma$. The model reproduces the exceptional normal stress behavior. The relative cross-linker stiffness softens the material without altering the overall characteristics. When considering measurements of actin networks with a specific actin concentration and a specific cross-linker concentration, the stiffness varies with different linker proteins. In particular, the comparison of the experimental data in [48, 118] reveals that networks with heavy meromyosin as linker proteins exhibit a higher stiffness than actin/filamin networks. These data are in qualitative agreement with the model for $\eta = 1$ and $\eta = 1/3$, respectively, suggesting different cross-linker properties.

Unterberger et al. [48] use the non-affine homogenization method, introduced by Miehe et al. [119], to obtain a mean stretch of the filaments and define the strain-energy function as $\Psi = nw$. The homogenized stretch λ_NA is defined as

$$\lambda_\mathrm{NA} = \left(\frac{1}{4\pi} \int_\Omega \lambda_\mathrm{AN}^q \, \mathrm{d}\Omega \right)^{1/q}, \tag{1.29}$$

say the q-root average over the surface of the micro-sphere Ω. This means, that the filament stretch is allowed to fluctuate around its affine value. The magnitude of this fluctuation is mediated by q. The current end-to-end distance of the average filament

is $r = \lambda_0 \lambda_{\mathrm{NA}} r_0$. The Cauchy stress tensor is calculated as

$$\boldsymbol{\sigma} = -p\mathbf{I} + \overline{\boldsymbol{\sigma}}, \qquad \overline{\boldsymbol{\sigma}} = \frac{n w' \lambda_{\mathrm{NA}}^{1-q}}{4\pi} \int_\Omega \lambda_{\mathrm{AN}}^{q-2} \mathbf{m} \otimes \mathbf{m} \, \mathrm{d}\Omega, \tag{1.30}$$

where $w' = f(\lambda_{\mathrm{NA}}) \lambda_0 r_0$. This model includes the eight-chain network as a special case for $q = 2$. The normal stress response in the simple shear experiment is

$$\sigma_{yy} \begin{cases} = 0 & \text{if } q = 2, \\ < 0 & \text{if } q < 2, \\ > 0 & \text{if } q > 2. \end{cases} \tag{1.31}$$

The latter case represents the exceptional normal stress of actin networks as described by Janmey et al. [39]. The model compares well with experimental data of actin/heavy meromyosin networks. It may be extended to the viscoelastic regime with k Maxwell elements parallel to the elastic contribution as shown in [120]. This extension is easiest accomplished in the reference configuration. Therefore, we pull back the Cauchy extra stress tensor $\overline{\boldsymbol{\sigma}}$ to the second Piola-Kirchhoff extra stress tensor $\overline{\mathbf{S}} = \mathbf{F}^{-1} \overline{\boldsymbol{\sigma}} \mathbf{F}^{-\top}$ (with the transformation rule for incompressible deformations). The viscoelastic second Piola-Kirchhoff stress is then [121]

$$\mathbf{S}_{\mathrm{ve}} = -p\mathbf{C}^{-1} + \overline{\mathbf{S}} + \sum_{\nu=1}^{k} \mathbf{Q}_\nu, \tag{1.32}$$

where $\mathbf{Q}_\nu$ are the non-equilibrium stress tensors. They are determined through the evolution equations

$$\dot{\mathbf{Q}}_\nu + \frac{\mathbf{Q}}{\tau_\nu} = \theta_\nu \dot{\overline{\mathbf{S}}}, \tag{1.33}$$

where the relaxation times τ_ν and the free-energy parameters θ_ν are material parameters associated with the viscous behavior of the material. After determining the non-equilibrium stress tensors $\mathbf{Q}_\nu$, we may push them into the current configuration, i.e. $\mathbf{q}_\nu = \mathbf{F} \mathbf{Q}_\nu \mathbf{F}^\top$, and obtain then viscoelastic Cauchy stress tensor

$$\boldsymbol{\sigma}_{\mathrm{ve}} = -p\mathbf{I} + \overline{\boldsymbol{\sigma}} + \sum_{\nu=1}^{k} \mathbf{q}_\nu. \tag{1.34}$$

Unterberger et al. [120] perform three experiments to determine the material parameters of the model: (i) large strain oscillation shear (LAOS), (ii) amplitude sweep and (iii) frequency sweep, see Fig. 1.19. They find that for a fixed frequency, only one Maxwell element (with one relaxation time τ_1 and free-energy parameter θ_1) is required a obtain a good fit over a large range of amplitudes, see Fig. 1.19(a) and (b). In order to also cover frequencies over three orders of magnitude, two additional Maxwell elements are required, see Fig. 1.19(c).

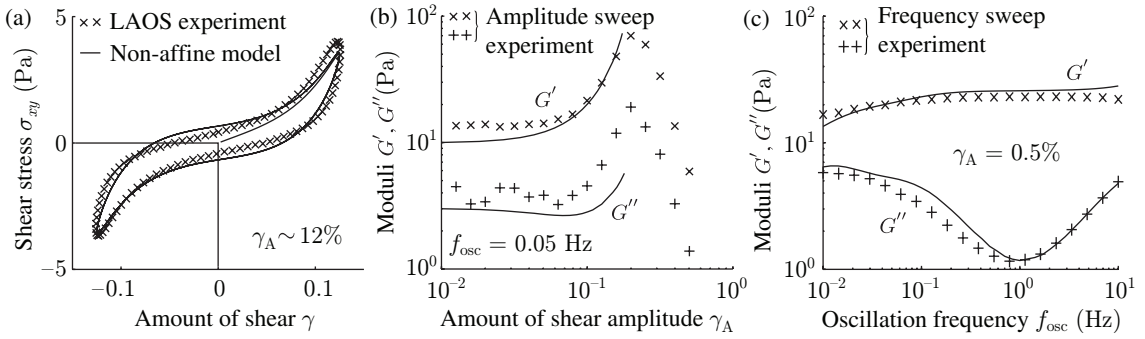

Figure 1.19: Simultaneous fit of three experiments investigating the viscoelasticity of an actin network. Adapted from [120].

All of these previously described continuum network models are capable of being implemented as custom materials into finite element (FE) programs. The FE method may then be used to solve problems which resemble more complex experiments. Indeed, Unterberger et al. [48, 120] use the non-affine viscoelastic material model to investigate the indentation of a sphere into a cross-linked actin network. This model is similar to the indentation of the tip of an atomic force microscope into a cell. Micropipette aspiration is simulated by a hollow droplet consisting of actin in [115, 120]. Qualitatively, the numerical models compare well to experiments conducted on living cells.

The full network models achieve a homogenization of the microstructure by integration over a micro-sphere Ω, see (1.26)–(1.30). Computationally, the evaluation is an expensive endeavor and calls for clever numerical schemes in order to efficiently obtain the desired results. Bažant and Oh [122] developed a method which allows the reduction of the integral to a discrete sum

$$\int_{\Omega} \mathbf{A}(\mathbf{M})\,\mathrm{d}\Omega \sim 4\pi \sum_{i=1}^{m} \mathbf{A}(\mathbf{M}^i) q^i, \tag{1.35}$$

where $\mathbf{A}$ is an arbitrary scalar or tensor associated with the direction $\mathbf{M}$. The $i = 1 \ldots m$ direction vectors $\mathbf{M}^i$, together with the appropriate integration weights q^i are provided in tables for different m. The simplest scheme with 42 directions is correct to the polynomial degree 9 and fully symmetric. Hence, half of the points ($m = 21$) and doubling the integration weights suffice to define the scheme. Table 1.1 restates the according values from [122].

Broedersz et al. [123, 124] use a completely different approach to model the components in actin networks by introducing an effective medium, in which a rigid rod (actin) of length L is connected to the surrounding linear elastic medium through

Table 1.1: Components M_k^i of the 21 radius vectors $\mathbf{M}^i$ of the unit hemisphere and associated integration weights q^i according to [122], Table 1 therein.

i	M_1^i	M_2^i	M_3^i	$q^i/2$
1	0.0	0.0	1.0	0.0265214244093
2	0.0	1.0	0.0	0.0265214244093
3	1.0	0.0	0.0	0.0265214244093
4	0.0	0.707106781187	0.707106781187	0.0199301476312
5	0.0	−0.707106781187	0.707106781187	0.0199301476312
6	0.707106781187	0.0	0.707106781187	0.0199301476312
7	−0.707106781187	0.0	0.707106781187	0.0199301476312
8	0.707106781187	0.707106781187	0.0	0.0199301476312
9	−0.707106781187	0.707106781187	0.0	0.0199301476312
10	0.836095596749	0.387907304067	0.387907304067	0.0250712367487
11	−0.836095596749	0.387907304067	0.387907304067	0.0250712367487
12	0.836095596749	−0.387907304067	0.387907304067	0.0250712367487
13	−0.836095596749	−0.387907304067	0.387907304067	0.0250712367487
14	0.387907304067	0.836095596749	0.387907304067	0.0250712367487
15	−0.387907304067	0.836095596749	0.387907304067	0.0250712367487
16	0.387907304067	−0.836095596749	0.387907304067	0.0250712367487
17	−0.387907304067	−0.836095596749	0.387907304067	0.0250712367487
18	0.387907304067	0.387907304067	0.836095596749	0.0250712367487
19	−0.387907304067	0.387907304067	0.836095596749	0.0250712367487
20	0.387907304067	−0.387907304067	0.836095596749	0.0250712367487
21	−0.387907304067	−0.387907304067	0.836095596749	0.0250712367487

n_{cl} compliant cross-linkers. Hence, they hypothesize that the actin filaments possess negligible compliance compared to the cross-linkers. Figure 1.20(a) and (b) schematically shows such a 'hairy rod' inside the effective medium in the reference and the current configuration. The tension f in the rod is determined by the force in the cross-links f_{cl}, i.e.

$$f(\varepsilon) = \frac{n_{\mathrm{cl}}}{L} \int_0^{L/2} f_{\mathrm{cl}}(x, \varepsilon)\, \mathrm{d}x, \tag{1.36}$$

where x is the position along the actin filament and ε is the extensional strain of a single linker protein. The force in the cross-link depends on the properties of the cross-link itself and on the elasticity of the effective medium. The linker proteins are modeled as worm-like chains using (1.13). The surrounding effective medium is either (i) linear elastic with a spring constant K_{EM} or (ii) self-consistent with the nonlinear elasticity of the hairy rods. In the latter case, the stiffness of the effective

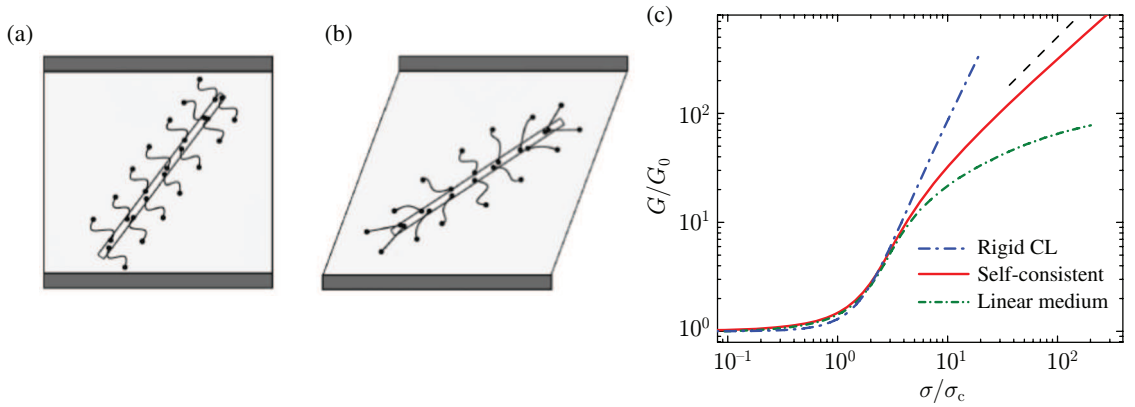

Figure 1.20: Effective medium approach. (a) Rigid rod connected to the surrounding elastic continuum through flexible cross-links. (b) Nonuniform deformation of the cross-links in the current configuration. (c) Normalized current shear modulus versus normalized shear stress for rigidly cross-linked semiflexible filaments, the self-consistent model and linear medium model. The dashed line indicates a slope of 1. Modified from [123, 124]

medium is

$$K_{\mathrm{EM}} = \frac{\alpha}{n_{\mathrm{cl}} L} \frac{\mathrm{d}f}{\mathrm{d}\varepsilon}, \tag{1.37}$$

where α is a geometric constant. Figure 1.20(c) shows a comparison of the two cases. Broedersz et al. [123] also add a rigidly cross-linked network consisting of semiflexible filaments [56]. In the high stress regime, the self-consistent model softens compared to the rigidly cross-linked network and attains a slope of 1 which is consistent with experimental data for actin/filamin networks from, e.g., [125]. The hairy rods may also be integrated into an affine network [124].

1.4 Summary and conclusion

The next higher scale in modeling after considering the network level spans from networks to cells. Additionally to the actin network, many more components of the cell contribute to the overall mechanics, especially other cytoskeletal proteins, the membrane and the nucleus. Certainly, all these constituents also interact with each other leading to very complex relationships. Only a few studies accept the challenge for modeling, often simplifying to a very high degree. For example, [126] use a fluid filled neo-Hookean membrane to account for different structures. [127] apply a linear viscoelastic model including various phenomena, i.e. network polymerization/depolymerization, swelling and network-membrane interaction. Discrete sets of filaments are included in the model of [18], which is divided into three layers. [128] create a tensegrity structure to model the osteocyte. Growth and remodeling of cells

with a micro-structural motivation is proposed by [20]. These models are naturally very crude due to the very limited knowledge of the complicated interactions of the components of the cell. They promote, however, numerous experiments.

1.4.1 Discussion

In this chapter we introduced mechanical models for actin which assembles into filaments and subsequently into networks. The smallest scale we focus on utilize molecular dynamics simulations dealing with only a few molecules. The method is based on simple physical laws and is, therefore, suitable to investigate a broad range of hypotheses. On this length scale, however, experimental validation of simulations is very challenging and in many cases impossible with current technology. We observe a similar situation for coarse-grained methods, where medium-sized filaments are considered. The continuum models for filaments neglect the mechanical features which arise from the molecular structure and the helical assembly of the molecules. The force-extension may be compared to experiments on single filaments. It turns out that in the regime where the end-to-end distance r approaches the contour length L, inextensible continuum models render the filaments too stiff. Only extensible models estimate the force for large extensions correctly and are also able to predict the behavior when r exceeds L.

Mikado models, with their arrangement of discrete filaments, are excellently suited to model effects of variations of filament and cross-linker properties including dynamic phenomena like protein unfolding and cross-linker kinetics on the network. The approach, however, still suffers from some limitations. First, current models are either two-dimensional and/or their representative volume element is of small size. For reliable predictions, which are fairly independent of the boundaries we require elements where the side length exceeds the filament length several times. This results in high computational cost and requires a high degree of parallelization in the future. With current computational power only relatively small representative volume elements are feasible to solve and this prevents the consideration of problems with sizes comparable to real systems. Some studies use linear filament models and allow only for small strains in the polymer chains. Interestingly, the networks still show the typical strain stiffening. To our knowledge, a systematic investigation concerning such assumptions with a comparison with networks comprising nonlinear filaments is missing in the literature.

While continuum mechanical models are very efficient in terms of computational cost, we loose microstructural information by homogenizing the network. The comparison by [104] of a two-dimensional version of the affine network model [37] to the discrete network model of [90] shows, that for small filament densities non-affine rearrangement dominates. However, the discrete network calculations approach the

affine shear stress values for high densities. We may generalize these conclusions to three-dimensional networks and require that affine continuum models should only be used to model densely cross-linked actin networks.

For both model types, i.e. Mikado models and continuum network models, the predictions are frequently compared to experimental data gained from rotational rheometry. In the models, however, the deformation mode is simple shear and the authors rely on the assumption that this mode approximates the rotational shear well. [129] show that this assumption is justified in a limited way. Especially, the normal stress response is dramatically dependent on the boundary conditions.

1.4.2 Open problems

Biomechanical modeling on small scales is a relatively young and emerging topic. It receives increasing attention since these scales are now also experimentally accessible through recent improvements in techniques. In this sense, we are only at the beginning of an exciting time, in which an endless number of issues is worth to be addressed. We want to highlight only a few of these issues, which often require a joint effort of experimentalists and researchers concerned with modeling.

- Improvements in experimental techniques on the nanoscale are needed to verify the mechanical properties of G-actin and the interaction between the molecules in a filament.

- Actin networks inside living cells build several structures with varying degree of anisotropy. In vitro reconstituted networks are believed to develop randomly and thus create an isotropic network. A quantification of the anisotropy of cross-linked actin networks may confirm the assumption of isotropy for in vitro networks and trigger improved models for in vivo actin.

- The importance of the type of cross-linker protein in experiments highlights the need for models considering their influence. The stiffness of the linkers and their interactions with the actin filaments potentially change the incremental bulk shear modulus.

- Various models for transient phenomena in cross-linked actin networks are proposed in the literature. For instance, actin polymerization/depolymerization or cross-linker kinetics strongly influence the mechanical behavior. Reliable experimental evidence for the mechanisms and corresponding material parameters are missing.

- The cytoskeleton consists of a multitude of proteins and interactions between actin networks and other cytoskeletal filaments are not considered. The tensegrity model [130, 131] might be a method to include such interactions. Attempts to do so are presented by, e.g., [132] and for whole cells by [128].

In conclusion, we are confronted with sophisticated models bearing enormous capabilities. The aspired verification of the results suggests many new experiments. On the other hand, we believe that there are still biomechanically relevant processes and mechanisms in actin and its networks which have not gained any attention yet. The interactions and collaborations between the disciplines which are concerned with actin, i.e. cell biology, biophysics and biochemistry, imaging and biomechanics, should be intensified and coordinated.

1.5 Organization of the thesis

This dissertation is a compilation of four scientific papers related to the continuum mechanical homogenization method as it is introduced in Section 1.3.4.

1. **M.J. Unterberger, K.M. Schmoller, A.R. Bausch and G.A. Holzapfel**, *A new approach to model cross-linked actin networks: Multi-scale continuum formulation and computational analysis*, Journal of the Mechanical Behavior of Biomedical Materials, 22:95–114, 2013.

   This study presents stress-strain data from rheological experiments on F-actin gels, cross-linked with heavy meromyosin with varying protein concentration. The constitutive model is based on the force-extension relationship of the single actin filament which is validated against experimental data from the literature. The non-affine homogenization method (1.29) is then introduced to derive a multi-scale continuum mechanical model for such networks. The homogenization parameter mediates the model and enables to capture the exceptional behavior. The physically interpretable material parameters are found to be in the meaningful range. The model is formulated as compressible material allowing the enforcement of incompressibility by means of a penalty function. The implementation into a finite element program is then straight-forward and the study concludes with an example which resembles the AFM indentation experiment.

2. **M.J. Unterberger, K.M. Schmoller, C. Wurm, A.R. Bausch and G.A. Holzapfel**, *Viscoelasticity of Cross-Linked Actin Networks: Experimental Tests, Mechanical Modeling and Finite Element Analysis*, Acta Biomaterialia, 9:7343–7353, 2013.

This study extends the previous findings by adding time dependency to the model. Cross-linked actin networks show viscoelastic properties in experiments. By plotting the Lissajous figure, we observe that strain-stiffening occurs in the sample and thus distorting the (linear) ellipse into a (nonlinear) S-shape. Further experiments reveal that the increase in storage modulus for large oscillation amplitudes is caused by this nonlinearity. Based on the nonlinear hyperelastic model we develop a viscous extension by adding Maxwell elements in parallel to the elastic contribution. Parameter identification is conducted to simultaneously fit experimental data over a large range of oscillation amplitudes and frequencies. Finite element simulations are conducted which resemble AFM indentation with a focus on the relaxation of the material by indenting to a constant depth. In a second simulation we qualitatively recover experimental results of micropipette aspiration of cells using a virtual droplet with an actin envelope.

3. **G.A. Holzapfel, M.J. Unterberger and R.W. Ogden**, *An affine constitutive model for cross-linked F-actin networks with compliant linker proteins*, submitted.

   In this second approach to constitutive modeling, we use the affine network model (1.27) to investigate the influence of cross-linker properties on the mechanics of the network. Cross-linked actin gels with defined actin and linker concentrations show large differences in stiffness for different linker proteins. We introduce a part of the linker at the end of the single actin filament as a serial spring to modify the stiffness of the protein compound. Furthermore, we prove that the affine network model also recovers the exceptional normal stress response of cross-linked actin networks. The finite element implementation uses the additive decomposition of the stress tensor and the elasticity tensor into a compressible and an isochoric part. Incompressibility is enforced by a penalty function. Subsequent simulations of the aspiration of a virtual droplet show reasonable behavior for both full aspiration and creep experiments.

4. **M.J. Unterberger, H. Weisbecker and G.A. Holzapfel**, *Torsion of a circular cylinder versus simple shear as a modeling basis for rheometer experiments: application to rubber and actin networks*, submitted.

   Parameter identification in the literature on the mechanics of cross-linked actin networks is conducted using data from rotational rheometry. However, the evaluation of the results is regularly conducted by assuming simple shear as the considered deformation mode. This study investigates the justification of this assumption. We find that indeed the results generated with simple shear deformation strongly deviate from the more realistic boundary conditions, i.e. torsion of a circular cylinder. This is particularly true for nonlinear materials

for which the differences can be up to 44% (eight-chain model). The affine network model proved also for the torsion of a cylinder to predict the correct sign of the normal force.

The relationship of these contributions to the existing literature was already presented in the introduction which is largely based on our review article:

5. **M.J. Unterberger and G.A. Holzapfel**, *Advances in modeling of filamentous actin and its cross-linked networks on multiple scales,* submitted.

Additionally, the following conference proceedings and a presented poster were part of the thesis:

1. **M.J. Unterberger and G.A. Holzapfel**, *Multi-scale modeling of a cell's actin cortex.* 82$^{\text{nd}}$ Annual Meeting of the International Association of Applied Mathematics and Mechanics (GAMM), Graz, Austria, April 18–22, 2011.

2. **M.J. Unterberger and G.A. Holzapfel**, *Mechanical properties and multi-scale modeling of biopolymer networks.* Workshop on Microscale Modeling in Biomechanics and Mechanobiology, Ericeira, Portugal, May 30–June 1, 2011.

3. **M.J. Unterberger and G.A. Holzapfel**, *Microstructurally-based modeling of viscoelastic properties of cross-linked F-actin networks.* IUTAM Symposium on Computer Models in Biomechanics: from Nano to Macro. Palo Alto, USA, August 30–September 2, 2011.

4. **G.A. Holzapfel, T.S.E Eriksson, M.J. Unterberger**, *Structurally-based Computation of the Biomechanical Response of Cardiovascular Tissues.* XI International Conference on Computational Plasticity Fundamentals and Applications (COMPLAS XI), Barcelona, Spain, September 7–9, 2011.

5. **M.J. Unterberger and G.A. Holzapfel**, *Multi-scale modeling of the viscoelastic behavior of cross-linked F-actin networks.* 8$^{\text{th}}$ European Solid Mechanics Conference (ESMC 2012), Graz, Austria, July 9–13, 2012.

6. **M.J. Unterberger and G.A. Holzapfel**, *Computational analysis of cross-linked F-actin networks using multi-scale models.* 6$^{\text{th}}$ European Congress on Computational Methods in Applied Sciences and Engineering (ECCOMAS 2012), Vienna, Austria, September 10–14, 2012.

7. **D.M. Pierce, M.J. Unterberger, T. Ricken and G.A. Holzapfel**, *A microstructurally-based continuum model of cartilage elasticity and permeability.* 12$^{\text{th}}$ U.S. National Congress on Computational Mechanics (USNCCM12), Raleigh, North Carolina, July 22–25, 2013.

8. **M.J. Unterberger, R.W. Ogden and G.A. Holzapfel**, *Constitutive modeling of cross-linked actin gels including the influence of linker proteins and viscoelasticity.* XII International Conference on Computational Plasticity Fundamentals and Applications (COMPLAS XII), Barcelona, Spain, September 3–5, 2013.

2 A NEW APPROACH TO MODEL CROSS-LINKED ACTIN NETWORKS: MULTI-SCALE CONTINUUM FORMULATION AND COMPUTATIONAL ANALYSIS

Abstract The mechanical properties of a cell are defined mainly by the cytoskeleton. One contributor within this three-dimensional structure is the actin cortex which is located underneath the lipid bilayer. It forms a nearly isotropic and densely cross-linked protein network. We present a continuum mechanical formulation for describing the mechanical properties of *in vitro* model systems based on their microstructure, i.e. the behavior of a single filament and its spatial arrangement. The network is considered elastic, viscous effects being neglected. Filamentous actin is a biopolymer with a highly nonlinear force-stretch relationship. This can be well described by a worm-like chain model that includes extensibility of the filament, which we call the β-model. A comparison with experimental data shows good agreement with values for the physically interpretable parameters. To make these properties applicable to three dimensions we used a non-affine micro-sphere network, which accounts for filaments, equally distributed in space. The assembled model results in a strain-energy density which is a function of the deformation gradient, and it is validated with experimental data from rheological experiments of *in vitro* reconstituted actin networks. The Cauchy stress and elasticity tensors are obtained within the continuum mechanics framework and implemented into a finite element program to solve boundary-value problems.

2.1 Introduction

The mechanics of cells and their substructures have a great influence on the development of diseases. Cancer, atherosclerosis or glaucoma can be related to mechanical abnormalities of the associated cells [6, 7, 9]. The cytoskeleton is most important for the mechanical response of the cell [133, 134]. It consists of polymers of proteins, for example, microtubules, intermediate filaments and actin, which are dynamically arranged into different morphologies by myriads of additional proteins. Close to the lipid bilayer is the actin cortex, an unstructured cross-linked network. It is connected to the cell membrane and plays a crucial role in the response of a cell to external stimuli [135]. In the present work we focus on the modeling of isotropically cross-linked *in vitro* systems which have a similar structure to the actin cortex. Alberts et

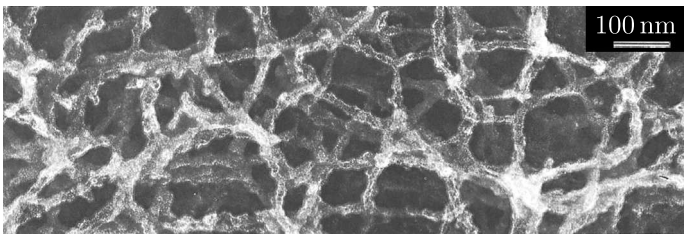

Figure 2.1: Electron micrograph of an actin/filamin network of a molar ratio of 1 : 50; modified from Niederman et al. [136].

al. [12, chap. 16] provide an extensive review of the underlying molecular biology of the cytoskeleton.

Actin is abundant in cells as globular monomer (G-actin) which polymerizes to filamentous (F-)actin. Together with other cytoskeletal proteins it drives protrusion, motility and cell division. It is a semi-flexible polymer, i.e. the chains are too stiff to form loops but are flexible enough to exhibit considerable thermal bending [37]. Two length scales are needed to describe this quantitatively. First, the contour length L, which is the arc-length of the chain along the polymer backbone and second, the persistence length L_p, which is a measure of the bending stiffness of polymers. In terms of length scales semi-flexibility means that $L \sim L_\mathrm{p}$. There is consensus that the persistence length of F-actin is about $16\,\mu$m [35].

In vivo the actin filaments are arranged into defined three-dimensional structures by a variety of cross-linking proteins. *In vitro* model systems are used to investigate the properties of these networks. Figure 2.1, modified from Niederman et al. [136], depicts a micrograph of a network consisting of actin and filamin. Most cross-linking proteins, for example, filamin [118, 137] and α-actinin [138], tend to cross-link F-actin into a network *and* bundle it at higher concentrations. An overview of important actin-binding proteins and the properties of resulting networks is given by Lieleg et al. [139]. Networks of heavy meromyosin (HMM), a truncated version of myosin II, in its rigor state, and F-actin never exhibit bundles as observed by Tharmann et al. [26]. For this reason we chose HMM as cross-linker for our experiments. Depending on the cross-linker the networks exhibit different mechanical properties [124, 140, 141], and their influence on the stiffness of the bulk material is measurable. However, a quantification of cross-linker behaviors is not yet accomplished. Kim et al. [101] used generic numbers for stretching, bending and torsional stiffness to distinguish two different cross-linkers. Scaling of material properties of cross-linked actin networks is investigated thoroughly in the literature [88, 142]. The elastic and viscous properties of the soft *in vitro* gels are characterized using bulk rheology experiments, which are conducted on reconstituted networks. In a rheometer two parallel plates shear the sample at constant gap size. Stricker et al. [143] and Lieleg et al. [139] provide comprehensive reviews of rheological experiments on actin networks.

In order to fully appreciate the results of experiments on cells, models are needed to describe the impact of changes in configuration on the mechanics. Phenomenological models, such as [144, 145], are widely used to model very special cases. In order to account for the complex microstructure of the material a subcellular perspective is needed. Computer simulations of networks can be performed in two ways: first, one can take a microscopic point of view, model each single filament and discretize the network by finite beam elements [146] or Brownian dynamics [101]. Second, one can take a macroscopic point of view, consider the network as a whole mechanical continuum, discretize it by solid elements and employ a suitable constitutive law [82, 147]. Whereas the first approach allows for a detailed computer aided analysis of microscopic mechanisms down to the molecular scale [148–150], the second one benefits from a vastly lower computational cost per simulated volume and is thus more suitable for the simulation of large systems where the relevant microscopic mechanisms have already been identified either by experiments or previous simulations using the first approach. In this paper we will focus on the second approach.

As a first step we consider the relation between the filament tensile force f and the end-to-end distance r, and later we use it to form a material model based on the microstructure. Liu and Pollack [36] showed that actin filaments exhibit a finite stiffness when r reaches L. Hence, an extensible filament model is needed. Based on the ideas of Kratky and Porod [71], semi-flexible polymers may be modeled using the worm-like chain which considers entropic unbending. Different approaches were used to mathematically describe the filament. Here we use a modified version of the single filament model by Holzapfel and Ogden [73] developed on purely mechanical arguments for extensible fibers.

The finite element method requires a continuum mechanical formulation of the constitutive equations. To capture the network properties a blurring of the actual structure is needed to obtain a continuum mechanical model. Palmer and Boyce [82] used the single filament model of MacKintosh et al. [56], which assumes inextensible fibers, in an eight-chain network (Arruda and Boyce [111]) to model the stress response of actin-scruin networks, which have been investigated by Gardel et al. [41]. Several network models have been proposed in the literature. Widely used is the aforementioned eight-chain network, which was developed for rubber elasticity. Unfortunately, it does not predict a normal force response in simple shear observed in experiments. This is an important mechanical feature which we do not want to neglect. Therefore, we propose to use the non-affine network model of Miehe et al. [119] which replicates our experimental data very well. Note that it includes the eight-chain network as a special case.

The purpose of this paper is to present a new nonlinear material model for cross-linked actin networks based on their micro-structure. We adopt the approach of Palmer and Boyce [82] using other models which capture the properties of the networks in a more

efficient way. Experiments on *in vitro* networks are conducted to obtain values for the parameters. Implementation into a finite element program is followed by the solution of an exemplary boundary-value problem. For the sake of simplicity, we need to neglect several features in this (first) modeling step. As pointed out earlier, we know little about the compliance of the cross-linker. Tharmann et al. [26] reported that the elastic response of actin-HMM networks is dominated by the stretching of filaments between cross-links and, therefore, we neglect the influence of the cross-linker in the present work. We consider cross-links as frictionless ball joints and expect to underestimate network stiffness by doing so. Stress-strain curves of reconstituted protein networks show hysteresis and viscous effects. Regarding cell biology, we do not account for the cell's ability to remodel, i.e. polymerization/depolymerization of F-actin. Interactions of the actin network with other cytoskeletal proteins and organelles are also not considered in the present work.

In Section 2.2 we introduce the worm-like chain model and present a single filament model, while Section 2.3 shows the homogenization and network building. Section 2.4 explains the sample preparation and the experimental protocol followed by a discussion of the experiments and the model fitting. To demonstrate the capabilities of the model, we present a parameter study in Section 2.5 as well as a representative boundary-value problem which resembles indentation of a cell with a spherical tip. Supplementary comments on the continuum mechanics used are made in Appendix 2.A.

2.2 Single filament model

The considered networks consist of single filaments which are cross-linked into a three-dimensional structure. We assume that the properties of the main constituent influence the behavior of the system. Understanding the behavior of F-actin is a first step in developing a three-dimensional constitutive relation for cross-linked actin networks. After reviewing the well-known worm-like chain model and some of its formulations, we bring its ideas into a practical equation for which we determine the parameters.

2.2.1 The worm-like chain model

Semi-flexible polymers are frequently described by worm-like chain models. Assume a filament with pinned ends, as depicted in Figure 2.2. Its main features are its geometry, i.e. the deviation u from the horizontal line, and the bending stiffness $B_0 = EI$, where E is the Young's modulus and I is the moment of inertia. Alternatively,

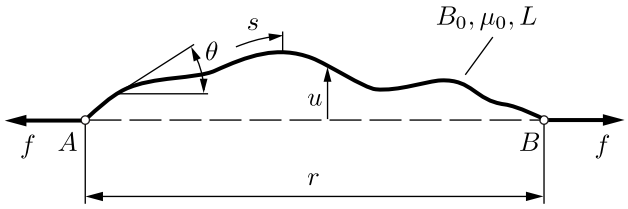

Figure 2.2: Undulated filament chain pinned at the end points A and B with arc-length s, contour length $L = s(B)$, end-to-end distance r, bending stiffness B_0, stretch modulus μ_0, tangent angle θ, and tensile force f.

the bending behavior can be characterized by relating the bending stiffness to the filament's thermal fluctuation through its persistence length L_p, which is given by

$$L_\mathrm{p} = \frac{B_0}{k_\mathrm{B}T}, \tag{2.1}$$

where k_B is the Boltzmann constant and T is the temperature. If the filament is considered to be extensible, the additional degree of freedom is incorporated through the stretch modulus μ_0.

The arc-length s is the coordinate measured along the protein backbone, whereas the contour length L denotes the length of this backbone. Another geometrical feature is the end-to-end distance r which is measured between the end points A and B on which f acts as a tensile force. The associated energy, say $\mathcal{E}$, can be written as [73]

$$\mathcal{E} = \frac{B_0}{2}\int_0^L \left(\frac{\partial^2 u}{\partial s^2}\right)^2 \mathrm{d}s + \frac{1}{2}\int_0^L f\left(\frac{\partial u}{\partial s}\right)^2 \mathrm{d}s - f(L - r_0), \tag{2.2}$$

where r_0 is the end-to-end distance of the filament at zero external force.

We are interested in a relationship between f and the normalized end-to-end distance, say r/L. Several publications present solutions for the worm-like chain model in order to obtain such a relationship. A list of well known models is given in Table 2.1, which is of course incomplete. The models are examined with respect to their usability in our modeling problem. The inextensible model of Marko and Siggia [29] as well as the extensible Odijk model [151] assume flexible polymers. This stands in contradiction with the already postulated semi-flexible property of F-actin. Another requirement for modeling actin is extensibility. Therefore, the inextensible model of MacKintosh et al. [56] is not suitable. Storm and Nelson [152] introduced the (inextensible) discrete persistent chain model which is a hybrid of the freely-jointed chain and the worm-like chain models. It is also able to model the overstretching transition of DNA excellently. Storm et al. [37] enhance the model by MacKintosh et al. [56] by describing extensible properties using an *ad hoc* approach. Blundell and Terentjev [85] derive another relation for inextensible filaments and use a similar argument to

Table 2.1: Filament models and their major properties in regard to stretch stiffness.

Model	Filament	Stretch stiffness
Marko and Siggia [29]	flexible	inextensible
Odijk [151]	flexible	extensible
MacKintosh et al. [56]	semi-flexible	inextensible
Storm and Nelson [152]	semi-flexible	inextensible
Storm et al. [37]	semi-flexible	extensible
Blundell and Terentjev [85]	semi-flexible	extensible
Holzapfel and Ogden [73]	universal	extensible

include extensibility. Holzapfel and Ogden [73] do not need to assume the degree of flexibility; extensibility is included from the beginning. They obtain and solve the governing equilibrium equations through mechanical analysis. Thus, we use it as a basis for our model and explain it in more detail in the next section.

2.2.2 Holzapfel-Ogden β-model

The model [73] was derived on the basis of a purely mechanical analysis, before it was generalized and compared with other models. In contrast to all other mentioned filament models, this one deals consistently with the extensibility of the fiber from the very beginning, and does not introduce an *ad hoc* additional term after deriving the inextensible model to consider extensibility. The kinematics of the filament introduces the curvature and considers the local filament stretch. With simple constitutive relations a differential equation similar to the Euler buckling problem is obtained. This governing equation is solved by approximating the polymer shape with a Fourier series. The force f is transformed to a dimensionless measure

$$f^\star = L^2/(\pi^2 B_0) f. \tag{2.3}$$

Linearization and truncation of the Fourier series obtained by solving the resulting linear equations, and using the dimensionless parameter

$$\alpha = \pi^2 B_0/(\mu_0 L^2), \tag{2.4}$$

which includes bending and stretching properties, the filament model becomes [73]

$$\frac{r}{L} = 1 + \alpha f^\star - \frac{(1+2\alpha f^\star)(1+\alpha f^\star)^2}{(1+f^\star+\alpha f^{\star 2})^2}(1 - r_0/L). \tag{2.5}$$

Note that $f^\star = f/(\alpha\mu_0)$ holds. We assume that a filament cannot act against a compressive force, i.e. $f = 0$ for $r < r_0$. Additional terms of the series contribute only marginally [73] and are, therefore, omitted. As a special case, the inextensible model is included in equation (2.5), i.e.

$$\frac{r}{L} = 1 - \frac{1 - r_0/L}{(f^\star + 1)^2}, \tag{2.6}$$

for $\mu_0 \to \infty$.

It can be shown that the models by MacKintosh et al. [56] and Blundell-Terentjev [85] models only differ from equation (2.6) through the exponent of the denominator in the second term which follows from the formulation of the series. Hence, we may generalize equation (2.6) by replacing the square by an arbitrary exponent β, and we extend the idea to equation (2.5), i.e.

$$\frac{r}{L} = 1 + \alpha f^\star - \frac{(1 + 2\alpha f^\star)(1 + \alpha f^\star)^\beta}{(1 + f^\star + \alpha f^{\star 2})^\beta}(1 - r_0/L). \tag{2.7}$$

Holzapfel and Ogden [74] provide a detailed derivation and discussion of the parameter β, together with a comparison to the models of MacKintosh et al. [56] and Blundell and Terentjev [85]. We calculate the partial derivative at $f^\star = 0$

$$\frac{\partial f^\star}{\partial(r/L)} = \frac{1}{\alpha + (\beta - \alpha\beta - 2\alpha)(1 - r_0/L)}. \tag{2.8}$$

Typical values for the parameters suggest that $\alpha \ll \beta$. Thus we set $\alpha = 0$ and obtain the simple expression $\partial f^\star/\partial(r/L) = [\beta(1 - r_0/L)]^{-1}$. Therefore, β is related to the initial stiffness of the filament, and subsequently we refer to β as the effective extensional number. Higher values for β mean a lower initial stiffness. Figure 2.3(a) shows plots of (2.7) for different effective extensional numbers, where $\alpha = 10^{-7}$ and $r_0/L = 0.9$ are on the order of the values we later derive from the fitting to experimental data. The force at $r = r_0$ must be zero, and hence all three curves start from the same point. For $r/L < 1$, the initial filament stiffness shows a strong influence on the relationship between the force and the normalized end-to-end distance. For $r/L \geq 1$, however, β hardly effects this relationship.

We now want to prepare the filament model to make it applicable to the network model which we present in Section 2.3. There is evidence that prestressed *in vitro* networks replicate properties of *in vivo* experiments [125]. We incorporate this in the unloaded network by assuming that the filaments are arranged having an initial end-to-end distance $\widetilde{r}$. This is related to r_0 through a pre-stretch $\lambda_0 = \widetilde{r}/r_0$. When deforming the network, the filament experiences a stretch relative to the initial end-to-end distance $\lambda = r/\widetilde{r}$, thus

$$r = \lambda\lambda_0 r_0. \tag{2.9}$$

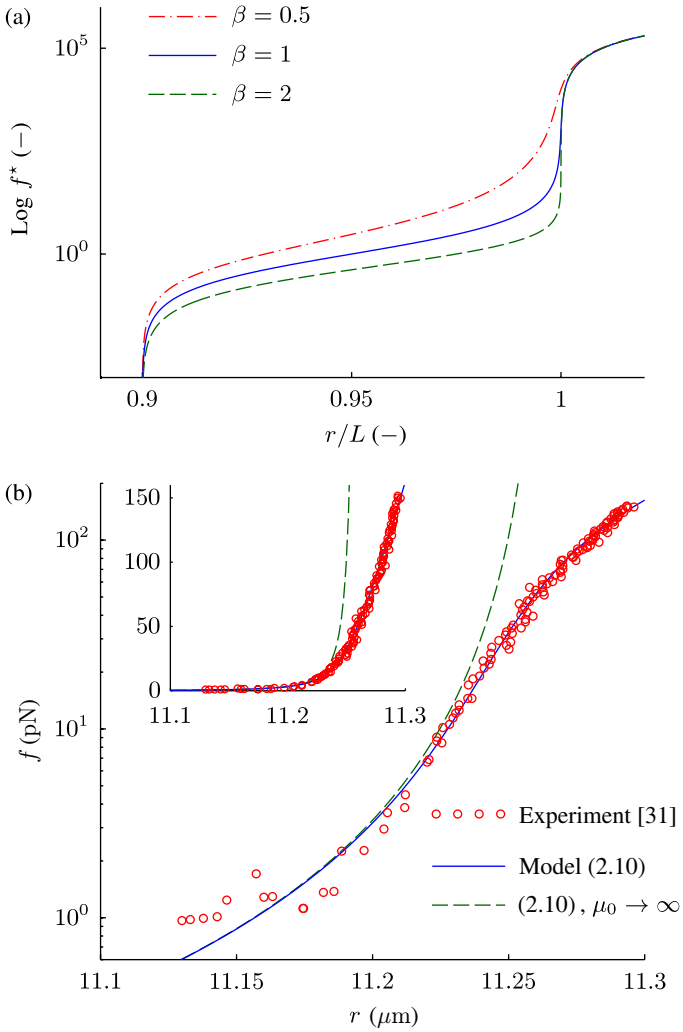

Figure 2.3: (a) Parameter study of equation (2.7) with $\beta = 0.5$, 1 and 2. (b) Stretching of a single actin filament. Experimental data obtained by Liu and Pollack [36], Figure 10b therein. Solid curves: model (2.10) with parameters $T = 294\,\mathrm{K}$, $L_\mathrm{p} = 16\,\mu\mathrm{m}$, $L = 11.264\,\mu\mathrm{m}$, $r_0 = 10.17\,\mu\mathrm{m}$, $\mu_0 = 38.6\,\mathrm{nN}$ and $\beta = 0.438$. Dashed curves: inextensible model with the same parameter values, but $\mu_0 \to \infty$. Inset: linear scale for the force.

Using equation (2.9) in (2.7) and by means of the definitions (2.3) and (2.4) we obtain

$$\frac{\lambda\lambda_0 r_0}{L} = 1 + \frac{f}{\mu_0} - \frac{(1+2f/\mu_0)(1+f/\mu_0)^\beta(1-r_0/L)}{[1+fL^2/(\pi^2 B_0) + f^2L^2/(\pi^2 B_0\mu_0)]^\beta}. \tag{2.10}$$

For a given stretch λ, this implicit equation can be solved for the force f, for example, using Brent's method [153]. For this purpose, we re-formulate equation (2.10) to the form $G(f) = 0$, where we know that the physically meaningful root must be larger

than the position of the equation's pole, which is located at $f = -\pi^2 B_0/L^2$. Bending stiffness and contour length are positive parameters and $f \geq 0$ must hold. Hence, we use $[0, \infty)$ as the root search interval when solving $G(f) = 0$.

The single filament model (2.10) requires some preparation before it is implemented into the network, particularly the first and second derivatives of the strain-energy function ψ_f with respect to λ, say ψ_f' and ψ_f'', respectively, which are calculated as follows. We can express the force in equation (2.10) as $f = \partial\psi_\mathrm{f}/\partial r$. By means of the chain rule and using equation (2.9) we arrive at

$$\psi_\mathrm{f}' = \frac{\partial\psi_\mathrm{f}}{\partial\lambda} = \frac{\partial\psi_\mathrm{f}}{\partial r}\frac{\partial r}{\partial\lambda} = \lambda_0 r_0 f. \tag{2.11}$$

For the second derivative we use an implicit differentiation method based on the chain rule. First, equation (2.11) is plugged into (2.10) and transformed into the form $H(\lambda, \psi_\mathrm{f}'(\lambda)) = 0$. The total derivative of H with respect to λ is then

$$\frac{\mathrm{d}H}{\mathrm{d}\lambda} = \frac{\partial H}{\partial\lambda} + \frac{\partial H}{\partial\psi_\mathrm{f}'}\frac{\partial\psi_\mathrm{f}'}{\partial\lambda} = 0, \tag{2.12}$$

and using the shorthand notation $\partial\psi_\mathrm{f}'/\partial\lambda = \psi_\mathrm{f}''$ we deduce that

$$\psi_\mathrm{f}'' = -\frac{\partial H/\partial\lambda}{\partial H/\partial\psi_\mathrm{f}'}. \tag{2.13}$$

A lengthy calculation and re-substitution of equations (2.3) and (2.4) gives

$$\psi_\mathrm{f}'' = \frac{\lambda_0^2 r_0^2 \mu_0/L}{1 + Y\left(\frac{1+\alpha f^\star}{1+f^\star+\alpha f^{\star 2}}\right)^\beta (1 - r_0/L)}, \tag{2.14}$$

where we have used the shorthand notation

$$Y = \frac{\beta}{\alpha}\frac{(1+2\alpha f^\star)^2}{1+f^\star+\alpha f^{\star 2}} - \beta\frac{1+2\alpha f^\star}{1+\alpha f^\star} - 2. \tag{2.15}$$

2.2.3 Parametrization of the β-model

Before advancing to the network level of the model we first want to determine the material parameters for the single filament. Equations (2.10) with (2.9) and (2.1) reveal six parameters which can be determined in a single filament experiment which measures f versus r, i.e. L, r_0, T, L_p, μ_0, β. The pre-stretch λ_0 is a network parameter, and values are determined later. The temperature T is an externally

defined variable and in experiments usually 21°C (294 K). Measurements of the persistence length of F-actin revealed a value of $L_p = 16\,\mu$m [35].

The experiments of Liu and Pollack [36] were conducted with single actin filaments by using bending cantilevers to determine f and a photodiode array for measuring r. The circles in Figure 2.3(b) are the data of a filament for which $L \sim 11.2\,\mu$m was measured. It showed a highly nonlinear behavior and a finite stiffness as r exceeds the contour length L. We used the nonlinear Least Squares tool (`lsqnonlin`) of MATLAB[1] with fixed L_p and T for fitting. With the free parameters L, r_0, μ_0 and β we found the set of values documented in the caption of Figure 2.3. The extensible β-model gives an excellent fit with reasonable numbers for the parameters used. The fitted value $L = 11.264\,\mu$m matches very well with the measured contour length $\sim 11.2\,\mu$m. The end-to-end distance at zero-force r_0 is $\sim 91\%$ of L and thus also reflects the semi-flexible character of actin filaments. Kojima et al. [59] found a stretch modulus of ~ 43.7 nN for F-actin, which is reasonably close to the fitted value 38.6 nN (note that the stretch modulus is linked with an unusual unit; however, we keep this terminology because of its use in the literature). The effective extensional number is $\beta = 0.438$.

For comparison, the inextensible version of the β-model is plotted as dashed curves in Figure 2.3(b). As expected, it diverges in the high stretch region because in inextensible models r cannot exceed L. This can be seen most dramatically in the inset of Figure 2.3(b), where we used a linear scale for the force. We quantified the sensitivity of the model to the fitting parameters. We varied the values by $\pm 5\%$ *ceteris paribus* and registered the relative change of f at $r = L$. However, the end-to-end distance at zero force r_0 and the contour length L are strongly coupled and, therefore, we assessed a change in their ratio r_0/L. The effects of r_0/L, μ_0 and β are $< 12\%$, $< 5\%$ and $< 7\%$, respectively.

2.3 Homogenization into a network—micro-sphere model

Numerical methods such as the finite element method require a suitable formulation of the problem. Nonlinear continuum mechanics provides a superior framework for implementation. Our goal is to integrate the strain-energy function (2.10) of the one-dimensional single filament into a three-dimensional environment. Various network models are proposed in the literature for obtaining a strain-energy density function Ψ, with most of them seemingly motivated from rubber elasticity. The micro-sphere model of Miehe et al. [119] adapts the idea of a full network (see Treloar [154]) together with a tube constraint. It adds energy to the total strain-energy density stemming from conformational restrictions of a considered filament introduced by

[1] Version 2009a, by The MathWorks Inc., Massachusetts, USA

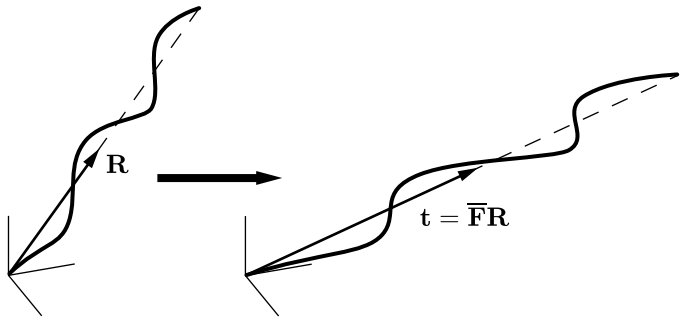

Figure 2.4: Deformation of a filament in three-dimensional space. The isochoric deformation gradient $\overline{\mathbf{F}}$ deforms the unit vector $\mathbf{R}$ in the reference configuration (left) into a new vector $\mathbf{t}$ in the current configuration (right).

neighboring filaments. To keep things simple, we will only consider the network part and neglect the constraining tube. Numerical experiments with the parameter values presented in this work and typical parameters for the tube part showed that the constraint has a minor influence on the final result ($< 4\%$) at 20% deformation.

2.3.1 Kinematics and strain-energy function

Changes in the configuration of a body are mapped using the deformation gradient $\mathbf{F}$. The right Cauchy-Green tensor $\mathbf{C} = \mathbf{F}^{\mathrm{T}}\mathbf{F}$ is our chosen measure for rotation independent deformation. We assume incompressibility for the considered material, so that the Jacobian is ideally $J = \det \mathbf{F} = 1$. We enforce this constraint in the finite element method by means of a compressible formulation together with an additional penalty parameter. Therefore, we use a multiplicative decomposition of the deformation gradient $\mathbf{F}$ into a volume changing (volumetric) $J^{1/3}\mathbf{I}$ and a volume preserving (isochoric) $\overline{\mathbf{F}}$ part, i.e.

$$\mathbf{F} = J^{1/3}\overline{\mathbf{F}}, \tag{2.16}$$

where $\det \overline{\mathbf{F}} = 1$. Defining the isochoric part of the right Cauchy-Green tensor $\overline{\mathbf{C}} = \overline{\mathbf{F}}^{\mathrm{T}}\overline{\mathbf{F}}$, this results in a decoupled representation of the strain-energy function [112, Sec. 6.4]

$$\Psi(\mathbf{C}) = \Psi_{\mathrm{vol}}(J) + \Psi_{\mathrm{iso}}(\overline{\mathbf{C}}), \tag{2.17}$$

where $\Psi_{\mathrm{vol}}(J)$ and $\Psi_{\mathrm{iso}}(\overline{\mathbf{C}})$ describe the volumetric and the isochoric elastic response of the material, respectively. Subsequently, we will just deal with the isochoric part. The volumetric contribution is extensively discussed by, for example, Holzapfel [112].

To obtain Ψ_{iso} we start by considering an arbitrarily oriented single filament in space as depicted in Figure 2.4. A unit vector $\mathbf{R}$ is defined to describe the direction between

the end points in the reference configuration. The isochoric deformation gradient transforms the reference vector into

$$\mathbf{t} = \overline{\mathbf{F}}\mathbf{R}, \tag{2.18}$$

where the direction as well as the length are in general altered. A filament, which was oriented in the $\mathbf{R}$-direction in the reference configuration is thus stretched according to

$$\overline{\lambda} = \frac{\|\mathbf{t}\|}{\|\mathbf{R}\|} = \|\mathbf{t}\|, \tag{2.19}$$

where $\| \bullet \|$ denotes the vector norm of $(\bullet)$. Recalling (2.18) and the definition of the vector norm, the usage of basic tensor algebra leads to

$$\overline{\lambda} = \sqrt{\mathbf{t} \cdot \mathbf{t}} = \sqrt{\mathbf{R} \cdot \overline{\mathbf{C}}\mathbf{R}}. \tag{2.20}$$

The $\mathbf{R}$-vectors of equally distributed filaments build a unit sphere on the microscopic scale, thus the model is called micro-sphere model. From equation (2.20) we may compute the stretch value in a single filament embedded in a micro-sphere. Subsequently, with the help of (2.10), the tensile force f can then be determined where $\overline{\lambda}$ should be replaced by λ.

Lanir [155] suggested summing up the strain energies ψ_{f}^i of the filaments in a unit reference volume to obtain a global strain-energy density, i.e.

$$\Psi_{\mathrm{iso}}(\overline{\mathbf{C}}) = \sum_{i=1}^{n} \psi_{\mathrm{f}}^i(\overline{\lambda}(\overline{\mathbf{C}})), \tag{2.21}$$

where n is the filament density, that is the number of filaments of the network in a unit reference volume. The idea for solving equation (2.21) is to calculate an averaged stretch λ of the filaments which allows us to calculate the filament strain energy only once for every point of the material. Miehe et al. [119], for example, used the micro-sphere to arrange the fibers in a three-dimensional structure. Here we want to adopt this approach to homogenize single filament stretches by using the assumption of an isotropic network. Therein, a unit sphere $\mathscr{S}$ is considered, where filaments are randomly distributed in space. We take the p-root average of the stretch, alternatively denoted by $\langle \bullet \rangle_p$, and define

$$\lambda = \langle \overline{\lambda} \rangle_p = \left(\frac{1}{|\mathscr{S}|} \int_{\mathscr{S}} \overline{\lambda}^p \mathrm{d}A \right)^{1/p}, \tag{2.22}$$

where A is the surface of the micro-sphere. Subsequently, we call p the averaging parameter. With this additional parameter we allow the micro-stretches to fluctuate around the macro-stretch and, therefore, we consider the effects originating from

non-affine deformation. Larger values of p can be related to a higher non-affinity of the deformation. Angle brackets without a subscript indicate $p = 1$. Using (2.22), the network strain energy, equation (2.21), can be rewritten as

$$\Psi_{\text{iso}}(\overline{\mathbf{C}}) = n\psi_{\text{f}}(\lambda(\overline{\mathbf{C}})). \tag{2.23}$$

It is straightforward to show that the homogenization (2.22) specializes to the eight-chain model of Arruda and Boyce [111] for $p = 2$. Transforming $\mathbf{R} \cdot \overline{\mathbf{C}}\mathbf{R}$ in (2.20) to spherical coordinates, and by means of the Jacobian determinant of the transformation law we can carry out the surface integral and obtain

$$\langle\overline{\lambda}\rangle_2 = \lambda_{\text{AB}} = \sqrt{\frac{\text{tr}\overline{\mathbf{C}}}{3}}, \tag{2.24}$$

where the subscript AB refers to Arruda and Boyce and $\text{tr}\overline{\mathbf{C}} = \overline{\mathbf{C}} : \mathbf{I}$ denotes the trace of the isochoric right Cauchy-Green tensor, where : signifies a double contraction.

2.3.2 Cauchy stress tensor

We look for a relationship between the deformation gradient $\mathbf{F}$ and the Cauchy stress tensor $\boldsymbol{\sigma}$, considering the strain-energy function (2.17) with its isochoric part (2.23). The Cauchy stress tensor

$$\boldsymbol{\sigma} = \boldsymbol{\sigma}_{\text{vol}} + \boldsymbol{\sigma}_{\text{iso}} \tag{2.25}$$

inherits the additive decomposition from (2.17). In the following, the focus lies on the volume preserving part of the strain-energy function. The Eulerian fourth-order projection tensor

$$\mathbb{P} = \mathbb{I} - \frac{1}{3}\mathbf{I} \otimes \mathbf{I} \tag{2.26}$$

is used to represent the deviatoric part ($\text{dev}\widetilde{\boldsymbol{\sigma}}$) of the fictitious stress tensor $\widetilde{\boldsymbol{\sigma}}$, i.e. (for more details see [112])

$$\boldsymbol{\sigma}_{\text{iso}} = \mathbb{P} : \widetilde{\boldsymbol{\sigma}}. \tag{2.27}$$

Here, $(\mathbb{I})_{abcd} = (\delta_{ac}\delta_{bd} + \delta_{ad}\delta_{bc})/2$ is the symmetric part of the fourth-order identity tensor, $\mathbf{I}$ is the second-order identity tensor, $\otimes$ denotes the dyadic product. The fictitious Cauchy stress tensor can be expressed as

$$\widetilde{\boldsymbol{\sigma}} = J^{-1}\overline{\mathbf{F}}\widetilde{\mathbf{S}}\overline{\mathbf{F}}^{\text{T}}, \qquad \widetilde{\mathbf{S}} = 2\frac{\partial\Psi_{\text{iso}}}{\partial\overline{\mathbf{C}}}, \tag{2.28}$$

where $\widetilde{\mathbf{S}}$ denotes the fictitious second Piola-Kirchhoff stress tensor. In Appendix 2.A we give a detailed derivation of equations (2.25)–(2.28).

We want to specify equation $(2.28)_2$ to finally obtain an explicit form for the fictitious Cauchy stress tensor $\widetilde{\boldsymbol{\sigma}}$. Using equation (2.23) and the chain rule as well as $(2.11)_1$, (2.22) and the Leibniz integral rule, we arrive at

$$\widetilde{\mathbf{S}} = 2n\frac{\partial\psi_{\mathrm{f}}(\lambda)}{\partial\lambda}\frac{\partial\lambda}{\partial\overline{\mathbf{C}}} = 2n\psi_{\mathrm{f}}'\frac{\partial}{\partial\overline{\mathbf{C}}}\langle\overline{\lambda}\rangle_p = 2n\psi_{\mathrm{f}}'\lambda^{1-p}\left\langle\overline{\lambda}^{p-1}\frac{\partial\overline{\lambda}}{\partial\overline{\mathbf{C}}}\right\rangle. \tag{2.29}$$

The partial derivative in $(2.29)_3$ can be worked out by means of $(2.20)_2$ and (2.18) as

$$\frac{\partial\overline{\lambda}}{\partial\overline{\mathbf{C}}} = \frac{\partial}{\partial\overline{\mathbf{C}}}\sqrt{\mathbf{R}\cdot\overline{\mathbf{C}}\mathbf{R}} = \frac{1}{2\overline{\lambda}}\frac{\partial(\mathbf{R}\cdot\overline{\mathbf{C}}\mathbf{R})}{\partial\overline{\mathbf{C}}} = \frac{1}{2\overline{\lambda}}\mathbf{R}\otimes\mathbf{R} = \frac{1}{2\overline{\lambda}}\overline{\mathbf{F}}^{-1}\mathbf{t}\otimes\mathbf{t}\overline{\mathbf{F}}^{-\mathrm{T}}, \tag{2.30}$$

where $\overline{\mathbf{F}}^{-\mathrm{T}}$ denotes the transpose of the inverse of $\overline{\mathbf{F}}$. Using equation $(2.30)_4$ in $(2.29)_3$ and defining

$$\mathbf{H} = \langle\overline{\lambda}^{p-2}\mathbf{R}\otimes\mathbf{R}\rangle = \langle\overline{\lambda}^{p-2}\overline{\mathbf{F}}^{-1}\mathbf{t}\otimes\mathbf{t}\overline{\mathbf{F}}^{-\mathrm{T}}\rangle, \tag{2.31}$$

we obtain

$$\widetilde{\mathbf{S}} = n\psi_{\mathrm{f}}'\lambda^{1-p}\mathbf{H}. \tag{2.32}$$

Applying equations (2.32) and $(2.31)_2$ to $(2.28)_1$, the fictitious Cauchy stress tensor $\widetilde{\boldsymbol{\sigma}}$ is worked out as

$$\widetilde{\boldsymbol{\sigma}} = J^{-1}\overline{\mathbf{F}}\widetilde{\mathbf{S}}\overline{\mathbf{F}}^{\mathrm{T}} = J^{-1}n\psi_{\mathrm{f}}'\lambda^{1-p}\mathbf{h} \quad\text{with}\quad \mathbf{h} = \langle\overline{\lambda}^{p-2}\mathbf{t}\otimes\mathbf{t}\rangle. \tag{2.33}$$

The same results were obtained by Miehe et al. [119] by using the Kirchhoff stress tensor $\boldsymbol{\tau} = J\boldsymbol{\sigma}$ instead, and applying Cartesian metric tensors.

Remark. The micro-sphere model adds three material parameters to those we need for the single filament, i.e. the pre-stretch λ_0, the filament density n and the averaging parameter p.

2.3.3 Elasticity tensor

A quadratic rate of convergence near the solution point within a finite element program requires the fourth-order elasticity tensor, which is the gradient of the stress function measuring the stress change resulting from a strain change. According to the structure of the strain-energy function (2.17) we may write for the (Eulerian) elasticity tensor $\mathbb{c}$ the additive decomposition consisting of the volumetric part $\mathbb{c}_{\mathrm{vol}}$ and the isochoric part $\mathbb{c}_{\mathrm{iso}}$, i.e.

$$\mathbb{c} = \mathbb{c}_{\mathrm{vol}} + \mathbb{c}_{\mathrm{iso}}, \tag{2.34}$$

where $\mathbb{c}_{\mathrm{vol}}$ is discussed in [112, Sec. 6.6]. We just focus here on the isochoric part $\mathbb{c}_{\mathrm{iso}}$. Therefore, we define the fictitious fourth-order elasticity tensor $\widetilde{\mathbb{C}}$ in the material

description (for more details see [112, Sec. 6.6]), and recall equations $(2.28)_2$ and (2.32)

$$\widetilde{\mathbb{C}} = 4\frac{\partial^2 \Psi_{\text{iso}}}{\partial \overline{\mathbf{C}} \partial \overline{\mathbf{C}}} = 2\frac{\partial \widetilde{\mathbf{S}}}{\partial \overline{\mathbf{C}}} = 2\frac{\partial}{\partial \overline{\mathbf{C}}}\left(n\psi_{\text{f}}' \lambda^{1-p} \mathbf{H}\right). \tag{2.35}$$

By introducing the shorthand notation $\mathbb{H} = 2\partial \mathbf{H}/\partial \overline{\mathbf{C}}$ and by working out $(2.35)_3$ using the product and chain rules, the definition $(2.31)_2$, and the properties $(2.29)_3$, $(2.30)_4$, we obtain

$$\widetilde{\mathbb{C}} = n\left[\psi_{\text{f}}'' \lambda^{2(1-p)} - (p-1)\psi_{\text{f}}' \lambda^{1-2p}\right] \mathbf{H} \otimes \mathbf{H} + n\psi_{\text{f}}' \lambda^{1-p} \mathbb{H}. \tag{2.36}$$

In order to calculate $\mathbb{H}$ we use equation $(2.31)_1$, the Leibniz integral rule and the product rule to obtain

$$\mathbb{H} = 2\frac{\partial \mathbf{H}}{\partial \overline{\mathbf{C}}} = 2\left\langle \frac{\partial}{\partial \overline{\mathbf{C}}}\left(\overline{\lambda}^{p-2} \mathbf{R} \otimes \mathbf{R}\right)\right\rangle = 2\left\langle \overline{\lambda}^{p-2} \frac{\partial}{\partial \overline{\mathbf{C}}}(\mathbf{R} \otimes \mathbf{R}) + \mathbf{R} \otimes \mathbf{R} \otimes \frac{\partial \overline{\lambda}^{p-2}}{\partial \overline{\mathbf{C}}}\right\rangle. \tag{2.37}$$

Note that $\partial(\mathbf{R} \otimes \mathbf{R})/\partial \overline{\mathbf{C}} = \mathbb{O}$ results in the fourth-order zero tensor. Using the chain rule as well as equations $(2.30)_3$ and (2.18) in $(2.37)_3$ we arrive at

$$\mathbb{H} = (p-2)\langle \overline{\lambda}^{p-4} \mathbf{R} \otimes \mathbf{R} \otimes \mathbf{R} \otimes \mathbf{R}\rangle = (p-2)\langle \overline{\lambda}^{p-4} \overline{\mathbf{F}}^{-1}\mathbf{t} \otimes \overline{\mathbf{F}}^{-1}\mathbf{t} \otimes \overline{\mathbf{F}}^{-1}\mathbf{t} \otimes \overline{\mathbf{F}}^{-1}\mathbf{t}\rangle. \tag{2.38}$$

We transform $\widetilde{\mathbb{C}}$ into the spatial description $\widetilde{\mathbb{c}}$ by using a push-forward operation of $\widetilde{\mathbb{C}}$ times a factor of J^{-1}, which, in index notation, gives

$$J(\widetilde{\mathbb{c}})_{abcd} = \overline{F}_{aA}\overline{F}_{bB}\overline{F}_{cC}\overline{F}_{dD}(\widetilde{\mathbb{C}})_{ABCD}, \tag{2.39}$$

a new relationship to be derived in Appendix 2.A. With (2.36), we then obtain

$$\begin{aligned} J(\widetilde{\mathbb{c}})_{abcd} = {} & n\left[\psi_{\text{f}}'' \lambda^{2(1-p)} - (p-1)\psi_{\text{f}}' \lambda^{1-2p}\right] \overline{F}_{aA}\overline{F}_{bB}\overline{F}_{cC}\overline{F}_{dD}(\mathbf{H} \otimes \mathbf{H})_{ABCD} \\ & + n\psi_{\text{f}}' \lambda^{1-p} \overline{F}_{aA}\overline{F}_{bB}\overline{F}_{cC}\overline{F}_{dD}\mathbb{H}_{ABCD}. \end{aligned} \tag{2.40}$$

A specification of the fourth-order tensors in (2.40), by using $(2.31)_2$, $(2.33)_2$ and $(2.38)_2$, gives

$$\overline{F}_{aA}\overline{F}_{bB}\overline{F}_{cC}\overline{F}_{dD}(\mathbf{H} \otimes \mathbf{H})_{ABCD} = (\mathbf{h} \otimes \mathbf{h})_{abcd}, \tag{2.41}$$

$$\overline{F}_{aA}\overline{F}_{bB}\overline{F}_{cC}\overline{F}_{dD}\mathbb{H}_{ABCD} = (p-2)\langle \overline{\lambda}^{p-4} \mathbf{t} \otimes \mathbf{t} \otimes \mathbf{t} \otimes \mathbf{t}\rangle_{abcd} = \mathbb{H}_{abcd}, \tag{2.42}$$

where we have introduced the shorthand notation $\mathbb{H}$. We re-substitute (2.41) and (2.42) in (2.40), and receive the fictitious elasticity tensor $\widetilde{\mathbb{c}}$ in the spatial description times J, via

$$J\widetilde{\mathbb{c}} = n\left[\psi_{\text{f}}'' \lambda^{2(1-p)} - (p-1)\psi_{\text{f}}' \lambda^{1-2p}\right] \mathbf{h} \otimes \mathbf{h} + n\psi_{\text{f}}' \lambda^{1-p} \mathbb{H}, \tag{2.43}$$

which is equivalent to the result of Miehe et al. [119]. Equation (2.43) contains an additional J, when compared with [119], because in our case it corresponds with the Cauchy stress tensor instead of the Kirchhoff stress tensor. The contribution of the single filament model is manifest in (2.43) through the derivatives of the single filament strain-energy function given in equations $(2.11)_3$ and (2.14), (2.15).

With (2.43), we can finally calculate the isochoric part of (2.34) which can be expressed as (also compare with [112, Sec. 6.6] and Appendix 2.A)

$$\mathbb{C}_{\text{iso}} = \mathbb{P} : \widetilde{\mathbb{C}} : \mathbb{P} + \frac{2}{3}\text{tr}(\widetilde{\boldsymbol{\sigma}})\mathbb{P} - \frac{2}{3}(\boldsymbol{\sigma}_{\text{iso}} \otimes \mathbf{I} + \mathbf{I} \otimes \boldsymbol{\sigma}_{\text{iso}}). \tag{2.44}$$

The stress tensors $\widetilde{\boldsymbol{\sigma}}$ and $\boldsymbol{\sigma}_{\text{iso}}$ are already known from equations (2.33) and (2.27), respectively.

2.3.4 Numerical aspects

Solving the spherical integrals to obtain the averaged quantities, i.e. equations $(2.22)_2$, $(2.33)_3$ and $(2.42)_2$, is the last issue to be resolved. Several approximations for this problem exist in the literature. Bažant and Oh [122], for example, provide a range of different schemes. Miehe et al. [119] chose the 21-point numerical integration method and showed that the values obtained are very close to the true values for well-behaved functions. The scheme includes 21 discrete unit vectors $\mathbf{R}^i$ distributed inside a hemisphere along with the associated integration weights $w^i/2$, with $i = 1, 2, \ldots, 21$. The symmetry of the constellation allows us to simply double the weights to integrate over the whole sphere. The values for the scheme are summarized in [122, Table 1] or [119, Table 2], where r^i_k $(k = 1, 2, 3)$ denote the three Cartesian components of $[\mathbf{R}^i] = [r^i_1, r^i_2, r^i_3]^{\text{T}}$.

The discretization of the continuous sphere into 21 radius vectors, i.e. $\mathbf{R} \to \mathbf{R}^i$, also results through (2.18) and (2.20) in discrete versions of $\mathbf{t} \to \mathbf{t}^i$ and $\overline{\lambda} \to \overline{\lambda}^i$, respectively. Using the integration scheme and equation (2.22), the homogenized stretch λ is calculated through

$$\lambda = \langle \overline{\lambda} \rangle_p \sim \left[\sum_{i=1}^{21} (\overline{\lambda}^i)^p w^i \right]^{1/p}. \tag{2.45}$$

The same approach is used to work out $(2.33)_3$ and $(2.42)_2$, i.e.

$$\mathbf{h} = \langle \overline{\lambda}^{p-2} \mathbf{t} \otimes \mathbf{t} \rangle \sim \sum_{i=1}^{21} (\overline{\lambda}^i)^{p-2} \mathbf{t}^i \otimes \mathbf{t}^i w^i, \tag{2.46}$$

$$\mathbb{H} = (p-2) \langle \overline{\lambda}^{p-4} \mathbf{t} \otimes \mathbf{t} \otimes \mathbf{t} \otimes \mathbf{t} \rangle \sim (p-2) \sum_{i=1}^{21} (\overline{\lambda}^i)^{p-4} \mathbf{t}^i \otimes \mathbf{t}^i \otimes \mathbf{t}^i \otimes \mathbf{t}^i w^i. \tag{2.47}$$

The schematic in Figure 2.5 shows a step-by-step flow chart for the computational steps to obtain the isochoric Cauchy stress tensor $\boldsymbol{\sigma}_{\text{iso}}$ and the related elasticity tensor $\mathbb{c}_{\text{iso}}$ from the given deformation gradient $\mathbf{F}$. The filament and the network models can be kept separated with only a few interactions. This separation is indicated in Figure 2.5 by the grey boxes. Next we assemble both models and calculate the solution. The inputs are $\mathbf{F}$, the material parameters, then $\mathbf{R}^i$ and w^i. First, $\overline{\mathbf{F}}$ is computed to determine the 21 deformed vectors $\mathbf{t}^i$. From that, the stretches $\overline{\lambda}^i$ can be calculated which are used for the averaged stretch λ, then $\mathbf{h}$ and $\mathbb{H}$. These steps belong to the micro-sphere model. Then, we obtain ψ_{f}' and ψ_{f}'' within the filament model. Eventually, the fictitious Cauchy stress tensor $\widetilde{\boldsymbol{\sigma}}$ and the related elasticity tensor $\widetilde{\mathbb{c}}$ can be determined, so that we arrive at the isochoric parts of the Cauchy stress tensor $\boldsymbol{\sigma}_{\text{iso}}$ and the elasticity tensor $\mathbb{c}_{\text{iso}}$.

2.4 Experimental approach to test an actin network

A determination of the actual values for the parameters is needed to make use of the model. Hence, this section introduces simple shear experiments conducted on reconstituted actin networks. We describe the sample preparation and the experimental protocol in Section 2.4.1, followed by a presentation of the resulting data in 2.4.2. Section 2.4.3 shows a comparison of the experimental data with the fitted model.

2.4.1 Sample preparation and rheology

Actin was purified from rabbit skeletal muscle by a modified protocol of Spudich and Watt [156], where an additional gel filtration step is done [157]. Lyophilized G-actin was stored at -21°C and for sample preparation it was dissolved in deionized water and dialyzed against G-buffer (2 mM Tris-HCl, 0.2 mM ATP, 0.2 mM $CaCl_2$, 0.2 mM DTT, 0.005 % NaN_3, pH 8.0) at 4°C. The solution was kept at 4°C and used within 10 days. HMM was prepared from myosin II by chymotrypsin digestion as in [158]. Polymerization was started through addition of an ATP-free 10× F-buffer (20 mM Tris-HCl, 20 mM $MgCl_2$, 1 M KCl, 2 mM DTT, 2 mM $CaCl_2$, pH 7.5). The solutions were gently mixed and loaded into the measuring chamber within one minute. Polymerization, cross-linking, and the transition of HMM to its rigor state was monitored by means of the storage modulus at 0.5 Hz.

The mechanical properties of the network were characterized with a stress-controlled rheometer (Physica MCR301, Anton Paar, Graz, Austria) at 21°C. The 50 mm parallel plate geometry was used with 160 μm plate separation. The deformation in rotational mode was increased at $\dot{\gamma} = 5\%/\text{s}$ until $\gamma = 500\%$, while torsional couple (shear stress) and normal force were recorded. The network was destroyed in all cases

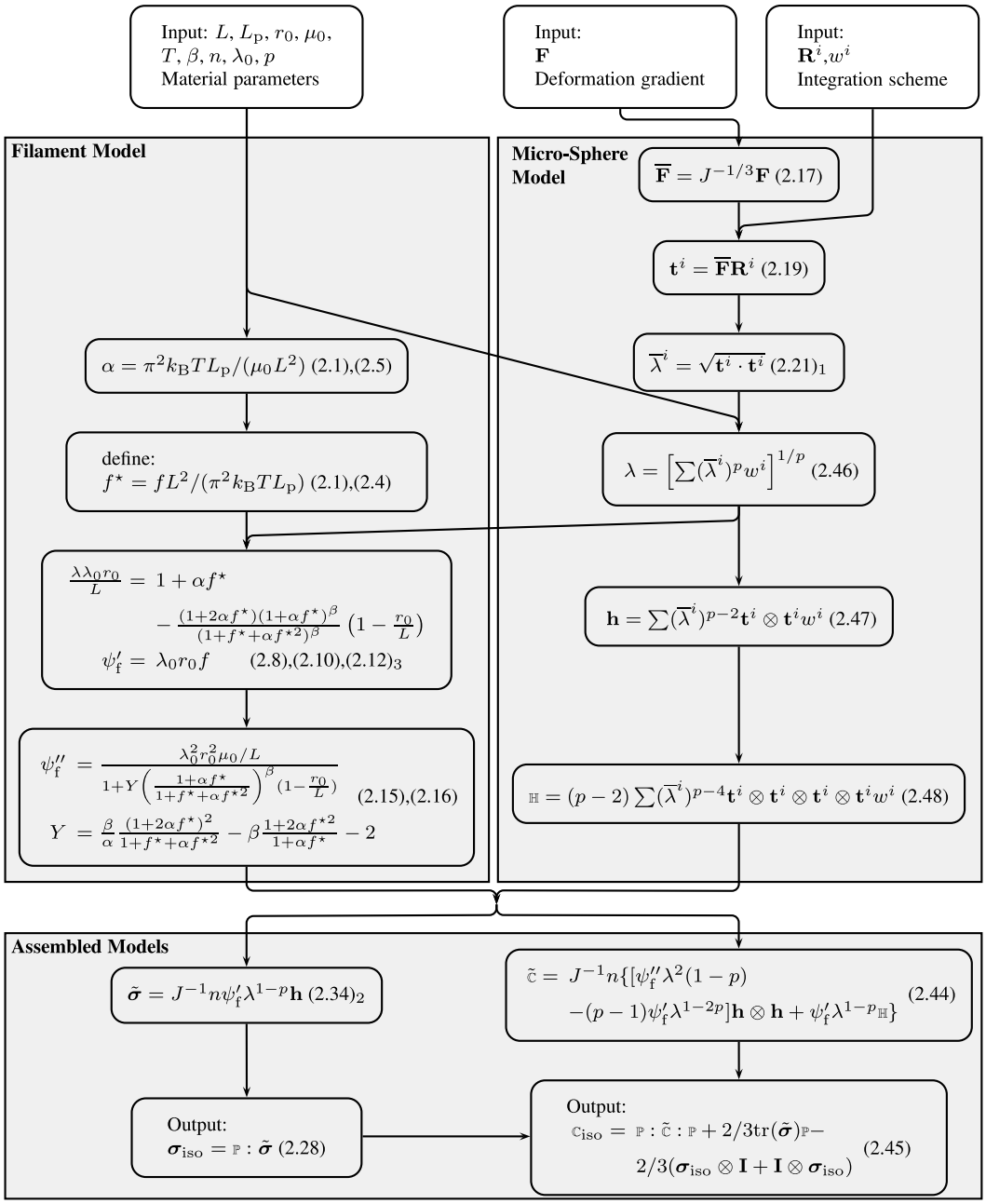

Figure 2.5: Flow chart of the algorithm as a summary of Sections 2.2.2 and 2.3. The micro-sphere model calculates λ from $\mathbf{F}$, which is used in the filament model. Both models are assembled to calculate $\boldsymbol{\sigma}_\mathrm{iso}$ and $\mathbb{C}_\mathrm{iso}$. Numbers in parentheses refer to the respective equations in the text. All parameters which need to be fed into the model are summarized in the top left box. The deformation gradient $\mathbf{F}$ depends on the problem to solve, while $\mathbf{R}^i$ and w^i can be found in [119, Table 2].

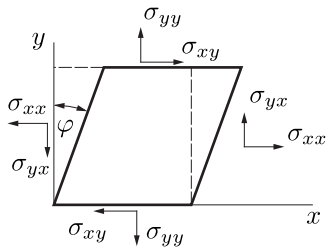

Figure 2.6: Simple shear with shear angle φ, deformation $\gamma = \tan\varphi$, (Cauchy) shear stresses $\sigma_{xy} = \sigma_{yx}$ and normal stresses σ_{xx} and σ_{yy}. The first index of a stress component characterizes the direction in which the stress works and the second index gives the direction of the outward pointing normal vector of the considered plane. The arrows indicate the positive directions of stresses. The dashed lines depict the reference configuration.

long before the maximum deformation was reached. Fifteen samples were tested, all with an actin concentration of $c_{\mathrm{A}} = 9.5\,\mu\mathrm{M}$. Three series with different cross-linker densities $R = 1/10$, $1/20$ and $1/40$ were tested, each with five experiments. The molar ratio of HMM to actin molecules, $R = c_{\mathrm{HMM}}/c_{\mathrm{A}}$, is widely used as a measure of the degree of cross-linking (see, for example, [139]). The distance between cross-links can be considered as an equivalent to the end-to-end distance r in the proposed model.

2.4.2 Simple shear behavior

The experimental setup of the bulk rheology with cone-plate geometry resembles simple shear conditions. However, a parallel plate setup was used to minimize the sample volume, and the error in assuming that the deformation approximates simple shear was assumed to be small. In simple shear, the surfaces that are perpendicular to the direction of the motion show an angle φ with respect to the reference configuration, as depicted in Figure 2.6. This angle is related to the shear deformation in the rheology experiment through $\gamma = \tan\varphi$.

The results of the experiment are depicted in Figure 2.7, which shows the Cauchy shear stress σ_{xy} and the Cauchy normal stress σ_{yy} versus the deformation γ. Additionally, we approximated the instantaneous shear modulus as $K = \partial\sigma_{xy}/\partial\gamma \sim \Delta\sigma_{xy}/\Delta\gamma$, which is a measure for the stiffness. The data from individual experiments are presented to highlight challenges in measuring the normal stress. The ascending data points in the shear stress diagrams, i.e. Figure 2.7(a),(d),(g), indicate a good reproducibility for a fixed R. Only the first measurement with $R = 1/40$ was slightly stiffer than the subsequent samples. Our focus for analysis and further processing lies only on strains below the point at which the maximal nonlinear stiffness is reached, i.e. the maximum in Figures 2.7(b),(e),(h). Beyond these points, an irreversible alteration

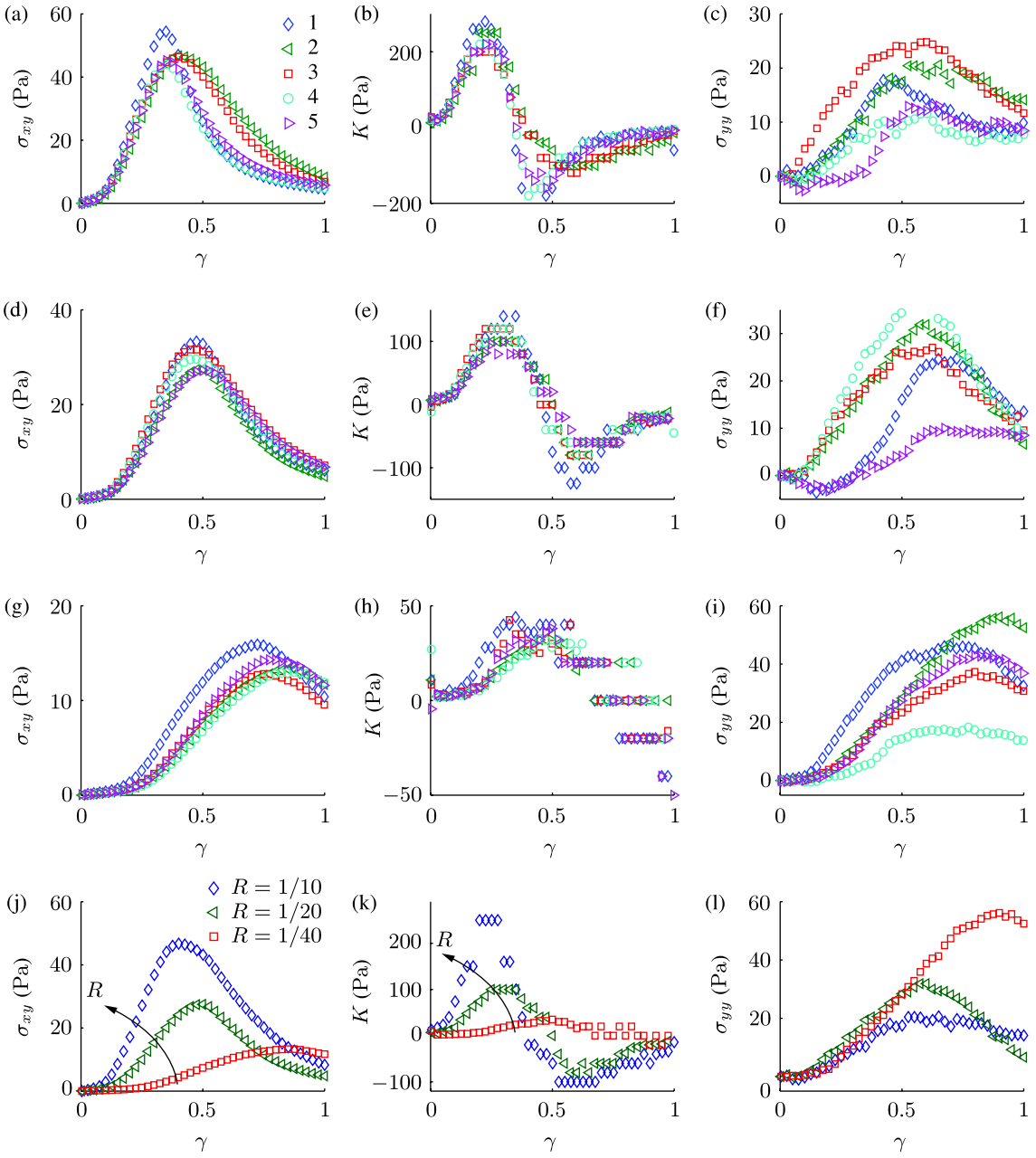

Figure 2.7: Results of the rheological experiments with constant actin concentration $c_A = 9.5\,\mu$M. Cauchy shear stress σ_{xy}, instantaneous shear modulus K and Cauchy normal stress σ_{yy} versus shear deformation γ are shown in the first column [(a), (d), (g) and (j)], second column [(b), (e), (h) and (k)] and third column [(c), (f), (i) and (l)], respectively. The five experiments for each cross-linker densitiy $R = 1/10$ (first row), $R = 1/20$ (second row) and $R = 1/40$ (third row) are depicted in (a)–(i), where the legend from (a) applies also to (b)–(i). The last row, (j)–(l), compares the second experiment for each R. The legend in (j) applies also to (k) and (l). The diagrams show only every fifth point to improve readability.

of the network and a rupture from the plates, as observed for actin bundle networks [159], might occur. The mean values of the shear stresses $\sigma_{xy,\max}$ at the inflection point are 17, 10, 3 Pa for $R = 1/10$, $1/20$, and $1/40$, respectively. With decreasing R the corresponding strains increase according to 0.2, 0.25 and 0.35. Figures 2.7(j),(k) compare σ_{xy} and K of the second experiment for each cross-linker density R.

The shear stress shows a relatively soft response in the small deformation regime and stiffens heavily with increasing γ. Comparing the curves for different cross-linker densities in Figure 2.7(j), we see a stiffer response the higher R becomes as the arrow indicates.

The bulk rheology provides a second set of information about the stress state of the sample. The force in the axial direction of the rotor F_{N} is evaluated from the first Piola-Kirchhoff normal stress $P_{yy} = F_{\mathrm{N}}/S$ (engineering stress), where S is the area of the measuring plate in reference configuration. We consider the deformation gradient of simple shear in matrix notation

$$[\mathbf{F}] = \begin{bmatrix} 1 & \gamma & 0 \\ 0 & 1 & 0 \\ 0 & 0 & 1 \end{bmatrix}, \tag{2.48}$$

where $J = 1$. The Piola transformation of the first Piola-Kirchhoff stress tensor into the Cauchy stress tensor is $\boldsymbol{\sigma} = J^{-1}\mathbf{FP}$. With equation (2.48), we observe the identity $\sigma_{yy} = P_{yy}$. The experimental results are illustrated in the Figures 2.7(c),(f),(i). All curves show a soft behavior for low γ, before they stiffen to a maximum, which is at a deformation comparable to the maximum of the shear stress data.

Janmey et al. [39] were the first to describe the typical normal force response of biopolymer networks, which acts in the negative direction of the rheometer's axis and coined the expression 'negative normal stress'. It means that the sample under shear deformation tries to decrease the distance between the plates and a tensile stress acts on the network. Eventually, this stress rips the network off the plates as observed for actin bundle networks [159]. With our definitions in Figure 2.6, however, the tensile stresses σ_{xx}, σ_{yy} acting on the sample have positive signs. These definitions are a standard convention in continuum mechanics which we employ in the present work to describe the material behavior. As a consequence the normal Cauchy stress σ_{yy} in [39] is inverted and thus positive. Hence, our experiments confirm the results of Janmey et al. [39]. The sign of the normal stress is important to note when comparing cross-linked networks of actin to rubber, because the Poynting effect predicts a stress in the opposite direction. Instead of calling the phenomenon negative normal stress as Janmey et al. [39] we would call it 'exceptional normal stress' behavior. The difference between actin networks and, for example, rubber can be illustrated by looking at the latter modeled as Mooney-Rivlin material under simple shear and

plane stress. The strain-energy function Ψ_{MR} for the Mooney-Rivlin material is

$$\Psi_{\mathrm{MR}} = c_1(I_1 - 3) + c_2(I_2 - 3), \tag{2.49}$$

where I_1 and I_2 are the first and second invariants of the right Cauchy-Green tensor $\mathbf{C}$, and c_1, $c_2 > 0$ are material parameters. Continuum mechanics reveals for the Cauchy stresses [112, Sec. 6.3]

$$\sigma_{xx} = 2c_1\gamma^2, \quad \sigma_{yy} = -2c_2\gamma^2, \quad \sigma_{xy} = 2(c_1 + c_2)\gamma. \tag{2.50}$$

Hence rubber shows, in accordance with Poynting, a compressive stress in the y-direction no matter what sign the deformation has, while actin networks are subjected to tensile stresses.

When having a closer look on the normal stress data, we observe more noise within a dataset and much higher variations between the experiments of a series compared to σ_{xy} for fixed values of R. Furthermore, in some cases, the normal stress obtains small negative values for small deformations, before it stiffens to high positive values. More precisely, this behavior is seen for the fifth sample of the $R = 1/10$ series as well as the first and the fifth samples of the $R = 1/20$ series. The comparison of the Cauchy normal stress σ_{yy} for the second samples of each series is depicted in Figure 2.7(l). In contrast to the scaling of the stiffness for different R we see for σ_{xy} and K, it is not possible to find such a scaling unambiguously for σ_{yy}. Our choice of data suggests that there is the same behavior for low γ independent from the cross-linker density. On the other hand, we can choose experiments in a way that we can see increasing stiffness with increasing R or the other way around.

In summary, we observed three features which are related to the quality of of the normal stress data: noise, variations in a series and ambiguous scaling. In this context, it must be noted, that the rheometer operates close to the normal force resolution limit of commercially available devices. All three effects may stem from the limitations of the experimental technique or from the inelastic phenomena which are neglected in the proposed model. For this reason, we subsequently make use of the normal stress data only with caution.

2.4.3 Fitted model parameters

The kinematics inside a rheometer is approximated by simple shear deformation with a plane stress condition. We fitted the assembled model to the resulting experimental data obtained from the rotational rheology experiment. In particular, we present parameter sets for the individual experiments as well as the median and the interquartile range (IR) for each cross-linker density R. As mentioned above the deformations of interest reduce from zero to the point of maximum stiffness. As a consequence, the

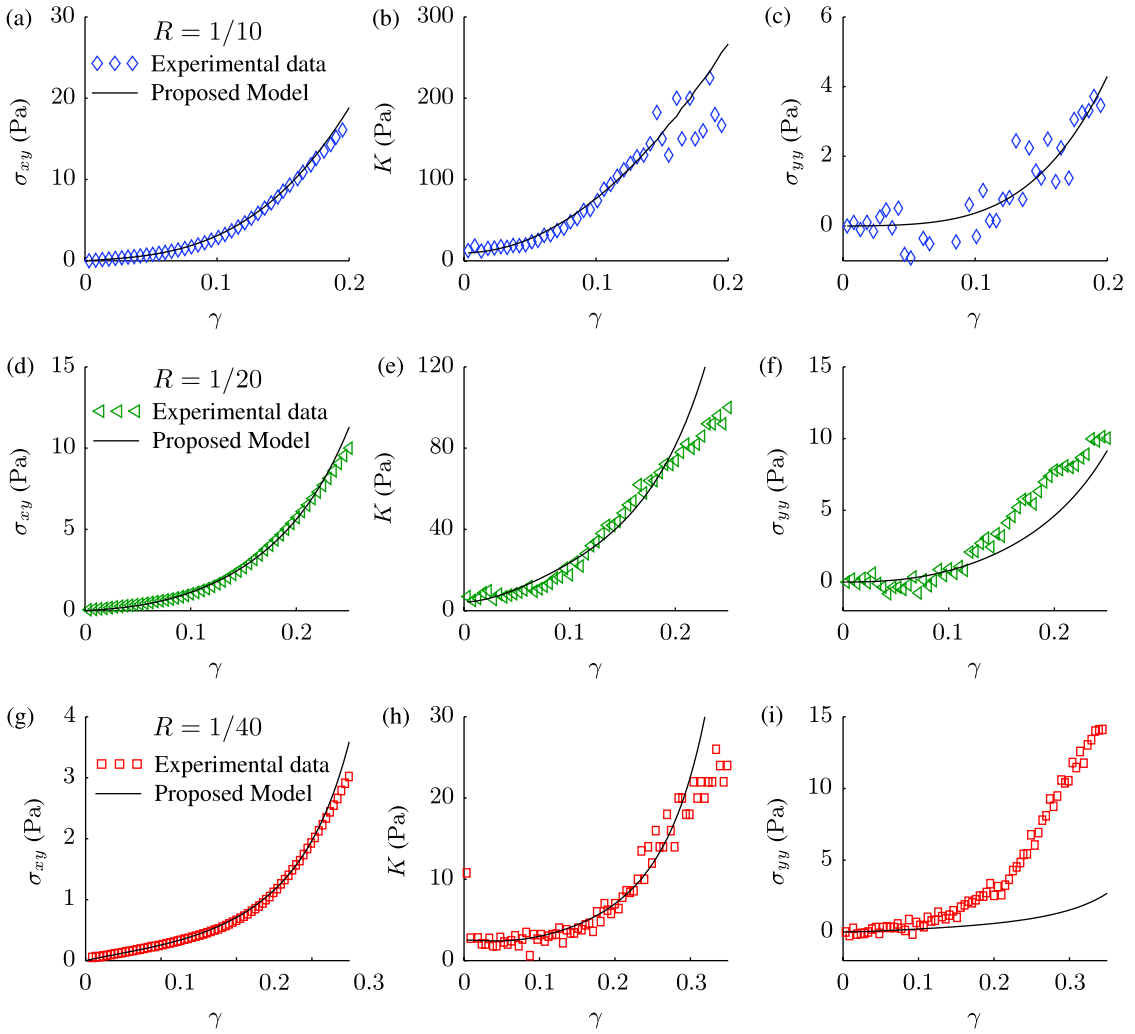

Figure 2.8: Fit of the proposed model to the experimental data of Fig. 2.7(j)-(l), this time showing all data points. Cauchy shear stress σ_{xy}, instantaneous shear modulus K and Cauchy normal stress σ_{yy} versus shear deformation γ are depicted in the first column [(a), (d) and (g)], second column [(b), (e) and (h)] and thrid column [(c), (f) and (i)], respectively. The first row (a)-(c) corresponds to $R = 1/10$, the second row (d)-(f) corresponds to $R = 1/20$ and the third row (g)-(i) corresponds to $R = 1/40$. The legend of the first subgraph in a row applies to also to the other diagrams in the row.

diagrams with the comparisons of the fitted model to the experiments in Figure 2.8 are limited to $\gamma = 0.2, 0.25, 0.35$ for $R = 1/10, 1/20, 1/40$, respectively. The samples which dropped to negative values for σ_{yy} before they stiffened (fifth sample of the $R = 1/10$ series; first and fifth sample of the $R = 1/20$ series) were excluded from the analysis because they mislead the optimization procedure.

The present model uses nine parameters, most of them are external (and controllable)

variables. In order to make the fits more reliable we fix most of these parameters by applying the knowledge about the single filament and the rheology experiment. The temperature during the experiment was held constant at $T = 294\,\mathrm{K}$. From the fit to the single filament data we adopt $L_\mathrm{p} = 16\,\mu\mathrm{m}$, $\mu_0 = 38.6\mathrm{nN}$ and $\beta = 0.438$. All samples in the experiment had an actin concentration of $c_\mathrm{A} = 9.5\,\mu\mathrm{M}$ ($1\,\mathrm{M} = 1\,\mathrm{mol/l}$), while the distance between cross-links and thus the contour length L was varied with R. According to Palmer and Boyce [82], we determined the number of filaments n in a unit volume through $n = \rho_\mathrm{L}/L$, where ρ_L is the actin length density to be determined in terms of c_A, the linear actin density $\rho_\mathrm{A} = 16\,\mathrm{MDa}/\mu\mathrm{m}$ [160], the molecular mass of each actin monomer $M_\mathrm{A} = 42\,\mathrm{kDa/monomer}$ and the Avogadro constant $N_\mathrm{A} = 6.022 \times 10^{23}\,\mathrm{monomers/mol}$, i.e. $\rho_\mathrm{L} = c_\mathrm{A} N_\mathrm{A} M_\mathrm{A}/\rho_\mathrm{A}$. We obtain a relationship between n and L as

$$n = \frac{c_\mathrm{A} N_\mathrm{A} M_\mathrm{A}}{L \rho_\mathrm{A}} = \frac{15.0\,\mu\mathrm{m}^{-2}}{L}. \tag{2.51}$$

The contour length L, the end-to-end distance at zero force r_0 and the pre-stretch λ_0 are external variables. The first is difficult to measure simultaneously with the experiment, while the second can only be observed for free single filaments. In the case of pre-stretches, however, we are not aware of a technique by which they can actually be quantified. Hence, we used these quantities together with the averaging parameter p as free parameters in the fitting procedure. We determined the values for the four parameters by means of MATLAB's nonlinear Least Squares tool (`lsqnonlin`). Both, the shear stress and the normal stress data were included in the objective function. When using unbiased fitting for these data with large, probably exponential strain stiffening, the region of low stresses may become underrepresented. Therefore, we used weights which decreased logarithmically from 1 to 0.1. To account for the uncertainty in the normal stress data, we employed 1/10 of the weights of σ_{xy} for σ_{yy}. As a measure for the goodness of fit we calculated the well-known coefficient of determination $\mathcal{R}^2$. We tested the robustness of the fitted parameters by varying the initial values of the free parameters substantially. The optimization converged rarely to another solution and if so, the numbers were not physically meaningful.

The results are summarized in Table 2.2, while Figure 2.8 depicts the experimental data from Figures 2.7(j)–(l) together with the fitted model. For $R = 1/10$ and $1/20$ we observe values for $\mathcal{R}^2$ close to one, suggesting a good fit which can be confirmed optically in the Figures 2.8(a)–(f). The fact that we have not seen a scaling of the normal stress in Figure 2.7(l) is reflected in the fits for $R = 1/40$, where the normal stress can only be captured with the correct (positive) trend. The coefficient of determination for this cross-linker density ranges between $\mathcal{R}^2 = 0.78$ to 0.85 and Figure 2.8(i) shows that the model is far away from the experimental normal stress data. However, the different weights for σ_{xy} and σ_{yy} cause that we still

Table 2.2: Model parameters with medians and interquartile ranges for different cross-linker densities R and constant actin concentration $c_A = 9.5\,\mu$M. Medians and interquartile ranges (IR) are given for each measurement series. The parameters $T = 294\,$K, $L_p = 16\,\mu$m, $\mu_0 = 38.6\,$nN, $\beta = 0.438$ and $nL = 15\,\mu\text{m}^{-2}$ apply to all fits.

$R = 1/10$	L (μm)	r_0 (μm)	λ_0 ($-$)	p ($-$)	$\mathcal{R}^2$
1	0.055	0.028	1.003	15.76	0.976
2	0.067	0.042	1.002	10.48	0.975
3	0.397	0.318	1.004	63.85	0.993
4	0.172	0.165	1.003	3.30	0.989
5	–	–	–	–	–
Median	0.120	0.104	1.003	13.12	0.983
IR	0.164	0.165	0.001	19.10	0.014
$R = 1/20$	L (μm)	r_0 (μm)	λ_0 ($-$)	p ($-$)	$\mathcal{R}^2$
1	–	–	–	–	–
2	1.052	0.868	1.010	72.01	0.975
3	0.769	0.632	1.004	66.35	0.977
4	0.988	0.818	1.007	84.15	0.963
5	–	–	–	–	–
Median	0.988	0.818	1.007	72.01	0.975
IR	0.142	0.118	0.003	8.90	0.007
$R = 1/40$	L (μm)	r_0 (μm)	λ_0 ($-$)	p ($-$)	$\mathcal{R}^2$
1	1.666	1.292	1.011	90.98	0.782
2	3.750	2.795	1.070	98.64	0.798
3	2.969	2.272	1.039	98.33	0.832
4	4.279	3.135	1.096	77.83	0.884
5	3.191	2.446	1.043	89.35	0.827
Median	3.191	2.446	1.043	90.98	0.827
IR	0.781	0.523	0.031	8.98	0.034

obtain an excellent fit for the shear stress, see Figures 2.8(g),(h). The uncertainty in the measured normal stress within a series with fixed R is the reason for a high IR. For example, the third and fourth measurements in the $R = 1/10$ series deviate obviously from the first and second measurements and cause the high IR of L, r_0 and p. The absence of a clear scaling of the normal stress data for different R makes it difficult to reliably quantify the scaling of the model parameters, hence we describe it qualitatively. With decreasing R, all four parameters increase. The end-to-end

distance at zero force r_0 is certainly always smaller than the contour length L and the pre-stretch is, in accordance with its definition, always larger than one. The scaling of p shows that the non-affinity of the networks increases if the cross-linker density decreases, which was reported earlier [41]. In order to obtain the full parameter set, the filament density n needs to be calculated by dividing $15\,\mu\mathrm{m}^{-2}$ by L. This results in values related to the medians of $n = 125$, 15.2, 4.7 filaments per $\mu\mathrm{m}^3$ for $R = 1/10$, 1/20, 1/40, respectively.

The extensibility of the filaments has minor importance for fitting the model to the rheological experiments. However, we used the extensible version for two reasons. First, the fiber stretch in shear experiments is relatively small. When modeling problems with higher filament stretch, we come close to the constraint $r/L = 1$, where the inextensible model becomes infinitely stiff which is unrealistic. Second, an iteration step in a finite element program may reach the constraint even if the solution of the problem is far away.

Note that in a real sample, the contour length of the filaments is not a constant but exponentially distributed. In the presented model we think of L as a representative mean length of the filament. The mean length of not cross-linked F-actin is 4–5μm [161]. By assuming that cross-linking shortens the contour length, we conclude that both L and r_0 in Table 2.2 are in a realistic range. Tharmann et al. [26] estimated the contour lengths of samples with $c_\mathrm{A} = 9.5\,\mu\mathrm{M}$ by means of scaling arguments between 1 and $3\,\mu$m for varying $R = 1/10$ to 1/40.

2.5 Representative numerical examples

In the following we present the characteristic features of the proposed model in the form of parameter studies; in particular, the influence of the parameters of the network, the averaging parameter p and the pre-stretch λ_0 on the simple shear behavior is studied. Finally, the capability of the finite element implementation is demonstrated by simulating the indentation of a rigid spherical tip of an atomic force microscope (AFM) cantilever into a surface.

2.5.1 Parameter studies of simple shear deformation

A study of the stresses for several p-values is given in the Figures 2.9(a)–(c), where the pre-stretch λ_0 is held constant with the value 1.007. The Cauchy shear stress σ_{xy}, as depicted in Figure 2.9(a), is approximately linear for smaller deformations and stiffens for larger values of γ. The tangent to the curve at $\gamma = 0\%$ indicates a stiffness against shear deformation from the very beginning, which is often referred to as *initial shear modulus* in the literature (see, for example, [82]). The variation of p induces

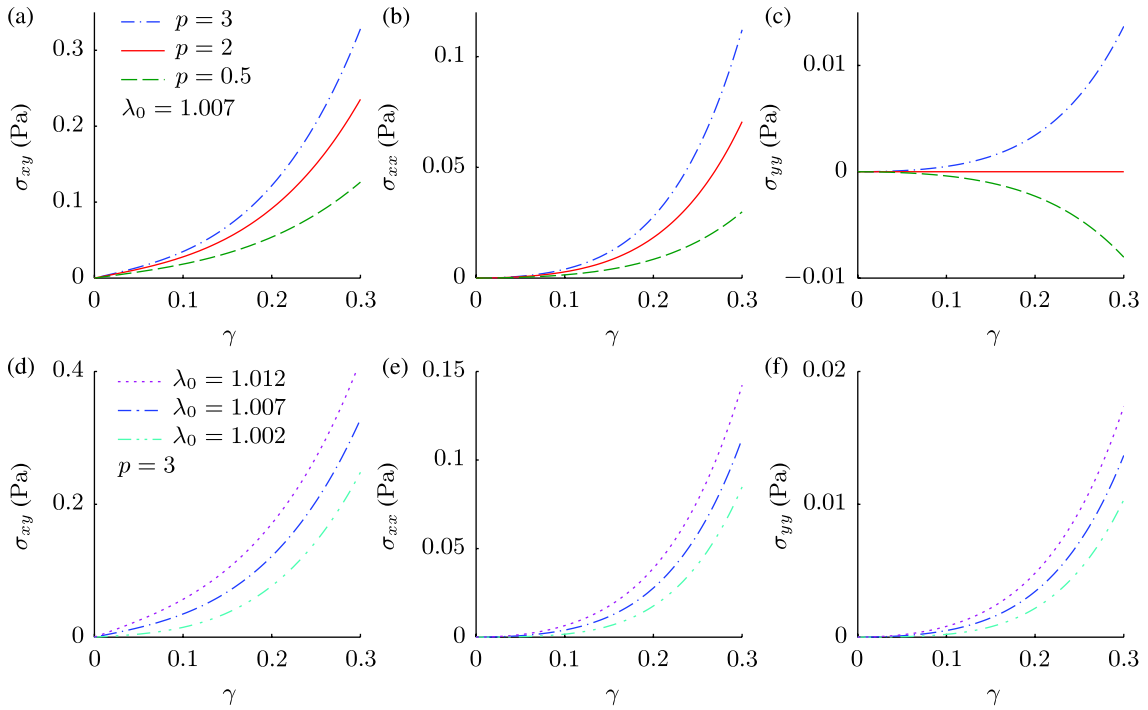

Figure 2.9: Representative plots for shear and normal Cauchy stresses σ_{xy}, σ_{xx} and σ_{yy} versus deformation γ for simple shear with parameters $L_\mathrm{p} = 16\,\mu\mathrm{m}$, $L = 0.988\,\mu\mathrm{m}$, $r_0 = 0.818\,\mu\mathrm{m}$, $\mu_0 = 38.6\,\mathrm{nN}$, $n = 15.2\,\mu\mathrm{m}^{-3}$, $\beta = 0.438$: (a)–(c) varying p-values by holding $\lambda_0 = 1.007$ constant; (d)–(f) varying pre-stretch by holding $p = 3$ constant. The legend in (a) also applies to (b) and (c), while the legend in (d) is also valid for (e) and (f).

a stiffer response as p increases. The normal Cauchy stress σ_{xx} shows a nonlinear behavior with a horizontal tangent at $\gamma = 0\%$. It varies significantly for $p = 0.5$, 2, 3, where higher values of p cause again a stiffer response (see Figure 2.9(b)). As pointed out previously, the micro-sphere model is equivalent to the eight-chain model [111] for $p = 2$, for which we see that the normal Cauchy stress σ_{yy} is identically equal to zero (see Figure 2.9(b)). For $p < 2$ the resulting stress σ_{yy} is negative while $p > 2$ shows the characteristic behavior for biopolymers, as discussed previously. This enables us to deal with a wide variety of solids, particularly with engineering materials and biopolymer networks by only adjusting the averaging parameter p.

The pre-stretch λ_0 is the second material parameter at which we want to have a closer look. Soft tissue biomechanics is strongly connected to residual stresses. A comparison of whole cell experiments with the rheology of *in vitro* actin networks (see, Shin et al. [21]) indicates that also the filaments in the cytoskeleton are stressed in the unloaded reference configuration. This is captured in the model by the parameter λ_0. Figures 2.9(d)–(f) show plots for the Cauchy stresses σ_{xy}, σ_{xx} and σ_{yy} versus γ for a fixed $p = 3$ and various λ_0. The normal stresses have similar characteristics

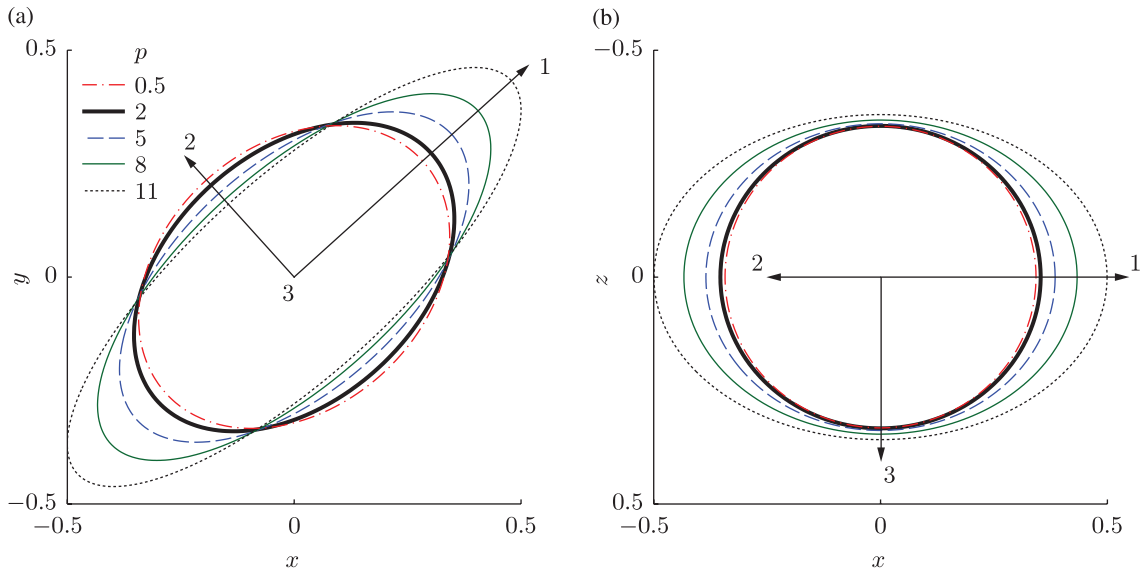

Figure 2.10: Visualization of the structural tensor $\mathbf{h}$ at $\gamma = 20\%$ deformation for p =0.5, 2, 5, 8 and 11. The 1-2-3-axes indicate the directions of the eigenvectors of $\mathbf{h}$.

with a horizontal tangent at $\gamma = 0\%$ and strong stiffening for large deformations. In Figure 2.9(d), the initial shear modulus can be seen excellently as well as the nonlinear response. The pre-stretch, here in the order of 0.2, 0.7 and 1.2%, strongly influences the magnitude of all stresses for rather small variations in its value. In summary, p changes or even inverts the normal Cauchy stress behavior (σ_{yy}), while λ_0 adjusts the Cauchy stresses σ_{xx}, σ_{yy}, σ_{xy}.

As observed the averaging parameter p has a great influence on the simple shear behavior of the material. To make this influence even more visible we illustrate the structural tensor $\mathbf{h}$, i.e. $(2.33)_2$, as an ellipsoid. The solution of the eigenvalue problem gives the lengths of the semi-axes. The corresponding eigenvectors indicate the orientation in space. In the reference configuration the ellipsoid specializes to a sphere with radius 1/3. Figure 2.10 depicts $\mathbf{h}$ at $\gamma = 20\%$ with $p = 0.5$, 2, 5, 8 and 11 in two normal projections. The coordinate system corresponds to the deformation gradient, as given in (2.48). We observe that the averaging parameter p does not change the orientation of the ellipsoid. However, a higher p leads to a stretch of the ellipsoid in the 1- and 3-directions as well as a contraction in the 2-direction.

2.5.2 Indentation of a spherical tip into a surface, finite element analysis

In order to demonstrate the capabilities of the proposed model we set up a simple boundary-value problem. In particular, we simulate the indentation of a rigid spherical tip into a surface, which resembles poking a cell with an atomic force microscope

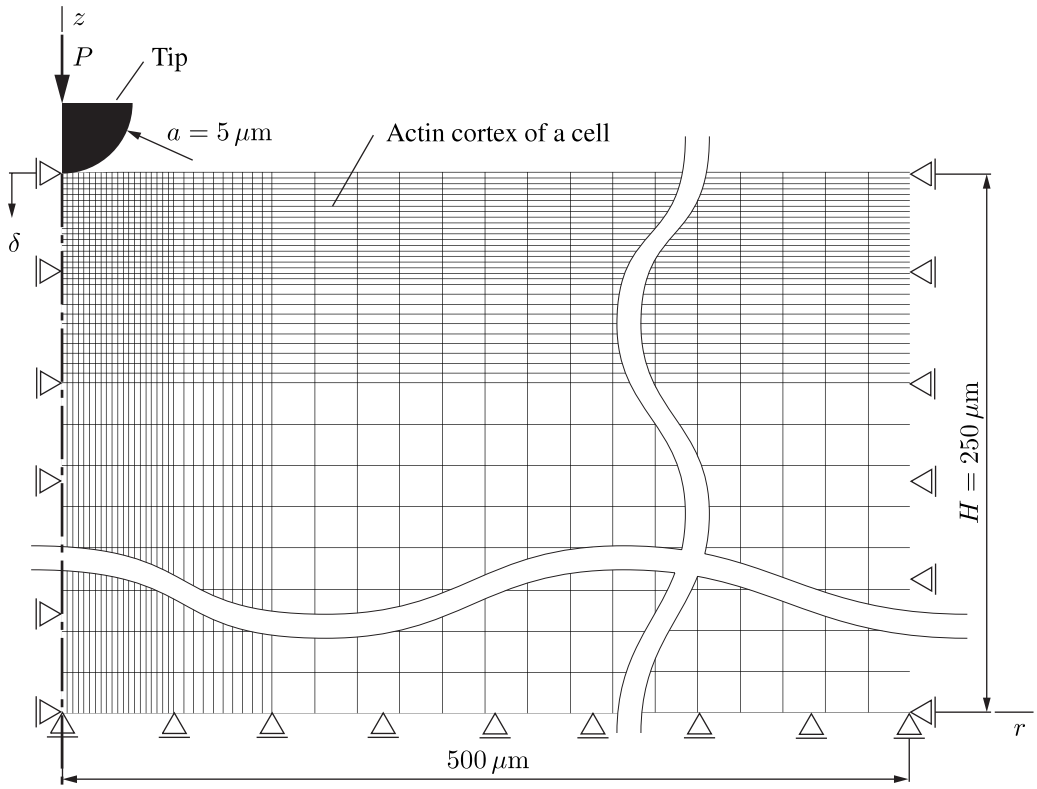

Figure 2.11: Finite element mesh and boundary conditions of an axisymmetric problem representing the indentation of a rigid spherical tip of an atomic force microscope cantilever into a surface, i.e. the actin cortex represented by an axisymmetric plate: indentation force P, indentation depth δ, tip radius a, material thickness H, radius of the plate $500\,\mu$m. The geometry is discontinuous, indicated by the curves, for better visibility of the point of the indentation.

(AFM) cantilever. The geometry is adopted from Lin et al. [162] and is large enough to be considered as an infinite half space, i.e. the dimensions do not replicate a typical cell. A spherical rigid tip with a radius $a = 5\,\mu m$ indents the surface. It is represented through an axisymmetric plate with a thickness of $H = 250\,\mu$m and a diameter of 1 mm. The radial dimension (r-direction) of the plate approximates an infinite half space. At the inner side of the plate, at $z = 0$, no displacements are possible in the z-direction, whereas that boundary can move horizontally (in the r-direction), as depicted in Figure 2.11. The symmetry condition can be seen at $r = 0$. The geometry is meshed with quadrilateral elements and refined close to the location of indentation marked by the black quarter circle in Figure 2.11, representing the tip of the AFM cantilever. For the analysis we use the previously determined medians of the material parameters for $R = 1/10$, as summarized in Table 2.2, except for the network averaging parameter p. For subsequent comparison with analytical results

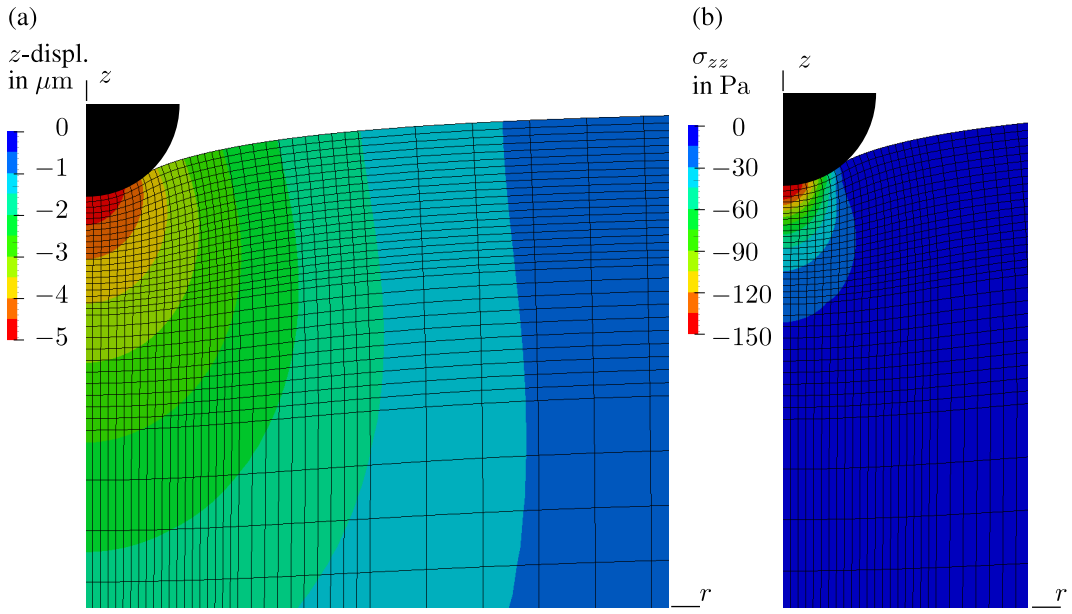

Figure 2.12: Axisymmetric finite element problem representing the indentation of a rigid spherical tip of an atomic force microscope cantilever into a surface: displacement (a) and normal Cauchy stress σ_{zz} (b) in the z-direction.

we use $p = 2$, thus the equivalent of the eight-chain model.

The material was implemented into the open source finite element analysis program FEAP[2]. The Q1/P0 mixed element formulation was used and incompressibility was enforced by means of the function $\Psi_{\text{vol}} = \kappa(J^2 - 1 - 2\ln J)/4$, where the bulk modulus κ served as a penalty parameter, which is more than three orders of magnitude larger than the initial shear modulus. The tip is a rigid sphere which is subject to an indentation force P against the z-direction. We assume that the tip penetrates $\delta = 5\,\mu\text{m}$ into the plate material. The interaction with the surface was performed through a frictionless contact algorithm. We achieved a quadratic rate of convergence for the Newton-Raphson algorithm in the finite element analysis. Figure 2.12 shows the resulting contour plots for the displacement and the Cauchy stress σ_{zz} in the z-direction. The maximum z-displacement and the Cauchy stress σ_{zz} are observed directly underneath the tip. A large zone is influenced in terms of the displacement around the point of the indentation. The stress plot in Figure 2.12(b) reveals a maximum compressive stress of $\sigma_{zz} \sim -150\,\text{Pa}$. The zone with larger stresses, however, is a rather small volume underneath the surface, where the tip is in contact.

Finally, we verify the results from the finite element analysis by means of an analytical model. Therefore, we extract the indentation force P in the z-direction as

[2]Version 8.2, by R.L. Taylor, University of California at Berkeley, USA

a function of the depth δ from the finite element analysis, and compare it with the (analytical) nonlinear force-depth relationship. The theory of Green et al. [163], refined by Beatty and Usmani [164] is valid for finite deformations of homogeneous and initially isotropic elastic half-spaces superimposed by small indentations. The force-depth relationship may be expressed as [165]

$$P = 2\pi \frac{\Gamma(\Psi)}{\Sigma(\Psi)} t(\delta), \tag{2.52}$$

where the functionals $\Gamma(\Psi)$ and $\Sigma(\Psi)$ depend on the strain energy Ψ stored in the cell and $t(\delta)$ is determined by the geometry of the rigid tip. The shape function of a spherical tip with radius a is

$$t(\delta) = \frac{4}{3\pi}\sqrt{a\delta^3}, \tag{2.53}$$

which was derived by Beatty and Usmani [164].

By assuming incompressibility and equibiaxial stretches in plane ($\lambda_1 = \lambda_2$), the change along the thickness (z-direction) can be expressed by the principal stretch

$$\lambda_3 = \lambda_1^{-2} = 1 - \frac{\delta}{H}. \tag{2.54}$$

The first invariant of the right Cauchy-Green tensor is, therefore, $I_1 = \mathrm{tr}\mathbf{C} = 2\lambda_1^2 + \lambda_1^{-4}$. To obtain $\Gamma(\Psi)$ and $\Sigma(\Psi)$ in equation (2.52) for a strain-energy function of the form $\Psi(I_1)$, Green et al. [163] derived, and Humphrey et al. [166] summarized the relationships

$$\Gamma = \frac{(A + K_1 B)\sqrt{K_1}}{1 + K_1} - \frac{(A + K_2 B)\sqrt{K_2}}{1 + K_2}, \tag{2.55}$$

$$\Sigma = \frac{K_1}{1 + K_1} - \frac{K_2}{1 + K_2}, \tag{2.56}$$

which are the desired functionals as required in (2.52). In these two equations the following values are needed for the computation, i.e.

$$A = 2\lambda_3^2 \psi_1, \qquad B = 2\lambda_1^2 \psi_1, \tag{2.57}$$

$$C = 4\lambda_1^2[\psi_1 + (\lambda_1^2 - \lambda_3^2)\psi_{11}], \tag{2.58}$$

$$D = 4\lambda_3^2[\psi_1 + (\lambda_3^2 - \lambda_1^2)\psi_{11}], \tag{2.59}$$

where $\psi_1 = \partial\Psi/\partial I_1$ and $\psi_{11} = \partial^2\Psi/\partial I_1^2$. Using equations (2.57)–(2.59) the dimensionless parameters K_1 and K_2 are the two solutions of the quadratic equation

$$BK^2 + (A + B - C - D)K + A = 0. \tag{2.60}$$

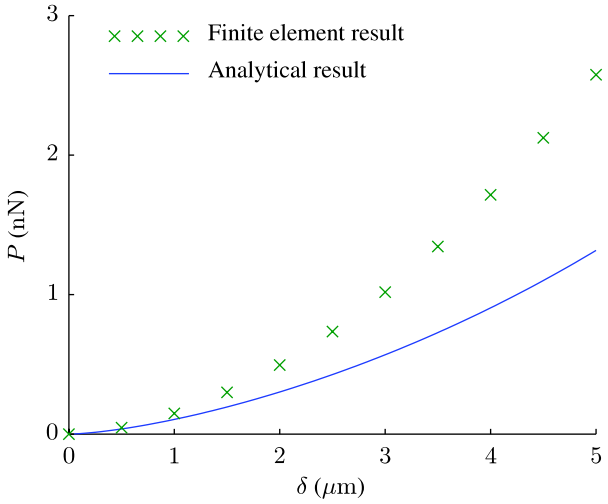

Figure 2.13: Indentation force P versus indentation depth δ obtained from the finite element analysis and the analytical solution according to (2.52)–(2.62).

In order to use the model (2.52)–(2.56), the strain-energy function is required to depend on the first invariant I_1 of $\mathbf{C}$. We used $p = 2$ in the finite element analysis; hence, we may use the equivalent homogenized filament stretch (2.24) according to Arruda and Boyce [111]. Considering incompressibility, equation (2.23) takes on the form $\Psi(I_1) = n\psi_\mathrm{f}(\lambda_\mathrm{AB}(I_1))$. By means of the chain rule and (2.24), the calculation of the first derivative of Ψ gives

$$\psi_1 = n\frac{\partial\psi_\mathrm{f}}{\partial I_1} = n\frac{\partial\psi_\mathrm{f}}{\partial\lambda_\mathrm{AB}}\frac{\partial\lambda_\mathrm{AB}}{\partial I_1} = \frac{n}{6\lambda_\mathrm{AB}}\psi_\mathrm{f}'. \tag{2.61}$$

The single filament contribution $\psi_\mathrm{f}' = \partial\psi_\mathrm{f}/\partial\lambda_\mathrm{AB}$ is given in $(2.11)_3$ with (2.10), where we substitute λ_AB for λ. The second derivative requires $(2.61)_3$, the product and chain rules, leading to

$$\psi_{11} = \frac{\partial\psi_1}{\partial I_1} = \frac{n}{6}\frac{\partial(\psi_\mathrm{f}'/\lambda_\mathrm{AB})}{\partial\lambda_\mathrm{AB}}\frac{\partial\lambda_\mathrm{AB}}{\partial I_1} = \frac{n}{36\lambda_\mathrm{AB}^3}(\psi_\mathrm{f}''\lambda_\mathrm{AB} - \psi_\mathrm{f}'), \tag{2.62}$$

where we recall equations (2.14), (2.15) for the computation of ψ_f''. Equations $(2.61)_3$ and $(2.62)_3$ are then used in (2.57), (2.59) to obtain $P(\delta)$.

We use the same material parameters as for the finite element analysis, i.e. we take the median values for $R = 1/10$ in Table 2.2. We compared the analytical results with the values obtained from the finite element calculations in Figure 2.13. As expected, the two models are identical for small δ. However, they diverge more and more when the indentation depth δ approaches the radius a at the spherical tip, i.e. the analytical model underestimates the indentation force P for larger indentation

depths. At maximum indentation $\delta = 5\,\mu$m, the relative error of the model (2.52)–(2.62) is $\sim 48\%$. The divergence of the two results arises from the assumption in the analytical model that a finite deformation is superimposed by an infinitesimal indentation. Hence, the good agreement for lower values of δ and worsening for larger indentations. This comparison gives us still good confidence in having an error-free implementation of the model.

2.6 Summary and concluding remarks

The present work introduces a new multi-scale model to describe the mechanics of reconstituted cross-linked actin networks, which are used as a model system for the actin cortex. On the micro-scale we modify the extensible β-model, a worm-like chain model, to describe the single filament properties of filamentous actin and prepare it for usage in the network model. We derive physically meaningful values for the interpretable material parameters together with an excellent fit to experimental data.

The three-dimensional, discrete structure of the network is homogenized into a continuous material on the macro-scale by means of the micro-sphere model. It is derived in the reference configuration and by applying a push-forward operation we obtain the equations for the Cauchy stress and elasticity tensors in the current configuration. Rheological experiments are conducted to determine the additional parameters for describing the network. We demonstrate that the assembled model is able to build a stable framework for solving more complex boundary-value problems such as the simulation of the indentation of an AFM cantilever tip into a surface.

In order to achieve the present continuum mechanical formulation we needed to employ several assumptions. In the following we summarize these assumptions we introduced throughout the present text and discuss their basis and which consequences and possible limitations they add to the model. We chose an extensible filament model to capture the experimental data. This model is well defined for all ranges of the end-to-end distance, and hence ensures numerical stability of the finite element implementation. The relationship between force and end-to-end distance can only be given in an implicit form which makes it necessary to employ a root search algorithm. The filaments are pre-stretched inside the network [125] and thus we introduced the material parameter λ_0. The key assumption for the constitutive modeling of a network of filaments was that the network strain energy equals the sum of the strain energy of the deformed filaments. This implies that the cross-links are frictionless ball joints around which the filaments can freely rotate. This common simplification in modeling of polymer networks [82, 155] is based on limited experimental evidence about how exactly cross-linkers interact with the actin filaments.

As a consequence, the strain energy of networks with cross-linkers which constrain the rotation of a filament against the neighboring filament and thus the network stiffness would slightly increase. On the other hand, compliant cross-linkers would affect the network stiffness the other way around. Due to a report that the elastic response of networks consisting of rigor-HMM and F-actin is dominated by filaments between cross-linked points [26] we assumed rigid cross-links. The choice of HMM as cross-linking protein is also essential for assuming isotropically cross-linked networks. Furthermore, it ensures that no bundling of filaments occurs over a large range of cross-linker concentrations [26]. Eventually, the isotropy and the absence of filament bundles is in agreement with the micro-sphere model as we used it. The exceptional normal stress response of cross-linked actin networks led us to the use of a non-affine network model with the key equation (2.22). This assumption ensures that we can predict both stress components which can be obtained from the experiments. Incompressibility and the assumption that rheological experiments can be described by simple shear deformation are two common simplifications from the literature [37, 82]. Incompressibility may be introduced due to the high water content of actin networks. The deformation gradient in rotational rheometry between parallel plates is not homogeneous and changes over the radius. Thus, simple shear is only an approximation of the real situation in an experimental sample.

Time dependent behavior stemming from cross-linker kinetics and actin polymerization/depolymerization and (probably) other phenomena resulting in viscoelastic properties was neglected. The present model, however, constitutes a sound framework for extension in this direction. A paper addressing the viscoelastic behavior of cross-linked actin networks was recently submitted [120]. In order to use this work as a basis for modeling a whole cell, several improvements are necessary. Other cytoskeletal proteins, intermediate filaments and microtubules, need to be considered as well as viscous effects. F-actin exists inside a cell also in various other forms, for example, stress fibers, where it builds an anisotropic material. Our model can be transferred to any other biopolymer network with a similar structure. All these ideas may be incorporated step by step into more advanced models in future work.

2.A Appendix

The Cauchy stress tensor (2.27) and its associated elasticity tensor (2.44) can be found in the literature (for example, [112, 167]). However, $\widetilde{\boldsymbol{\sigma}}$ and $\widetilde{\mathbb{c}}$ are usually defined in terms of derivatives with respect to the isochoric part of the left Cauchy-Green tensor $\overline{\mathbf{b}} = \overline{\mathbf{F}}\overline{\mathbf{F}}^{\mathrm{T}}$, and are not presented in the forms (2.28) and (2.39), respectively. In our case, the strain-energy function (2.17) of the micro-sphere network is given in terms of $\overline{\mathbf{C}}$, and we therefore need $\widetilde{\boldsymbol{\sigma}}$ and $\widetilde{\mathbb{c}}$ in the form we have used in (2.28)

and (2.35), respectively. The derivation is straightforward but could not be found elsewhere. Hence, this is now shown here in a compact form.

As a starting point, the well established relations in [112, chap. 6] are used. Due to the fact that soft materials show geometrical nonlinearity, tensors can be expressed in the reference configuration (Lagrangian description) and the current configuration (Euler description). A meaningful stress measure in the reference configuration is the second Piola-Kirchhoff stress tensor $\mathbf{S}$. This and its associated elasticity tensor are defined as

$$\mathbf{S} = 2\frac{\partial \Psi}{\partial \mathbf{C}}, \qquad \mathbb{C} = 2\frac{\partial \mathbf{S}}{\partial \mathbf{C}}. \tag{2.63}$$

They can be transformed to the current configuration by means of a push-forward operation times a factor of J^{-1} to give

$$\boldsymbol{\sigma} = J^{-1}\mathbf{F}\mathbf{S}\mathbf{F}^{\mathrm{T}}, \tag{2.64}$$

$$(\mathbb{c})_{abcd} = J^{-1}F_{aA}F_{bB}F_{cC}F_{dD}(\mathbb{C})_{ABCD}, \tag{2.65}$$

where index notation is used for the elasticity tensor. It is known that an additive decomposition of the strain-energy function Ψ into the volumetric and isochoric parts, i.e. $\Psi = \Psi_{\mathrm{vol}}(J) + \Psi_{\mathrm{iso}}(\overline{\mathbf{C}})$, results in two terms for the stress and elasticity tensors. Thus,

$$\mathbf{S} = \mathbf{S}_{\mathrm{vol}} + \mathbf{S}_{\mathrm{iso}}, \qquad \mathbb{C} = \mathbb{C}_{\mathrm{vol}} + \mathbb{C}_{\mathrm{iso}}. \tag{2.66}$$

The volumetric parts are thoroughly worked out in [112] and after pushing forward they can be written as

$$\boldsymbol{\sigma}_{\mathrm{vol}} = u\mathbf{I}, \qquad \mathbb{c}_{\mathrm{vol}} = (u+s)\mathbf{I}\otimes\mathbf{I} - 2u\mathbb{I}, \tag{2.67}$$

$$\text{with} \quad u = \Psi'_{\mathrm{vol}}(J), \qquad s = J\Psi''_{\mathrm{vol}}(J), \tag{2.68}$$

where $(\bullet)'$ denotes the derivative of the quantity $(\bullet)$ with respect to J. The assumption of incompressibility allows us to use any standard penalty function for Ψ_{vol}.

2.A.1 Isochoric cauchy stress

Concentrating now on the isochoric part of the second Piola-Kirchhoff stress tensor $\mathbf{S}$, [112, sec. 6.4] shows that

$$\mathbf{S}_{\mathrm{iso}} = J^{-2/3}\mathbb{P} : \widetilde{\mathbf{S}}, \qquad \widetilde{\mathbf{S}} = 2\frac{\partial \Psi_{\mathrm{iso}}}{\partial \overline{\mathbf{C}}}. \tag{2.69}$$

The Lagrangian fourth-order projection tensor is defined as

$$\mathbb{P} = \mathbb{I} - \frac{1}{3}\mathbf{C}^{-1}\otimes\mathbf{C}, \tag{2.70}$$

and it furnishes the physically correct deviatoric operator in the Lagrangian description, i.e. $\mathbb{P} : \widetilde{\mathbf{S}} = \mathrm{Dev}\widetilde{\mathbf{S}} = \widetilde{\mathbf{S}} - (1/3)[\widetilde{\mathbf{S}} : \mathbf{C}]\mathbf{C}^{-1}$. By introducing the relation $\boldsymbol{\sigma}_{\mathrm{iso}} = J^{-1}\overline{\mathbf{F}}(\mathbb{P} : \widetilde{\mathbf{S}})\overline{\mathbf{F}}^{\mathrm{T}}$ from $(6.94)_2$ in [112], we obtain

$$\boldsymbol{\sigma}_{\mathrm{iso}} = J^{-1}\overline{\mathbf{F}}\widetilde{\mathbf{S}}\overline{\mathbf{F}}^{\mathrm{T}} - \frac{1}{3}J^{-1}\overline{\mathbf{F}}([\widetilde{\mathbf{S}} : \overline{\mathbf{C}}]\overline{\mathbf{C}}^{-1})\overline{\mathbf{F}}^{\mathrm{T}}. \tag{2.71}$$

Knowing that tensors can change their locations within a double contraction like $\mathbf{A} : \mathbf{BC} = \mathbf{B}^{\mathrm{T}}\mathbf{A} : \mathbf{C}$, where $\mathbf{A}$, $\mathbf{B}$, and $\mathbf{C}$ are arbitrary second-order tensors (which gives $\widetilde{\mathbf{S}} : \overline{\mathbf{C}} = \overline{\mathbf{F}}\widetilde{\mathbf{S}}\overline{\mathbf{F}}^{\mathrm{T}} : \mathbf{I}$), and considering that a double contraction of two second-order tensors gives a scalar, equation (2.71) can be rewritten as

$$\boldsymbol{\sigma}_{\mathrm{iso}} = J^{-1}\overline{\mathbf{F}}\widetilde{\mathbf{S}}\overline{\mathbf{F}}^{\mathrm{T}} - \frac{1}{3}(J^{-1}\overline{\mathbf{F}}\widetilde{\mathbf{S}}\overline{\mathbf{F}}^{\mathrm{T}} : \mathbf{I})\mathbf{I}. \tag{2.72}$$

The definition of the fictitious Cauchy stress tensor $\widetilde{\boldsymbol{\sigma}} = J^{-1}\overline{\mathbf{F}}\widetilde{\mathbf{S}}\overline{\mathbf{F}}^{\mathrm{T}}$ can be introduced, then equation (2.72) has the form of the Eulerian deviator, and hence it can be expressed using a projection tensor in the form which is given in (2.27) and (2.28).

2.A.2 Isochoric elasticity tensor

A similar approach is used to derive the fictitious elasticity tensor $\widetilde{\mathbb{c}}$ in the spatial description. Before proceeding it is necessary to introduce some notation such as

$$\mathbb{P}^{\mathrm{T}} = \mathbb{I} - \frac{1}{3}\mathbf{C} \otimes \mathbf{C}^{-1}, \tag{2.73}$$

$$(\mathbf{C}^{-1} \odot \mathbf{C}^{-1})_{ABCD} = \frac{1}{2}(C^{-1}_{AC}C^{-1}_{BD} + C^{-1}_{AD}C^{-1}_{BC}), \tag{2.74}$$

$$\hat{\mathbb{P}} = \mathbf{C}^{-1} \odot \mathbf{C}^{-1} - \frac{1}{3}\mathbf{C}^{-1} \otimes \mathbf{C}^{-1}, \tag{2.75}$$

where the first equation represents the transpose of the projection tensor $\mathbb{P}$ and $\hat{\mathbb{P}}$ denotes a modified projection tensor. In [112, sec. 6.6] the relation for the isochoric elasticity tensor $\mathbb{C}_{\mathrm{iso}}$ in the material description was derived, i.e.

$$\mathbb{C}_{\mathrm{iso}} = J^{-4/3}\mathbb{P} : \widetilde{\mathbb{C}} : \mathbb{P}^{\mathrm{T}} + \frac{2}{3}\mathrm{Tr}(J^{-2/3}\widetilde{\mathbf{S}})\hat{\mathbb{P}} - \frac{2}{3}(\mathbf{C}^{-1} \otimes \mathbf{S}_{\mathrm{iso}} + \mathbf{S}_{\mathrm{iso}} \otimes \mathbf{C}^{-1}), \tag{2.76}$$

with the fictitious elasticity tensor $\widetilde{\mathbb{C}} = 4\partial^2\Psi_{\mathrm{iso}}/(\partial\overline{\mathbf{C}}\partial\overline{\mathbf{C}})$ in the material description. The relation (2.65) has to be applied to receive the related spatial description of $\widetilde{\mathbb{C}}$. Its linear property allows its usage separately on every term, and following that, one can put together the equation again. The key technique for executing the operations is

applying index notation which, subsequently, is used several times. For convenience, for the three terms in (2.76), we use the shorthand notation

$$\mathbb{C}_{\text{iso}} = \mathbb{X} + \frac{2}{3}\mathbb{Y} - \frac{2}{3}\mathbb{Z}, \tag{2.77}$$

and define $\boldsymbol{\chi}_*(\bullet)$ to denote the push-forward operation.

First Term $\mathbb{X}$. We use the definition of the projection tensor (2.70) in the Lagrangian description, and its transpose (2.73) to expand $\mathbb{X}$ as

$$\mathbb{X} = J^{-4/3}\mathbb{P} : \widetilde{\mathbb{C}} : \mathbb{P}^{\mathrm{T}} = \mathbb{K} - \frac{1}{3}\mathbb{L} + \frac{1}{9}\mathbb{M}. \tag{2.78}$$

For notational simplicity we have introduced the abbreviations

$$\mathbb{K} = J^{-4/3}\widetilde{\mathbb{C}}, \tag{2.79}$$

$$\mathbb{L} = J^{-4/3}[(\mathbf{C}^{-1} \otimes \mathbf{C}) : \widetilde{\mathbb{C}} + \widetilde{\mathbb{C}} : (\mathbf{C} \otimes \mathbf{C}^{-1})], \tag{2.80}$$

$$\mathbb{M} = J^{-4/3}(\mathbf{C}^{-1} \otimes \mathbf{C}) : \widetilde{\mathbb{C}} : (\mathbf{C} \otimes \mathbf{C}^{-1}). \tag{2.81}$$

The push-forward of $\mathbb{K}$ times a factor of J^{-1} furnishes the fictitious elasticity tensor $\widetilde{\mathbb{c}}$ in the spatial description. With the multiplicative decomposition of the deformation gradient (2.16), we obtain (compare with (2.39))

$$\boldsymbol{\chi}_*(\mathbb{K})_{abcd} = J^{-1}\overline{F}_{aA}\overline{F}_{bB}\overline{F}_{cC}\overline{F}_{dD}(\widetilde{\mathbb{C}})_{ABCD} = (\widetilde{\mathbb{c}})_{abcd}, \tag{2.82}$$

where we have used the index notation, which we will also use in the following for the push-forward of $\mathbb{L}$ and $\mathbb{M}$.

We note that $C_{AB} = J^{2/3}\overline{F}_{aA}\delta_{ab}\overline{F}_{bB}$ and $C^{-1}_{AB} = J^{-2/3}\overline{F}^{-1}_{aA}\delta_{ab}\overline{F}^{-1}_{bB}$ so that we can deduce from (2.80) that

$$\begin{aligned}
&\boldsymbol{\chi}_*(\mathbb{L})_{abcd} = \\
&= \boldsymbol{\chi}_*[J^{-4/3}\{(\mathbf{C}^{-1} \otimes \mathbf{C}) : \widetilde{\mathbb{C}} + \widetilde{\mathbb{C}} : (\mathbf{C} \otimes \mathbf{C}^{-1})\}]_{abcd} \\
&= J^{-1}\overline{F}_{aA}\overline{F}_{bB}\overline{F}_{cC}\overline{F}_{dD}\left[(\mathbf{C}^{-1} \otimes \mathbf{C})_{ABMN}(\widetilde{\mathbb{C}})_{MNCD} + (\widetilde{\mathbb{C}})_{ABMN}(\mathbf{C} \otimes \mathbf{C}^{-1})_{MNCD}\right] \\
&= J^{-1}\overline{F}_{aA}\overline{F}_{bB}\overline{F}_{cC}\overline{F}_{dD}\left[C^{-1}_{AB}C_{MN}(\widetilde{\mathbb{C}})_{MNCD} + (\widetilde{\mathbb{C}})_{ABMN}C_{MN}C^{-1}_{CD}\right] \\
&= \delta_{ab}\delta_{mn}[J^{-1}\overline{F}_{mM}\overline{F}_{nN}\overline{F}_{cC}\overline{F}_{dD}(\widetilde{\mathbb{C}})_{MNCD}] + [J^{-1}\overline{F}_{aA}\overline{F}_{bB}\overline{F}_{mM}\overline{F}_{nN}(\widetilde{\mathbb{C}})_{ABMN}]\delta_{mn}\delta_{cd} \\
&= [(\mathbf{I} \otimes \mathbf{I}) : \widetilde{\mathbb{c}} + \widetilde{\mathbb{c}} : (\mathbf{I} \otimes \mathbf{I})]_{abcd},
\end{aligned} \tag{2.83}$$

where basic rules of tensor algebra and (2.82) have been applied. We use now the same technique to derive the push-forward of $\mathbb{M}$ times a factor of J^{-1}. With $(2.82)_2$ we have

$$\begin{aligned}
\boldsymbol{\chi}_*(\mathbb{M})_{abcd} &= \boldsymbol{\chi}_*[J^{-4/3}(\mathbf{C}^{-1}\otimes\mathbf{C}) : \widetilde{\mathbb{C}} : (\mathbf{C}\otimes\mathbf{C}^{-1})]_{abcd} \\
&= \boldsymbol{\chi}_*\left[J^{-4/3}(\mathbf{C}^{-1}\otimes\mathbf{C})_{ABMN}(\widetilde{\mathbb{C}})_{MNOP}(\mathbf{C}\otimes\mathbf{C}^{-1})_{OPCD}\right]_{abcd} \\
&= J^{-4/3}(F_{aA}F_{bB}C^{-1}_{AB})\left(J^{-1}F_{mM}\delta_{mn}F_{nN}(\widetilde{\mathbb{C}})_{MNOP}F_{oO}\delta_{op}F_{pP}\right)(F_{cC}F_{dD}C^{-1}_{CD}) \\
&= \delta_{ab}\delta_{mn}\left[J^{-1}\overline{F}_{mM}\overline{F}_{nN}\overline{F}_{oO}\overline{F}_{pP}(\widetilde{\mathbb{C}})_{MNOP}\right]\delta_{op}\delta_{cd} \\
&= [(\mathbf{I}\otimes\mathbf{I}) : \widetilde{\mathbb{c}} : (\mathbf{I}\otimes\mathbf{I})]_{abcd} \qquad (2.84)
\end{aligned}$$

In conclusion we may bring together $(2.82)_2$, $(2.83)_5$, and $(2.84)_5$ and summarize with (2.78) to achieve

$$\begin{aligned}
\boldsymbol{\chi}_*(\mathbb{X}) &= \boldsymbol{\chi}_*(J^{-4/3}\mathbb{P} : \widetilde{\mathbb{C}} : \mathbb{P}^{\mathrm{T}}) \\
&= \widetilde{\mathbb{c}} - \frac{1}{3}[(\mathbf{I}\otimes\mathbf{I}) : \widetilde{\mathbb{c}} + \widetilde{\mathbb{c}} : (\mathbf{I}\otimes\mathbf{I})] + \frac{1}{9}[(\mathbf{I}\otimes\mathbf{I}) : \widetilde{\mathbb{c}} : (\mathbf{I}\otimes\mathbf{I})] \\
&= \left(\mathbb{I} - \frac{1}{3}\mathbf{I}\otimes\mathbf{I}\right) : \widetilde{\mathbb{c}} : \left(\mathbb{I} - \frac{1}{3}\mathbf{I}\otimes\mathbf{I}\right) = {}_{\mathbb{P}} : \widetilde{\mathbb{C}} : {}_{\mathbb{P}}, \qquad (2.85)
\end{aligned}$$

where the projection tensor (2.26) has been used.

Second Term $\mathbb{Y}$. Considering the second term of (2.76) and pushing it forward, we find with the property (2.75), the fictitious Cauchy stress tensor $(2.33)_1$ and the projection tensor (2.26), that

$$\begin{aligned}
\boldsymbol{\chi}_*(\mathbb{Y}) &= \boldsymbol{\chi}_*[\mathrm{Tr}(J^{-2/3}\widetilde{\mathbf{S}})\hat{\mathbb{P}}] \\
&= \boldsymbol{\chi}_*\left[(J^{-2/3}\widetilde{\mathbf{S}} : \mathbf{C})\left(\mathbf{C}^{-1}\odot\mathbf{C}^{-1} - \frac{1}{3}\mathbf{C}^{-1}\otimes\mathbf{C}^{-1}\right)\right] \\
&= (\overline{\mathbf{F}}\widetilde{\mathbf{S}}\overline{\mathbf{F}}^{\mathrm{T}} : \mathbf{I})\left[\boldsymbol{\chi}_*(\mathbf{C}^{-1}\odot\mathbf{C}^{-1}) - \frac{1}{3}\boldsymbol{\chi}_*(\mathbf{C}^{-1}\otimes\mathbf{C}^{-1})\right] \\
&= (\widetilde{\boldsymbol{\sigma}} : \mathbf{I})\left(\mathbb{I} - \frac{1}{3}\mathbf{I}\otimes\mathbf{I}\right) = \mathrm{tr}(\widetilde{\boldsymbol{\sigma}})_{\mathbb{P}}, \qquad (2.86)
\end{aligned}$$

where we used again the scalar property of the double contraction of two second-order tensors. It is easy to show that $\boldsymbol{\chi}_*(\hat{\mathbb{P}}) = J^{-1}{}_{\mathbb{P}}$ holds.

Third Term $\mathbb{Z}$. A transformation of the last term of (2.76) from the reference to the current configuration is also straightforward. By considering that the push-forward (and multiplication with a factor J^{-1}) of a dyadic product of second-order

tensors is $\boldsymbol{\chi}_*(\mathbf{A} \otimes \mathbf{B}) = J^{-1}\mathbf{F}\mathbf{A}\mathbf{F}^{\mathrm{T}} \otimes \mathbf{F}\mathbf{B}\mathbf{F}^{\mathrm{T}}$, we obtain

$$\boldsymbol{\chi}_*(\mathbb{Z}) = \boldsymbol{\chi}_*(\mathbf{C}^{-1} \otimes \mathbf{S}_{\mathrm{iso}} + \mathbf{S}_{\mathrm{iso}} \otimes \mathbf{C}^{-1}) = \mathbf{I} \otimes \boldsymbol{\sigma}_{\mathrm{iso}} + \boldsymbol{\sigma}_{\mathrm{iso}} \otimes \mathbf{I}, \tag{2.87}$$

where the relation $\boldsymbol{\sigma}_{\mathrm{iso}} = J^{-1}\mathbf{F}\mathbf{S}_{\mathrm{iso}}\mathbf{F}^{\mathrm{T}}$ has been used. According to (2.77) we can now put together the parts $(2.84)_4$, $(2.86)_5$ and $(2.87)_2$ so that we obtain equation (2.44).

Acknowledgements

We are grateful to Anita Haider for her help with the visualization of the structural tensor. We thank M. Rusp for the actin preparation. This work was partly supported by Deutsche Forschungsgemeinschaft (DFG) through Grant No. BA2029/8 and the Cluster of Excellence Nanosystems Initiative Munich. KMS thanks Jan Skotheim for support and acknowledges support from CompInt in the framework of the ENB Bayern and the IGSSE.

3 VISCOELASTICITY OF CROSS-LINKED ACTIN NETWORKS: EXPERIMENTAL TESTS, MECHANICAL MODELING AND FINITE ELEMENT ANALYSIS

Abstract Filamentous actin is one of the main constituents of the eukaryotic cytoskeleton. The actin cortex, a densely cross-linked network, resides underneath the lipid bilayer. In the present work we propose a continuum mechanical formulation for describing the viscoelastic properties of *in vitro* actin networks, which serve as model systems for the cortex, by including the microstructure, i.e. the behavior of a single filament and its spatial arrangement. The modeling of the viscoelastic response in terms of physically interpretable parameters is conducted using a multiscale approach consisting of two steps: modeling of the single filament response of F-actin by a worm-like chain model including the extensibility of the filament, and assembling the 3D biopolymer network by using the micro-sphere model which accounts for filaments equally distributed in space. The viscoelastic effects of the network are taken into account using a generalized Maxwell model. The Cauchy stress and elasticity tensors are obtained within a continuum mechanics framework and implemented into a finite element program. The model is validated on the network level using large strain experiments on reconstituted actin gels. Comparisons of the proposed model to rheological experiments recover reasonable values for the material parameters. Finite element simulations of the indentation of a sphere on a network slab and the aspiration of a droplet in a micro-pipette allow for further insights of the viscoelastic behavior of actin networks.

3.1 Introduction

The cytoskeleton is composed of various biopolymers and gives mechanical stability to cells. Mechanical cell properties may significantly deviate from the average physiological characteristics and, therefore, can be related to diseases such as malaria, asthma, arthritis, atherosclerosis, glaucoma or cancer [3–9]. Knowledge about the mechanical properties of cells may improve the insight and diagnosis of pathologies [10]. The most abundant protein of the cytoskeleton is the biopolymer actin, located in various structures within the cell. One of them is a cross-linked network arranged mainly underneath the lipid bilayer called actin cortex. A large number of different

actin binding proteins exist in a cell which are capable of cross-linking F-actin to networks. The type of cross-linker affects the network architecture and its mechanical properties [139].

In vitro reconstituted cross-linked actin gels serve as model systems for the cellular actin network. Bulk rheology is a powerful method to characterize the mechanical properties of such gels. Two more recent reviews document the capabilities of the method [139, 143]. Several studies experimentally investigated the viscoelasticity of actin networks with various cross-linkers [21, 32, 118, 140, 168, 169], and some propose simplified models [26, 32, 169]. Comparisons of experimental data with finite element simulations of unit cells filled with randomly oriented filaments [102, 138, 170] give valuable insights in the mechanisms that govern actin networks. The studies mentioned above analyze the storage and loss moduli obtained from oscillatory experiments in the linear regime. Cells, however, undergo deformations which involve large strains where the mechanical behavior of the cytoskeleton is highly nonlinear. Therefore, experimental procedures are needed that allow characterization of such effects and modeling efforts for biopolymer networks should include them. A mechanical model should also be transferable to other problems to analyze the outcome of more complex experiments, e.g., atomic force microscopy (AFM) on living cells. Large amplitude oscillation shear (LAOS) [171] can be used to characterize the highly nonlinear mechanical response of actin gels. Semmrich et al. [172] used this technique to investigate entangled actin filaments and Xu et al. [173] conducted LAOS experiments on actin/α-actinin networks.

Discrete models such as [88, 97, 102, 146] are based on the idea to distribute and then cross-link the filaments in representative volume elements to investigate the elastic and viscoelastic properties of actin networks. Considering the computational cost these models are not (yet) suitable to consider larger problems such as the computational analysis of a micro-pipette aspiration test. Therefore, continuum models are useful to facilitate finite element analyses of more complex boundary-value problems because such models 'smear out' the microstructure. To our knowledge, the model of Morse [174] seems to be the only viscoelastic continuum model for (entangled) biopolymers. Elastic models which are motivated by the microstructure and are designed to capture the quasi-static mechanical response were developed recently [48, 82]. These models are assemblies of the worm-like chain model [76] and network models to obtain three-dimensional continuum mechanical formulations. A variety of approaches are suggested in the literature to solve the governing equations of the worm-like chain model and to consider extensibility of chains, see, e.g., [29, 56, 73, 85, 151, 152]. The network models available in the literature, e.g., [37, 107, 111, 114, 119, 147, 175, 176] differ notably in complexity. The non-affine models [119, 147] proved to capture the exceptional normal stress response of semiflexible biopolymer networks [39].

In the present paper we propose a microstructurally motivated, nonlinear viscoelastic continuum mechanical model which is able to describe a variety of effects, as observed with different types of experiments. A detailed derivation of the elastic contribution of the model, reviewed in this paper, is given in [48]. We used the worm-like chain model introduced by Holzapfel and Ogden [74] to describe single actin filaments. Based on the equilibrium equations in [74] a force-extension relationship is derived by considering extensibility of the fibers, a property of F-actin observed by experiments [36]. We chose the non-affine micro-sphere model by Miehe et al. [119] because it captures the exceptional normal stress response observed in rheological experiments, and it is straightforward to implement into finite element programs. We used a simple (phenomenological) generalized Maxwell model as an extension of the nonlinear network model [112, Chap. 6.10], although there exists an extension for the non-affine micro-sphere model [177] that uses phenomenological parameters similar to our approach. However, it introduces three parameters per prototype chain (analogous to Maxwell elements) instead of two, as we do.

We used *in vitro* reconstituted cross-linked actin gels, characterized with bulk rheology, as a model system for the cellular actin network. Heavy meromyosin (HMM), a truncated version of myosin II, in its rigor form binds actin filaments into three-dimensional networks without creating bundles at any concentration [26]. We chose HMM in its rigor form to obtain a cross-linked actin network without bundled filaments. We accomplished to describe the storage and loss moduli as determined with oscillatory experiments but also analyze the nonlinear behavior using LAOS. We showed that the model presented in the paper can fit the results of the conducted experiments very well and found values for all physically interpretable parameters which can be well compared to the literature. Toward the end we present a computational study of relaxation and creep experiments to make sure that the finite element implementation is correct. Then we present a finite element simulation of the indentation of a slab, consisting of an actin network, with a spherical tip. The setup is similar to experiments which are conducted using AFM, e.g., [178]. The last example shows the aspiration of an actin network droplet into a micropipette. The results are very similar to those observed in experiments on living cells [52, 179].

3.2 Materials and methods

The first part of this section introduces the experimental protocol we used to reconstitute and characterize *in vitro* actin networks. Subsequently we model the viscoelastic behavior of cross-linked actin networks by first considering a single filament. The resulting relationship between tensile force and end-to-end distance is then used in a viscoelastic continuum framework.

3.2.1 Experimental setup

Actin was purified from rabbit skeletal muscle using the protocol described in [156], where an additional gel filtration step was performed [157]. G-actin was lyophilized and stored at -21°C. It was dissolved in deionized water and dialyzed against G-buffer (2 mM Tris-HCl, 0.2 mM ATP, 0.2 mM $CaCl_2$, 0.2 mM DTT, 0.005 % NaN_3, pH 8.0) at 4°C for sample preparation. The solution was kept at 4°C and used within 10 days. Chymotrypsin digestion of myosin II, as in [158], was used to prepare the cross-linker HMM.

Polymerization of G-actin to F-actin was started after adding HMM through an ATP-free 10× F-buffer (20 mM Tris-HCl, 20 mM $MgCl_2$, 1 M KCl, 2 mM DTT, 2 mM $CaCl_2$, pH 7.5). The solutions were gently mixed and loaded into the rheometer within one minute. Polymerization, cross-linking, and the transition of HMM to its rigor state were monitored by following the storage modulus at 0.5 Hz. The samples contained $c_{\mathrm{A}} = 9.5\,\mu$M actin with a cross-linker ratio of $R = 1/10$, where c_{A} denotes the actin concentration and R is defined as $c_{\mathrm{HMM}}/c_{\mathrm{A}}$ with the HMM-concentration c_{HMM}.

Three rheological experiments were conducted: LAOS, amplitude sweep and frequency sweep. All experiments were conducted at 21°C. LAOS measurements were performed with a stress-controlled AR-G2, TA Instruments, New Castle, USA and were used to elaborate the relation between elastic and viscous effects. Experiments were performed with a 40 mm parallel plate geometry, a 300 μm measuring gap and an oscillation frequency f_{osc} of 0.05 Hz. The raw values of angular displacement φ and resulting motor torque M were collected and converted into shear strain γ and applied shear stress σ_{M} by means of the geometrical constants C_γ and C_σ, i.e. $\gamma = C_\gamma \varphi$ and $\sigma_{\mathrm{M}} = C_\sigma M$. The smoothing spline of `MATLAB` [180] was used to remove noise from the stress signal which was then corrected for the instruments inertia I to obtain the shear stress σ_{xy} acting on the sample, i.e. $\sigma_{xy} = \sigma_{\mathrm{M}} - m\ddot{\gamma}$, with $m = IC_\sigma/C_\gamma$ [172]. The raw values of the experiments could then be plotted in a diagram showing the shear stress σ_{xy} versus the shear strain γ.

In addition to the raw values, we calculated the storage modulus G' and the loss modulus G'', which, for linear viscoelastic materials, are defined as [181]

$$G' = \frac{\sigma_{xy,\mathrm{A}}}{\gamma_{\mathrm{A}}} \cos\delta, \qquad G'' = \frac{\sigma_{xy,\mathrm{A}}}{\gamma_{\mathrm{A}}} \sin\delta, \tag{3.1}$$

where $\sigma_{xy,\mathrm{A}}$ and γ_{A} are the amplitudes of the shear stress σ_{xy} and the shear strain γ, respectively. The phase shift angle between input and response signal is denoted by δ and is often referred to as the loss angle. Because these moduli are convenient quantities to show the behavior of the reconstituted network and the model over a large range of deformation amplitudes, we used them also in the nonlinear regime.

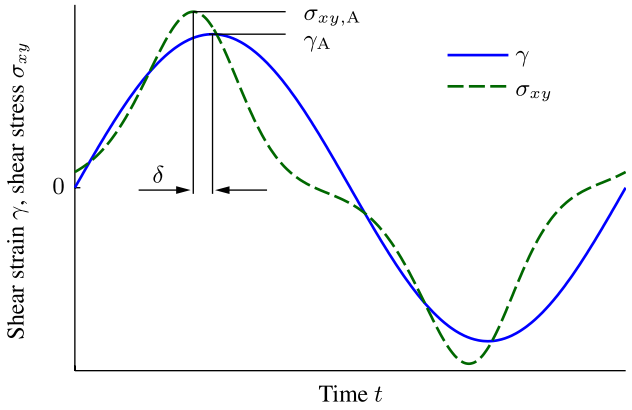

Figure 3.1: Phase shift δ in the γ-t and σ_{xy}-t diagrams for the calculation of the moduli G' and G'' in the nonlinear viscoelastic regime with the shear strain amplitude γ_{A} and the shear stress amplitude $\sigma_{xy,\mathrm{A}}$. The system is in steady state.

For this purpose we need to define a generalized phase shift δ, as illustrated in Fig. 3.1, by keeping in mind that the physical interpretation of the values changes.

An amplitude sweep, i.e. an oscillation experiment in which the amplitude is gradually increased, was recorded over a strain range of $\gamma_{\mathrm{A}} = 1\%$ to 50%. By constantly increasing the oscillation frequency, we also performed a frequency sweep ($f_{\mathrm{osc}} = 0.01\,\mathrm{Hz}$ to $10\,\mathrm{Hz}$ with $\gamma_{\mathrm{A}} = 0.5\%$) for an identical sample on a stress-controlled rheometer (Physica MCR301, Anton Paar, Graz, Austria). The geometry consisted of a 50 mm parallel plate device with 160 μm plate separation.

3.2.2 Single filament

Here we briefly describe the mechanical behavior of a single filament by means of an extensible worm-like chain model. The goal is to relate the end-to-end distance r of the filament to the tensile force f which acts on the ends with pinned boundary conditions. The equations used here are introduced by Unterberger et al. [48] and extensively discussed by Holzapfel and Ogden [74]. The contour length L, the end-to-end distance r_0 at zero force and the persistence length L_{p} are characteristics of a filament. The latter correlates with the bending stiffness B_0, i.e.

$$B_0 = k_{\mathrm{B}} T L_{\mathrm{p}}, \tag{3.2}$$

where T is the temperature and k_{B} is the Boltzmann constant.

We define a shorthand notation for the dimensionless force $f^\star$ and a parameter α related to the filament's extensibility, i.e.

$$f^\star = \frac{f L^2}{\pi^2 B_0}, \quad \alpha = \frac{\pi^2 B_0}{\mu_0 L^2} \tag{3.3}$$

to simplify the relation between r and f. The extensibility is described by the stretch modulus μ_0. Thus, we use the model derived in [73] and modified in [48],

$$\frac{r}{L} = 1 + \alpha f^\star - \frac{(1+2\alpha f^\star)(1+\alpha f^\star)^\beta}{(1+f^\star+\alpha f^{\star 2})^\beta}(1 - r_0/L), \tag{3.4}$$

where the initial stiffness of the filament is adjusted by the effective extensional number β. The extensibility of the model was derived in a consistent manner, starting with kinematics [73], unlike the rather *ad hoc* enhancements of inextensible models, as suggested in, e.g., [37, 104, 151]. Holzapfel and Ogden [74] have recently shown that in the inextensible limit ($\mu_0 \to \infty$) relation (3.4) is a generalized form of the models introduced in [56, 85]. The integration of this filament model requires the knowledge of the initial end-to-end distance $\widetilde{r}$ inside a network, i.e. r before the material is deformed. In a prestretched network $\widetilde{r}$ is larger than r_0 and we define a related prestretch as $\lambda_0 = \widetilde{r}/r_0$. The current end-to-end distance r changes with the deformation of the material, and it is described through the stretch $\lambda = r/\widetilde{r}$. Consequently, r is related to r_0 according to

$$r = \lambda\lambda_0 r_0. \tag{3.5}$$

Integration of the single filament model (3.4) into the network requires the first derivative of the filament's free energy ψ_f with respect to the stretch λ. With $\partial\psi_\mathrm{f}/\partial r = f$ and (3.5) we obtain

$$\psi_\mathrm{f}' = \frac{\partial\psi_\mathrm{f}}{\partial\lambda} = \lambda_0 r_0 f, \tag{3.6}$$

where the prime denotes the derivative with respect to λ. Calculation of the consistent tangent matrix within a finite element formulation requires the second derivative $\psi_\mathrm{f}'' = \partial^2\psi_\mathrm{f}/\partial\lambda\partial\lambda$. Thus,

$$\psi_\mathrm{f}'' = \frac{\lambda_0^2 r_0^2 \mu_0/L}{1 + Y\left(\frac{1+\alpha f^\star}{1+f^\star+\alpha f^{\star 2}}\right)^\beta (1 - r_0/L)}, \tag{3.7}$$

where the abbreviation

$$Y = \frac{\beta}{\alpha}\frac{(1+2\alpha f^\star)^2}{1+f^\star+\alpha f^{\star 2}} - \beta\frac{1+2\alpha f^\star}{1+\alpha f^\star} - 2 \tag{3.8}$$

has been introduced.

3.2.3 Continuum mechanical model

The link between the one-dimensional pulling of a single filament and the deformation of a three-dimensional network of assembled single filaments is established by

using the elastic network theory. We homogenize the stretch of randomly oriented filaments over a unit sphere in a non-affine way [119] and the energy stored in the continuum is assumed to be the sum of the energies stored in the individual filaments. Viscoelasticity is then introduced through additional non-equilibrium stress tensors which may be interpreted as contributions from Maxwell elements.

Kinematics and Helmholtz free-energy function

We use the deformation gradient $\mathbf{F}$ to describe the deformation of the continuum to the current configuration. The Jacobian determinant $J = \det \mathbf{F} > 0$ is a measure for the volume change; for incompressible materials $J = 1$ hold. Because of the high water content of the medium in which actin gels reside we assume volume-preserving deformations. In order to obtain a model formulation suitable for an implementation in a finite element program we use a multiplicative split of $\mathbf{F}$ into a volumetric part $J^{1/3}\mathbf{I}$ and an isochoric part $\overline{\mathbf{F}} = J^{-1/3}\mathbf{F}$, where $\det \overline{\mathbf{F}} = 1$. This results in an additive decomposition of the Helmholtz free-energy density Ψ which we introduce per unit reference volume.

Subsequently, we use the right Cauchy-Green tensor $\mathbf{C} = \mathbf{F}^{\mathrm{T}}\mathbf{F}$ and define its isochoric part as $\overline{\mathbf{C}} = \overline{\mathbf{F}}^{\mathrm{T}}\overline{\mathbf{F}}$. By means of a generalized Maxwell model according to, e.g., Holzapfel [112, Chap. 6.10] we represent the viscous contribution. It adds $\nu = 1, \ldots, m$ parallel elements to the elastic part of the material. The dissipative effects are described by the internal variables $\mathbf{\Gamma}_\nu$ which are akin to $\mathbf{C}$. Their isochoric parts $\overline{\mathbf{\Gamma}}_\nu$ are akin to $\overline{\mathbf{C}}$. We introduce the configurational free energies $\Upsilon_{\mathrm{iso}\,\nu}$ to characterize the non-equilibrium state of the viscoelastic solid, which may be seen as a dissipative potential. The decoupled representation of the Helmholtz free-energy density Ψ is then [112, Chap. 6.10]

$$\Psi(\mathbf{C}, \mathbf{\Gamma}_1, \ldots, \mathbf{\Gamma}_m) = \Psi^{\infty}_{\mathrm{vol}}(J) + \Psi^{\infty}_{\mathrm{iso}}(\overline{\mathbf{C}}) + \sum_{\nu=1}^{m} \Upsilon_{\mathrm{iso}\,\nu}(\overline{\mathbf{C}}, \overline{\mathbf{\Gamma}}_\nu), \tag{3.9}$$

where $(\bullet)^{\infty}$ refers to the equilibrium, i.e. the elastic response. Incompressibility is enforced for the elastic part of (3.9) by a penalty function. Specific forms for $\Psi^{\infty}_{\mathrm{vol}}$ can be found in, e.g., [112, Chap. 6.5]. The elastic isochoric response $\Psi^{\infty}_{\mathrm{iso}}$ is governed by the sum of the single filament energies, more precisely the filament density n times the averaged filament energy, i.e.

$$\Psi^{\infty}_{\mathrm{iso}} = n\psi_{\mathrm{f}}(\lambda). \tag{3.10}$$

Subsequently, we consider isotropically distributed filaments in the three-dimensional space. The orientation of a filament in the reference configuration can be described

by the radius vector $\mathbf{R}$, which is transformed to the current configuration according to

$$\mathbf{t} = \overline{\mathbf{F}}\mathbf{R}, \tag{3.11}$$

where $\mathbf{t}$ is the deformed radius vector. The stretch $\overline{\lambda}$ of a filament, which was originally oriented in the $\mathbf{R}$-direction, is

$$\overline{\lambda} = \|\mathbf{t}\|, \tag{3.12}$$

where $\|\bullet\|$ denotes the Euclidian norm of $(\bullet)$. A set of randomly oriented filaments can be represented by a microscopic unit sphere. We define the p-root averaging operator of a field $v(\mathbf{R})$ as

$$\langle v(\mathbf{R})\rangle_p = \left[\frac{1}{|\mathscr{S}|}\int_{\mathscr{S}} v(\mathbf{R})^p \mathrm{d}A\right]^{1/p} \sim \left[\sum_{i=1}^{21} v^i(\mathbf{R}^i)^p w^i\right]^{1/p}, \tag{3.13}$$

where the integral may be approximated by the numerical integration scheme of Bažant and Oh [122]. These authors define 21 discrete points $\mathbf{R}^i$ together with associated integration weights w^i [122, Table 1]. We homogenize $\overline{\lambda}$, i.e. [119]

$$\lambda = \langle\overline{\lambda}\rangle_p = \left(\frac{1}{|\mathscr{S}|}\int_{\mathscr{S}} \overline{\lambda}^p \,\mathrm{d}A\right)^{1/p}, \tag{3.14}$$

where $\mathrm{d}A$ is an infinitesimal area element of the surface $\mathscr{S}$ and p allows non-affine fluctuations of $\overline{\lambda}$ around the affine value. A parameter study and related discussion of p is provided in [48]. The purpose of the averaging parameter is to capture the correct exceptional normal stress response [39] of the model in a shear experiment while simultaneously fitting the shear stress data.

Elastic parts of the stress and elasticity tensors

The second Piola-Kirchhoff stress tensor $\mathbf{S} = 2\partial\Psi/\partial\mathbf{C}$ may be derived from the decoupled representation of Ψ, as provided in (3.9). Thus [112],

$$\mathbf{S} = \mathbf{S}^\infty_{\mathrm{vol}} + \mathbf{S}^\infty_{\mathrm{iso}} + \sum_{\nu=1}^{m} \mathbf{Q}_\nu, \tag{3.15}$$

where $\mathbf{S}^\infty_{\mathrm{vol}}$, $\mathbf{S}^\infty_{\mathrm{iso}}$ and $\mathbf{Q}_\nu$ denote the volumetric, the isochoric-elastic and the isochoric-non-equilibrium parts, respectively. The volumetric part is given as

$$\mathbf{S}^\infty_{\mathrm{vol}} = J\overline{p}\mathbf{C}^{-1}, \qquad \overline{p} = \mathrm{d}\Psi^\infty_{\mathrm{vol}}/\mathrm{d}J, \tag{3.16}$$

see, e.g., [112, Chap. 6.4]. We define now the fourth-order projection tensor [112]

$$\mathbb{P} = \mathbb{I} - \frac{1}{3}\mathbf{C}^{-1} \otimes \mathbf{C}, \tag{3.17}$$

with the symmetric part of the fourth-order unity tensor $\mathbb{I}$. It is used together with the fictitious second Piola-Kirchhoff stress tensor $\widetilde{\mathbf{S}}$, as derived in [48], i.e.

$$\widetilde{\mathbf{S}} = 2\partial\Psi^{\infty}_{\mathrm{iso}}/\partial\overline{\mathbf{C}} = n\psi'_{\mathrm{f}}\lambda^{1-p}\mathbf{H}, \tag{3.18}$$

to obtain $\mathbf{S}^{\infty}_{\mathrm{iso}} = J^{-2/3}\mathbb{P} : \widetilde{\mathbf{S}}$. The structural tensor $\mathbf{H}$ in (3.18) is specified as

$$\mathbf{H} = \langle\overline{\lambda}^{p-2}\mathbf{R} \otimes \mathbf{R}\rangle, \tag{3.19}$$

(here we have used the shorthand notation $\langle v\rangle = \langle v\rangle_1$), and thus

$$\mathbf{S}^{\infty}_{\mathrm{iso}} = J^{-2/3}n\psi'_{\mathrm{f}}\lambda^{1-p}\mathbb{P} : \mathbf{H}. \tag{3.20}$$

The non-equilibrium parts $\mathbf{Q}_\nu$ of (3.15) will be introduced in the subsequent section.

The elasticity tensor in the Lagrangian description decouples by analogy with (3.9) and (3.15), i.e.

$$\mathbb{C} = \mathbb{C}^{\infty}_{\mathrm{vol}} + \mathbb{C}^{\infty}_{\mathrm{iso}} + \mathbb{C}_{\mathrm{vis}}, \tag{3.21}$$

where $\mathbb{C}^{\infty}_{\mathrm{vol}}$, $\mathbb{C}^{\infty}_{\mathrm{iso}}$ and $\mathbb{C}_{\mathrm{vis}}$ denote the volumetric, isochoric and viscous terms, respectively. Recalling definition $(3.16)_2$, the volumetric part is $\mathbb{C}^{\infty}_{\mathrm{vol}} = J\widetilde{p}\mathbf{C}^{-1} \otimes \mathbf{C}^{-1} - 2J\overline{p}\mathbf{C}^{-1} \odot \mathbf{C}^{-1}$ with $\widetilde{p} = \overline{p} + J\mathrm{d}\overline{p}/\mathrm{d}J$ and $(\mathbf{C}^{-1} \odot \mathbf{C}^{-1})_{ABCD} = (C^{-1}_{AC}C^{-1}_{BD} + C^{-1}_{AD}C^{-1}_{BC})/2$. In the numerical examples, as presented below, we chose $\Psi^{\infty}_{\mathrm{vol}} = \kappa(J^2 - 1 - 2\log J)/4$ as a penalty function which results in $\overline{p} = \kappa(J - J^{-1})/2$ and $\widetilde{p} = \kappa J$, where κ is a user-specified penalty parameter.

Defining the transpose of the projection tensor, i.e. $\mathbb{P}^{\mathrm{T}} = \mathbb{I} - (\mathbf{C} \otimes \mathbf{C}^{-1})/3$, and the modified projection tensor $\widehat{\mathbb{P}} = \mathbf{C}^{-1} \odot \mathbf{C}^{-1} - (\mathbf{C}^{-1} \otimes \mathbf{C}^{-1})/3$, the isochoric elastic part of the elasticity tensor is [112]

$$\mathbb{C}^{\infty}_{\mathrm{iso}} = J^{-4/3}\mathbb{P} : \widetilde{\mathbb{C}} : \mathbb{P}^{\mathrm{T}} + \frac{2}{3}\mathrm{Tr}(J^{-2/3}\widetilde{\mathbf{S}})\widehat{\mathbb{P}} - \frac{2}{3}(\mathbf{C}^{-1} \otimes \mathbf{S}^{\infty}_{\mathrm{iso}} + \mathbf{S}^{\infty}_{\mathrm{iso}} \otimes \mathbf{C}^{-1}), \tag{3.22}$$

where the fictitious elasticity tensor is $\widetilde{\mathbb{C}} = \partial\widetilde{\mathbf{S}}/\partial\overline{\mathbf{C}}$, and the trace is $\mathrm{Tr}(\bullet) = (\bullet) : \mathbf{C}$. We introduce the notation [48]

$$\mathbb{H} = (p-2)\langle\overline{\lambda}^{p-4}\mathbf{R} \otimes \mathbf{R} \otimes \mathbf{R} \otimes \mathbf{R}\rangle \tag{3.23}$$

and obtain the fourth-order fictitious elasticity tensor $\widetilde{\mathbb{C}}$ as [48]

$$\widetilde{\mathbb{C}} = \left[n\psi''_{\mathrm{f}}\lambda^{2(1-p)} - (p-1)n\psi'_{\mathrm{f}}\lambda^{1-2p}\right]\mathbf{H} \otimes \mathbf{H} + n\psi'_{\mathrm{f}}\lambda^{1-p}\mathbb{H}. \tag{3.24}$$

Note that (3.20) and (3.24) incorporate the properties of the single filament through ψ'_{f}, i.e. eq. (3.6), and ψ''_{f}, i.e. eqs. (3.7) and (3.8).

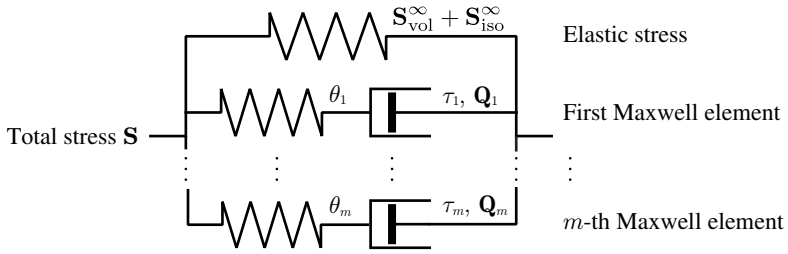

Figure 3.2: Schematic model of a viscoelastic material. The total stress $\mathbf{S}$ decomposes according to (3.15). The spring in the first row represents the elastic stress, while the m Maxwell elements in the remaining rows stand for the non-equilibrium stresses $\mathbf{Q}_\nu$, $\nu = 1, \dots, m$. The mechanical properties of the springs and dashpots of the Maxwell elements are defined by the free-energy parameters θ_ν and the relaxation times τ_ν, respectively.

Viscous parts of the stress and elasticity tensors and algorithmic solution of the evolution equations

The isochoric non-equilibrium stress tensors $\mathbf{Q}_\nu$ in (3.15) are defined through the dissipative potentials $\Upsilon_{\mathrm{iso}\,\nu}$ as [112]

$$\mathbf{Q}_\nu = J^{-2/3}\mathbb{P} : \widetilde{\mathbf{Q}}_\nu, \qquad \widetilde{\mathbf{Q}}_\nu = 2\frac{\partial \Upsilon_{\mathrm{iso}\,\nu}(\overline{\mathbf{C}}, \overline{\mathbf{\Gamma}}_\nu)}{\partial \overline{\mathbf{C}}}. \tag{3.25}$$

We introduce now a set of differential equations and initial conditions as evolution equations for $\mathbf{Q}_\nu$ to describe the transient behavior of the material, see, e.g., [112, 182]. Thus,

$$\dot{\mathbf{Q}}_\nu + \frac{\mathbf{Q}_\nu}{\tau_\nu} = \theta_\nu \dot{\mathbf{S}}^{\infty}_{\mathrm{iso}}, \qquad \mathbf{Q}_\nu^{0^+} = (J^{-2/3}\mathbb{P} : \widetilde{\mathbf{Q}}_\nu)|_{t=0^+}, \tag{3.26}$$

where the non-dimensional free-energy parameters θ_ν are related to the relaxation times τ_ν. Figure 3.2 provides a possible interpretation for these parameters and displays a schematic representation of the decomposition (3.15). The elastic parts $\mathbf{S}^{\infty}_{\mathrm{vol}} + \mathbf{S}^{\infty}_{\mathrm{iso}}$ are condensed as nonlinear spring in the first row. The non-equilibrium stresses $\mathbf{Q}_\nu$ may be identified by the Maxwell elements in the remaining rows. The free-energy parameters θ_ν and relaxation times τ_ν may be identified as properties of the springs and dashpots, respectively.

Equations (3.26) are valid for the time interval $t \in [0^+, \bar{t}\,]$, where the instantaneous response at $t = 0^+$ is characterized by $\mathbf{Q}_\nu^{0^+}$. However, we assume a stress-free reference configuration so that $\mathbf{Q}_\nu|_{t=0^+} = \mathbf{O}$. Convolution integrals provide a closed form solution for $(3.26)_1$, i.e.

$$\mathbf{Q}_\nu = \exp(-t_n/\tau_\nu)\mathbf{Q}_\nu^{0^+} + \int_{t=0^+}^{t=\bar{t}} \exp[-(t_n - t)/\tau_\nu]\theta_\nu \dot{\mathbf{S}}^{\infty}_{\mathrm{iso}}(t)\,\mathrm{d}t. \tag{3.27}$$

Consider now the time discretization with M intervals $0^+ = t_0 < \cdots < t_{M+1} = \bar{t}$ with a typical closed time sub-interval $[t_n, t_{n+1}]$ and a time increment $\Delta t = t_{n+1} - t_n$. Assume that the second Piola-Kirchhoff stress tensor $\mathbf{S}_n$ at time t_n and its decomposition according to (3.15) is known. We want now to advance the solution to time t_{n+1} in order to solve the integral in (3.27), i.e.

$$\mathbf{S}_{n+1} = \left(\mathbf{S}^{\infty}_{\mathrm{vol}} + \mathbf{S}^{\infty}_{\mathrm{iso}} + \sum_{\nu=1}^{m} \mathbf{Q}_{\nu} \right)_{n+1} . \tag{3.28}$$

The equilibrium stress tensors $\mathbf{S}^{\infty}_{\mathrm{vol}}$ and $\mathbf{S}^{\infty}_{\mathrm{iso}}$ are derived from finite elasticity, $(3.16)_1$ and (3.20), independently from the viscous contribution. We can split the convolution integral according to $\int_{0^+}^{t_{n+1}} (\bullet)\, \mathrm{d}t = \int_{0^+}^{t_n} (\bullet)\, \mathrm{d}t + \int_{t_n}^{t_{n+1}} (\bullet)\, \mathrm{d}t$. The first term is known from $\mathbf{S}_n$ while the second term can be solved by means of the midpoint rule, i.e. $t \sim (t_{n+1} + t_n)/2$. This results in a recurrence update formula for the non-equilibrium stress tensor, i.e. [112]

$$\mathbf{Q}_{\nu\, n+1} = \mathcal{H}_{\nu\, n} + \theta_{\nu} \exp\left(-\frac{\Delta t}{2\tau_{\nu}} \right) (\mathbf{S}^{\infty}_{\mathrm{iso}})_{n+1}, \tag{3.29}$$

where the history term is introduced as

$$\mathcal{H}_{\nu\, n} = \exp\left(-\frac{\Delta t}{2\tau_{\nu}} \right) \left[\exp\left(-\frac{\Delta t}{2\tau_{\nu}} \right) \mathbf{Q}_{\nu\, n} - \theta_{\nu} (\mathbf{S}^{\infty}_{\mathrm{iso}})_n \right]. \tag{3.30}$$

The viscous part $(\mathbb{C}_{\mathrm{vis}})_{n+1}$ of the elasticity tensor at time t_{n+1} is [112]

$$(\mathbb{C}_{\mathrm{vis}})_{n+1} = (\mathbb{C}^{\infty}_{\mathrm{iso}})_{n+1} \sum_{\nu=1}^{m} \theta_{\nu} \exp\left(-\frac{\Delta t}{2\tau\nu} \right) \tag{3.31}$$

so that

$$\mathbb{C}_{n+1} = \left[\mathbb{C}^{\infty}_{\mathrm{vol}} + \left\{ 1 + \sum_{\nu=1}^{m} \theta_{\nu} \exp\left(-\frac{\Delta t}{2\tau_{\nu}} \right) \right\} \mathbb{C}^{\infty}_{\mathrm{iso}} \right]_{n+1} \tag{3.32}$$

defines the elasticity tensor in the Lagrangian description at time t_{n+1}.

Stress and elasticity tensors in the Eulerian description

For the actual analysis of problems we are interested in the true stresses, i.e. the Cauchy stress tensor $\boldsymbol{\sigma}$ and its associated elasticity tensor $\mathbb{c}$. At t_{n+1} we use the Piola transformation to obtain the Cauchy stress tensor

$$\boldsymbol{\sigma}_{n+1} = (J^{-1} \mathbf{F} \mathbf{S} \mathbf{F}^{\mathrm{T}})_{n+1}, \tag{3.33}$$

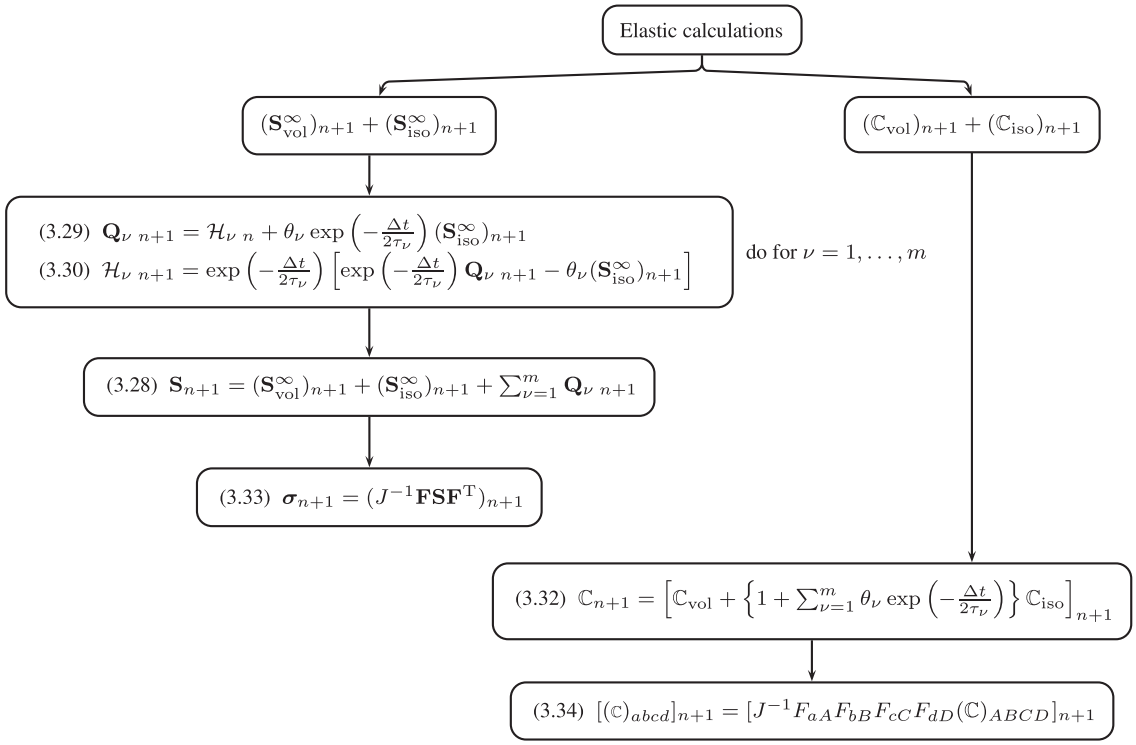

Figure 3.3: Flowchart for the algorithmic steps required to compute the viscous parts of the Cauchy stress and elasticity tensors. The necessary equations are accompanied with reference to the text.

and its associated elasticity tensor $\mathbb{c}_{n+1}$ in the spatial description, i.e.

$$[(\mathbb{c})_{abcd}]_{n+1} = [J^{-1}F_{aA}F_{bB}F_{cC}F_{dD}(\mathbb{C})_{ABCD}]_{n+1}. \tag{3.34}$$

In summary, the inputs of the model are the deformation gradient and the material parameters. First we need to calculate the elastic parts of the Cauchy stress and elasticity tensors according to the Section 3.2.3. Subsequently, the necessary algorithmic steps for the computation of the viscous parts of $\boldsymbol{\sigma}_{n+1}$ and $\mathbb{c}_{n+1}$ are condensed, see Fig. 3.3.

3.3 Results and discussion

The mechanical models introduced in Sections 3.2.2 and 3.2.3 are able to capture important viscoelastic features of actin networks in addition to their elastic properties, as demonstrated in [48]. We present here fits of the network model to experimental data. The goal of the fitting is to obtain consistent model parameters for *all*

presented experiments and not to achieve the best match for each experiment individually. We verify the implementation of the model into a finite element program by comparing the numerical results with the analytical solutions. Finally, we show the capability of the network model to capture more complex boundary-value problems; two examples are provided: indentation test on a slab of actin network using AFM and micropipette aspiration.

The deformation mode produced by rheometer experiments is assumed to be simple shear. For reasons of comparison we also implemented the analytical solution in `MATLAB`, where we used a kinematic constraint to enforce incompressibility. Hence, we replaced eq. $(3.16)_1$ by $\mathbf{S}^{\infty}_{\mathrm{vol}} = -q\mathbf{C}^{-1}$, where q serves as a Lagrange multiplier. We assumed a plane stress state i.e. $\sigma_{zz} = \sigma_{xz} = \sigma_{yz} = 0$ which gives an additional equation for determining q.

3.3.1 LAOS, amplitude sweep

The first set of experiments, i.e. the LAOS measurements, provide an excellent basis to evaluate the viscoelastic behavior of the network material at fixed amplitude and frequency. The resulting curves in the σ_{xy}-γ-space are called Lissajous curves and their study is of increasing interest for soft solids [171]. When excited with a harmonic deformation, a linear viscoelastic material responds with a harmonic, phase shifted stress. Therefore, the Lissajous curve becomes an ellipse. The area within the hysteresis loop is a measure for the dissipation of the viscoelastic material. The ellipse distorts if the material is nonlinear. The nonlinear viscoelastic behavior is reflected in Fig. 3.4(a), where the Lissajous curve from the experiment for a shear strain amplitude of $\gamma_{\mathrm{A}} \sim 12\%$ is indicated by crosses. From the three measured cycles, only the last one is shown, as the response reached a steady state. These data were used to fit the proposed model by means of the nonlinear least squares function (`lsqnonlin`) in `MATLAB`, using the trust-region-reflective algorithm.

We seek to reuse a maximum of information about the parameter values we obtained in the analysis of the purely elastic model [48], and focus here on the determination of parameters associated with the viscous contributions. This reduces the number of free parameters which are determined in the fitting procedure and leads to a more stable execution of the algorithm. The temperature T in the experiments was 294 K. The persistence length L_{p} of F-actin is reported in the literature as $16\,\mu$m [35]. A fit of the single filament model (3.2)–(3.4) to experimental data obtained by Liu and Pollack [36] was carried out earlier [48], and here we adopt the obtained parameter values: $\beta = 0.438$ and $\mu_0 = 38.6\,$nN. Following the arguments of [48], the product of the filament density n and the contour length L for an actin concentration of $c_{\mathrm{A}} = 9.5\,\mu$M is $nL = 15\,\mu\mathrm{m}^{-2}$. Fitting of the elastic part of the proposed model to experimental data of reconstituted actin networks suggests a value for the averaging

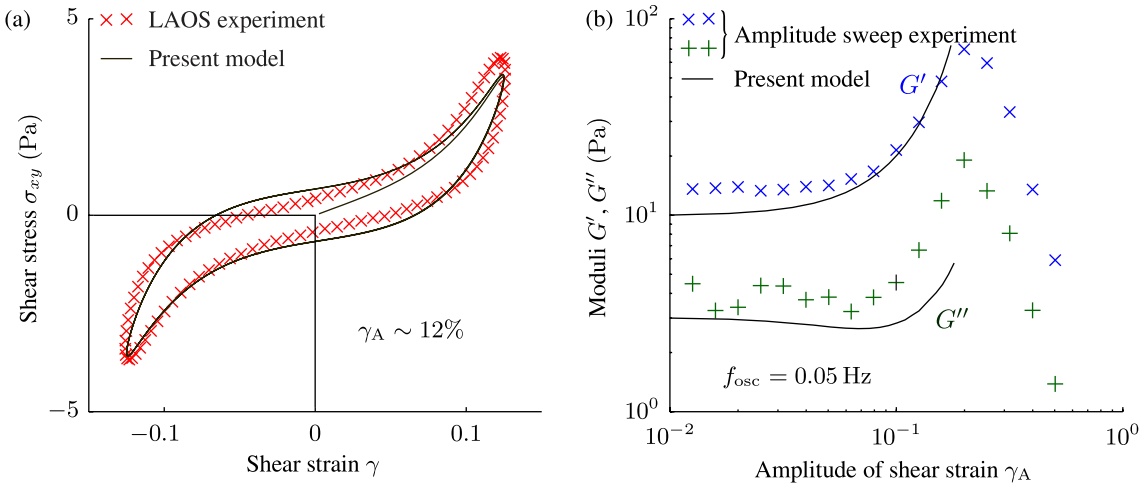

Figure 3.4: Fit of the presented viscoelastic model to experimental data. Crosses indicate experimental data and solid curves are generated with the presented model while parameters are taken from Table 3.1. (a) LAOS — shear stress σ_{xy} vs. shear strain γ at a shear strain amplitude of $\gamma_A \sim 12\%$ representing the Lissajous curve, where for better readability only every fiftieth data point is shown. (b) Amplitude sweep — storage modulus G' and loss modulus G'' vs. amplitude of shear strain γ_A at a constant oscillation frequency of $f_{osc} = 0.05\,\text{Hz}$.

parameter p of 13.12, [48]. Tharmann et al. [26] estimated the junction-to-junction length of *in vitro* samples at $c_A = 9.5\,\mu\text{M}$ by means of scaling arguments as $1\,\mu\text{m}$ for $R = 1/10$, and thus we adopt this value for $r_0 = 1\,\mu\text{m}$. Preliminary numerical experiments in the frequency domain suggested that a relaxation time of $\tau_1 = 2\,\text{s}$ mediates the loss modulus at $f_{osc} = 0.5\,\text{Hz}$. During the fitting procedure we held the parameters T, L_p, β, μ_0, nL, p, r_0, τ_1 constant. The target function was evaluated for three oscillation cycles to ensure that steady state is reached. The free parameters and their calculated values are (i) the contour length L of the filament between two cross-links ($1.048\,\mu\text{m}$), (ii) the pre-stretch λ_0 of the filament inside the network in the reference configuration (1.012), and (iii) the viscoelastic parameter, i.e. the free-energy parameter $\theta_1 = 0.835$ related to the relaxation time; only one Maxwell element is used. All parameters are summarized in Table 3.1.

The results of the proposed model are illustrated in Fig. 3.4(a) as a solid curve. We show all three cycles of the model and, therefore, the curve starts in the origin of the diagram. Because of the short relaxation time, the mechanical response collapses almost immediately after initiation with the steady state curve. The proposed model matches the experimental data very well. The associated coefficient of determination $\mathcal{R}^2$ is 0.982. The ratio r_0/L is about 95% which supports the assumption of semi-flexible fibers. The value for the contour length L is also comparable to the *in vivo* length of an actin filament [15]. By comparing the contour length of the presented

Table 3.1: Parameters for the viscoelastic model with a single Maxwell element. Elastic parameters are in the upper part while viscous parameters are in the lower part. For a visualization see Fig. 3.4.

Variable	Symbol	Value	Unit
Temperature	T	294	K
Persistence length	L_p	16	μm
Effective extensional number	β	0.438	–
Stretch modulus	μ_0	38.6	nN
Filament density	n	14.31	$\mu\mathrm{m}^{-3}$
Averaging parameter	p	13.12	–
End-to-end distance at zero force	r_0	1	μm
Contour length	L	1.048	μm
Initial stretch	λ_0	1.012	–
Relaxation time	τ_1	2	s
Free-energy parameter	θ_1	0.835	–

model to the contour length obtained for the purely elastic model [48], we observe a notably smaller value for the elastic model. We propose that viscous effects are always present in cross-linked actin networks, and thus the purely elastic model underestimated this value.

From the LAOS data we calculated for various amplitudes of shear strain γ_A both the storage modulus G' and the loss modulus G'', according to (3.1) (see Fig. 3.4(b)). Both moduli are rather constant for small γ_A, particularly $G' \sim 14\,\mathrm{Pa}$ and $G'' \sim 4\,\mathrm{Pa}$ until $\gamma_\mathrm{A} \sim 6\%$. In this small strain regime the mechanical behavior of the sample is linearly viscoelastic which can be confirmed by checking the corresponding elliptically-shaped Lissajous curves. The moduli rise for higher strain amplitudes [26] unlike it is observed for the viscoelastic response of rubber, i.e. the Payne effect, see, e.g., [183]. In the present case the increase in the moduli can be attributed to the strain stiffening of actin networks. The values increase until a maximum at $\gamma_\mathrm{A} = 0.2$ after which the moduli G' and G'' drop far below their values of the linear regime. We assume a similar network detachment from the rheometer's plates, as reported by Schmoller et al. [159]. In addition, also forced bond dissociation of individual cross-links [139, 184], which was modeled recently using two-dimensional discrete networks [96], may contribute to the drastic decrease of the non-linear moduli. Along these lines, we could not detect a steady state behavior for the LAOS data beyond the maxima of the moduli. Therefore, we neglect the data for $\gamma_\mathrm{A} > 20\%$ in subsequent considerations. The proposed model with the set of parameters from Table 3.1 fits the experimental data well over a large range of strain amplitudes up to $\gamma_\mathrm{A} < 16\%$, right before the network detaches from the measuring plates (see Fig. 3.4(b)). Nevertheless,

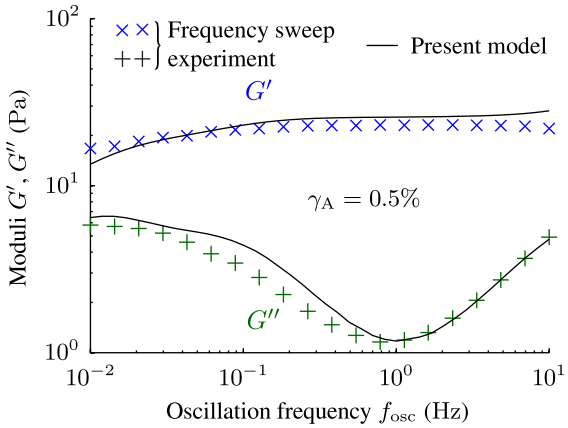

Figure 3.5: Fit of the proposed model with three Maxwell elements to data of a frequency sweep experiment at a shear strain amplitude of $\gamma_A = 0.5\%$. Storage modulus G' and loss modulus G'' vs. oscillation frequency f_{osc}. Elastic parameters are taken from Table 3.1, while viscous parameters are from Table 3.2.

the model slightly underestimates G' in the linear regime and G'' over the whole γ_A-range.

3.3.2 Frequency sweep

We measured the storage and loss moduli (G', G'') for the frequency sweep experiment for which we have used the same sample composition as for the other experiments. The experimental data are plotted in Fig. 3.5. The storage modulus G' is fairly constant ($G' \sim 20\,\mathrm{Pa}$) over the whole range of frequencies. In contrast, we observe a loss modulus of $G'' \sim 6\,\mathrm{Pa}$ for low frequencies before it drops to a minimum of $G'' \sim 1.1\,\mathrm{Pa}$ at 8 Hz. It increases again for higher frequencies which is in agreement with earlier studies [26, 185].

Above we deduced that the model with a single Maxwell element and therefore with one relaxation time τ_1 captures the behavior of the reconstituted cross-linked actin network over a large range of shear strains. The oscillation frequency in the experiment was constant. In contrast to this, the oscillation frequency is varied over three orders of magnitude in the frequency sweep experiment. Therefore, a single Maxwell element, i.e. one relaxation time, is not able to capture the experimental data of the frequency sweep. Preliminary numerical experiments showed that three Maxwell elements are needed to reproduce the G''-data over the whole frequency range as seen in Fig. 3.5. While fixing the parameters from Table 3.1 we have added two more Maxwell elements. Table 3.2 summarizes the identified parameter values for the relaxation times τ_ν and the free-energy parameters θ_ν, $\nu = 1, 2, 3$. The curves

Table 3.2: Viscous parameters for the model with three Maxwell elements.

Maxwell element number	ν	1	2	3
Relaxation time	τ_ν (s)	2	0.007	15
Free-energy parameter	θ_ν (-)	0.835	1.6	1.4

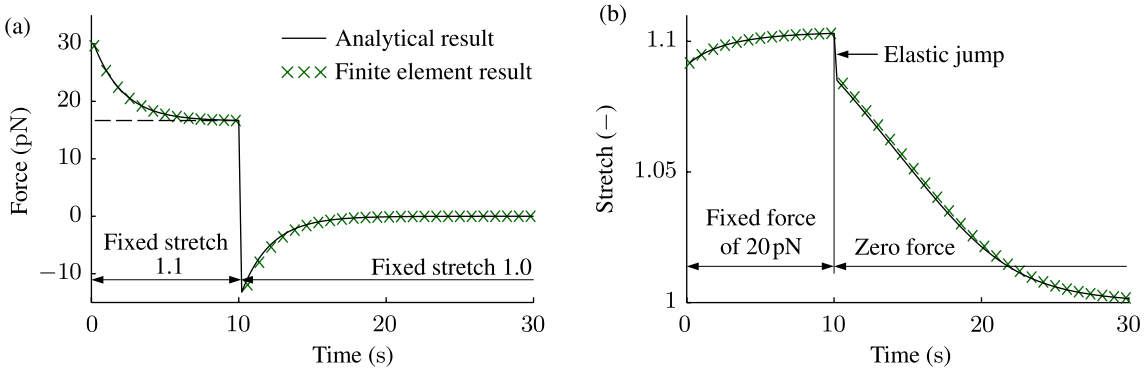

Figure 3.6: Creep and relaxation experiments: comparison of analytical results, obtained from MATLAB, with numerical results, generated with FEAP, of numerical experiments performed on a unit cube. For reasons of readability only every fourth data point of the finite element analysis is shown. (a) The force relaxes to a constant value after setting the stretch to 1.1 at time 0 s. The dashed line indicates the asymptotic solution. Another relaxation is observed after setting the stretch back to 1 at time 10 s with the asymptotic force value 0 pN. (b) In the creep experiment a constant force of 20 pN is applied at time 0 s. When the force is set to zero at time 10 s, the stretch returns to zero. At both instances, where the force is changed, elastic jumps can be observed.

resulting from the proposed model are then plotted against the experimental data, see Fig. 3.5. Both moduli show a good agreement with the experimental data.

3.3.3 Creep and relaxation experiments using finite elements

The models proposed in Sections 3.2.2 and 3.2.3 were implemented in the open source software FEAP [186] by creating a user-defined material. For the purpose of verification we then compared the finite element results with the analytical results obtained from MATLAB. For the subsequent finite element analyses we used the proposed model with a single Maxwell element, with the parameters given in Table 3.1. The penalty parameter κ was set to be three orders of magnitude higher than the initial shear modulus.

Figure 3.6(a) illustrates a numerical relaxation experiment of a uniaxial tensile test.

We fixed the stretch and simultaneously measured the force exerted on a cubic sample with 1 μm side length. Starting from zero deformation, we increased the stretch of the incompressible block to 1.1 at time 0 s within one time step, i.e. $\Delta t = 10$ ms. The immediate force response of about 30 pN relaxed in an exponential way to about 17 pN. The asymptotic solution is indicated in Fig. 3.6(a) by a dashed line. After setting the stretch back to 1 at time 10 s, the force overshoots into the negative domain and relaxes with exponential decay to 0 pN. A comparison of the numerical data obtained from the finite element analysis with the analytical results reveals a very good match.

In a creep experiment with the same geometrical and material setting as above, the stretch varied while the tensile force is fixed. We increased the force up to 20 pN within one time step. After experiencing an instantaneous stretch of about 1.09, the sample creeps slowly towards an asymptotic value. We then released the tensile force to 0 pN before reaching the steady state at time 10 s. The analytical solution in Fig. 3.6(b) clearly exhibits an elastic shrinking, indicated by the arrow, before it creeps back to 1, i.e. the reference configuration. The numerical results follow exactly the analytical solution. By achieving quadratic convergence during the finite element analysis and with the good comparison, we conclude that the finite element implementation is correct.

3.3.4 Indentation of a spherical tip on a network slab

The numerical example in this section aims to resemble an indentation test on a cell using AFM. The used geometry and boundary conditions are adopted from the related example in [48], see Fig. 11 therein. In particular, a spherical tip with a radius of 5 μm indents a cylindrical slab of cross-linked actin network. We use a cylindrical coordinate system, where the r-axis points in the radial direction and the z-axis in the axial direction of the sample. It approximates an infinite half space with a thickness of 250 μm and a radius of 500 μm. Therefore, the geometry is large enough to eliminate boundary effects but remains outside of the natural geometry range of such networks. The elements are based on a three-field variational principle (Q1/P0) to avoid volumetric locking. A symmetry boundary condition at $r = 0$ is enforced to furnish an axisymmetric setup. At the bottom of the sample, at $z = 0$, no displacements in the z-direction are allowed. At the boundary on the side surface, i.e. at $r = 500\,\mu$m, we allow displacements only in the z-direction. We employ a contact condition between the sphere and the surface by means of a penalty function. The numerical experiment starts at time $t = 0$ s. The sphere is forced to indent the surface by 5 μm within 2 s (time $t = 2$ s). Thereafter, the indenter remains in its current position for 18 s ($t = 20$ s) to wait for the material to reach its fully relaxed state.

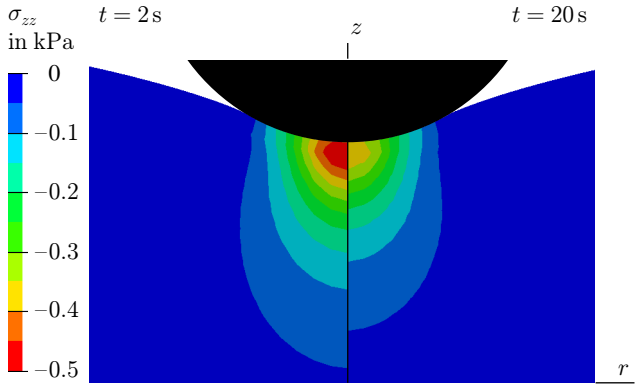

Figure 3.7: Contour plot of the normal Cauchy stress σ_{zz} of a cylindrical slab of cross-linked actin network which is indented by a spherical tip. The left panel shows the stress distribution immediately after the maximum indentation is reached, at time $t = 2\,\mathrm{s}$. The right panel depicts the relaxed state at $t = 20\,\mathrm{s}$

.

The normal Cauchy stress component in the z-direction, i.e. σ_{zz}, immediately after the maximum indentation is reached and in the relaxed state is depicted in Fig. 3.7. Note that Fig. 3.7 only shows the region of interest. In the left half of Fig. 3.7 we observe high stress concentration underneath the indenter which diminishes rapidly with increasing distance to the surface. The maximum stress value is about $-0.5\,\mathrm{kPa}$. After relaxation of the material, the stresses reduce to a maximum of about $-0.39\,\mathrm{kPa}$, see the right half of Fig. 3.7. The amount of the stress drop can be attributed to the free-energy parameter θ_1.

In vivo F-actin networks are known to rupture at a few Pascal of stress, and they will never experience the stress magnitudes shown in this example. There are several reasons why our computed results do deviate from an *in vivo* situation. First, the cross-links or filaments will break when critical strain values are reached. Furthermore, they are subject to a continuous generation, degeneration and reorganization of filaments and, therefore, would respond to disturbances like indentation of the surface. Second, the assumption of an infinite half-space is good for an academic analysis but does not correspond to the boundary conditions found in AFM experiments. For a more sophisticated setup we would need to consider a fluid, representing the cytosol, underneath a thin layer of actin network which is confined by the lipid bilayer membrane. With such a setup, the main deformation mode would transform from compression to bending of the cortex. Third, we do not know the actual *in vivo* actin and cross-linker concentrations but we rather assumed a material used in *in vitro* experiments. These limitations, together with the much more complex composition of living cells are challenges to tackle in future modeling attempts.

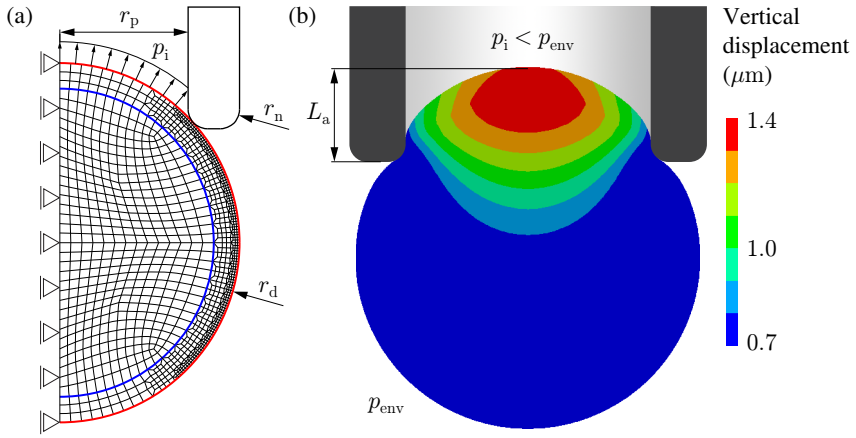

Figure 3.8: Aspiration of a droplet into a micro-pipette. A very soft (neo-Hookean) core inside a thin envelope of cross-linked actin network. The pressure difference between outside (p_{env}) and inside (p_{i}) the micro-pipette causes the droplet to suck in. (a) Boundary conditions of the problem with the radius r_{p} of the pipette, the radius r_{d} of the droplet, and the radius r_{n} of the nozzle. The bold blue curve separates the soft core from the envelope and the bold red curve indicates the surface of the droplet. (b) Representative results from the finite element analysis showing the aspiration length L_{a}.

3.3.5 Micro-pipette aspiration test

The final numerical example is also related to cell mechanics, in particular to a micro-pipette aspiration test. The review of Hochmuth [54] provides an introduction to the experimental procedures, also discussing a simple membrane-based model. A large number of finite element simulations already exist in the literature. For example, erythrocytes were examined by Discher et al. [187], who based their model on the hexagonal spectrin network. They considered the structural proteins as worm-like chains. Most other analyses used purely phenomenological models, e.g., a compressible neo-Hookean model extended by an Upper Convected Maxwell model [188] or elastic force and swelling force models [127], to point out just a few.

Experiments with fibroblasts showed a linear relationship between the pressure difference Δp (between the environment and the internal of the micro-pipette) and the total projection length L_{a} (see Fig. 3.8(b)) [179]. Similar results were reported for chondrocytes by Jones et al. [52], who also estimated viscoelastic properties by measuring the creep of the cells by fixing Δp. We show here similar results for a droplet using our micro-structurally motivated viscoelastic model.

Various geometries were introduced for the analyses in the papers mentioned above which we use here as a guideline to design the present example. Our chosen axisymmetric geometry, the discretization and boundary conditions are depicted in Fig. 3.8(a). The droplet with radius $r_{\text{d}} = 7\,\mu$m touches the nozzle of the pipette

which has an inner radius $r_\mathrm{p} = 5\,\mu$m. The radius of the nozzle is $r_\mathrm{n} = 0.75\,\mu$m. We adopt here the approach of Monteiro et al. [189] and separate the droplet into two compartments, i.e. a stiff envelope, represented by the proposed material model, and a very soft core, which we assume to be a neo-Hookean solid. The border between the two materials is indicated by a bold (blue) curve in Fig. 3.8(a), at a radius of $6\,\mu$m. We exploit the symmetry of the problem and apply the appropriate boundary conditions. A contact constraint is enforced between the surface of the droplet, indicated by a bold (red) curve, and the rigid pipette by means of a penalty solution method. We used the meshing program `CUBIT` [190] to discretize the geometry, and the mesh was refined at regions where contact occurs to minimize the stick-slip-effects. Pressure boundary conditions are employed as follower loads on surface nodes inside the pipette representing a pressure p_i, which is smaller than the environmental pressure p_env resulting to the pressure difference $\Delta p = p_\mathrm{env} - p_\mathrm{i}$. For post-processing we measure the projection length L_a.

The stiff envelope is modeled as an F-actin network with material parameters from Table 3.1. Monteiro et al. [189] estimated the properties of the inner part of a cell, given as a neo-Hookean solid, much softer than the outer part by allowing little compression. Therefore, we also used the neo-Hookean model with 10 Pa Young's modulus and with a Poisson's ratio of 0.4. Similar limitations as in the previous section apply to the following numerical experiments.

We used the same element technology as in the previous example. In a first numerical experiment, the droplet is aspirated by linearly increasing Δp until the droplet completely enters the micro-pipette. This experiment was conducted three times with different pressure difference rates. First, Δp was increased by about 20 Pa/s (subsequently referred to as 'fast'); second, the experiment was calculated with a ten times slower pressure difference rate ('medium'); third, Δp was very slowly increased so that no viscous effects could be detected ('quasi-static'). A representative plot of the deformed droplet with colors indicating the vertical displacement in μm is given in Fig. 3.8(b).

The numerical results are summarized in Fig. 3.9(a), where the aspiration length L_a, normalized with the pipette diameter r_p is plotted versus the pressure difference Δp. The data points for the three pressure difference rates (fast, medium, quasi-static) have similar characteristics and can be divided into three parts. A very soft initial phase, characterized by a large normalized aspiration length $L_\mathrm{a}/r_\mathrm{p}$, and a relatively small pressure difference Δp until a bulk of the droplet has entered the micro-pipette. In the second phase, which starts for all three pressure difference rates at $L_\mathrm{a}/r_\mathrm{p} \sim 0.8$, we observe a *linear* increase of the normalized aspiration length indicated by the dashed line. As the droplet is completely aspirated, we enter the third phase where the gradient of the curves increases again. Because we assume frictionless contact, there is no increase in the pressure difference required to move the

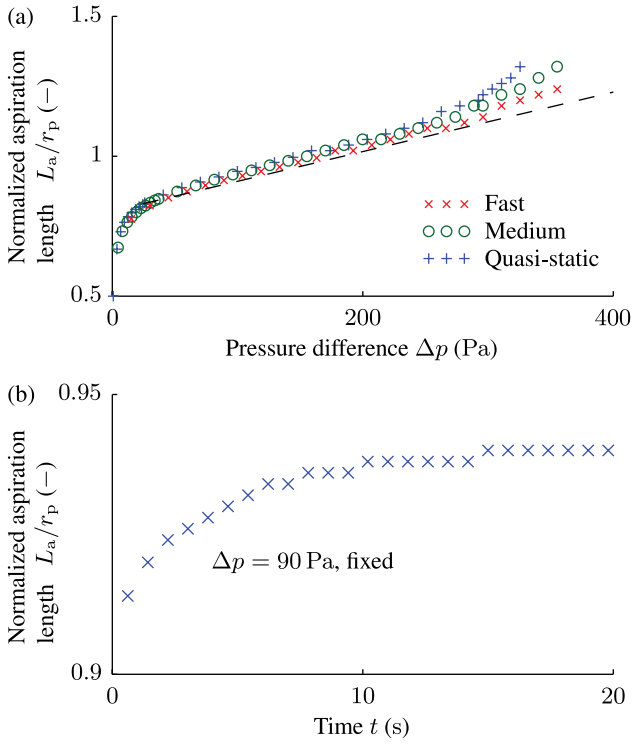

Figure 3.9: Results of the numerical aspiration experiments. (a) Normalized aspiration length L_a/r_p versus pressure difference Δp, where Δp was increased at various speeds. The dashed line indicates the linear part of the aspiration process. (b) Normalized aspiration length versus time t for a creep experiment.

fully aspirated droplet into the micro-pipette. Therefore, our calculations, using the Newton-Raphson algorithm, become unstable and eventually terminate. The linear regime is well reflected by experimental data of cells [52, 179], and the described instability was predicted earlier [54].

In a second numerical example, the viscoelastic response is analyzed in more detail by using the parameter set provided in Table 3.1. In particular we analyzed a creep experiment. In the simulation we increased the pressure difference Δp to 90 Pa within 0.2 s. Thereafter, we fixed this value for the (experimental) time of 20 s. Figure 3.9(b) depicts the normalized aspiration length L_a/r_p versus the experimental time t. At $t = 0$ we identify an instantaneous normalized aspiration length of 0.91. Starting with a relatively steep gradient, the curve flattens towards an asymptotic value around 0.94. This behavior is also in qualitative agreement with experimental observations of cells [52, 179].

3.4 Summary and conclusion

We presented a novel viscoelastic model for cross-linked F-actin networks motivated by the underlying microstructure. We used a worm-like chain model for a single filament and considered the extensibility by using the stretch modulus. The non-affine network model integrates the filaments three-dimensionally by a homogenization over a unit sphere. The viscous contribution was implemented by means of a generalized Maxwell model. Formulations of the stress tensor together with the elasticity tensor enabled us to conduct a straightforward implementation into a finite element program.

The proposed network model is able to capture the experimental data obtained from rheological tests for a large range of shear strains and strain rates. It may capture the typical pronounced nonlinear behavior of viscoelastic biomaterials such as stress relaxation and creep. The LAOS experiments give precious insights into the viscoelastic behavior of biopolymer networks undergoing large strains. Data for amplitude sweep and frequency sweep experiments are well captured by the proposed network model. The expected stress relaxation and creep behavior can also be seen in numerical indentation experiments. A finite element model of a stiff (actin network) envelope holding a very soft core can replicate prominent viscoelastic mechanical properties of a droplet aspirated into a micro-pipette. The proposed network model may be used to describe the mechanical response of cross-linked *in vitro* F-actin networks. Furthermore, it may serve as a component in a whole cell model, in particular to approximate the behavior of the actin cortex.

Acknowledgements

We thank M. Rusp for the actin preparation. This work was partly supported by the Deutsche Forschungsgemeinschaft (DFG) through Grant No. BA2029/8 and the Cluster of Excellence Nanosystems Initiative Munich. KMS acknowledges support from CompInt in the framework of ENB Bayern and IGSSE and thanks J. Skotheim for hospitality.

4 AN AFFINE CONSTITUTIVE MODEL FOR CROSS-LINKED F-ACTIN NETWORKS WITH COMPLIANT LINKER PROTEINS

Abstract Cross-linked actin networks are important building blocks of the cytoskeleton. In order to gain deeper insights into experimental data, adequate models are required. We introduce an affine constitutive network model for cross-linked F-actin networks and specialize it to reproduce the behavior of *in vitro* reconstituted model networks. Naturally we are able to obtain the experimentally observed normal stress response of cross-linked actin networks observed in rheometer tests. In the present study an extensive analysis is performed applying the proposed model to simple shear deformation. The physically interpretable parameters can be scaled according to the literature. We consider the compliance of cross-linker proteins by enhancing existing single filament models with a serial nonlinear element. Implementation into a finite element program is straightforward. It allows parameter studies of, e.g., micropipette aspiration experiments which are presented as numerical examples to emphasize the strength of this approach.

4.1 Introduction

The cytoskeleton is a network of proteins, which give a cell its shape and its ability for motility and division. Actin is one of these many proteins and underneath the lipid bilayer it builds a cross-linked isotropic structure. *In vitro* reconstituted actin gels, cross-linked with actin binding proteins, serve as model systems which are characterized by nonlinear stiffening and viscoelasticity [38] in rheological experiments. Furthermore, they exhibit an exceptional normal stress in simple shear experiments [39], an unusual property with regard to technical polymer networks like rubbers.

Actin binding proteins may attach to actin and link two filaments together. They are also referred to as cross-linking proteins or linker proteins. Different linkers are known to form gels, where networks with filamin [38, 125, 140], scruin [21, 41] and heavy meromyosin (HMM) in its rigor state [26, 48, 118] are extensively studied. The type of linker protein strongly influences the mechanical response of the network [140] by changing the network's morphology and by the intrinsic compliance of the linker. In this sense, according to Tharmann et al. [26], HMM is extraordinary because (i) it creates isotropic networks without bundles over a large range of linker concentrations;

(ii) in actin networks cross-linked with rigor-HMM, the compliance of the individual filaments is dominated by their thermal fluctuations and the compliance of the individual cross-linking molecules does not alter this picture; (iii) the mechanics of such networks can be described by the affine deformation of single filaments between two cross-linking points alone.

Continuum mechanical models for cross-linked actin networks not only seek to explain the mechanics of the *in vitro* model systems but also aim to interpret the results of more complicated experiments in cell mechanics. Many of these models are based on the network's microstructure and adopt the idea of integrating the single filament response into a network [155]. An algorithmic treatment for affine and non-affine networks, the micro-sphere models, was given by Miehe et al. [119]. The affine network model was adopted for modeling the mechanics of collagen in arteries [191, 192]. Applications of the filament to network approach to the elasticity of actin networks were proposed earlier [48, 82]. The first of these models, however, is limited by its inability to capture the normal stress response under simple shear, while the second uses a non-affinity parameter which is not intuitive. Motivated by statistics of chain linking, a maximal advance path constraint was recently introduced to make non-affinity easier to grasp [147]. The model, however, is very expensive in terms of computational cost and therefore not very practicable. Unterberger et al. [120] developed a model based on [48] which also considers viscoelasticity.

In the present study, we show that an affine full network model is capable of capturing not only the shear stress but also the normal stress behavior of semiflexible biopolymers. We use scaling arguments from the literature to relate material parameters to protein concentrations of samples in bulk rheology. Furthermore, we add the contribution from compliant linkers to the model which soften actin gels. The model may be enhanced by considering viscoelasticity by adding Maxwell elements. The calibration of the proposed model may be performed through shear deformation data from bulk rheology. It can be used to interpret experiments with complicated geometries and boundary conditions such as atomic force microscopy or micro-pipette aspiration. The model allows to perform parameter studies in virtual experiments.

We introduce the continuum mechanical framework and the network model in Section 4.2. Section 4.3 applies the model to simple shear deformation, shows the correct normal stress response and specializes to rigid and compliant cross-links. Some aspects of the numerical treatment of the proposed model in a finite element program and a computational example are given in Section 4.4. We finalize the present work with a summary and concluding remarks in Section 4.5.

4.2 Mechanics of fibrous networks

Consider a soft elastic continuum which is deformed so that the deformation gradient is $\mathbf{F}$ and the right Cauchy-Green tensor is $\mathbf{C} = \mathbf{F}^{\mathrm{T}}\mathbf{F}$. We introduce the volume ratio $J = \det\mathbf{F} > 0$, apply a multiplicative split of $\mathbf{F}$ and define the volume preserving (isochoric) part of the deformation gradient $\overline{\mathbf{F}}$ and its volumetric part $J^{1/3}\mathbf{I}$, where $\det\overline{\mathbf{F}} = 1$, and $\mathbf{I}$ is the second-order identity tensor. This, together with the isochoric right Cauchy-Green tensor $\overline{\mathbf{C}} = \overline{\mathbf{F}}^{\mathrm{T}}\overline{\mathbf{F}}$, reads

$$\mathbf{F} = J^{1/3}\overline{\mathbf{F}}, \qquad \mathbf{C} = J^{2/3}\overline{\mathbf{C}}. \tag{4.1}$$

Suppose that a family of fiber is embedded in this material, which we refer to as the matrix, and each fiber deforms with the matrix. Then, a single fiber with orientation $\mathbf{M}$ in the reference configurations maps to the orientation $\mathbf{m}$ in the current configurations by $\overline{\mathbf{F}}$, i.e.

$$\mathbf{m} = \overline{\mathbf{F}}\mathbf{M}. \tag{4.2}$$

By introducing the stretch $\lambda = J^{1/3}\bar{\lambda}$ in the fiber, where $\bar{\lambda}$ is the modified stretch, then the fourth modified pseudo-invariant $\bar{I}_4$ may be written in the form

$$\bar{I}_4 = \bar{\lambda}^2 = \mathbf{M}\cdot\overline{\mathbf{C}}\mathbf{M} = \mathbf{m}\cdot\mathbf{m}. \tag{4.3}$$

Let $\rho(\mathbf{M})$ be the relative angular density of fibers so that

$$\frac{1}{4\pi}\int_{\Omega}\rho(\mathbf{M})\,\mathrm{d}\Omega = 1, \tag{4.4}$$

where Ω is the unit sphere. The isochoric strain energy of a single fiber is $w_{\mathrm{iso}}(\bar{\lambda})$ so that the strain energy over all orientations is

$$n\int_{\Omega}\rho(\mathbf{M})w_{\mathrm{iso}}(\bar{\lambda})\,\mathrm{d}\Omega, \tag{4.5}$$

by assuming that all fibers have the same properties, i.e. the same form of $w_{\mathrm{iso}}(\bar{\lambda})$, and n is the number of fibers per unit reference volume. If there are different types of fibers with energies $w_{k\,\mathrm{iso}}(\bar{\lambda})$ and densities $\rho_k(\mathbf{M})$, n_k, $k = 1, 2, 3\ldots$, then (4.5) is replaced by

$$\sum_k n_k\int_{\Omega}\rho_k(\mathbf{M})w_{k\,\mathrm{iso}}(\bar{\lambda})\,\mathrm{d}\Omega, \tag{4.6}$$

and (4.4) by

$$\sum_k \frac{1}{4\pi}\int_{\Omega}\rho_k(\mathbf{M})\,\mathrm{d}\Omega = 1. \tag{4.7}$$

Now for simplicity we consider only one type of fiber so that (4.5) serves as the basis. Suppose the volume fraction of fibers is ν and that of the isotropic matrix is $1-\nu$. The strain-energy function (for the matrix and the fibers) per unit reference volume is then

$$\Psi_{\text{iso}}(\overline{\mathbf{C}}, \mathbf{M}) = n \int_{\Omega} \rho(\mathbf{M}) w_{\text{iso}}(\bar{\lambda}) \, \mathrm{d}\Omega + (1-\nu)\Psi_{\text{iso}}^{\text{mat}}(\overline{\mathbf{C}}), \tag{4.8}$$

where $\Psi_{\text{iso}}^{\text{mat}}$ is the energy stored in the matrix material per unit reference volume. The volume fraction of the fibers is $\nu = nLS_0$, where L is the contour length of a single fiber and $S_0 \sim 25\,\text{nm}^2$ [59] is its reference cross-sectional area assuming all fibers have the same contour length and cross-sectional area. Note that in general w_{iso} depends on the material constants which themselves depend on the concentration and compliance of actin binding proteins (which we refer to as linkers here), and this is included implicitly in the form of w_{iso}. Factors which need to be taken into consideration are the mean length of the filaments between the cross-links, the concentration of actin and the concentration of linkers. At this point we do not need to make these dependencies explicit. This will be considered in the Sections 4.3.4 and 4.3.5.

Transient behavior is always present in biopolymer networks. We want to consider this phenomenon by an additive extension of the elastic model by viscous terms. A method within the framework of nonlinear continuum mechanics at finite strains was introduced by Simo [193], see also Holzapfel [112, 121], and it was recently used for modeling cross-linked actin networks [120]. We only want to display the key equations and refer for further studies of the matter to the relevant papers.

While the modified right Cauchy-Green tensor $\overline{\mathbf{C}}$ characterizes the kinematics of the elastic deformation, we keep track of the viscous contributions using m internal variables $\boldsymbol{\Gamma}_\upsilon$, $\upsilon = 1, \ldots, m$. The non-equilibrium response is then described by the configurational free energies Υ_υ. The Helmholtz free-energy function Ψ is then split additively, i.e.

$$\Psi = \Psi_{\text{vol}}(J) + \Psi_{\text{iso}}(\overline{\mathbf{C}}, \mathbf{M}) + \sum_{\upsilon=1}^{m} \Upsilon_\upsilon(\overline{\mathbf{C}}, \boldsymbol{\Gamma}_\upsilon), \tag{4.9}$$

where Ψ_{vol} is a given scalar-valued function of J describing the volumetric (dilational) elastic response of the material. Note, however, that for numerical purposes we use here

$$\Psi_{\text{vol}}(J) = \kappa \mathcal{G}, \qquad \mathcal{G} = \frac{1}{4}(J^2 - 1 - 2\ln J), \tag{4.10}$$

where κ is a (positive) penalty parameter and $\mathcal{G}$ serves as a penalty function motivated mathematically, without physical relevance. The penalty method for incompressibility is the basis for the numerical approach, see also Section 8.3 in [194].

4.2.1 Second Piola-Kirchhoff stress tensor

The split in (4.9) results in an analogous split of the total second Piola-Kirchhoff stress tensor $\mathbf{S} = 2\partial\Psi/\partial\mathbf{C}$, i.e.

$$\mathbf{S} = \mathbf{S}_{\text{vol}}(J) + \mathbf{S}_{\text{iso}}(\overline{\mathbf{C}}, \mathbf{M}) + \sum_{\upsilon=1}^{m} \mathbf{Q}_\upsilon(\overline{\mathbf{C}}, \boldsymbol{\Gamma}_\upsilon), \tag{4.11}$$

where $\mathbf{S}$ consists of a purely volumetric elastic contribution $\mathbf{S}_{\text{vol}}$, a purely isochoric elastic contribution $\mathbf{S}_{\text{iso}}$ and additional internal tensor variables $\mathbf{Q}_\upsilon$, $\upsilon = 1, \dots, m$, which may be interpreted as non-equilibrium stresses (coming from Maxwell elements) in the sense of non-equilibrium thermodynamics. Note that $\mathbf{Q}_\upsilon$ are variables related (conjugate) to $\boldsymbol{\Gamma}_\upsilon$, $\upsilon = 1, \dots, m$, with the internal constitutive equations $\mathbf{Q}_\upsilon = -2\partial\Upsilon_\upsilon(\overline{\mathbf{C}}, \boldsymbol{\Gamma}_\upsilon)/\partial\boldsymbol{\Gamma}_\upsilon$, $\upsilon = 1, \dots, m$.

The volumetric stress contribution is defined as

$$\mathbf{S}_{\text{vol}} = Jp^\star\mathbf{C}^{-1}, \qquad p^\star = \frac{\mathrm{d}\Psi_{\text{vol}}(J)}{\mathrm{d}J}. \tag{4.12}$$

By means of the fourth-order Lagrangian projection tensor $\mathbb{P} = \mathbb{I} - (\mathbf{C}^{-1} \otimes \mathbf{C})/3$, we define the deviatoric (isochoric) part of the second Piola-Kirchhoff stress tensor as [194]

$$\mathbf{S}_{\text{iso}} = J^{-2/3}\mathbb{P} : \widetilde{\mathbf{S}}, \tag{4.13}$$

where $\widetilde{\mathbf{S}} = 2\partial\Psi_{\text{iso}}/\partial\overline{\mathbf{C}}$ is the fictitious Cauchy stress tensor and $\mathbb{I}$ is the symmetric part of the fourth-order identity tensor. Hence, with (4.8), a straightforward calculation gives

$$\widetilde{\mathbf{S}} = n\int_\Omega \rho(\mathbf{M})\bar{\lambda}^{-1}w'_{\text{iso}}(\bar{\lambda})\mathbf{M}\otimes\mathbf{M}\,\mathrm{d}\Omega + 2(1-\nu)\frac{\partial\Psi^{\text{mat}}_{\text{iso}}(\overline{\mathbf{C}})}{\partial\overline{\mathbf{C}}}, \tag{4.14}$$

where the second term is the contribution of the isotropic matrix material. Here, and subsequently in this section, we use the prime as a convenient short-hand notation for $(\bullet)' = \mathrm{d}(\bullet)/\mathrm{d}\bar{\lambda}$.

The transient behavior is introduced by $\mathbf{Q}_\upsilon$ in (4.11), which is assumed to satisfy the evolution equations with the relaxation times τ_υ and the free-energy parameters θ_υ as material parameters, i.e.

$$\dot{\mathbf{Q}}_\upsilon + \frac{\mathbf{Q}_\upsilon}{\tau_\upsilon} = \theta_\upsilon\dot{\mathbf{S}}_{\text{iso}}, \tag{4.15}$$

where the dot denotes the material time derivative. The initial conditions at time $t = 0^+$ are assumed to be $\mathbf{Q}_\upsilon|_{t=0^+} = \mathbf{0}$. The present approach is characterized by two features which make it easy to apply to any existing hyperelastic constitutive model.

First, the additive split of the free-energy function (4.9) allows to evaluate only the elastic contribution and then add as many Maxwell elements as necessary. Second, the algorithmic treatment of the transient equations as discussed in [120, 121] results in a simple evaluation of the time integrals which arise from (4.15).

4.2.2 Cauchy stress tensor

The Cauchy stress tensor $\boldsymbol{\sigma}$ is obtained by the push-forward $\boldsymbol{\sigma} = J^{-1}\mathbf{F}\mathbf{S}\mathbf{F}^{\mathrm{T}}$ of (4.11). Hence, we obtain the additive decomposition

$$\boldsymbol{\sigma} = \boldsymbol{\sigma}_{\mathrm{vol}} + \boldsymbol{\sigma}_{\mathrm{iso}} + \sum_{\upsilon=1}^{m} \mathbf{q}_{\upsilon}, \tag{4.16}$$

where $\boldsymbol{\sigma}_{\mathrm{vol}} = p^{\star}(J)\mathbf{I}$ is the purely volumetric stress contribution, with $p^{\star}$ defined in $(4.12)_2$. The fourth-order Eulerian projection tensor $\mathbb{P} = \mathbb{I} - (\mathbf{I} \otimes \mathbf{I})/3$ is used to obtain the isochoric (deviatoric) part of the Cauchy stress tensor, i.e.

$$\boldsymbol{\sigma}_{\mathrm{iso}} = \mathbb{P} : \widetilde{\boldsymbol{\sigma}}, \tag{4.17}$$

where $\widetilde{\boldsymbol{\sigma}}$ is the fictitious Cauchy stress tensor. With the orientation $\mathbf{m}$ in the current configurations, according to (4.2), this can then be worked out to

$$\widetilde{\boldsymbol{\sigma}} = nJ^{-1} \int_{\Omega} \rho(\mathbf{M}) \bar{\lambda}^{-1} w'_{\mathrm{iso}}(\bar{\lambda}) \mathbf{m} \otimes \mathbf{m} \, \mathrm{d}\Omega + 2(1-\nu) J^{-1} \overline{\mathbf{F}} \frac{\partial \Psi^{\mathrm{mat}}_{\mathrm{iso}}}{\partial \overline{\mathbf{C}}} \overline{\mathbf{F}}^{\mathrm{T}}. \tag{4.18}$$

The spatial form of $\mathbf{Q}_{\upsilon}$, as used in (4.16), is simply given by $\mathbf{q}_{\upsilon} = J^{-1}\mathbf{F}\mathbf{Q}_{\upsilon}\mathbf{F}^{\mathrm{T}}$.

4.2.3 Elasticity tensor

The linearization of the weak form of the equilibrium equations in finite element programs requires the Eulerian elasticity tensor $\mathbb{c}$ related to the Cauchy stress tensor $\boldsymbol{\sigma}$. The structure of the strain-energy function Ψ in terms of the additive decomposition is also present in the elasticity tensor, i.e. $\mathbb{c} = \mathbb{c}_{\mathrm{vol}} + \mathbb{c}_{\mathrm{iso}} + \sum_{\upsilon} \mathbb{c}_{\mathrm{vis}\,\upsilon}$, where $\mathbb{c}_{\mathrm{vol}} = \tilde{p}\mathbf{I} \otimes \mathbf{I} - 2p^{\star}\mathbb{I}$, with $\tilde{p} = p^{\star} + J\mathrm{d}p^{\star}/\mathrm{d}J$, is the purely volumetric contribution. The purely isochoric contribution is derived as [167]

$$\mathbb{c}_{\mathrm{iso}} = \mathbb{P} : \widetilde{\mathbb{c}} : \mathbb{P} + \frac{2}{3}\mathrm{tr}(\widetilde{\boldsymbol{\sigma}})\mathbb{P} - \frac{2}{3}(\boldsymbol{\sigma}_{\mathrm{iso}} \otimes \mathbf{I} + \mathbf{I} \otimes \boldsymbol{\sigma}_{\mathrm{iso}}), \tag{4.19}$$

with the definition of the fourth-order fictitious elasticity tensor $\widetilde{\mathbb{c}}$ in the spatial description. According to [48, Appendix], in the index notation, we have $(\widetilde{\mathbb{c}})_{abcd} =$

$4J^{-1}\overline{F}_{aA}\overline{F}_{bB}\overline{F}_{cC}\overline{F}_{dD}\,[\partial^2_{\overline{\mathbf{C}}\,\overline{\mathbf{C}}}\Psi_{\mathrm{iso}}(\overline{\mathbf{C}})]_{ABCD}$, where $\overline{F}_{iI}$ are components of the isochoric deformation gradient. With the help of (4.14) it is straightforward to obtain

$$4\frac{\partial^2\Psi_{\mathrm{iso}}(\overline{\mathbf{C}})}{\partial\overline{\mathbf{C}}\partial\overline{\mathbf{C}}} = n\int_\Omega \rho(\mathbf{M})\bar{\lambda}^{-2}[w''_{\mathrm{iso}}(\bar{\lambda}) - \bar{\lambda}^{-1}w'_{\mathrm{iso}}(\bar{\lambda})]\mathbf{M}\otimes\mathbf{M}\otimes\mathbf{M}\otimes\mathbf{M}\,\mathrm{d}\Omega + 4(1-\nu)\frac{\partial^2\Psi^{\mathrm{mat}}_{\mathrm{iso}}(\overline{\mathbf{C}})}{\partial\overline{\mathbf{C}}\partial\overline{\mathbf{C}}}, \tag{4.20}$$

where the short-hand notation $(\bullet)'' = \mathrm{d}(\bullet)'/\mathrm{d}\bar{\lambda}$ has been used. Finally, with the use of (4.2) we may achieve the fictitious elasticity tensor

$$\widetilde{\mathbb{c}} = nJ^{-1}\int_\Omega \rho(\mathbf{M})[w''_{\mathrm{iso}}(\bar{\lambda}) - \bar{\lambda}^{-1}w'_{\mathrm{iso}}(\bar{\lambda})]\bar{\lambda}^{-2}\mathbf{m}\otimes\mathbf{m}\otimes\mathbf{m}\otimes\mathbf{m}\,\mathrm{d}\Omega + \widetilde{\mathbb{c}}^{\mathrm{mat}}_{\mathrm{iso}}, \tag{4.21}$$

where the index notation of the tensor $\widetilde{\mathbb{c}}^{\mathrm{mat}}_{\mathrm{iso}}$ is given by $(\widetilde{\mathbb{c}}^{\mathrm{mat}}_{\mathrm{iso}})_{abcd} = 4J^{-1}(1-\nu)\overline{F}_{aA}\overline{F}_{bB}\overline{F}_{cC}\overline{F}_{dD}\,[\partial^2_{\overline{\mathbf{C}}\,\overline{\mathbf{C}}}\Psi^{\mathrm{mat}}_{\mathrm{iso}}(\overline{\mathbf{C}})]_{ABCD}$. For the explicit expression of the algorithmic elasticity tensor $\mathbb{c}_{\mathrm{vis}\,v}$ in the Eulerian description, the viscous contribution, the reader is referred to [182, 194].

4.3 Analysis of the elastic network material

In the following we assume a purely elastic response ($\mathbf{q}_v = \mathbf{0}$) and recall that we consider an incompressible material. In order to achieve analytical solutions we may not employ the decoupling of the deformation gradient so that the deviatoric projection (4.13), (4.17) becomes obsolete. Hence, the analogue of (4.16)-(4.18), for an elastic contribution, is simply the Cauchy stress tensor

$$\boldsymbol{\sigma} = n\int_\Omega \rho(\mathbf{M})\lambda^{-1}w'(\lambda)\mathbf{m}\otimes\mathbf{m}\,\mathrm{d}\Omega + 2(1-\nu)\mathbf{F}\frac{\partial\Psi_{\mathrm{mat}}}{\partial\mathbf{C}}\mathbf{F}^{\mathrm{T}} - p\mathbf{I}, \tag{4.22}$$

where p is a Lagrange multiplier which can be identified as a hydrostatic pressure. Subsequently, a prime denotes the derivative with respect to the stretch λ, Ψ_{mat} is the energy stored in the matrix material, while w is the energy stored in one fiber.

4.3.1 Application to simple shear

Experiments on networks using rheometers produce torsion which is approximated theoretically by simple shear (see, for example, [37]). For simple shear in the (X_1, X_2) plane the matrix of $\mathbf{F}$ is given by

$$[\mathbf{F}] = \begin{bmatrix} 1 & \gamma & 0 \\ 0 & 1 & 0 \\ 0 & 0 & 1 \end{bmatrix}, \tag{4.23}$$

where γ is the amount of shear. We work in terms of spherical polar angles Θ and Φ and take

$$[\mathbf{M}] = [\sin\Theta\cos\Phi, \sin\Theta\sin\Phi, \cos\Theta]^{\mathrm{T}}, \tag{4.24}$$

where $\Theta \in [0, \pi]$ and $\Phi \in [-\pi, \pi]$. Then the corresponding vector in the deformed configuration has components

$$[\mathbf{m}] = [\mathbf{F}][\mathbf{M}] = \begin{bmatrix} \sin\Theta(\cos\Phi + \gamma\sin\Phi) \\ \sin\Theta\sin\Phi \\ \cos\Theta \end{bmatrix}, \tag{4.25}$$

and hence

$$\lambda^2 = \mathbf{m}\cdot\mathbf{m} = 1 + \sin^2\Theta(\gamma\sin 2\Phi + \gamma^2\sin^2\Phi). \tag{4.26}$$

If the fibers are equally distributed in all directions we consider an isotropic distribution and $\rho = 1$. In this case, from (4.22) we obtain

$$\boldsymbol{\sigma} = n\int_\Omega \frac{w'(\lambda)}{\lambda}\mathbf{m}\otimes\mathbf{m}\sin\Theta\,\mathrm{d}\Theta\,\mathrm{d}\Phi + \boldsymbol{\sigma}_{\mathrm{mat}}, \qquad \boldsymbol{\sigma}_{\mathrm{mat}} = 2(1-\nu)\mathbf{F}\frac{\partial\Psi_{\mathrm{mat}}}{\partial\mathbf{C}}\mathbf{F}^{\mathrm{T}} - p\mathbf{I}, \tag{4.27}$$

where $\boldsymbol{\sigma}_{\mathrm{mat}}$ is the part of the stress due to the matrix.

By using $(4.27)_1$ and (4.25) the components of stress are then given by

$$\sigma_{11} = n\int_\Omega \frac{w'(\lambda)}{\lambda}(\cos\Phi + \gamma\sin\Phi)^2\sin^3\Theta\,\mathrm{d}\Theta\,\mathrm{d}\Phi + \sigma_{\mathrm{mat}\,11}, \tag{4.28}$$

$$\sigma_{22} = n\int_\Omega \frac{w'(\lambda)}{\lambda}\sin^2\Phi\sin^3\Theta\,\mathrm{d}\Theta\,\mathrm{d}\Phi + \sigma_{\mathrm{mat}\,22}, \tag{4.29}$$

$$\sigma_{33} = n\int_\Omega \frac{w'(\lambda)}{\lambda}\cos^2\Theta\sin\Theta\,\mathrm{d}\Theta\,\mathrm{d}\Phi + \sigma_{\mathrm{mat}\,33}, \quad \sigma_{13} = \sigma_{23} = 0, \tag{4.30}$$

$$\sigma_{12} = n\int_\Omega \frac{w'(\lambda)}{\lambda}\sin\Phi(\cos\Phi + \gamma\sin\Phi)\sin^3\Theta\,\mathrm{d}\Theta\,\mathrm{d}\Phi + \sigma_{\mathrm{mat}\,12}. \tag{4.31}$$

We recall that for an isotropic material the universal relation [195, Eq. (4.4.15)]

$$\sigma_{\mathrm{mat}\,11} - \sigma_{\mathrm{mat}\,22} - \gamma\sigma_{\mathrm{mat}\,12} = 0 \tag{4.32}$$

holds. It can then be shown (see Appendix 4.A) that this relation also holds for the total stress used here, i.e.

$$\sigma_{11} - \sigma_{22} - \gamma\sigma_{12} = n\int_\Omega \frac{w'(\lambda)}{\lambda}(\cos 2\Phi + \gamma\sin\Phi\cos\Phi)\sin^3\Theta\,\mathrm{d}\Theta\,\mathrm{d}\Phi = 0. \tag{4.33}$$

In general we take $w'(\lambda) > 0$ for $\lambda > 1$ and $w'(\lambda) = 0$ for $\lambda \le 1$. If λ is less than one then we assume that the filament does not support compression and we, therefore,

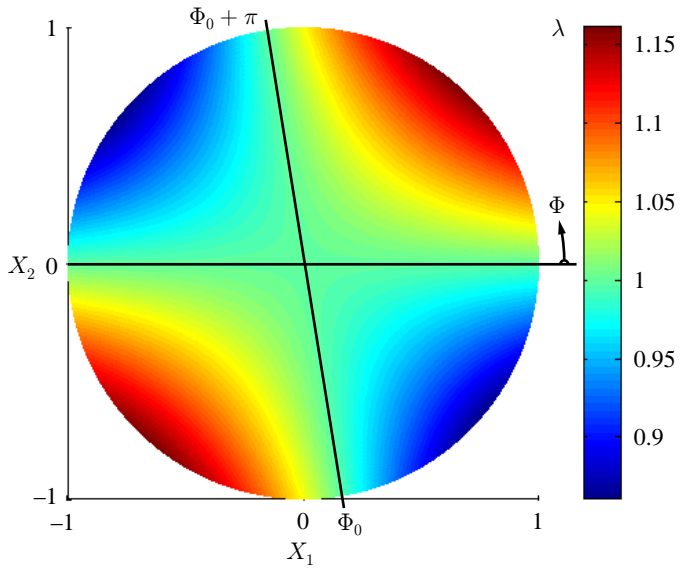

Figure 4.1: Filament stretch λ projected on the reference unit micro-sphere for $\gamma = 0.3$.

exclude any contribution of $w'(\lambda)$ from the integration for the angles for which $w'(\lambda)$ is negative. The critical value Φ_0 for λ to be greater than one can be deduced from (4.26), i.e. $\tan\Phi_0 = -2/\gamma$, provided $\gamma > 0$. The tangent is a periodic function with period π usually defined for $(-\pi/2, \pi/2)$. The interval of Φ, however, is $\Phi \in [-\pi, \pi]$. Therefore, we obtain two solutions for the tangent, particularly (a negative) Φ_0 and (a positive) $\Phi_0 + \pi$. We obtain positive values for λ in two regions within the initial domain of Φ, i.e. $[-\pi, \Phi_0] \cup [0, \Phi_0 + \pi]$. For the second angle, the integration domain is $\Theta \in [0, \pi]$. This can be seen in Fig. 4.1, where a unit sphere with color coded λ is projected into the x_1-x_2-plane. The borders of the integration domain are indicated with black lines. Note that Fig. 4.1 depicts fiber stretches on the reference unit sphere and thus corresponds with the Lagrangian strain ellipsoid [195, Sec. 2.2.5]. In the current configuration the filaments are not only stretched but also rotated. Recall that the relation for the first principal stretch direction for isotropic materials under simple shear in the current configuration is located at $\tan 2\Phi_\mathrm{c} = 2/\gamma$, see [195, Eq. (2.2.59)]. Differently from that, Fig. 4.1 depicts the direction of maximum stretch at

$$\Phi_\mathrm{r} = \frac{\Phi_0 + \pi}{2} \tag{4.34}$$

in the reference configuration.

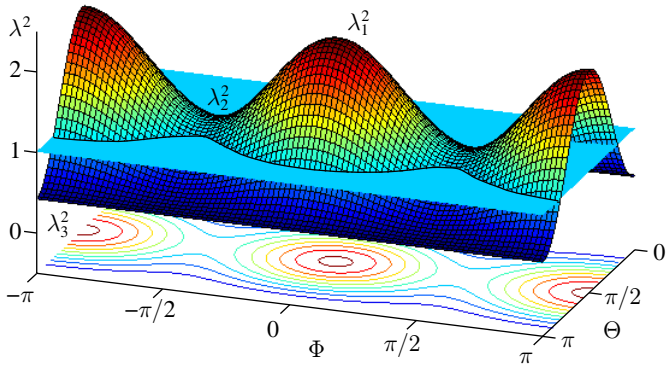

Figure 4.2: Squared stretch λ^2 over the spherical angles Φ and Θ, where $\lambda_1 > \lambda_2 > 1$ and λ_3 are the principal stretches. The relevant integration domain lies above the 1-plane.

4.3.2 Integration limits for arbitrary deformations

We may take a closer look on the integration domain using the spectral decomposition of the right Cauchy-Green tensor $\mathbf{C} = \lambda_a^2 \widehat{\mathbf{N}}_a \otimes \widehat{\mathbf{N}}_a$, where $a = 1, 2, 3$, λ_a are the principal stretches (square root of the eigenvalues of $\mathbf{C}$) and $\widehat{\mathbf{N}}_a$ are the principal referential directions (eigenvectors of $\mathbf{C}$). The values of the principal stretches can be ordered so that $\lambda_1 > \lambda_2 > \lambda_3$. Then, we can find a proper orthogonal tensor $\mathbf{Q}$ which rotates the basis in which we describe the problem so that the first principal stretch λ_1 is oriented in a spherical coordinate system with $\Theta = \pi/2$ and $\Phi = 0$. The second principal stretch λ_2 occurs in $\Theta = \pi/2$ and $\Phi = \pi/2$ and λ_3 is at $\Theta = 0$. We can define the rotated right Cauchy-Green tensor as $\widetilde{\mathbf{C}} = \mathbf{Q}^{\mathrm{T}}\mathbf{C}\mathbf{Q}$ with the matrix representation $[\widetilde{\mathbf{C}}] = \mathrm{diag}[\lambda_1^2, \lambda_2^2, \lambda_3^2]^{\mathrm{T}}$. We rewrite $(4.26)_1$ as $\lambda^2 = \mathbf{M}\cdot\widetilde{\mathbf{C}}\mathbf{M}$ and obtain for incompressible materials, i.e. $\lambda_1\lambda_2\lambda_3 = 1$,

$$\lambda^2 = \lambda_1^2 \sin^2\Theta\cos^2\Phi + \lambda_2^2 \sin^2\Theta \sin^2\Phi + \frac{1}{\lambda_1^2\lambda_2^2}\cos^2\Theta. \tag{4.35}$$

Figure 4.2 illustrates the topology of the squared stretch (similar to Fig. 4.1 in Section 4.3.1) in the Φ-Θ-space for the selected principal stretches $[\lambda_1, \lambda_2, \lambda_3] = [1.5, 1.03, 0.65]$. The integration domain contributing to the Cauchy stress tensor (4.22) is the region, where λ^2 is above the 1-plane.

We can distinguish several cases with different integration area shapes in terms of the principal stretches, as illustrated in Fig. 4.3. Therein, the grey area indicates the relevant integration area in the Θ-Φ-space. The nonspecific deformation of Fig. 4.2 is given in Fig. 4.3(a) together with three basic deformation modes (b)–(d), particularly equibiaxial extension or unconfined compression, simple shear and uniaxial extension. Observe that in the case of simple shear, Fig. 4.3(c), because of the different formulation of the problem we obtain a differently shaped integration domain, as

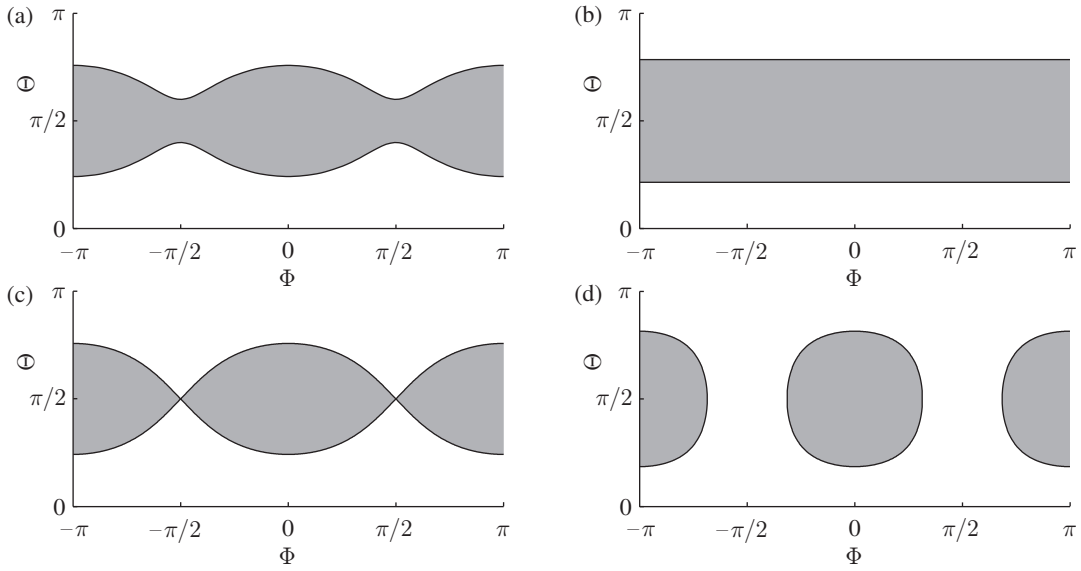

Figure 4.3: The grey shaded areas are the integration domains for different deformation types: (a) $\lambda_1 > \lambda_2 > 1$ ... nonspecific deformation from Fig. 4.2; (b) $\lambda_1 = \lambda_2 > 1$ ... equibiaxial extension or unconfined compression; (c) $\lambda_1 > 1 = \lambda_2$ ... simple shear; (d) $\lambda_2 = \lambda_3 < 1$ ... uniaxial extension.

described in Section 4.3.1, which suggested a rectangular area. For all cases the areas are π-periodic in Φ. This means that when the unit sphere of integration is divided in two hemispheres, λ possesses a rotational symmetry between those hemispheres. This important property may be exploited when applying a numerical scheme for solving the integral in (4.22) in the case of isotropy, as it is done in Section 4.

4.3.3 Specialization of the material model

Consider now an isotropic matrix material for which the strain energy Ψ_{mat} is a function of the invariants I_1 and I_2 of the left Cauchy-Green tensor $\mathbf{b} = \mathbf{F}\mathbf{F}^{\mathrm{T}}$, where $I_1 = \mathrm{tr}\mathbf{b}$ and $I_2 = \mathrm{det}\mathbf{b}\ \mathrm{tr}(\mathbf{b}^{-1})$. The Cauchy stress tensor is then given by

$$\boldsymbol{\sigma}_{\mathrm{mat}} = 2(1-\nu)[\psi_1\mathbf{b} + \psi_2(I_1\mathbf{b} - \mathbf{b}^2)] - p\mathbf{I}, \tag{4.36}$$

where $\psi_i = \partial\Psi_{\mathrm{mat}}/\partial I_i$, $i = 1, 2$. Hence, for simple shear we get $\sigma_{\mathrm{mat}\,22} - \sigma_{\mathrm{mat}\,33} = -2\psi_2\gamma^2(1-\nu)$. Without loss of generality we may take $\sigma_{33} = 0$ because of the incompressibility constraint (p is arbitrary). Then $\sigma_{\mathrm{mat}\,33} = -n\int \lambda^{-1}w'(\lambda)\cos^2\Theta\sin\Theta\,\mathrm{d}\Theta\,\mathrm{d}\Phi$ and (4.29) gives

$$\sigma_{22} = n\int_\Omega \frac{w'(\lambda)}{\lambda}\left(\sin^2\Phi\sin^3\Theta - \cos^2\Theta\sin\Theta\right)\mathrm{d}\Theta\,\mathrm{d}\Phi - 2\psi_2\gamma^2(1-\nu). \tag{4.37}$$

For realistic material models ψ_2 is positive and thus the second term is *negative*. Similarly,

$$\sigma_{12} = n \int_\Omega \frac{w'(\lambda)}{\lambda} \sin\Phi(\cos\Phi + \gamma \sin\Phi) \sin^3\Theta \, \mathrm{d}\Theta \, \mathrm{d}\Phi + 2(1-\nu)(\psi_1 + \psi_2)\gamma, \tag{4.38}$$

wherein the second term is *positive* since $2(\psi_1 + \psi_2)$ equals the shear modulus μ of the matrix when evaluated in the reference configuration.

A specific example of Ψ_{mat} is the Mooney-Rivlin material for which

$$\Psi_{\mathrm{mat}} = c_1(I_1 - 3) + c_2(I_2 - 3), \tag{4.39}$$

where c_1, c_2 are positive material constants. Then, from (4.36), we obtain

$$\sigma_{\mathrm{mat}\,22} = -2c_2\gamma^2(1-\nu) - n \int_\Omega \frac{w'(\lambda)}{\lambda} \cos^2\Theta \sin\Theta \, \mathrm{d}\Theta \, \mathrm{d}\Phi, \quad \sigma_{\mathrm{mat}\,12} = (1-\nu)\mu\gamma, \tag{4.40}$$

with $\mu = 2(c_1 + c_2)$.

In the integrands of (4.28)–(4.31) we need the term w'/λ. When λ is close to one (γ is small) the integrals can be formed explicitly because then we expand a truncated Taylor series with (4.26) and use the approximation $\sqrt{1+x} \sim 1 + x/2$ to obtain

$$\begin{aligned} \lambda^{-1} w'(\lambda) \sim w''(1)[\gamma \sin^2\Theta \sin\Phi \cos\Phi + \frac{1}{2}\gamma^2 \sin^2\Theta \sin^2\Phi - \gamma^2 \sin^4\Theta \sin^2\Phi \cos^2\Phi] \\ + \frac{1}{2} w'''(1) \gamma^2 \sin^4\Theta \sin^2\Phi \cos^2\Phi, \end{aligned} \tag{4.41}$$

which is correct to the second order in γ. By using standard trigonometric integrals with integration limits for small, positive γ ($\Phi_0 = -\pi/2$), then (4.37), in particular, yields

$$\sigma_{22} \sim \underbrace{n w''(1) \left(\frac{4}{15}\gamma + \frac{2\pi}{21}\gamma^2 \right) + n w'''(1) \frac{2\pi}{15}\gamma^2}_{\flat} \underbrace{-2c_2\gamma^2}_{\sharp}(1-\nu). \tag{4.42}$$

where the term $\flat$ is > 0 under our assumptions, and the term $\sharp$ is < 0 with the Mooney-Rivlin material parameter $c_2 > 0$.

For the neo-Hookean material, in particular, $c_2 = 0$ and σ_{22} is then positive. Hence, the network model generates a positive normal stress (which is called a 'negative normal stress' in the biophysics literature [39]). If the sample height would not be constrained then the material would become thinner in the x_2-direction.

4.3.4 Example of w with rigid cross-Links

Let us now take $w(\lambda)$ to correspond to the filament model derived in the Appendix 4.B. Then the total normal and shear stresses are given by

$$\sigma_{22} = n\frac{\pi^2 B_0}{aL}\int_\Omega \frac{1}{\lambda}\left[\left(\frac{a-1}{a-\lambda}\right)^{\beta+1} - 1\right]\left(\sin^2\Phi\sin^3\Theta - \cos^2\Theta\sin\Theta\right)\,\mathrm{d}\Theta\,\mathrm{d}\Phi \\ -2c_2\gamma^2(1-\nu), \tag{4.43}$$

$$\sigma_{12} = n\frac{\pi^2 B_0}{aL}\int_\Omega \frac{1}{\lambda}\left[\left(\frac{a-1}{a-\lambda}\right)^{\beta+1} - 1\right]\sin\Phi(\cos\Phi + \gamma\sin\Phi)\sin^3\Theta\,\mathrm{d}\Theta\,\mathrm{d}\Phi \\ +\mu\gamma(1-\nu), \tag{4.44}$$

where L is the contour length, $a = L/r_0$ and r_0 is the end-to-end distance of a single filament in the unloaded state and λ is given by $(4.26)_2$. The bending stiffness is B_0 which is given as $k_\mathrm{B}TL_\mathrm{p}$, where $k_\mathrm{B} = 1.38\cdot 10^{-23}\,\mathrm{Nm/K}$ is the Boltzmann constant, T is the ambient temperature and L_p is the persistence length. Finally, if required, the component σ_{11} follows from the universal relation (4.33). The properties of the Mooney-Rivlin material are well known and hence we subsequently want to neglect the contribution from the matrix material, i.e. $c_1 = c_2 = 0$.

The used filament model is inextensible, i.e. the filament locks ($f \to \infty$) when $r \to L$. Then locking of the bulk material appears when $\lambda \to a$ for the fibers in the direction of the maximum principal stretch at the critical amount of shear γ_crit. This situation is reached when

$$1 + \gamma_\mathrm{crit}\sin 2\Phi_\mathrm{r} + \gamma_\mathrm{crit}^2\sin^2\Phi_\mathrm{r} = a^2 \tag{4.45}$$

holds, where we used (4.26) with $\Theta = \pi/2$. As an example, we obtain $\gamma_\mathrm{crit} = 0.36$ for $a = 1.2$ by considering that Φ_r is also dependent on γ_crit through Eq. (4.34).

We can relate the material parameters r_0 and n to experimental inputs. In bulk rheology samples are prepared with a defined concentration of actin monomers c_actin and a concentration of actin binding proteins c_ABP. Based on considerations of MacKintosh et al. [56] the scaling of the distance between two cross-links, i.e. r_0, was derived for rigor HMM/actin networks by Tharmann et al. [26] as

$$r_0 \sim L_\mathrm{p}^{1/5}(c_\mathrm{actin}c_\mathrm{ABP})^{-2/5}. \tag{4.46}$$

In particular, if $c_\mathrm{actin} = 9.5\,\mu\mathrm{M}$ ($1\,\mathrm{M} = 1\,\mathrm{mol/l}$) and assuming that L_p is constant (4.46) becomes

$$r_0 = 1.6\,c_\mathrm{ABP}^{-2/5}, \tag{4.47}$$

where we neglect consistency of units and obtain r_0 in μm provided c_ABP is given in μM. The relationship between n and c_actin with a given contour length was derived

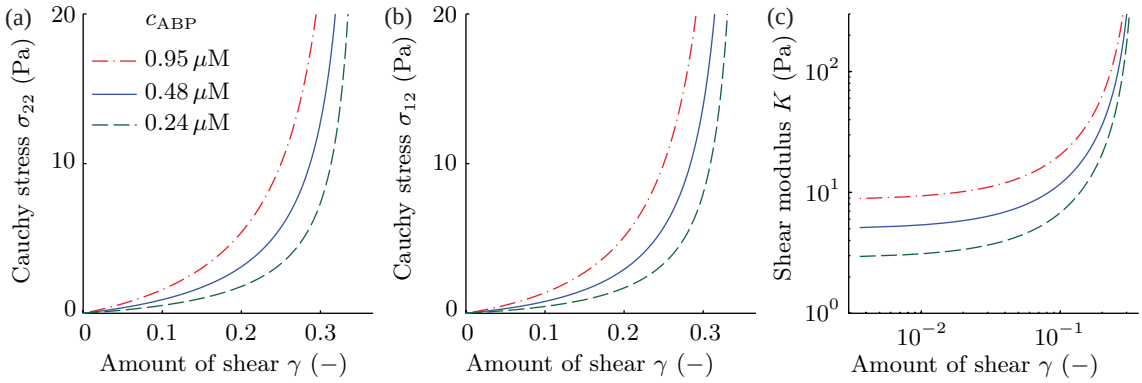

Figure 4.4: Model response for simple shear with varying ABP concentrations $c_{\mathrm{ABP}} = 0.95$, 0.48 and 0.24 μM: (a) Cauchy normal stress σ_{22}; (b) Cauchy shear stress σ_{12}; (c) shear modulus K versus amount of shear γ.

earlier [48, 82] to be

$$n = \frac{c_{\mathrm{A}} N_{\mathrm{A}} M_{\mathrm{A}}}{L \rho_{\mathrm{A}}}, \tag{4.48}$$

where $N_{\mathrm{A}} = 6.022 \cdot 10^{23}\,\mathrm{mol}^{-1}$ is the Avogadro constant, $M_{\mathrm{A}} = 42\,\mathrm{kDa}$ is the molecular mass of each actin monomer and $\rho_{\mathrm{A}} = 16\,\mathrm{MDa}/\mu\mathrm{m}$ is the linear actin density in a filament.

For varying c_{ABP} Fig. 4.4 shows the relationships σ_{22} to γ and σ_{12} to γ without a matrix ($c_1 = c_2 = 0\,\mathrm{Pa}$) and actin concentration $c_{\mathrm{actin}} = 9.5\,\mu\mathrm{M}$ at ambient temperature $T = 294\,\mathrm{K}$. Other typical values are $L_{\mathrm{p}} = 16\,\mu\mathrm{m}$ [35], $\beta = 1$. We assume that the filament is 20% longer than its end-to-end distance, i.e. $a = L/r_0 = 1.2$. The material parameters r_0, L and n are derived from (4.47), the definition of a and (4.48), respectively. Table 4.1 summarizes the used values for three linker concentrations which are 1/10, 1/20 and 1/40 of the actin concentration, i.e. $c_{\mathrm{ABP}} = 0.95$, 0.48 and 0.24 μM. The third plot in Fig. 4.4 shows the instantaneous shear modulus $K = \partial\sigma_{12}/\partial\gamma$ which is a widely used measure for the network stiffness in the biophysics literature.

Up to a reasonable small distance of the amount of shear from the asymptote defined by (4.45), the curves in Fig. 4.4 reproduce the overall behavior of actin gels cross-linked with HMM very well [26, 48]. Characteristic is the very soft initial response and the pronounced nonlinear strain stiffening for both stress components. The shear and normal stress are on the same order of magnitude which was seen earlier [39, 48]. The shear modulus K is relatively constant for small γ and goes towards infinity when approaching the asymptote. This asymptote indicates unphysical behavior of the model for strains $\gamma > 0.25$ and is founded in the choice of an inextensible filament model. The framework (4.22), however, allows to use any extensible filament model,

Table 4.1: Material parameters derived for varying linker densities according to (4.47), $L/r_0 = 1.2$ and (4.48).

$c_{\mathrm{ABP}}(\mu\mathrm{M})$	r_0 (μm)	L (μm)	n ($\mu\mathrm{m}^{-3}$)
0.95	1.63	1.96	7.65
0.48	2.15	2.58	5.82
0.24	2.83	3.40	4.41

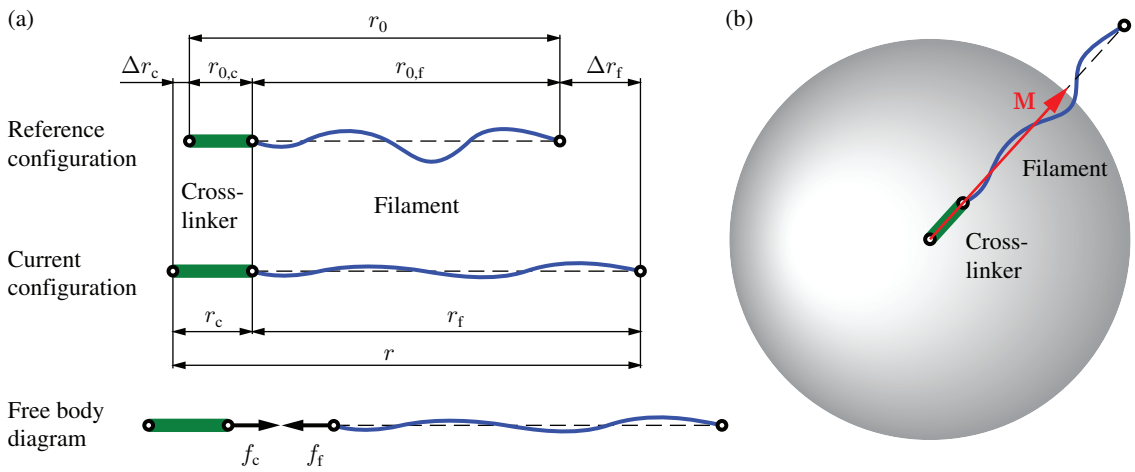

Figure 4.5: Filament with linker: (a) fiber (compound) consisting of a filament (blue, wavy curve) and a linker residue (bold, green line) with end-to-end distances at zero force $r_{0,\mathrm{f}}$ and $r_{0,\mathrm{c}}$, respectively, and their total r_0. The deformed end-to-end distances are r_f and r_c with their total r. The deformation is divided into filament deformation Δr_f and linker deformation Δr_c. The free body diagram illustrates the equilibrium state $f_\mathrm{f} = f_\mathrm{c}$. (b) Fiber compound in the reference configuration oriented in space within a micro-sphere and the reference direction vector $\mathbf{M}$.

e.g., [48, 73] or Appendix 4.C, instead. This would eliminate the point of infinite stiffness at the critical amount of shear γ_{crit} and would lead to a shear modulus at high values of γ comparable to [26].

4.3.5 Example of w with compliant cross-links

Now consider a fiber compound as depicted in Fig 4.5(a). It consists of a thermally fluctuating actin filament and a linker residue. Subsequently, we will omit the word compound and refer only to fibers. We assume that the linker residue can only carry

loads in axial direction. In the reference configuration we apply no force and the components filament and linker residue have the end-to-end distances $r_{0,\mathrm{f}}$ and $r_{0,\mathrm{c}}$, respectively. The total end-to-end distance at zero force adds up to $r_0 = r_{0,\mathrm{f}} + r_{0,\mathrm{c}}$. After deforming the fiber, i.e. in the current configuration, the end-to-end distances change to r_f for the filament and r_c for the linker residue with their sum

$$r = r_\mathrm{f} + r_\mathrm{c} \tag{4.49}$$

Furthermore, we define the stretches of the filament and the linker residue as

$$\lambda_\mathrm{f} = r_\mathrm{f}/r_{0,\mathrm{f}}, \qquad \lambda_\mathrm{c} = r_\mathrm{c}/r_{0,\mathrm{c}}, \tag{4.50}$$

respectively. Note that we do not change the definition of the total stretch and recall

$$r = \lambda r_0. \tag{4.51}$$

Applying this equation to (4.49) and with definitions (4.50), we obtain the relationship between the stretch measures

$$\lambda r_0 = \lambda_\mathrm{f} r_{0,\mathrm{f}} + \lambda_\mathrm{c} r_{0,\mathrm{c}}. \tag{4.52}$$

The total strain energy of the fiber is $w(\lambda) = w_\mathrm{f}(\lambda_\mathrm{f}) + w_\mathrm{c}(\lambda_\mathrm{c})$, which is related to the force acting on the fiber components. We use $(4.59)_1$ to define the force acting on the filament

$$f_\mathrm{f}(\lambda_\mathrm{f}) = \frac{\pi^2 B_0}{L^2}\left[\left(\frac{a-1}{a-\lambda_\mathrm{f}}\right)^{\beta+1} - 1\right], \tag{4.53}$$

where we now consider only the stretch of the filament. Because knowledge about the compliance of cross-linking proteins is limited we want to model nonlinear cross-links which have a proportional stiffness to the actin filaments. Note, however, that the force f_c acting on the linker and on the filament f_f must be equal, i.e. $f = f_\mathrm{c} = f_\mathrm{f}$; see the free body diagram in Fig. 4.5(a). We decompose the total deformation $\Delta r = r - r_0$ of the fiber into the elongation of the filament $\Delta r_\mathrm{f} = r_\mathrm{f} - r_{0,\mathrm{f}}$ and the elongation of the linker residue $\Delta r_\mathrm{c} = r_\mathrm{c} - r_{0,\mathrm{c}}$, so that $\Delta r = \Delta r_\mathrm{f} + \Delta r_\mathrm{c}$. Assume now that the force equilibrium between linker and filament results in the relationship $\Delta r_\mathrm{f} = \eta \Delta r$, where $\eta \in (0, 1]$ is a material parameter which modulates the linker stiffness. The endpoints of the interval denote special cases, where $\eta = 1$ indicates a perfectly rigid linker and $\eta = 0$ means that the linker has no stiffness. We exclude the latter because it is physically meaningless. Using $(4.50)_1$ and (4.51), we obtain

$$\lambda_\mathrm{f} = \eta \frac{r_0}{r_{0,\mathrm{f}}}(\lambda - 1) + 1 \tag{4.54}$$

for the nonlinear linker behavior. The stretch of the linker λ_c may be obtained with (4.52).

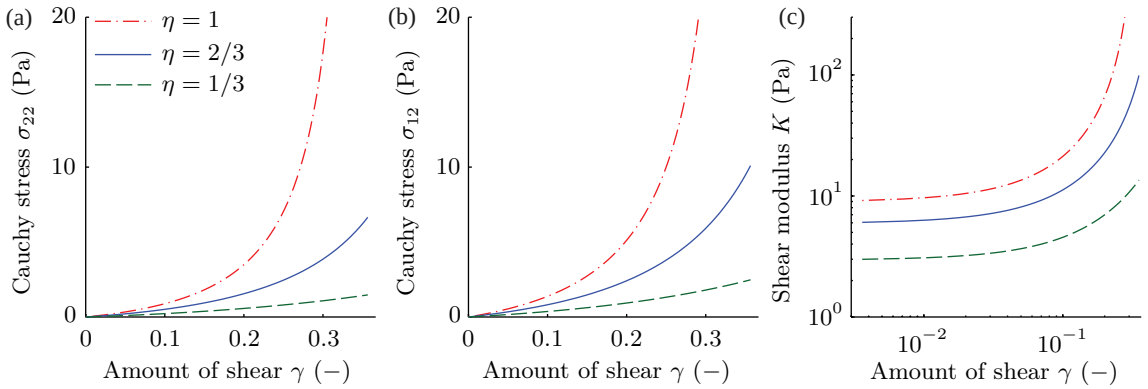

Figure 4.6: Model response for simple shear with constant ABP concentrations and varying nonlinear linker compliance $\eta = 1, 2/3, 1/3$: (a) Cauchy normal stress; (b) Cauchy shear stress; (c) shear modulus versus amount of shear.

Finally we use the considerations above in the network setting as it is illustrated in Fig. 4.5(b). The force f is calculated from (4.53) and the partial derivative of the strain energy with respect to the total stretch is

$$w'(\lambda) = f r_0, \tag{4.55}$$

which can be used in (4.22) to determine the Cauchy stress.

We use the parameter set for $c_{\mathrm{ABP}} = 0.95\,\mu\mathrm{M}$ from Section 4.3.4 and we note that the end-to-end distance at zero force r_0 in the previous section transforms in this section to $r_{0,\mathrm{f}}$. We assume that the linker residue is very short, e.g., $r_{0,\mathrm{c}} = 1\,\mathrm{nm}$. Normal stress, shear stress and shear modulus for varying $\eta = 1$, $2/3$ and $1/3$ are depicted in Fig. 4.6. Indeed, the dash-dotted curves for $\eta = 1$, coincide with the corresponding curves in Fig. 4.4. The characteristics of the curves is similar for all η. The less stiff the linker is compared to the filament, i.e. the smaller η is, the softer is the overall response of the bulk material. The asymptote of the curves shifts to higher amounts of shear as η is decreased. It can be determined by first plugging (4.54) in (4.53). By means of the resulting denominator, i.e. using $[r_{0,\mathrm{f}}(a-1)/(\eta r_0) + 1]^2$ for the right hand side in (4.45) instead of a^2, we calculate γ_{crit}. With the used numbers we obtain $\gamma_{\mathrm{crit}} = 0.53$ and 0.98 for $\eta = 2/3$ and $1/3$, respectively. We want to compare these results of the model with experimental data, specifically for cross-linked actin networks with different types of linker proteins but equal concentrations $c_{\mathrm{actin}} = 9.5\,\mu\mathrm{M}$ and $c_{\mathrm{ABP}} = 0.95\,\mu\mathrm{M}$. The curves for rigid linker in Fig. 4.6 are on the same order as the data presented for actin networks cross-linked with HMM in its rigor form [48]. It was reported for networks with this type of linker that the elastic response is dominated by the entropic stretching of filaments between cross-linked points [26] and thus we expect it to behave very stiff or almost rigid. On the other hand the shear modulus data with filamin as linker [118] are well reflected by the

curve in Fig. 4.6(c) for $\eta = 1/3$. Neglecting other arguments, e.g., interaction of filaments, rotational stiffness of linkers and others, this observation suggests that the stiffness of the linkers is a key property of cross-linked actin networks.

4.4 Numerical treatment and representative example

In the considerations in Section 4.3, we employed an inextensible filament model. The asymptotes arising from this formulation, however, may cause unfavorable conditions within a numerical solution procedure such as the finite element method. In order to increase the reliability of the Newton-Raphson algorithm, we subsequently use the extensible version of the filament model, introduced in Appendix 4.B, which is briefly summarized in Appendix 4.C. The extensibility of the filament is modulated by the additional material parameter μ_0. This version of the model proved to be suitable to fit data from stretching experiments conducted on single actin chains also in the high stretch regime [48].

The integrals over the unit sphere as in (4.14), (4.18), (4.21) or (4.22) are solved using standard numerical procedures, e.g., the adaptive Simpson quadrature, as realized, for example, in `MATLAB`. However, this method is very costly in terms of computation and only viable for a basic analysis, as shown in the previous sections. For solving more complex problems we need a more efficient scheme. An excellent method for the evaluation of integrals over a sphere was suggested by Bažant and Oh [122] with $m = 42$ distinct direction vectors $\mathbf{M}^i$, $i = 1, 2, \ldots, m$. The symmetry of the method together with the symmetry discussed in Section 4.3.2 allows us to use only half of the directions and double the integration weights q^i. The integrals transform then according to

$$\int_\Omega \mathbf{A}(\mathbf{M})\,\mathrm{d}\Omega \sim 4\pi \sum_{i=1}^{m} \mathbf{A}(\mathbf{M}^i) q^i, \tag{4.56}$$

where $\mathbf{A}$ is a tensor-valued function. A table with the direction vectors and the associated integration weights can be found in [122, Table 1].

We implement the proposed model according to the formulation in Section 4.2 in the open source finite element analysis program `FEAP` [196]. In order to avoid volumetric locking, we use an element which is based on a three-field variational principle.

4.4.1 The impact of different linkers and a change in viscosity: micro-pipette aspiration

The strength of a three-dimensional continuum mechanical model is that it can be applied to any mechanical experiment. The proposed model may be calibrated with

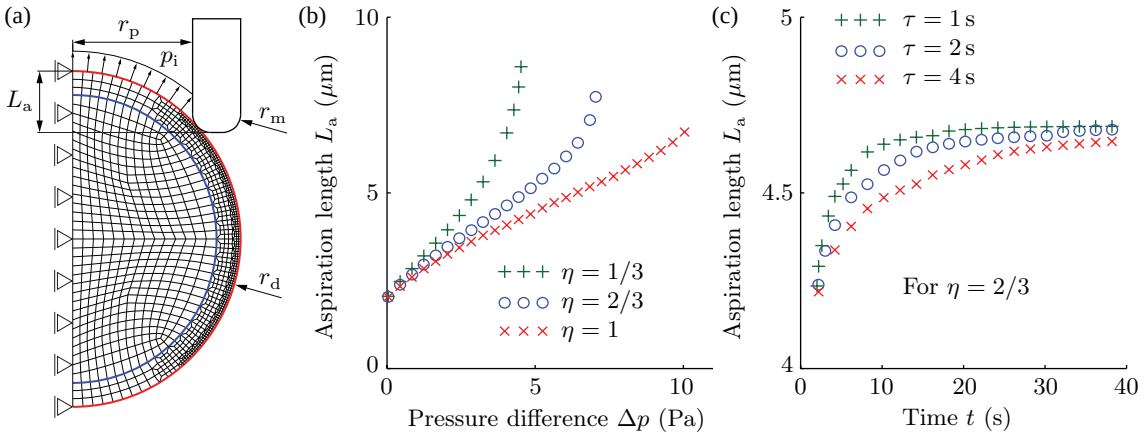

Figure 4.7: Micropipette aspiration of a cross-linked actin droplet: (a) geometry and boundary conditions; (b) aspiration length L_a versus pressure difference Δp for varying cross-linker stiffness $\eta = 1$, 2/3, 1/3; (c) aspiration length L_a versus time t for varying relaxation times $\tau = 4$, 2, 1 s, at $\eta = 2/3$.

data from shear experiments first, before it is used to interpret the outcome of experiments with more complicated conditions in terms of geometry and boundary. In cell mechanics, indentation by atomic force microscopy or micro-pipette aspiration are examples. In the following, we concentrate on the latter.

The setup of the virtual experiment is similar to [120] and inspired by *in vitro* experiments on cells, see, e.g., [52, 179]. A droplet consisting of a cross-linked actin envelope and a very soft inside is aspirated into a pipette, see Fig. 4.7(a). The division of the droplet into two compartments is adopted from [189]. The inside of the droplet is only required to achieve numerical stability during the calculations and does not contribute to the overall mechanical response. The droplet has a radius of $r_d = 7\,\mu$m. The actin envelope is $1\,\mu$m thick with the bold blue semicircle in Fig. 4.7(a) denoting the interface. The droplet is aspirated into a pipette with radius $r_p = 5\,\mu$m of which the mouth is rounded with a radius of $r_m = 0.75\,\mu$m. The pressure difference between the environment and the pipette is realized by applying a tensile follower load p_i on those nodes of the axisymmetric setup, which lie inside the pipette or passed the mound during the experiment. Between the rigid pipette and the surface of the droplet, we employ a frictionless contact condition.

The constitutive relation for the actin envelope is the present model, i.e. an isotropic ($\rho = 1$) cross-linked network of filaments which are extensible. We include compliant linkers exhibiting nonlinear behavior and the viscoelasticity of the material is modeled using one Maxwell element ($m = 1$). We reuse the material parameters from the previous sections and recall: the end-to-end distance $r_{0,f} = 1.63\,\mu$m at zero force of the filament, the end-to-end distance $r_{0,c} = 1\,$nm at zero force of the linker, the

contour length $L = 1.96\,\mu$m, the persistence length $L_\mathrm{p} = 16\,\mu$m, the filament density $n = 7.65\,\mu\mathrm{m}^{-3}$, the temperature $T = 294\,\mathrm{K}$ and $\beta = 1$. The extensibility of the filaments is defined through $\mu_0 = 38.6\,\mathrm{nN}$. The parameter values for the Maxwell element, the free-energy parameter $\theta = 0.835$ and the relaxation time $\tau = 2\,\mathrm{s}$ are adopted from [48]. The penalty method for incompressibility requires the penalty parameter κ, see $(4.10)_1$. In preliminary studies we obtained values for κ which are large enough to ensure incompressibility (the result of the computations converges to a value by increasing κ) and small enough to allow stable computations. The core material is a compressible neo-Hookean material with Young's modulus 10 Pa and Poisson's ratio 0.4 [189].

In a first experiment the pipette fully aspirates the droplet very slowly, i.e. in a quasi-static manner for varying cross-linker compliances $\eta = 1,\ 2/3,\ 1/3$. In Fig. 4.7(b), we plot the aspiration length L_a as a function of the pressure difference Δp between the environment and the inside of the pipette, i.e. $\Delta p = p_\mathrm{i}$. Note that for a droplet, L_a is larger than zero in the reference configuration because of its curvature. In our example, the value of L_a at the start of the experiment is $2\,\mu$m. The data points in Fig. 4.7(b) are characterized by a linear part at low pressure differences, as it was observed experimentally [52, 179]. The linear part is followed by an instability as predicted earlier [54], where a small increase in pressure causes a large increase in aspiration length. When the droplet is almost fully aspirated, the tangent to the data points becomes vertical. This means, that the deformation in one time step is large and, eventually, the Newton-Raphson algorithm fails to converge. This happens at decreasing pressures for decreasing values of η, i.e. 10, 7 and 4.5 Pa for $\eta = 1,\ 2/3$ and $1/3$, respectively. This means that the lower the stiffness of the droplet is, the smaller is the required pressure difference to fully aspirate it. Furthermore, during the whole process of aspiration, decreasing stiffness of the network material cause a higher aspiration length at a specified pressure difference.

The second experiment shows the influence of the material's viscosity, where we aspirate the droplet only partly and let it creep further inside the pipette. We increase the pressure difference to 4 Pa within 2 s and hold it constant for another 38 s. Fig. 4.7(c) shows the aspiration length L_a versus time t. We hold the linker compliance $\eta = 2/3$ constant and vary $\tau = 4,\ 2$ and 1 s. The courses of the data points for all relaxation times resemble typical creep curves in aspiration tests of cells [52, 179]. At the time after which the full pressure is applied, i.e. $t = 2\,\mathrm{s}$, all three samples show an aspiration length of about $L_\mathrm{a} = 4.2\,\mu$m. Thereafter, the droplets creep further inside the pipette at different speeds, depending on the relaxation time τ. Specifically, a shorter relaxation time lets the droplet creep faster. All samples tend toward a steady state value of $\sim 4.7\,\mu$m.

4.5 Summary and concluding remarks

In the present work we propose a general affine and incompressible network model which considers arbitrarily distributed filaments and the influence of a ground substance, the isotropic matrix. We derive the Cauchy stress tensor, apply it to simple shear and show that, neglecting the ground substance, the model correctly reproduces the normal stress response of isotropically cross-linked actin networks under rheological experiments [39]. For rigid linkers, we can estimate material parameters from scaling arguments and obtain a stress-strain behavior comparable to experimental results of actin-HMM networks. The stiffness can be lowered by means of nonlinear compliant linkers which reflects the softer response of actin-filamin networks with the same protein concentrations as actin-HMM networks. In an isotropic network, we observe symmetry in the filament stretch which simplifies the numerical treatment of the integrals over the unit sphere. For the finite element implementation we enforce incompressibility using a penalty function in a compressible formulation of the equations. Furthermore, the elasticity tensor is given and viscoelasticity may be added in a modular way. We demonstrate that virtual experiments resembling micro-pipette aspiration are similar to the results obtained from cell experiments.

Within the present study we employ a number of assumptions which may lead to limitations to the model. We want to briefly review these assumptions and discuss their justifications and possible consequences. The network model, introduced in Section 4.2 and specified in Section 4.3 is based on five basic simplifications: (i) the filaments deform in an affine manner; (ii) they possess a constant junction-to-junction distance and (iii) have equal length with equal material properties; (iv) filaments can only bear tensile loads and are ineffective under compression; (v) there are no interactions between any two filaments which are connected through a cross-link. The first assumption is justified for densely cross-linked networks [41], i.e. relatively high actin and linker concentrations which are the scope of our analysis. The second and third simplifications are acceptable if the number of filaments involved in an experiment is large enough so that we may use their average behavior. The sample volumes in bulk rheology make us confident that these assumptions are legitimate. Actin filaments are very thin compared to their length. Compressive forces will be barely noticeable and thus the fourth assumption is justified. This assumption is also required to ensure convexity of the strain-energy function and thus numerical stability. We adopted the last assumption because little is known about the interaction between two individual filaments connected by a linker protein.

In Section 4.3 we use additional simplifications to make the considerations more accessible. The proposed model, however, is not limited to these. Isotropy is shown to be present in reconstituted networks in rheology [26]. In cells, however, this will not be the case. Future work may include the determination of the angular

density $\rho(\mathbf{M})$ from tomographic data of living cells. The inextensible filament model limits the analysis to moderate levels of shear strain. The locking of the model may be fixed using an extensible model as it is done in the numerical analysis in Section 4.4. The analytical considerations are conducted assuming a fully elastic response while cross-linked actin networks clearly exhibit also viscous properties. The analysis, however, may also be enhanced with parallel Maxwell elements to capture viscoelasticity. Eventually, we assume that the linker proteins may only bear axial loads. This is an enhancement of the negligence of interactions between neighboring filaments and the same reasoning as above applies.

In conclusion, we are able to conduct studies varying only one parameter at a time very easily. Hence, the possibilities of experimentalists are extended and the impact of phenomena known in cell mechanics may be studied in more detail using this model.

4.A Appendix: Universal relation

For fixed values of Θ and γ we obtain from $(4.26)_2$

$$\lambda \mathrm{d}\lambda = \gamma \sin^2\Theta(\cos 2\Phi + \gamma \sin\Phi\cos\Phi)\mathrm{d}\Phi. \tag{4.57}$$

If we change the variables Φ to λ in eq. $(4.33)_2$ then we obtain

$$n \int_{\Theta} \sin\Theta \int_{\lambda} w'(\lambda)\,\mathrm{d}\lambda\,\mathrm{d}\Theta. \tag{4.58}$$

The relevant ranges of values of Θ and Φ are $0 \to \pi$ and $0 \to \Phi_0$, respectively. But if we regard λ as a function of Θ and Φ and write $\lambda(\Theta,\Phi)$ then $\lambda(\Theta,0) = \lambda(\Theta,\Phi_0) = 1$ and the λ-integral in (4.58) vanishes. Thus, the universal relation (4.33) holds.

4.B Appendix: Inextensible filament model

The filament model according to [48, 73, 74] is given as

$$f^\star = f\frac{L^2}{\pi^2 B_0} = \left(\frac{1-r_0/L}{1-r/L}\right)^{\beta+1} - 1, \qquad \frac{r_0}{L} = 1 - \frac{L}{\pi^2 L_\mathrm{p}}, \tag{4.59}$$

where f is the force in the filament, $f^\star$ is a dimensionless force, L_p is the persistence length, L is the contour length and β is a non-negative constant. By setting $a = L/r_0$ and $\lambda = r/r_0$, then from $(4.59)_1$

$$f^\star = \left(\frac{a-1}{a-\lambda}\right)^{\beta+1} - 1. \tag{4.60}$$

In terms of the energy function we write

$$w^\star(\lambda) = \frac{L^2}{\pi^2 r_0 B_0} w(\lambda) \tag{4.61}$$

and obtain

$$f^\star = \frac{\mathrm{d}w^\star}{\mathrm{d}\lambda}, \qquad w^\star(\lambda) = \frac{(a-1)^{\beta+1}}{(a-\lambda)^\beta}\frac{1}{\beta} - \lambda + 1 - \frac{a-1}{\beta}, \tag{4.62}$$

so that

$$w^\star(1) = 0, \qquad w^{\star\prime}(\lambda) = \frac{\mathrm{d}w^\star}{\mathrm{d}\lambda} = \left(\frac{a-1}{a-\lambda}\right)^{\beta+1} - 1, \qquad w^{\star\prime}(1) = 0. \tag{4.63}$$

It is then easy to show that $4w^{\star\prime\prime}(1) + w^{\star\prime\prime\prime}(1) > 0$, and hence the term $\flat$ in the expression (4.42) is positive.

4.C Appendix: Extensible filament model

The extensible version of filament model (4.59) is given in [48, 73, 74]. We introduce the stretch modulus μ_0, define the shorthand notation $\alpha = \pi^2 B_0/(\mu_0 L^2)$ and recall the relationship between stretch and dimensionless force

$$\frac{\lambda_\mathrm{f} r_{0,\mathrm{f}}}{L} = 1 + \alpha f^\star - \frac{(1+2\alpha f^\star)(1+\alpha f^\star)^\delta}{(1+f^\star+\alpha f^{\star 2})^\delta}(1 - r_{0,\mathrm{f}}/L), \tag{4.64}$$

where $\delta = (\beta+1)^{-1}$. The first and second partial derivatives of the strain energy $w(\lambda_\mathrm{f})$ with respect to the actin stretch λ_f are then

$$\begin{aligned} w' &= r_0 f, \\ w'' &= \frac{r_0^2 \mu_0 / L}{1 + \left(\dfrac{\delta}{\alpha}\dfrac{(1+2\alpha f^\star)^2}{1+f^\star+\alpha f^{\star 2}} - \delta\dfrac{1+2\alpha f^\star}{1+\alpha f^\star} - 2\right)\left(\dfrac{1+\alpha f^\star}{1+f^\star+\alpha f^{\star 2}}\right)^\delta \left(1 - \dfrac{r_{0,\mathrm{f}}}{L}\right)}. \end{aligned} \tag{4.65}$$

5 TORSION OF A CIRCULAR CYLINDER VERSUS SIMPLE SHEAR AS A MODELING BASIS FOR RHEOMETER EXPERIMENTS: APPLICATION TO RUBBER AND ACTIN NETWORKS

Abstract Experiments on cross-linked actin networks conducted with a rheometer and parallel-plate geometry resemble torsion of a circular cylinder undergoing large deformation. A common approximation for the analysis of such experiments is simple shear. We compare the solutions of five material models for the torsion of a cylinder with simple shear. We introduce the problem by means of rubber elasticity and show that the approximation for materials with linear shear elasticity may be reasonable. In the case of cross-linked actin networks, however, the strong strain-stiffening behavior causes higher deviations of simple shear from the more realistic torsion boundary conditions. Furthermore, we show that the eight-chain model cannot account for the correct normal stress behavior of cross-linked actin networks. An affine network model reproduces the correct sign for the normal stress for both versions of the boundary conditions. The two solutions, however, differ drastically so that an approximation of the deformation mode in a parallel-plate rheometer by simple shear is questionable.

5.1 Introduction

Rotational rheology with a parallel-plate geometry is the state-of-the-art experimental method for the mechanical characterization of cross-linked actin networks. The deformation of the samples in such experiments resembles the torsion of a cylinder. In several previous studies, however, simple shear was used as an approximation for the real situation in parallel-plate rheometry, see, e.g., [37, 48, 82].

During experiments with a parallel-plate rheometer and plate radius R the axial force $\widetilde{N}$ and the applied torsion couple $\widetilde{M}_\mathrm{t}$ are recorded and transformed into a normal stress component $\widetilde{\sigma}$ and a shear stress component $\widetilde{\tau}$, respectively. Thus [197],

$$\widetilde{\sigma} = \frac{\widetilde{N}}{\pi R^2}, \qquad \widetilde{\tau} = \frac{2\widetilde{M}_\mathrm{t}}{\pi R^3}, \tag{5.1}$$

where the superimposed tilde is used to identify the values obtained from experimental tests.

The problem of the torsion of a cylinder undergoing large deformations in the context of rubber elasticity was solved in the seminal paper series on 'large elastic deformations of isotropic materials' by Rivlin, see, e.g., [198]. Torsion couple and axial force for the well known neo-Hookean model and the Mooney-Rivlin model are also established in several text books, see, e.g., [197]. Refined models for rubber, for example the Yeoh model [199], may account for material nonlinearities of rubber.

In the case of cross-linked actin networks we distinguish two modeling approaches. First, discrete models [101, 146, 148–150] are excellent to investigate the mechanics of a network on the filament scale. They are, however, expensive in terms of computational cost and, therefore, in general, only simple shear of a representative volume is considered. The second modeling approach aims for microstructurally motivated continuum models [37, 48, 82, 115]. This approach models the properties of a single actin filament first to obtain a force-stretch relationship. Based on that, a network model is employed subsequently to homogenize the discrete microstructure. In our study the parameters of the resulting continuum mechanical constitutive model are interpretable as the properties of the single filaments and the network topology.

In the present study, we show that simple shear may be used for certain materials to investigate the shear stress response. Furthermore, we show that using an affine network model for modeling cross-linked actin networks, we obtain a positive normal stress (also in the simple shear case) which is in accordance with [39]. On the other hand, the eight-chain model lacks this important property. Subsequently, we distinguish three types of notation: (i) the tilde ($\widetilde{\bullet}$) indicates rheological experiments with its measures as in (5.1), (ii) the hat ($\widehat{\bullet}$) characterizes values which are related to simple shear, while (iii) no specific symbol refers to the torsion of a cylinder.

Section 5.2 establishes the governing equations for the torsion of a cylinder and provides solutions for three constitutive models mainly used for rubber. Subsequently, in Section 5.3, we compare the torsion of these models with simple shear and define associated error measures. In Section 5.4 we focus on models for cross-linked actin networks. Specifically, we investigate an eight-chain model and an affine constitutive model for cross-linked F-actin networks. In the final Section 5.5 we provide a discussion and conclude the study.

5.2 Analytical solution of the torsion of a cylinder

In this section we provide the necessary kinematics required for the analysis of the torsion of a cylinder at finite strains. We introduce the most general form of a stress relation in terms of the strain invariants in the Eulerian description and show its relationships to the torsion couple and the axial force. Subsequently, we specialize the material model and present solutions for some isotropic constitutive models.

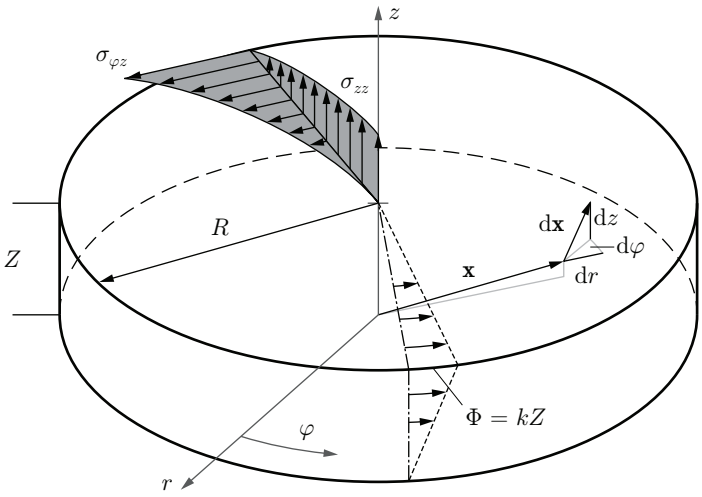

Figure 5.1: Cylinder under torsion (dimensions R and Z) and an cylindrical coordinate system (r, φ, z). The components of the tangent vector $\mathrm{d}\mathbf{x}$ associated with $\mathbf{x}$ are $\mathrm{d}r$, $\mathrm{d}\varphi$ and $\mathrm{d}z$. The dash-dotted lines on the cylinder in the reference configuration deform to the dotted lines in the current configuration. The angle of rotation is $\Phi = kZ$, defined through the intensity of torsion k. The gray areas schematically represent the distributions of shear stress $\sigma_{\varphi z}$ and normal stress σ_{zz} over the radius r.

5.2.1 Required nonlinear continuum mechanics

Consider an incompressible circular cylinder with radius R and height Z in cylindrical polar coordinates (r, φ, z), as depicted in Fig. 5.1. A point in the reference and the current configuration is characterized by the position vectors $\mathbf{X}$ and $\mathbf{x}$, respectively. The index zero is employed to note the coordinates in the reference configuration, i.e. (r_0, φ_0, z_0). Hence, we describe the deformation through

$$r = r_0, \qquad \varphi = \varphi_0 + kz_0, \qquad z = z_0, \tag{5.2}$$

where the intensity of torsion is k, with the unit m^{-1}. The angle Φ by which the top surface is rotated with respect to the bottom surface is $\Phi = kZ$. Let us now introduce a material tangent vector $\mathrm{d}\mathbf{X}$ to a material curve and a spatial tangent vector $\mathrm{d}\mathbf{x}$ to a spatial curve so that their matrix representations read

$$[\mathrm{d}\mathbf{X}] = \begin{bmatrix} \mathrm{d}r_0 \\ r_0\,\mathrm{d}\varphi_0 \\ \mathrm{d}z_0 \end{bmatrix}, \qquad [\mathrm{d}\mathbf{x}] = \begin{bmatrix} \mathrm{d}r \\ r\,\mathrm{d}\varphi \\ \mathrm{d}z \end{bmatrix}. \tag{5.3}$$

With (5.2), the deformation gradient $\mathbf{F}$ in matrix representation is then

$$[\mathbf{F}] = \begin{bmatrix} 1 & 0 & 0 \\ 0 & 1 & kr \\ 0 & 0 & 1 \end{bmatrix}, \tag{5.4}$$

where $\mathrm{d}\mathbf{x} = \mathbf{F}\,\mathrm{d}\mathbf{X}$. The first invariant $I_1 = \mathrm{tr}\mathbf{C}$ of the right Cauchy-Green tensor $\mathbf{C} = \mathbf{F}^\top\mathbf{F}$ is

$$I_1 = k^2r^2 + 3. \tag{5.5}$$

Note that $J = \det\mathbf{F} = 1$ characterizes a volume-preserving deformation.

Assume now that the constitutive relation of the material can be expressed by the strain-energy function $\Psi(\mathbf{C})$ in terms of the right Cauchy-Green tensor. This assumption ensures that rigid body motions do not affect the energy stored in the material. Therefore, the stress tensor is also independent of rigid body motions. The Cauchy stress tensor is then given as

$$\boldsymbol{\sigma} = \overline{\boldsymbol{\sigma}} - p\mathbf{I}, \tag{5.6}$$

where $\overline{\boldsymbol{\sigma}} = 2\mathbf{F}(\partial\Psi/\partial\mathbf{C})\mathbf{F}^\top$ and p is the Lagrange multiplier associated with the incompressibility constraint which can be interpreted as a hydrostatic pressure. Assuming a static problem and neglecting body forces, the equation of motion simplifies to

$$\mathrm{div}\boldsymbol{\sigma} = \mathbf{0}. \tag{5.7}$$

The key component in (5.7) is the equilibrium in the radial direction, i.e.

$$\frac{\mathrm{d}\sigma_{rr}}{\mathrm{d}r} + \frac{1}{r}(\sigma_{rr} - \sigma_{\varphi\varphi}) = 0, \tag{5.8}$$

while the equations for the circumferential and the axial directions lead to the conclusion that p does not change through the sample thickness or in the circumferential direction, but only in the radial direction. By using (5.6) in (5.8), we obtain

$$\frac{\mathrm{d}p}{\mathrm{d}r} = \frac{\mathrm{d}\overline{\sigma}_{rr}}{\mathrm{d}r} + \frac{1}{r}(\overline{\sigma}_{rr} - \overline{\sigma}_{\varphi\varphi}). \tag{5.9}$$

The radial normal stress on the side surface of the cylinder must vanish, leading to the boundary condition $\sigma_{rr}|_{r=R} = 0$. Then, the integration of (5.9) gives

$$p = \overline{\sigma}_{rr} + \int_R^r (\overline{\sigma}_{rr} - \overline{\sigma}_{\varphi\varphi})\frac{\mathrm{d}r^\star}{r^\star} \tag{5.10}$$

for the hydrostatic pressure. This equation combines the equilibrium equations with the boundary conditions, and hence all components of (5.6) are determined.

When conducting an experiment, see Fig. 5.1, we rotate the top plate with respect to the bottom one by an angle Φ while holding the distance Z between the plates constant. Simultaneously we measure the torsion couple M_t applied to the sample and the required axial force N to keep the distance between the plates constant. The axial force N is simply given by

$$N = \int_A \sigma_{zz}\,\mathrm{d}A, \tag{5.11}$$

where A is the top surface of the cylinder. The torsion couple M_t is obtained by integration of the shear stress, which is force per deformed area, multiplied by the lever r, i.e.

$$M_\mathrm{t} = \int_A r\sigma_{\varphi z}\,\mathrm{d}A. \tag{5.12}$$

Note that for the cylinder $\mathrm{d}A = r\,\mathrm{d}r\,\mathrm{d}\varphi$, with $\varphi \in [0, 2\pi]$ and $r \in [0, R]$.

5.2.2 Specialization of the material model

Assume now an isotropic material from which we can express the strain-energy function $\Psi(I_1, I_2)$ in terms of the first and second invariants (I_1, I_2) of the left Cauchy-Green tensor $\mathbf{b} = \mathbf{F}\mathbf{F}^\top$. The third invariant $I_3 = J^2 = 1$ constitutes the kinematic constraint of incompressibility. Note that these invariants are identical to those of the right Cauchy-Green tensor $\mathbf{C}$. Then, the first term in (5.6) is [112]

$$\overline{\boldsymbol{\sigma}} = 2\psi_1\mathbf{b} - 2\psi_2\mathbf{b}^{-1}, \tag{5.13}$$

where $\psi_i = \partial\Psi/\partial I_i$, $i = 1, 2$. With (5.4), we obtain the matrix representation of the left Cauchy-Green tensor $\mathbf{b}$ and its inverse $\mathbf{b}^{-1}$, i.e.

$$[\mathbf{b}] = \begin{bmatrix} 1 & 0 & 0 \\ 0 & 1+k^2r^2 & kr \\ 0 & kr & 1 \end{bmatrix}, \qquad [\mathbf{b}^{-1}] = \begin{bmatrix} 1 & 0 & 0 \\ 0 & 1 & -kr \\ 0 & -kr & 1+k^2r^2 \end{bmatrix}, \tag{5.14}$$

respectively. Using the components $\overline{\sigma}_{rr}$ and $\overline{\sigma}_{\varphi\varphi}$ of (5.13) in (5.10), the Cauchy stress components are then given according to (5.6) in the closed forms

$$\sigma_{rr}(r) = 2k^2\int_R^r \psi_1 r^\star\,\mathrm{d}r^\star, \qquad \sigma_{\varphi\varphi}(r) = 2\psi_1 k^2r^2 + 2k^2\int_R^r \psi_1 r^\star\,\mathrm{d}r^\star, \tag{5.15}$$

$$\sigma_{zz}(r) = -2\psi_2 k^2r^2 + 2k^2\int_R^r \psi_1 r^\star\,\mathrm{d}r^\star, \quad \sigma_{\varphi z}(r) = 2kr(\psi_1+\psi_2). \tag{5.16}$$

The axial force N and the torsion couple M_t are calculated according to (5.11) and (5.12). Thus, with (5.16) we obtain the explicit expressions in terms of ψ_1 and ψ_2, i.e.

$$N = 4\pi k^2\int_0^R \left(-\psi_2 r^2 + \int_R^r \psi_1 r^\star\,\mathrm{d}r^\star\right) r\,\mathrm{d}r, \qquad M_\mathrm{t} = 4\pi k\int_0^R (\psi_1+\psi_2) r^3\,\mathrm{d}r. \tag{5.17}$$

5.2.3 Solutions for some isotropic constitutive rubber models

For subsequent analyses consider now three different material models. The Mooney-Rivlin model and its specialization, i.e. the neo-Hookean model, are very frequently used models in rubber elasticity. Thereby, the shear modulus is constant. Finally, we use the Yeoh model as a representative model for a variable shear modulus.

The strain-energy function of the Mooney-Rivlin material is

$$\Psi^{\mathrm{MR}} = c_1(I_1 - 3) + c_2(I_2 - 3), \tag{5.18}$$

where c_1 and c_2 are positive material constants. Hence, eqs. $(5.16)_1$ and $(5.17)_2$ simplify to

$$\sigma_{zz}^{\mathrm{MR}} = -c_1 k^2 \left(R^2 - r^2\right) - 2c_2 k^2 r^2, \qquad N^{\mathrm{MR}} = -\pi k^2 R^4 \left(\frac{c_1}{2} + c_2\right). \tag{5.19}$$

For convenience, we introduce now the shear modulus μ according to

$$\mu = 2(c_1 + c_2), \tag{5.20}$$

where we require $c_1 + c_2 > 0$ in order to achieve a physically correct behavior. Hence, for a neo-Hookean material model of the form

$$\Psi^{\mathrm{NH}} = \frac{\mu}{2}(I_1 - 3), \tag{5.21}$$

with $c_2 = 0$ in (5.20), (5.19) become

$$\sigma_{zz}^{\mathrm{NH}} = -\frac{1}{2}\mu k^2 \left(R^2 - r^2\right), \qquad N^{\mathrm{NH}} = -\frac{\pi}{4}\mu k^2 R^4. \tag{5.22}$$

These results can also be found in the literature, see, e.g., the textbook of Macosko [197] or the extensive work of Rivlin [46, 200–202], with different approaches for the derivation. The negative sign of the axial force was confirmed experimentally by Rivlin and Saunders [46], following experiments on wires performed by Poynting [45].

By evaluating $(5.16)_2$ and $(5.17)_2$, the shear stress and the torsion couple are given by

$$\sigma_{\varphi z}^{\mathrm{MR}} = \sigma_{\varphi z}^{\mathrm{NH}} = \mu k r, \qquad M_{\mathrm{t}}^{\mathrm{MR}} = M_{\mathrm{t}}^{\mathrm{NH}} = \pi \mu k R^4/2, \tag{5.23}$$

respectively. These expressions hold for both material models, where μ is defined in (5.20). Note the high sensitivity of the torsion couple in $(5.23)_2$ to changes in the radius R.

Figure 5.2 shows the Cauchy shear stress $\sigma_{\varphi z}$ and the normal stress σ_{zz} as a function of the radius r for the neo-Hookean and the Mooney-Rivlin model. The radius of

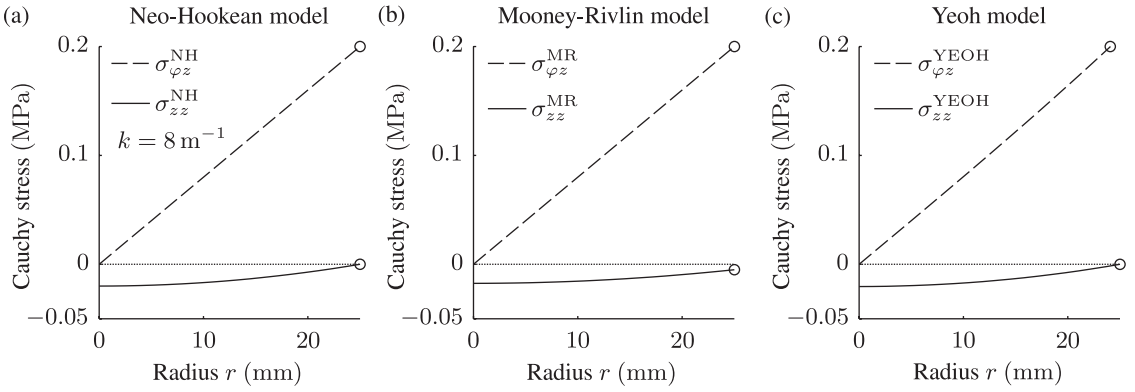

Figure 5.2: Cauchy shear stress $\sigma_{\varphi z}^{\mathrm{NH}}$, $\sigma_{\varphi z}^{\mathrm{MR}}$, $\sigma_{\varphi z}^{\mathrm{YEOH}}$ and normal stress $\sigma_{zz}^{\mathrm{NH}}$, $\sigma_{zz}^{\mathrm{MR}}$, $\sigma_{zz}^{\mathrm{YEOH}}$ versus the radius r at the intensity of torsion $k = 8\,\mathrm{m}^{-1}$ for the neo-Hookean model (a), the Mooney-Rivlin model (b) and the Yeoh model (c). The stress values at the outer radius R, marked by circles, correspond to the simple shear solution characterized by the amount of shear $\gamma = kR = 0.2$ (compare with Section 5.3). Note that the Mooney-Rivlin model predicts a non-zero normal stress at the outer radius.

the cylinder is $R = 25\,\mathrm{mm}$ and the intensity of torsion is $k = 8\,\mathrm{m}^{-1}$. Both material models possess a shear modulus of $\mu = 1\,\mathrm{MPa}$ while the Mooney-Rivlin model uses the additional relation $c_1 = 7c_2$ [46]. The relationship of the shear stress $\sigma_{\varphi z}$ and the radius r is linear, see $(5.23)_1$, and both models provide the same result. The normal stress $\sigma_{zz}^{\mathrm{NH}}$ for the neo-Hookean material, see Fig. 5.2(a), is compressive (denoted by a negative sign) with the largest magnitude at the center of the disc. It vanishes at the outer surface in contrast to the normal stress $\sigma_{zz}^{\mathrm{MR}}$ for the Mooney-Rivlin model, see Fig. 5.2(b), which shows a finite compressive stress at the outer surface.

The Yeoh model [199] is an example for a constitutive equation with a variable shear stiffness and it is given by

$$\Psi^{\mathrm{YEOH}} = d_1(I_1 - 3) + d_2(I_1 - 3)^2 + d_3(I_1 - 3)^3, \tag{5.24}$$

with the three material constants $d_1 > 0$, $d_2 < 0$, $d_3 > 0$. With this model the equations $(5.16)_1$ and $(5.17)_1$ give the normal stress $\sigma_{zz}^{\mathrm{YEOH}}$ and the axial force N^{YEOH} according to

$$\sigma_{zz}^{\mathrm{YEOH}} = -d_1k^2(R^2 - r^2) - d_2k^4(R^4 - r^4) - d_3k^6(R^6 - r^6), \tag{5.25}$$

$$N^{\mathrm{YEOH}} = -\frac{\pi}{2}d_1k^2R^4 - \frac{2\pi}{3}d_2k^4R^6 - \frac{3\pi}{4}d_3k^6R^8. \tag{5.26}$$

The shear stress $\sigma_{\varphi z}^{\mathrm{YEOH}}$ and the torsion couple $M_{\mathrm{t}}^{\mathrm{YEOH}}$ are calculated from $(5.16)_2$

and $(5.17)_2$, i.e.

$$\sigma_{\varphi z}^{\mathrm{YEOH}} = 2kr(d_1 + 2d_2k^2r^2 + 3d_3k^4r^4), \tag{5.27}$$

$$M_{\mathrm{t}}^{\mathrm{YEOH}} = \pi kR^4\left(d_1 + \frac{4}{3}d_2k^2R^2 + \frac{3}{2}d_3k^4R^4\right). \tag{5.28}$$

The relationships between the Cauchy stress components, i.e. $\sigma_{\varphi z}^{\mathrm{YEOH}}$ and $\sigma_{zz}^{\mathrm{YEOH}}$, and the radius r are depicted in Fig. 5.2(c). The behavior is very similar to the neo-Hookean model. The nonlinear terms in (5.24), however, generate a convex curve for the shear stress. Further analysis of the Yeoh model is presented in the subsequent sections.

For all introduced models closed-form solutions for the axial force N and the torsion couple M_{t}, resulting from the deformation characterized through (5.4), can be obtained. We may directly compare those values to the respective quantities, say $\widetilde{N}$ and $\widetilde{M_{\mathrm{t}}}$, measured in experiments, as it was done by Rivlin and Saunders [46]. The calculation of the stress measures (5.1) is, hence, not necessary for parameter identification. We can also solve the torsion of a circular cylinder by means of the finite element method which we discuss in the Appendix.

5.3 Simple shear as an approximation for the torsion of a circular cylinder

In this section we compare the deformation due to torsion with that of simple shear and highlight the errors which result from the approximation of rheological data by simple shear. Note that from the stress components obtained from simple shear we cannot obtain values for the torsion couple and the axial force in a natural way. Thus, the model stresses are compared to the experimental stress values from (5.1), for parameter identification.

We define simple shear as a homogeneous plane deformation. The amount of shear is γ and the deformation gradient $\mathbf{F}$ of simple shear in a cartesian coordinate system (x, y, z) with shear in the y-direction and the normal direction z becomes

$$[\mathbf{F}] = \begin{bmatrix} 1 & 0 & 0 \\ 0 & 1 & \gamma \\ 0 & 0 & 1 \end{bmatrix}. \tag{5.29}$$

Observe the similarity between (5.4) and (5.29). The expression for the Cauchy stress tensor in (5.6) is still valid. The assumption of a plane stress state, i.e. $\widehat{\sigma}_{xx} =$

$\widehat{\sigma}_{xy} = \widehat{\sigma}_{xz} = 0$, enables the calculation of p and leads to the non-zero Cauchy stress components for simple shear, i.e. [112]

$$\widehat{\sigma}_{yy} = 2\psi_1\gamma^2, \qquad \widehat{\sigma}_{zz} = -2\psi_2\gamma^2, \qquad \widehat{\sigma}_{yz} = 2(\psi_1 + \psi_2)\gamma. \tag{5.30}$$

Consider now the relations for the normal stress $(5.16)_1$ and the shear stress $(5.16)_2$ of the cylinder at the outer radius R and compare them to $(5.30)_2$ and $(5.30)_3$. By setting $k = \gamma/R$, we find that the stress state of the simple shear deformation *equals* the stress state at the outer surface of the cylinder under torsion, see the circles in Fig. 5.2. This observation also holds when ψ_1 and ψ_2 are functions of the radius r, as it is, in general the case; see, e.g., the Yeoh model.

In a rheological experiment with parallel plates, a single shear stress value is calculated from the torsion couple by comparing $(5.23)_2$ at $r = R$ with $(5.30)_3$ at the outer radius, resulting in an expression analogous to $(5.1)_2$. Let us, therefore, restate (5.1) for hypothetical experiments as

$$\sigma^i = \frac{N^i}{\pi R^3}, \qquad \tau^i = \frac{2M_{\mathrm{t}}^i}{\pi R^3}, \tag{5.31}$$

where $i = \mathrm{NH}, \mathrm{MR}$ refers to the neo-Hookean model and the Mooney-Rivlin model, respectively. The relation $(5.31)_2$, however, does not hold for other (nonlinear) materials, e.g., when comparing (5.27) with (5.28). Hence, when we use $(5.31)_2$ for the Yeoh model ($i = \mathrm{YEOH}$), it denotes a value of shear stress in this nonlinear material which does not coincide with the simple shear solution, see Fig. 5.3(a). This observation may be generalized for all material models where ψ_1 or ψ_2 are dependent on r. Figure 5.3 compares the results of a hypothetical experiment, where the torsion couple and axial force of Section 5.2 are evaluated according to (5.31) to the simple shear approximation for the Yeoh model and the Mooney-Rivlin model. The parameters for the Yeoh model are $d_1 = 0.5\,\mathrm{MPa}$, $d_2 = -d_1/2$ and $d_3 = d_1/6$, while the Mooney-Rivlin parameters remain those introduced in the previous section. The shear stress τ^{YEOH} for the nonlinear Yeoh model, Fig. 5.3(a), is higher than the simple shear approximation $\widehat{\sigma}_{yz}^{\mathrm{YEOH}}$, while the shear stresses τ^{MR} and $\widehat{\sigma}_{yz}^{\mathrm{MR}}$ for the Mooney-Rivlin model with its constant shear modulus, Fig. 5.3(b), coincide. Recall, that for simple shear $\widehat{\sigma}_{zz}^{\mathrm{YEOH}} = 0$ if $\psi_2 = 0$, see $(5.30)_2$. Considering, for example, the Yeoh model, Fig. 5.3(a), the value is zero everywhere. On the other hand, the average normal stress σ^i calculated from $(5.31)_1$ implies the compressive force, as discussed in Section 5.2. For the Mooney-Rivlin material, Fig. 5.3(b), where $\psi_2 = c_2$ we obtain the correct tendency of the normal stress $\widehat{\sigma}_{zz}^{\mathrm{MR}}$ behavior. The curves, however, do not coincide.

Assume now that we approximate the shear stress data of a hypothetical experiment using the equation $(5.30)_3$ for simple shear. Then, by identifying $\widehat{\sigma}_{yz}^i$ with τ^i in $(5.31)_2$ we obtain an estimated torsion couple of $\widehat{M_{\mathrm{t}}}^i = \pi(\psi_1 + \psi_2)\gamma R^3$. This expression only

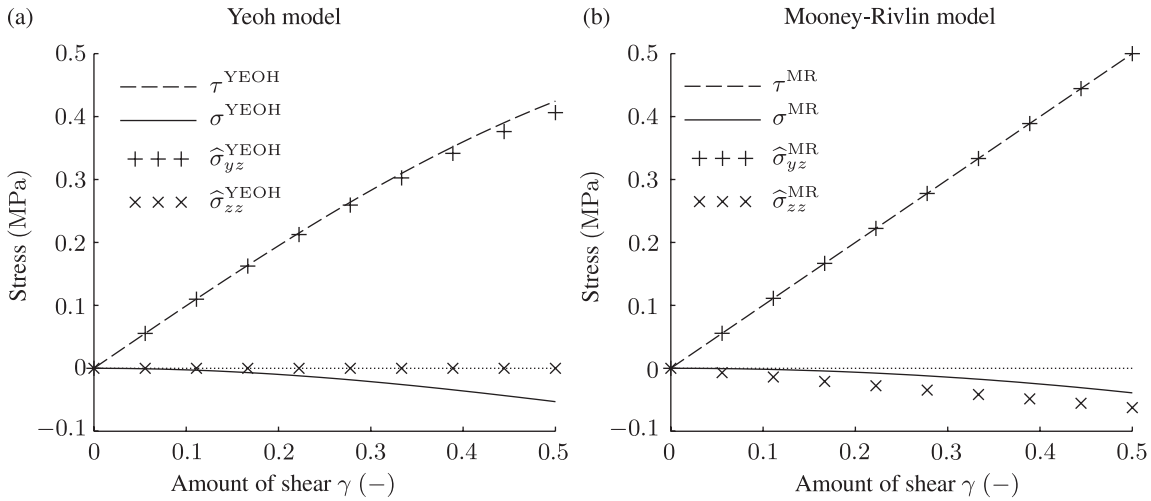

Figure 5.3: Shear stress (τ^i, $\widehat{\sigma}^i_{yz}$, $i = \mathrm{YEOH}, \mathrm{MR}$) and normal stress ($\sigma^i$, $\widehat{\sigma}^i_{zz}$) versus the amount of shear γ for the Yeoh model (a) and the Mooney-Rivlin model (b). The curves for τ^i and σ^i denote the stresses from a hypothetical experiment obtained with relation (5.31). The simple shear approximation $\widehat{\sigma}^i_{yz}$ and $\widehat{\sigma}^i_{zz}$ is denoted by crosses.

recovers the torsion couple calculated from (5.12) for a constant shear modulus. For nonlinear models, however, a discrepancy between the estimated torsion couple and the real torsion couple becomes apparent. For example, for the Yeoh model, by using the relations $\gamma = Rk$ and $I_1 = k^2R^2 + 3$, the error is

$$e^{\mathrm{YEOH}}_{M_\mathrm{t}} = \left| \frac{\widehat{M_\mathrm{t}}^{\mathrm{YEOH}} - M_\mathrm{t}^{\mathrm{YEOH}}}{M_\mathrm{t}^{\mathrm{YEOH}}} \right| = \left| \frac{2d_2\gamma^2/3 + 3d_3\gamma^4/2}{d_1 + 4d_2\gamma^2/3 + 3d_3\gamma^4/2} \right|. \tag{5.32}$$

The error for the models with linear shear elasticity is zero. For the Yeoh model with our parameter values at $\gamma = 0.5$ we obtain $e^{\mathrm{YEOH}}_{M_\mathrm{t}} = 8\%$.

For the quantification of the axial force error we may define a measure analogous to (5.32). For the Mooney-Rivlin material we obtain

$$e^{\mathrm{MR}}_N = \left| \frac{\widehat{N}^{\mathrm{MR}} - N^{\mathrm{MR}}}{N^{\mathrm{MR}}} \right| = \left| \frac{2c_2 - c_1}{c_1 + 2c_2} \right|. \tag{5.33}$$

Observe, that in this case, the error is independent of the amount of shear. The error is $e^{\mathrm{MR}}_N = 56\%$ with the previously given parameters.

5.4 Implications to continuum models for cross-linked actin networks

We introduce two network models, i.e. the eight-chain model [111] originally developed for rubber elasticity and an affine constitutive model for cross-linked actin networks [115] to apply the findings of the previous sections. Since this type of network models is able to use any filament model, described by a strain-energy function, the choice for a specific filament model is of minor importance here. We are primarily interested in the effect of the network models on the mechanical response and, therefore, we use one filament model for both networks to visualize their difference.

Consider an actin filament for which we desire to use a relationship between the stretch λ and the tensile force f of the form [48, 74]

$$\lambda\frac{r_0}{L} = 1 + \alpha f^\star - \frac{(1+2\alpha f^\star)(1+\alpha f^\star)^\delta}{(1+f^\star+\alpha f^{\star 2})^\delta}(1-r_0/L), \tag{5.34}$$

where we have used the shorthand notation $\alpha = \pi^2 k_\mathrm{B} T L_\mathrm{p}/(\mu_0 L^2)$ and the dimensionless force $f^\star = fL^2/(\pi^2 k_\mathrm{B} T L_\mathrm{p})$ with the parameters: Boltzmann constant k_B, temperature T, persistence length L_p, stretch modulus μ_0 and contour length L of the filament. In addition, we have used the relative extensional number δ and the end-to-end distance r_0 at zero force (note that r_0 is not identical to the reference radius introduced in (5.2)). We require that the filaments bear only tensile loads and set $f = 0$ for the case that $\lambda \leq 1$. From this chain model we may calculate the strain energy $w(\lambda)$ for a single filament and the partial derivative of the filament strain energy with respect to the stretch λ is by chain rule $w' = fr_0$ [48].

5.4.1 Eight-chain model

The eight-chain model [111] was recently combined with the chain model by MacKintosh et al. [56] and applied to actin networks [82]. This network model considers a cubic representative volume element containing eight polymer chains which are attached to each other at the center of the cube. The other ends of the filaments are connected to the vertices of the cube. Instead of the MacKintosh et al. model we use (5.34) and define the total chain stretch as

$$\lambda = \lambda_0 \lambda_\mathrm{AB}, \tag{5.35}$$

where λ_0 is the pre-stretch, which is required to achieve a non-zero initial shear modulus, and [111]

$$\lambda_\mathrm{AB} = \sqrt{I_1/3} = \sqrt{(k^2 r^2 + 3)/3} \tag{5.36}$$

is the homogenized chain stretch obtained from the eight-chain model, where the explicit expression for the first invariant (5.5) has been used. With the filament density n, the strain-energy function for the filament network is $\Psi = nw$. Then, with the chain rule and the properties (5.35) and (5.36) we get

$$\psi_1 = \frac{n\lambda_0}{6\lambda_{\mathrm{AB}}} w', \qquad \psi_2 = 0. \tag{5.37}$$

These relations we then use in (5.16) to obtain $\sigma_{zz}^{\mathrm{AB}}$ and $\sigma_{\varphi z}^{\mathrm{AB}}$ by means of numerical integration. Consequently, from (5.17), we are able to calculate the axial force N^{AB} and the torsion couple $M_{\mathrm{t}}^{\mathrm{AB}}$.

In Fig. 5.4(a) and (c) we illustrate the plots for the eight-chain model, equivalent to the Figs. 5.2 and 5.3. The material parameters we used are: end-to-end distance at zero force $r_0 = 1.63\,\mu\mathrm{m}$, persistence length $L_{\mathrm{p}} = 16\,\mu\mathrm{m}$, relative extensional number $\delta = 0.5$, filament density $n = 8.57\,\mu\mathrm{m}^{-3}$, contour length $L = 1.78\,\mu\mathrm{m}$, stretch modulus $\mu_0 = 117.5\,\mathrm{pN}$, $\lambda_0 = 1.001$. The shear stress $\sigma_{\varphi z}^{\mathrm{AB}}$ increases nonlinearly over the radius r, while the normal stress $\sigma_{zz}^{\mathrm{AB}}$ shows a similar characteristics as the neo-Hookean model (compare with Fig. 5.2(a)). Again, the simple shear solution is recovered at $r = R$, indicated by the circle. In Fig. 5.4(c), the simple shear solution for the shear stress $\widehat{\sigma}_{yz}^{\mathrm{AB}}$ overestimates the result for the hypothetical experiment. In analogy to $(5.32)_1$, the error at $\gamma = 0.2$ is $e_{M_{\mathrm{t}}}^{\mathrm{AB}} = 44\%$. Recall that the strain-energy function of the eight-chain model is only dependent on the first invariant I_1 of the right Cauchy-Green tensor, and thus the simple shear solution predicts a zero normal stress $\widehat{\sigma}_{zz}^{\mathrm{AB}}$ according to $(5.30)_2$. The torsion of the cylinder gives again a negative normal stress. This behavior is similar to the neo-Hookean and the Yeoh models.

5.4.2 Affine constitutive model for cross-linked F-actin networks

For the affine constitutive model we consider now an actin filament whose orientation in the three-dimensional space can be described by the Cartesian unit vector $\mathbf{M}$ in the reference configuration. Applying the deformation gradient $\mathbf{F}$ on the orientation vector $\mathbf{M}$ gives the deformed direction vector $\mathbf{m} = \mathbf{F}\mathbf{M}$. The stretch of the filament is then given by the length of $\mathbf{m}$, i.e. [112]

$$\lambda = (\mathbf{m} \cdot \mathbf{m})^{1/2} = (\mathbf{M} \cdot \mathbf{C}\mathbf{M})^{1/2}. \tag{5.38}$$

The first part of the Cauchy stress tensor (5.6) for an isotropic filament distribution is calculated as [115]

$$\overline{\boldsymbol{\sigma}}^{\mathrm{AN}} = n \int_{\Omega} \frac{w'}{\lambda} \mathbf{m} \otimes \mathbf{m} \, \mathrm{d}\Omega, \tag{5.39}$$

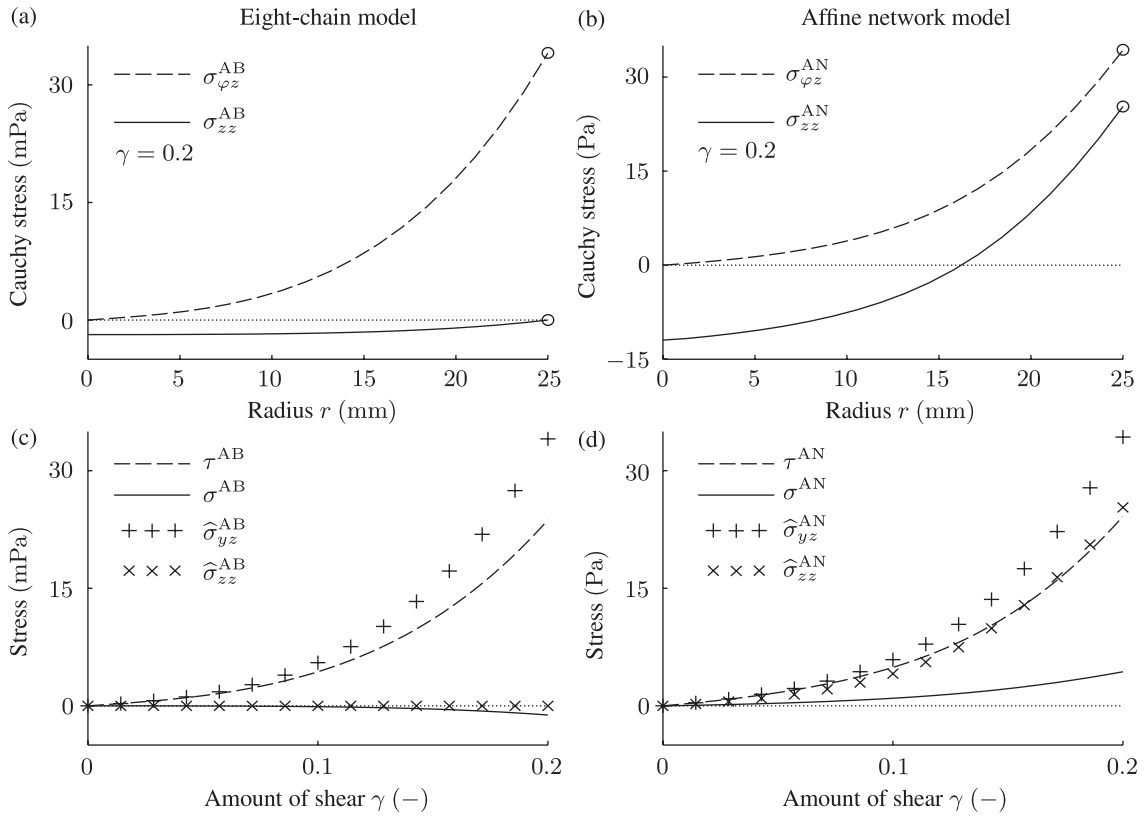

Figure 5.4: Cauchy shear stress $\sigma_{\varphi z}^{\mathrm{AB}}$, $\sigma_{\varphi z}^{\mathrm{AN}}$ and normal stress $\sigma_{zz}^{\mathrm{AB}}$, $\sigma_{zz}^{\mathrm{AN}}$ versus the radius r for the eight-chain model (a) and the affine network (b) at an amount of shear of $\gamma = 0.2$. The encircled values at $R = 25\,\mathrm{mm}$ are the simple shear solutions. Stresses versus the amount of shear γ for the eight-chain model (c) and the affine network (d). The curves τ^{AB}, τ^{AN} and σ^{AB}, σ^{AN} refer to the shear and normal stress as obtained from a hypothetical experiment according to (5.31). The simple shear approximation, i.e. the stresses $\widehat{\sigma}_{yz}^{\mathrm{AB}}$, $\widehat{\sigma}_{yz}^{\mathrm{AN}}$ and $\widehat{\sigma}_{zz}^{\mathrm{AB}}$, $\widehat{\sigma}_{zz}^{\mathrm{AN}}$, is denoted by the crosses. For the affine network model the positive normal stress $\sigma_{zz}^{\mathrm{AN}}$ at the outer part of the cylinder generates a positive axial force and thus positive values for σ^{AN}.

where the superscript AN stands for the affine network model. By using $\mathbf{F}$ from (5.4) the orientation vector in spherical coordinates is

$$[\mathbf{M}] = \begin{bmatrix} \sin\theta\cos\varphi \\ \sin\theta\sin\varphi \\ \cos\theta \end{bmatrix}, \qquad [\mathbf{m}] = [\mathbf{FM}] \begin{bmatrix} \sin\theta\cos\varphi \\ \sin\theta\sin\varphi + kr\cos\theta \\ \cos\theta \end{bmatrix}, \tag{5.40}$$

in the reference and the current configuration, respectively. According to (5.38), the filament stretch λ is then

$$\lambda = [1 + kr(\sin\varphi\sin 2\theta + kr\cos^2\theta)]^{1/2}. \tag{5.41}$$

By means of a numerical integration we can solve the integral in (5.39) and calculate the hydrostatic pressure (5.10). By noting that

$$\int_{\Omega} \mathbf{A}(\varphi,\theta)\,\mathrm{d}\Omega = \int_{\varphi=0}^{2\pi}\int_{\theta=0}^{\pi} \mathbf{A}(\varphi,\theta)\sin\theta\,\mathrm{d}\theta\,\mathrm{d}\varphi, \tag{5.42}$$

where $\mathbf{A}(\varphi,\theta)$ is an arbitrary second-order tensor, we may obtain the Cauchy stress tensor $\boldsymbol{\sigma}^{\mathrm{AN}}$ according to (5.6) which, eventually, allows the numerical evaluation of (5.11) and (5.12) to calculate the axial force N^{AN} and the torsion couple $M_{\mathrm{t}}^{\mathrm{AN}}$. In the case of simple shear, we assume a plane stress state, i.e. $\widehat{\sigma}_{xx}^{\mathrm{AN}} = \widehat{\sigma}_{xy}^{\mathrm{AN}} = \widehat{\sigma}_{xz}^{\mathrm{AN}} = 0$ and identify $p = \overline{\sigma}_{xx}^{\mathrm{AN}}$ to obtain the shear and normal stress components $\widehat{\sigma}_{yz}^{\mathrm{AN}}$ and $\widehat{\sigma}_{zz}^{\mathrm{AN}}$, respectively.

Figure 5.4(b) illustrates the distributions of the Cauchy shear stress $\sigma_{\varphi z}^{\mathrm{AN}}$ and the normal stress $\sigma_{zz}^{\mathrm{AN}}$ versus the radius r. By comparing this with the corresponding Fig. 5.4(a) of the eight-chain model, we observe that the values are three orders of magnitude larger. It is worth noting that we used for all parameters the identical values and the only variation is the network model. The characteristic difference of the affine network model compared to the eight-chain model is the normal stress which changes its sign at $r \sim 17\,\mathrm{mm}$ and it is positive at the outer surface of the cylinder. This results in a positive axial force N^{AN}. The comparison of the simple shear solution with the hypothetical experiment is depicted in Fig. 5.4(d). Similar to the eight-chain model, the shear stress $\widehat{\sigma}_{yz}^{\mathrm{AN}}$ for simple shear overestimates the response τ^{AN} of the hypothetical experiment for the affine network model. The error $e_{M_{\mathrm{t}}}^{\mathrm{AN}} = 42\%$ is smaller compared to the eight-chain model, however, it is still a substantial deviation. The simple shear solution for the normal stress $\widehat{\sigma}_{zz}^{\mathrm{AN}}$ is much larger than the torsion solution and is on the same order as the shear stress $\widehat{\sigma}_{yz}^{\mathrm{AN}}$. For both boundary conditions, we observe a positive normal stress which is a characteristic of many cross-linked biopolymer networks [39]. The error calculated in analogy to $(5.33)_1$ is $e_N^{\mathrm{AN}} = 480\%$.

Finally, we compare the two sets of boundary conditions to experimental data taken from [48], with an actin concentration of $9.5\,\mu\mathrm{M}$ and a cross-linker concentration of $0.95\,\mu\mathrm{M}$ (the ratio is 1/10). Therein, the authors show for five identically composed samples that the shear stress has a little variation between the experiments while they observed large differences for the normal stress. Therefore, here we consider two extreme cases, specifically the experiments with the numbers 3 and 1, which we subsequently call Experiment a and Experiment b, respectively, to highlight the consequences. For most material constants we can take values obtained earlier in the literature. Following the arguments in [82], based on the actin concentration, we assume that $nL = 15\,\mu\mathrm{m}^{-2}$ [48, 115]. The end-to-end distance at zero force $r_0 = 1.63\,\mu\mathrm{m}$ is derived for the given actin concentration from scaling arguments [26, 115]. The persistence length was measured to be $L_{\mathrm{p}} = 16\,\mu\mathrm{m}$ [35]. For the

Table 5.1: Parameters of the affine network model fitted to two experiments from [48], i.e. the contour length L and the stretch modulus μ_0, for the plots shown in Fig. 5.5, in addition to the relative difference between the parameters for simple shear and torsion of a cylinder normalized with respect to the torsion of a cylinder.

Experiment	a		b	
Parameter	L (μm)	μ_0 (pN)	L (μm)	μ_0 (pN)
Simple shear	1.77	44.2	1.75	24.9
Torsion of a cylinder	1.78	98.2	1.78	117.5
Relative difference	0.006	0.55	0.017	0.79

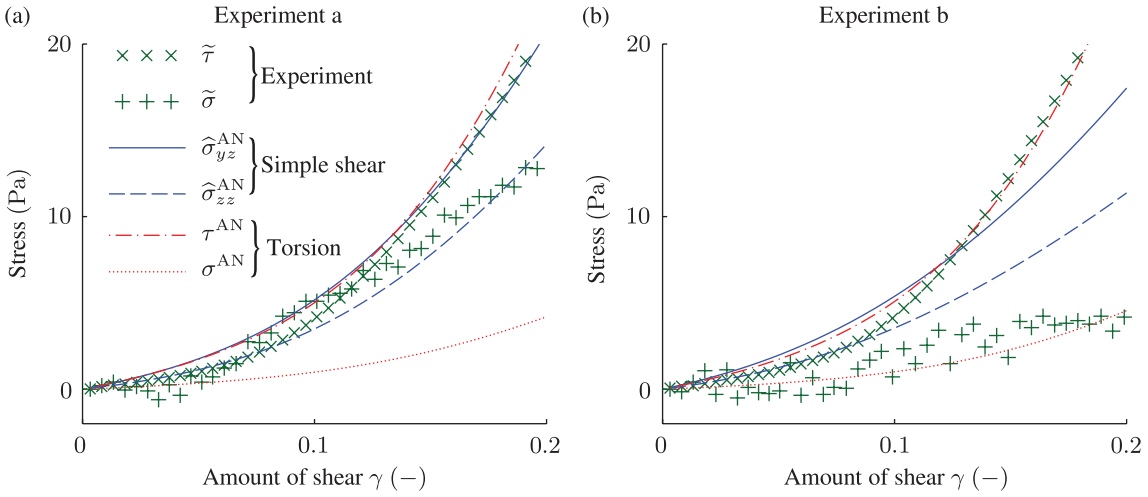

Figure 5.5: Fits of the affine network model to two experimental data sets characterized by the shear stress $\widetilde{\tau}$ and the normal stress $\widetilde{\sigma}$, from [48]. The uncertainty in measuring the axial force results in a better fit for the simple shear solution $\widehat{\sigma}_{yz}^{\mathrm{AN}}$ and $\widehat{\sigma}_{zz}^{\mathrm{AN}}$ in (a) or the torsion of a cylinder τ^{AN} and σ^{AN} in (b). The legend in (a) also applies to (b).

relative extensional number we use $\delta = 0.5$. The temperature in the experiment was $T = 294\,\mathrm{K}$ and the radius of the measuring plate was $R = 25\,\mathrm{mm}$. This leaves us with two free parameters in this fit: (i) the contour length L and (ii) the stretch modulus μ_0.

By means of the 'trust-region reflective' algorithm in MATLAB's[1] `lsqnonlin` function without weighting we obtain the values documented in Table 5.1, with the corresponding plots depicted in Fig 5.5. In the case of Experiment a (see Fig. 5.5(a)), the magnitudes of the shear $\widetilde{\tau}$ and the normal stress $\widetilde{\sigma}$ are on the same order. As already pointed out by means of Fig. 5.4(b) this behavior is well comparable to the

[1]Version R2010b, by The MathWorks Inc., Massachusetts, USA

results obtained from simple shear. The corresponding fit ($\widehat{\sigma}_{yz}^{\mathrm{AN}}$ and $\widehat{\sigma}_{zz}$) shows good agreement with the experimental data while the curves for the torsion of a circular cylinder (τ^{AN} and σ^{AN}) show strong deviations. The parameter values for the best fit differ between the different boundary conditions by 0.5% for the contour length and 55% for the stretch modulus.

When we consider Experiment b (Fig. 5.5(b)), we observe a completely different situation. The experimental data of this sample shows a normal stress $\widetilde{\sigma}$ which is only a small portion of the shear stress $\widetilde{\tau}$. Hence, in this case, the boundary conditions for the torsion of a cylinder give the better fit compared to simple shear. The obtained parameters differ by 1.7% and 79% for L and μ_0, respectively.

5.5 Discussion and Conclusion

In this study we introduced torsion of a circular cylinder to model the mechanical response that occur in a rotational parallel-plate rheometer, and we provided three illustrative examples for constitutive models in rubber elasticity: neo-Hooke, Mooney-Rivlin, Yeoh. We compared these results with the solution for simple shear and defined quantitative measures for the errors which occur due to this approximation. Finally, we applied the method to two more complex models for cross-linked actin networks, where the errors are even more pronounced.

The parallel-plate geometry leading to the torsion of a cylinder is characterized by a shear deformation of kr which is dependent on the radius r. This property leads to a non-homogeneous shear stress in the sample. A constant shear deformation over the radius can be achieved for materials with constant shear modulus and a cone-and-plate geometry of the measuring chamber. This testing setup would eliminate the discrepancies between simple shear and torsion for the shear stress. The hydrostatic pressure in (5.6), however, would still generate a normal stress varying with the radius. Therefore, single stress values cannot represent the complex stress state of samples in rotational rheometry. The definitions (5.1) can only serve as auxiliary quantities with the known consequences in mind.

Stress measures calculated from experiments are convenient to use in the modeling and the parameter identification by approximating the real boundary conditions with simple shear. The torsion couple is correctly captured for models with constant shear moduli (neo-Hooke and Mooney-Rivlin models) while a varying shear modulus imposes an error. We never observed an exact reproduction of the axial force through the simple shear approximation, however, simple shear can capture the correct tendency for the axial force for some material models, e.g., Mooney-Rivlin. Models with a strain-energy function only dependent on I_1, e.g., the neo-Hooke, Yeoh and the eight-chain models, unfortunately, do an incorrect prediction of the normal stress $\widehat{\sigma}_{zz}$

in simple shear, namely zero. Considering actin network models, the torsion solution for the eight-chain model predicts a negative axial force which is in contrast to experimental results. For the affine network model, we obtained predictions for a positive normal stress for both boundary conditions. This result suggests that it makes this model more suitable for cross-linked actin networks. The difference in the predicted axial force between simple shear and torsion of a cylinder is very large which makes a simple shear approximation questionable. Compared to the Yeoh model, the larger deviation of the shear stress from the linear behavior appears to impose also a larger error for the estimation of the torsion couple for the actin network models (AB: 44%; AN: 42%).

Experimental data of cross-linked actin networks available from rotational rheometry suffer from a low reliability of the axial force response [48]. The fact that we were able to fit the model with simple shear boundary conditions must not lead to the conclusion that simple shear provides a good approximation of the torsion of a cylinder. By picking a different sample with essentially identical shear stress behavior we can obtain a reasonably good fit to the model with torsion boundary conditions. Therefore, the axial force data from experiments can only serve as a correct trend for the real behavior, while a reliable measurement can only be conducted for the shear component.

In this study we focussed on the quasi-static behavior of samples in rotational rheometry. This allowed us to confine our investigations within the relatively simple framework of elasticity. When conducting rheological experiments on soft gels, one is also interested in the viscoelastic properties of the material. Protocols with oscillatory strain provide the storage modulus G' and the loss modulus G'' versus, for instance, the oscillation frequency. These measures are closely related to the shear stress trough

$$G' = \frac{\widetilde{\tau}_\mathrm{A}}{\gamma_\mathrm{A}} \cos\delta, \qquad G'' = \frac{\widetilde{\tau}_\mathrm{A}}{\gamma_\mathrm{A}} \sin\delta, \tag{5.43}$$

where the subscript A denotes the amplitude of the respective quantity and δ is the phase angle between $\widetilde{\tau}$ and γ. Hence, the errors we investigated in the quasi-static case also translate to the viscoelastic moduli.

Throughout the present work we assumed that the conditions in the rotational rheometer with a parallel-plate geometry can be modeled as a torsion of a cylinder. This was convincingly supported by experiments on vulcanized rubbers [46]. In the case of cross-linked actin networks, we need to consider that these materials are soft gels and the behavior may differ from that of solids. The consistency of such samples may cause that the ideal boundary conditions which we can assume for the torsion of a rubber cylinder are slightly altered. Another issue may be that the hydrostatic pressure field in the gel can be equilibrated by fluid flow. Hence, the relatively large differences for the axial force within an experimental sequence with identical protein

concentrations may stem from the uncertainty in the boundary conditions or partial pressure equilibration. The influence due to fluid flow may be studied by enhancing the current approach in a poroelastic way.

Simple shear, in general, is not a good approximation for the torsion of a cylinder and as a consequence for rheological experiments. Only for isotropic materials with constant shear moduli, the torsion couple is represented exactly by simple shear. Hence, one needs to be careful and aware of the consequences when defining single values for the stress components to describe the complex stress state in a sample undergoing a rheological experiment. Certainly, stress measures are convenient for the comparison of different samples. When it comes to parameter identification, however, we strongly advise to make use of the measured quantities, i.e. axial force and torsion couple. The large variations in the measured axial force during experiments of cross-linked actin filaments also call for improved rheometer designs or a more reliable measuring technique. Current experiments also cannot reveal the true stress distribution over the cylinder radius. Regarding the unusual normal stress distribution with a change in sign, it would be helpful to develop measuring chambers which enable to elucidate the real normal stress distribution in soft samples.

Appendix: Some finite element solutions

The torsion of a cylinder undergoing large strains may also be solved with numerical methods. At a first glance, a treatment with the finite element method seems to be a simple and straight-forward task. Though, the assumption of incompressibility and the fact that shear is the main mode of deformation cause severe numerical problems (volumetric and shear locking) in the solution of such problems.

We use the commercial software Abaqus[2] to solve the problem for a mesh generated with Cubit[3] and the use of the neo-Hookean model. The cross-section is discretized by using the 'circle' meshing scheme of Cubit with 16 elements along the x- and y-axes. In a first attempt we use a mesh with four elements through-the-thickness (the z-direction) eight-node hexahedrons with a hybrid formulation (C3D8H), i.e. the hydrostatic pressure is an independent field variable to avoid volumetric locking. The resulting distribution of the normal stress σ_{zz} is smooth and does not show typical signs of locking behavior for this particular arrangement, as depicted in Fig. 5.6(a). However, the normal stress turns out to predict an opposite sign compared to the analytical solution, see the dashed curve in Fig. 5.6(c). We assume that this behavior results from shear locking.

[2]Abaqus Standard, Version 6.11-2, Dassault Systèmes Simulia Corp., USA
[3]Cubit, Version 11.0, Sandia Corporation, USA

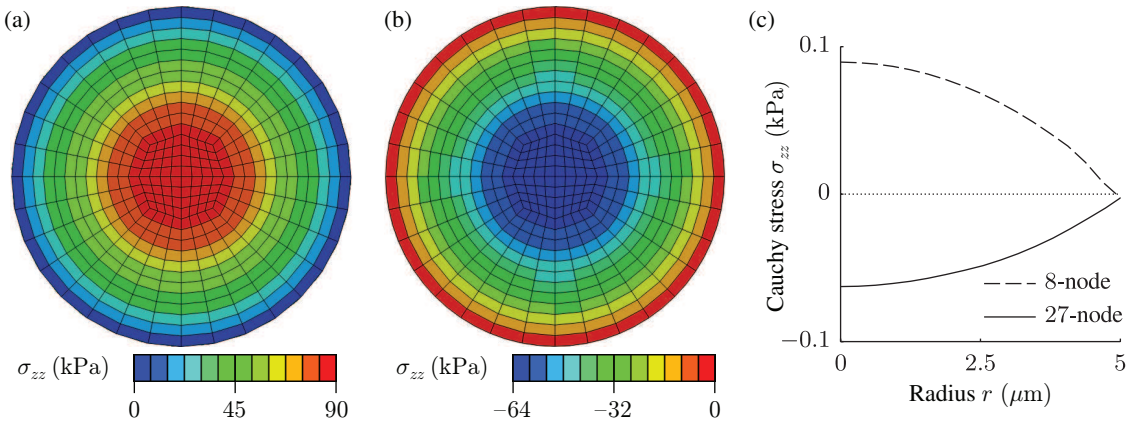

Figure 5.6: Normal Cauchy stress fields σ_{zz} (element stresses, not smoothened by post-processing software) for eight-node hexahedrons C3D8H (a) and 27-node elements C3D27H (b) modeled with the neo-Hookean material; stress versus radius for both finite element results (c); parameters: cylinder radius $R = 5\,\text{mm}$, four elements in thickness, amount of shear $\gamma = 0.2$, shear modulus $\mu = 0.56\,\text{MPa}$.

Two possible measures can improve the fidelity of the finite element approximation: (i) using higher-order elements and (ii) doing a mesh refinement. When using 20-node serendipity elements (C3D20H) the results show clearly checkerboarding. This outcome is not too surprising because the finite element literature, see, e.g., [203], does not recommend serendipity elements for nearly incompressible and incompressible materials. The Lagrangian quadratic element in a hybrid formulation (C3D27H) eliminates both volumetric and shear locking for the model with four elements through-the-thickness, see Fig. 5.6(b) and the solid curve in Fig. 5.6(c). Note that we also obtain the correct solution with the C3D8H element by increasing the number of elements through-the-thickness to at least 15.

REFERENCES

[1] Janmey PA, Weitz DA. Dealing with mechanics: mechanisms of force transduction in cells. *Trends Biochem. Sci.* 2004; **29**:364–370.

[2] Kaunas R, Nguyen P, Usami S, Chien S. Cooperative effects of rho and mechanical stretch on stress fiber organization. *PNAS* 2005; **102**:15 895–15 900.

[3] Nash GB, O'Brien E, Gordon-Smith EC, Dormandy JA. Abnormalities in the mechanical properties of red blood cells caused by plasmodium falciparum. *Blood* 1989; **74**:855–861.

[4] An SS, Fabry B, Trepat X, Wang N, Fredberg JJ. Do biophysical properties of the airway smooth muscle in culture predict airway hyperresponsiveness? *Am. J. Respir. Cell Mol. Biol.* 2006; **35**:55–64.

[5] Trickey WR, Lee GM, Guilak F. Viscoelastic properties of chondrocytes from normal and osteoarthritic human cartilage. *J. Orthop. Res.* 2000; **18**:891–898.

[6] Ohashi T, Sato M. Remodeling of vascular endothelial cells exposed to fluid shear stress: experimental and numerical approach. *Fluid Dyn. Res.* 2005; **37**:40–59.

[7] Zeng D, Juzkiw T, Read AT, Chan DWH, Glucksberg MR, Ethier CR, Johnson M. Young's modulus of elasticity of Schlemm's canal endothelial cells. *Biomech. Model. Mechanobiol.* 2010; **9**:19–33.

[8] Guck J, Schinkinger S, Lincoln B, Wottawah F, Ebert S, Romeyke M, Lenz D, Erickson HM, Ananthakrishnan R, Mitchell D, *et al.*. Optical deformability as an inherent cell marker for testing malignant transformation and metastatic competence. *Biophys. J.* 2005; **88**:3689–3698.

[9] Suresh S. Biomechanics and biophysics of cancer cells. *Acta Biomater.* 2007; **3**:413–438.

[10] Lee GYH, Lim CT. Biomechanics approaches to studying human diseases. *Trends Biotechnology* 2007; **25**:111–118.

[11] Holzapfel GA. Lecture notes on: Biomechanics of biological tissues. Graz University of Technology, Austria 2013.

[12] Alberts B, Johnson A, Lewis J, Raff M, Roberts K, Walter P. *Molecular Biology of the Cell*. 5th edn., Garland Science: New York, 2008.

[13] Vale RD. The molecular motor toolbox for intracellular transport. *Cell* 2003; **112**:467–480.

[14] Mizuno D, Tardin C, Schmidt CF, MacKintosh FC. Nonequilibrium mechanics of active cytoskeletal networks. *Science* 2007; **315**:370–373.

[15] Fernández P, Pullarkat PA, Ott A. A master relation defines the nonliear viscoelasticity of single fibroblasts. *Biophys. J.* 2006; **90**:3796–3805.

[16] Yamaoka H, Matsushita S, Shimada Y, Adachi T. Multiscale modeling and mechanics of filamentous actin cytoskeleton. *Biomech. Model. Mechanobiol.* 2012; **11**:291–302.

[17] McCue S, Noria S, Langille BL. Shear-induced reorganization of endothelial cell cytoskeleton and adhesion complexes. *Trends Cardiovasc. Med.* 2004; **14**:143–151.

[18] Ananthakrishnan R, Guck J, Wottawah F, Schinkinger S, Lincoln B, Romeyke M, Moon T, Käs J. Quantifying the contribution of actin networks to the elastic strength of fibroblasts. *J. Theor. Biol.* 2006; **242**:502–516.

[19] Parekh SH, Chaudhuri O, Theriot JA, Fletcher DA. Loading history determines the velocity of actin-network growth. *Nature Cell Biol.* 2005; **7**:1219–1223.

[20] Na S, Meininger GA, Humphrey JD. A theoretical model for F-actin remodeling in vascular smooth muscle cells subjected to cyclic stretch. *J. Theor. Biol.* 2007; **246**:87–99.

[21] Shin JH, Gardel ML, Mahadevan L, Matsudaira P, Weitz DA. Relating microstructure to rheology of a bundled and cross-linked F-actin network in vitro. *PNAS* 2004; **101**:9636–9641.

[22] Yamashiro-Matsumura S, Matsumura F. Intracellular localization of the 55-kD actin-bundling protein in cultured cells: spatial relationships with actin, alpha-actinin, tropomyosin, and fimbrin. *J. Cell Biol.* 1986; **103**:631–640.

[23] Cohan CS, Welnhofer EA, Zhao L, Matsumura F, Yamashiro S. Role of the actin bundling protein fascin in growth cone morphogenesis: Localization in filopodia and lamellipodia. *Cell Motil. Cytoskeleton* 2001; **48**:109–120.

[24] Hartwig JH, Tyler J, Stossel TP. Actin-binding protein promotes the bipolar and perpendicular branching of actin filaments. *J. Cell Biol.* 1980; **87**:841–848.

[25] Shin JH, Mahadevan L, So PT, Matsudaira P. Bending stiffness of a crystalline actin bundle. *J. Mol. Biol.* 2004; **337**:255–261.

[26] Tharmann R, Claessens MM, Bausch AR. Viscoelasticity of isotropically cross–linked actin networks. *Phys. Rev. Lett.* 2007; **98**:088 103.

[27] Humphrey JD. *Cardiovascular Solid Mechanics. Cells, Tissues, and Organs.* Springer-Verlag: New York, 2002.

[28] Isambert H, Venier P, Maggs AC, Fattoum A, Kassab R, Pantaloni D, Carlier MF. Flexibility of actin filaments derived from thermal fluctuations: Effect of bound nucleotide, phalloidin and muscle regulatory proteins. *J. Bio. Chem.* 1995; **270**:437–444.

[29] Marko JF, Siggia ED. Stretching DNA. *Macromolecules* 1995; **28**:8759–8770.

[30] Gittes F, Mickey B, Nettleton J, Howard J. Flexural rigidity of microtubules and actin filaments measured from thermal fluctuations in shape. *J. Cell Biochem.* 1993; **120**:923–934.

[31] Ott A, Magnasco M, Simon A, Libchaber A. Measurement of the persistence length of polymerized actin using flourescence microscopy. *Phys. Rev. E Stat. Nonlin. Soft Matter Phys.* 1993; **48**:1642–1647.

[32] Janmey PA, Hvidt S, Käs J, Lerche D, Maggs A, Sackman E, Schliwa M, Stossel TP. The mechanical properties of actin gels. Elastic modulus and filament motions. *J. Bio. Chem.* 1994; **269**:503–513.

[33] Roos WH, Roth A, Konle J, Presting H, Sackmann E, Spatz JP. Freely suspended actin cortex models on arrays of microfabricated pillars. *Chemphyschem.* 2003; **4**:872–877.

[34] Haraszti T, E-M Clemen A, Spatz JP. Biomimetic F-actin cortex models. *Chemphyschem.* 2009; **10**:2777–2786.

[35] Le Goff L, Hallatschek O, Frey E, Amblard F. Tracer studies on F-actin fluctuations. *Phys. Rev. Lett.* 2002; **89**:258 101.

[36] Liu X, Pollack GH. Mechanics of F-actin characterized with microfrabicated cantilevers. *Biophys. J.* 2002; **83**:2705–2715.

[37] Storm C, Pastore JJ, MacKintosh FC, Lubensky TC, Janmey PA. Nonlinear elasticity in biological gels. *Nature* 2005; **435**:191–194.

[38] Janmey PA, Hvidt S, Lamb J, Stossel TP. Resemblance of actin-binding protein/actin gels to covalently crosslinked networks. *Nature* 1990; **345**:89–92.

[39] Janmey PA, McCormick ME, Rammensee S, Leight JL, Georges PC, MacKintosh FC. Negative normal stress in semiflexible polymer gels. *Nat. Mater.* 2007; **6**:48–51.

[40] Wagner B, Tharmann R, Haase I, Fischer M, Bausch AR. Cytoskeletal polymer networks: The molecular structure of cross-linkers determines macroscopic properties. *PNAS* 2006; **103**:13 974–13 978.

[41] Gardel ML, Shin JH, MacKintosh FC, Mahadevan L, Matsudaira P, Weitz DA. Elastic behavior of cross-linked and bundled actin networks. *Science* 2004; **304**:1301–1305.

[42] Wen Q, Basu A, Winer JP, Yodh A, Janmey PA. Local and global deformations in a strain-stiffening fibrin gel. *New J. Phys.* 2007; **9**:428.

[43] DiDonna BA, Lubensky TC. Nonaffine correlations in random elastic media. *Phys. Rev. E Stat. Nonlin. Soft Matter Phys.* 2005; **72**:066 619.

[44] Hatami-Marbini H, Picu RC. Effect of fiber orientation on the non–affine deformation of random fiber networks. *ACTAM2* 2009; **205**:77–84.

[45] Poynting JH. On pressure perpendicular to the shear planes in finite pure shears, and on the lengthening of loaded wires when twisted. *Proc. R. Soc. Lond. A* 1909; **82**:546–559.

[46] Rivlin RS, Saunders DW. Large elastic deformations of isotropic materials. VII. experiments on the deformation of rubber. *Philos. T. Roy. Soc.* 1951; **A243**:251–288.

[47] Conti E, MacKintosh FC. Cross–linked networks of stiff filaments exhibit negative normal stress. *Phys. Rev. Lett.* 2009; **102**:088 102.

[48] Unterberger MJ, Schmoller KM, Bausch AR, Holzapfel GA. A new approach to model cross-linked actin networks: Multi-scale continuum formulation and computational analysis. *J. Mech. Behav. Biomed. Mater.* 2013; **22**:95–114.

[49] Lin-Gibson S, Pathak JA, Grulke EA, Wang H, Hobbie EK. Elastic flow instability in nanotube suspensions. *Phys. Rev. Lett.* 2004; **92**:048 302.

[50] Vaziri A, Gopinath A, Deshpande VS. Continuum-based computational models for cell and nuclear mechanics. *J. Mech. Mater. Struct.* 2007; **2**:1169–1191.

[51] Vaziri A, Gopinath A. Cell and biomolecular mechanics in silico. *Nat. Mater.* 2008; **7**:15–23.

[52] Jones WR, Ting-Beall HP, Lee GM, Kelley SS, Hochmuth RM, Guilak F. Alterations in the Young's modulus and volumetric properties of chondrocytes isolated from normal and osteoarthritic human cartilage. *J. Biomech.* 1999; **32**:119–127.

[53] Rico F, Roca-Cusachs P, Gavara N, Farré R, Rotger M, Navajas D. Probing mechanical properties of living cells by atomic force microscopy with blunted pyramidal cantilever tips. *Phys. Rev. E Stat. Nonlin. Soft Matter Phys.* 2005; **72**:021 914.

[54] Hochmuth RM. Review: Micropipette aspiration of living cells. *J. Biomech.* 2000; **33**:15–22.

[55] Mahaffy RE, Park S, Gerde E, Käs J, Shih CK. Quantitative analysis of the viscoelastic properties of thin regions of fibroblasts using atomic force microscopy. *Biophys. J.* 2004; **86**:1777–1793.

[56] MacKintosh FC, Käs J, Janmey PA. Elasticity of semiflexible biopolymer networks. *Phys. Rev. Lett.* 1995; **75**:4425–4428.

[57] Alder BJ, Wainwright TE. Studies in molecular dynamics. I. General method. *J. Chem. Phys.* 1959; **31**:459–466.

[58] Matsushita S, Adachi T, Inoue Y, Hojo M, Sokabe M. Evaluation of extensional and torsional stiffness of single actin filaments by molecular dynamics analysis. *J. Biomech.* 2010; **43**:3162–3167.

[59] Kojima H, Ishijima A, Yanagida T. Direct measurement of stiffness of single actin filaments with and without tropomyosin by in vitro nanomanipulation. *Proc. Natl. Acad. Sci. USA* 1994; **91**:12 962–12 966.

[60] Matsushita S, Inoue Y, Hojo M, Sokabe M, Adachi T. Effect of tensile force on the mechanical behavior of actin filaments. *J. Biomech.* 2011; **44**:1776–1781.

[61] Chu JW, Voth GA. Coarse-grained modeling of the actin filament derived from atomistic-scale simulations. *Biophys. J.* 2006; **90**:1572–1582.

[62] Deriu MA, Bidone TC, Mastrangelo F, Di Benedetto G, Soncini M, Montevecchi FM, Morbiducci U. Biomechanics of actin filaments: A computational multi-level study. *J. Biomech.* 2011; **44**:630–636.

[63] Yogurtcu ON, Kim JS, Sun SX. A mechanochemical model of actin filaments. *Biophys. J.* 2012; **103**:719–727.

[64] Fan J, Saunders MG, Voth GA. Coarse-graining provides insights on the essential nature of heterogeneity in actin filaments. *Biophys. J.* 2012; **103**:1334–1342.

[65] Fan J, Saunders MG, Haddadian EJ, Freed KF, De La Cruz EM, Voth GA. Molecular origins of cofilin-linked changes in actin filament mechanics. *J. Mol. Biol.* 2013; **425**:1225–1240.

[66] Ming D, Kong Y, Wu Y, Ma J. Substructure synthesis method for simulating large molecular complexes. *PNAS* 2003; **100**:104–109.

[67] Ming D, Kong Y, Wu Y, Ma J. Simulation of F-actin filaments of several microns. *Biophys. J.* 2003; **85**:27–35.

[68] Wu Y, Ma J. Refinement of F-actin model against fiber diffraction data by long-range normal modes. *Biophys. J.* 2004; **86**:116–124.

[69] Yamaoka H, Adachi T. Coupling between axial stretch and bending/twisting deformation of actin filaments caused by a mismatched centroid from the center axis. *Int. J. Mech. Sci.* 2010; **52**:329–333.

[70] Matsushita S, Inoue Y, Adachi T. Quantitative analysis of extension-torsion coupling of actin filaments. *Biochem. Biophys. Res. Commun.* 2012; **420**:710–713.

[71] Kratky O, Porod G. Röntgenuntersuchung gelöster Fadenmoleküle. *Recl. Trav. Chim. Pays-Bas.* 1949; **68**:1106–1123.

[72] Fixman M, Kovac J. Polymer conformational statistics. III modified Gaussian models of stiff chains. *J. Chem. Phys.* 1973; **58**:1564–1568.

[73] Holzapfel GA, Ogden RW. On the bending and stretching elasticity of biopolymer filaments. *J. Elasticity* 2011; **104**:319–342.

[74] Holzapfel GA, Ogden RW. Elasticity of biopolymer filaments. *Acta Biomater.* 2013; **9**:7320–7325.

[75] Antman SS. *Nonlinear Problems of Elasticity.* 2nd edn., Springer: New York, 2005.

[76] Bustamante C, Marko JF, Siggia ED, Smith SB. Entropic elasticity of λ-phage DNA. *Science* 1994; **265**:1599–1600.

[77] Bouchiat C, Wang MD, Allemand JF, Strick T, Block SM, Croquette V. Estimating the persistence length of a worm-like chain molecule from force-extension measurements. *Biophys. J.* 1999; **76**:409–413.

[78] MacKintosh FC. Polymer-based models of cytoskeleton networks. *Cytoskeletal Mechanics: Models and Measurements*, Mofrad MRK, Kamm RD (eds.). Cambridge University Press: Cambridge, 2006; 152–169.

[79] Purohit PK, Arsenault ME, Goldman Y, Bau HH. The mechanics of short rod-like molecules in tension. *Int. J. Non-Linear Mech.* 2008; **43**:1056–1063.

[80] Keller D, Swigon D, Bustamante C. Relating single-molecule measurements to thermodynamics. *Biophys. J.* 2003; **84**:733–738.

[81] Hori Y, Prasad A, Kondev J. Stretching short biopolymers by fields and forces. *Phys. Rev. E Stat. Nonlin. Soft Matter Phys.* 2007; **75**:041 904.

[82] Palmer JS, Boyce MC. Constitutive modeling of the stress-strain behavior of F-actin filament networks. *Acta Biomater.* 2008; **4**:597–612.

[83] Cohen A. A padé approximant to the inverse Langevin function. *Rheol. Acta* 1991; **30**:270–273.

[84] Landau LD, Lifschitz EM. *Course of Theoretical Physics: Statistical Physics*, vol. 5. First edn., Pergamon Press: Oxford, 1958.

[85] Blundell JR, Terentjev EM. Stretching semiflexible filaments and their networks. *Macromolecules* 2009; **42**:5388–5394.

[86] Blundell JR, Terentjev EM. Semiflexible filaments subject to arbitrary interactions: a Metropolis Monte Carlo approach. *Soft Matter* 2011; **7**:3967–3974.

[87] Wilhelm J, Frey E. Elasticity of stiff polymer networks. *Phys. Rev. Lett.* 2003; **91**:108 103.

[88] Head DA, Levine AJ, MacKintosh FC. Distinct regimes of elastic response and deformation modes of cross-linked cytoskeletal and semiflexible polymer networks. *Phys. Rev. E Stat. Nonlin. Soft Matter Phys.* 2003; **68**:061 907.

[89] Head DA, Levine AJ, MacKintosh FC. Deformation of cross-linked semiflexible polymer networks. *Phys. Rev. Lett.* 2003; **91**:108 102.

[90] Onck PR, Koeman T, van Dillen T, van der Giessen E. Alternative explanation of stiffening in cross-linked semiflexible networks. *Phys. Rev. Lett.* 2005; **95**:178 102.

[91] Missel AR, Bai M, Klug WS, Levine AJ. Affine-nonaffine transition in networks of nematically ordered semiflexible polymers. *Phys. Rev. E Stat. Nonlin. Soft Matter Phys.* 2010; **82**:041 907.

[92] Heussinger C, Schaefer B, Frey E. Nonaffine rubber elasticity for stiff polymer networks. *Phys. Rev. E Stat. Nonlin. Soft Matter Phys.* 2007; **76**:031 906.

[93] Head DA, Levine AJ, MacKintosh FC. Mechanical response of semiflexible networks to localized perturbations. *Phys. Rev. E Stat. Nonlin. Soft Matter Phys.* 2005; **72**:061 914.

[94] Mizuno D, Head DA, MacKintosh FC, Schmidt CF. Active and passive microrheology in equilibrium and nonequilibrium systems. *Macromolecules* 2008; **41**:7194–7202.

[95] DiDonna BA, Levine AJ. Unfolding cross-linkers as rheology regulators in F-actin networks. *Phys. Rev. E Stat. Nonlin. Soft Matter Phys.* 2007; **75**:041 909.

[96] Abhilash AS, Purohit PK, Joshi SP. Stochastic rate-dependent elasticity and failure of soft fibrous networks. *Soft Matter* 2012; **8**:7004–7016.

[97] Huisman EM, van Dillen T, Onck PR, Van der Giessen E. Three-dimensional cross-linked F-actin networks: relation between network architecture and mechanical behavior. *Phys. Rev. Lett.* 2007; **99**:208 103.

[98] Huisman EM, Storm C, Barkema GT. Monte Carlo study of multiply crosslinked semiflexible polymer networks. *Phys. Rev. E Stat. Nonlin. Soft Matter Phys.* 2008; **78**:051 801.

[99] Huisman EM, Storm C, Barkema GT. Frequency-dependent stiffening of semiflexible networks: A dynamical nonaffine to affine transition. *Phys. Rev. E Stat. Nonlin. Soft Matter Phys.* 2010; **82**:061 902.

[100] Gittes F, MacKintosh FC. Dynamic shear modulus of a semiflexible polymer network. *Phys. Rev. E Stat. Nonlin. Soft Matter Phys.* 1998; **58**:R1241–R1244.

[101] Kim T, Hwang W, Kamm RD. Computational analysis of a cross-linked actin-like network. *Exp. Mech.* 2009; **49**:91–104.

[102] Kim T, Hwang W, Lee H, Kamm RD. Computational analysis of viscoelastic properties of crosslinked actin networks. *PLoS Comput. Biol.* 2009; **5**:e1000 439.

[103] Žagar G, Onck PR, Van der Giessen E. Elasticity of rigidly cross-linked networks of athermal filaments. *Macromolecules* 2011; **44**:7026–7033.

[104] Van Dillen T, Onck PR, Van der Giessen E. Models for stiffening in cross-linked biopolymer networks: A comparative study. *J. Mech. Phys. Solids* 2008; **56**:2240–2264.

[105] Lee H, Pelz B, Ferrer JM, Kim T, Lang MJ, Kamm RD. Cytoskeletal deformation at high strains and the role of cross-link unfolding or unbinding. *Cell. Mol. Bioeng.* 2009; **2**:28–38.

[106] Cyron CJ, an A R Bausch KWM, Wall WA. Micromechanical simulations of biopolymer networks with finite elements. *J. Comput. Phys.* 2013; **244**:236–251.

[107] Flory PJ, Rehner Jr J. Statistical mechanics of cross-linked polymer networks. *J. Chem. Phys.* 1943; **11**:512–526.

[108] Treloar LRG. The elasticity of a network of long-chain molecules—III. *Trans. Faraday Soc.* 1946; **42**:83–94.

[109] Wang MC, Guth E. Statistical theory of networks of non-gaussian flexible chains. *J. Chem. Phys.* 1952; **20**:1144–1157.

[110] Treloar LRG. *The Physics of Rubber Elasticity.* 3rd edn., Oxford University Press: Oxford, 1975.

[111] Arruda EM, Boyce MC. A three–dimensional constitutive model for the large stretch behavior of rubber elastic materials. *J. Mech. Phys. Solids* 1993; **41**:389–412.

[112] Holzapfel GA. *Nonlinear Solid Mechanics. A Continuum Approach for Engineering.* John Wiley & Sons: Chichester, 2000.

[113] Treloar LRG, Riding G. A non-gaussian theory for rubber in biaxial strain I. mechanical properties. *Proc. R. Soc. Lond. A* 1979; **369**:261–280.

[114] Wu PD, van der Giessen E. On improved network models for rubber elasticity and their applications to orientation hardening in glassy polymers. *J. Mech. Phys. Solids* 1993; **41**:427–456.

[115] Holzapfel GA, Unterberger MJ, Ogden RW. An affine constitutive model for cross-linked F-actin networks with compliant linker proteins 2013; **Submitted**.

[116] Wilhelm J, Frey E. Radial distribution function of semiflexible polymers. *Phys. Rev. Lett.* 1996; **77**:2581–2584.

[117] Van Oosterwyck H, Rodríguez JF, Doblaré M, García JMA. An affine micro-sphere-based constitutive model, accounting for junctional sliding, can capture F-actin network mechanics. *Comput. Methods Biomech. Biomed. Engin.* 2012; **In press**.

[118] Schmoller KM, Lieleg O, Bausch AR. Structural and viscoelastic properties of actin/filamin networks: Cross-linked versus bundled networks. *Biophys. J.* 2009; **97**:83–89.

[119] Miehe C, Göktepe S, Lulei F. A micro-macro approach to rubber-like materials – Part I: The non-affine micro-sphere model of rubber elasticity. *J. Mech. Phys. Solids* 2004; **52**:2617–2660.

[120] Unterberger MJ, Schmoller KM, Wurm C, Bausch AR, Holzapfel GA. Viscoelasticity of cross-linked actin networks: experimental tests, mechanical modeling and finite element analysis. *Acta Biomater.* 2013; **9**:7343–7353.

[121] Holzapfel GA. On large strain viscoelasticity: Continuum formulation and finite element applications to elastomeric structures. *Int. J. Numer. Meth. Engng* 1996; **39**:3903–3926.

[122] Bažant ZP, Oh BH. Efficient numerical integration on the surface of a sphere. *Z. Angew. Math. Mech.* 1986; **66**:37–49.

[123] Broedersz CP, Storm C, MacKintosh FC. Nonlinear elasticity of composite networks of stiff biopolymers with flexible linkers. *Phys. Rev. Lett.* 2008; **101**:118 103.

[124] Broedersz CP, Storm C, MacKintosh FC. Effective–medium approach for stiff polymer networks with flexible cross–links. *Phys. Rev. E Stat. Nonlin. Soft Matter Phys.* 2009; **79**:061 914.

[125] Gardel ML, Nakamura F, Hartwig JH, Crocker JC, Stossel TP, Weitz DA. Prestressed F–actin networks cross–linked by hinged filamins replicate mechanical properties of cells. *PNAS* 2006; **103**:1762–1767.

[126] Yamada H, Ishiguro H, Tamagawa M. Mechanical behavior and structural changes of cells subjected to mechanical stimuli: Deformation, freezing, and shock waves. *Biomechanics at micro- and nanoscale levels*, vol. 1, Wada H (ed.). World Scientific, New Jersey, 2005.

[127] Herant M, Marganski WA, Dembo M. The mechanics of neutrophils: synthetic modeling of three experiments. *Biophys. J.* 2003; **84**:3389–3413.

[128] Kardas D, Nackenhorst U, Balzani D. Computational model for the cell-mechanical response of the osteocyte cytoskeleton based on self-stabilizing tensegrity structures. *Biomech. Model. Mechanobiol.* 2013; **12**:167–183.

[129] Unterberger MJ, Weisbecker H, Holzapfel GA. Torsion of a circular cylinder versus simple shear as a modeling basis for rheometer experiments: application to rubber and actin networks 2013; **Submitted**.

[130] Ingber DE. Cellular tensegrity: defining new rules of biological design that govern the cytoskeleton. *J. Cell Sci.* 1993; **104**:613–627.

[131] Ingber DE. Mechanobiology and diseases of mechanotransduction. *Ann. Med.* 2003; **35**:564–577.

[132] Sultan C, Stamenović D, Ingber DE. A computational tensegrity model predicts dynamic rheological behaviors in living cells. *Ann. Biomed. Eng.* 2004; **32**:520–530.

[133] Kasza KE, Rowat AC, Liu J, Angelini TE, Brangwynne CP, Koenderink GH, Weitz DA. The cell as a material. *Curr. Opin. Cell Biol.* 2007; **19**:101–107.

[134] Tee SY, Bausch AR, Janmey PA. The mechanical cell. *Curr. Biol.* 2009; **19**:R745–R748.

[135] Alenghat FJ, Ingber DE. Mechanotransduction: All signals point to cytoskeleton, matrix, and integrins. *Science's stke* 2002; **119**:6–9.

[136] Niederman R, Amrein PC, Hartwig J. Three–dimensional structure of actin filaments and of an actin gel made with actin–binding protein. *J. Cell Biol.* 1983; **96**:1400–1413.

[137] Kasza KE, Koenderink GH, Lin YC, Broedersz CP, Messner W, Nakamura F, Stossel TP, MacKintosh FC, Weitz DA. Nonlinear elasticity of stiff biopolymers connected by flexible linkers. *Phys. Rev. E Stat. Nonlin. Soft Matter Phys.* 2009; **79**:041 928–1–041 928–5.

[138] Lieleg O, Schmoller KM, Cyron CJ, Luan Y, Wall WA, Bausch AR. Structural polymorphism in heterogeneous cytoskeletal networks. *Soft Matter* 2009; **5**:1796–1803.

[139] Lieleg O, Claessens MMAE, Bausch AR. Structure and dynamics of cross-linked actin networks. *Soft Matter* 2010; **6**:218–225.

[140] Schmoller KM, Lieleg O, Bausch AR. Cross-linking molecules modify composite actin networks independently. *Phys. Rev. Lett.* 2008; **101**:118 102.

[141] Courson DS, Rock RS. Actin cross-link assembly and disassembly mechanics for α-actinin and fascin. *J. Bio. Chem.* 2010; **285**:26 350–26 357.

[142] Kasza KE, Broedersz CP, Koenderink GH, Lin YC, Messner W, Millman EA, Nakamura F, Stossel TP, MacKintosh FC, Weitz DA. Actin filament length tunes elasticity of flexibly cross-linked actin networks. *Biophys. J.* 2010; **99**:1091–1100.

[143] Stricker J, Falzone T, Gardel ML. Mechanics of the F-actin cytoskeleton. *J. Biomech.* 2010; **43**:9–14.

[144] Gent AN. A new constitutive relation for rubber. *Rubber Chem. Technol.* 1996; **69**:59–61.

[145] Ogden RW, Saccomandi G, Sgura I. On worm-like chain models within the three-dimensional continuum mechanics framework. *Proc. R. Soc. Lond. A* 2006; **462**:749–768.

[146] Cyron CJ, Wall WA. Finite-element approach to Brownian dynamics of polymers. *Phys. Rev. E Stat. Nonlin. Soft Matter Phys.* 2009; **80**:066 704.

[147] Tkachuk M, Linder C. The maximal advance path constraint for the homogenization of materials with random network microstructure. *Philos. Mag.* 2012; **92**:2779–2808.

[148] Buxton GA, Clarke N, Hussey PJ. Actin dynamics and the elasticity of cytoskeletal networks. *Express Polym. Lett.* 2009; **3**:579–587.

[149] Inoue Y, Tsuda S, Nakagawa K, Hojo M, Adachi T. Modeling myosin-dependent rearrangement and force generation in an actomyosin network. *J. Theor. Biol.* 2011; **281**:65–73.

[150] Chen P, Shenoy VB. Strain stiffening induced by molecular motors in active crosslinked biopolymer networks. *Soft Matter* 2011; **7**:355–358.

[151] Odijk T. Stiff chains and filaments under tension. *Macromolecules* 1995; **28**:7016–7018.

[152] Storm C, Nelson PC. Theory of high-force DNA stretching and overstretching. *Phys. Rev. E Stat. Nonlin. Soft Matter Phys.* 2003; **67**:051 906.

[153] Brent R. *Algorithms for Minimization without Derivatives*. Prentice-Hall: Englewood Cliffs, 1973.

[154] Treloar LRG. The photoelastic properties of short-chain molecular networks. *Trans. Faraday Soc.* 1954; **50**:881–896.

[155] Lanir Y. Constitutive equations for fibrous connective tissues. *J. Biomech.* 1983; **16**:1–12.

[156] Spudich JA, Watt S. The regulation of rabbit skeletal muscle contraction. I. biochemical studies of the interaction of the tropomyosin–troponin complex with actin and the proteolytic fragments of myosin. *J. Bio. Chem.* 1971; **246**:4866–4871.

[157] MacLean-Fletcher S, Pollard TD. Identification of a factor in conventional muscle actin preparations which inhibits actin filament self-association. *Biochem. Biophys. Res. Commun.* 1980; **96**:18–27.

[158] Uhde J, Keller M, Sackmann E, Parmeggiani A, Frey E. Internal motility in stiffening actin–myosin networks. *Phys. Rev. Lett.* 2004; **93**:268 101.

[159] Schmoller KM, Fernández P, Arevalo RC, Blair DL, Bausch AR. Cyclic hardening in bundled actin networks. *Nat. Commun.* 2010; **1**:134–140.

[160] Steinmetz MO, Stoffler D, Müller SA, Jahn W, Wolpensinger B, Goldie KN, Engel A, Faulstich H, Aebi U. Evaluating atomic models of F-actin with an undecagold-tagged phalloidin derivative. *J. Mol. Biol.* 1998; **276**:1–6.

[161] Burlacu S, Janmey PA, Borejdo J. Distribution of actin filament lengths measured by fluorescence microscopy. *Am. J. Physiol. Cell Physiol.* 1992; **262**:C569–C577.

[162] Lin DC, Shreiber DI, Dimitriadis EK, Horkay F. Spherical indentation of soft matter beyond the Hertzian regime: numerical and experimental validation of hyperelastic models. *Biomech. Model. Mechanobiol.* 2009; **8**:345–358.

[163] Green AE, Rivlin RS, Shield RT. General theory of small elastic deformations superimposed on finite elastic deformations. *Proc. R. Soc. Lond. A* 1952; **211**:128–154.

[164] Beatty MF, Usmani SA. On the indentation of a highly elastic half-space. *Quart. J. Mech. Appl. Math.* 1975; **28**:47–62.

[165] Na S, Sun Z, Meininger GA, Humphrey JD. On atomic force microscopy and the constitutive behavior of living cells. *Biomech. Model. Mechanobiol.* 2004; **3**:75–84.

[166] Humphrey JD, Halperin HR, Yin FCP. Small indentation superimposed on a finite equibiaxial stretch: implications for cardiac mechanics. *J. Appl. Mech.* 1991; **58**:1108–1111.

[167] Miehe C. Aspects of the formulation and finite element implementation of large strain isotropic elasticity. *Int. J. Numer. Meth. Engng* 1994; **37**:1981–2004.

[168] Luan Y, Lieleg O, Wagner B, Bausch AR. Micro- and macrorheological properties of isotropically cross-linked actin networks. *Biophys. J.* 2008; **94**:688–693.

[169] Broedersz CP, Kasza KE, Jawerth LM, Munster S, Weitz DA, MacKintosh FC. Measurement of nonlinear rheology of cross-linked biopolymer gels. *Soft Matter* 2010; **6**:4120–4127.

[170] Head DA, MacKintosh FC, Levine AJ. Nonuniversality of elastic exponents in random bond-bending networks. *Phys. Rev. E Stat. Nonlin. Soft Matter Phys.* 2003; **68**:025 101.

[171] Ewoldt RH, McKinley GH, Hosoi AE. New measures for characterizing nonlinear viscoelasticity in large amplitude oscillatory shear. *J. Rheol.* 2008; **52**:1427–1458.

[172] Semmrich C, Larsen RJ, Bausch AR. Nonlinear mechanics of entangled F-actin solutions. *Soft Matter* 2008; **4**:1675–1680.

[173] Xu J, Tseng Y, Wirtz D. Strain hardening of actin filament networks. *J. Bio. Chem.* 2000; **275**:35 886–35 892.

[174] Morse DC. Viscoelasticity of concentrated isotropic solutions of semiflexible polymers. 1. model and stress tensor. *Macromolecules* 1998; **31**:7030–7043.

[175] James HM, Guth E. Theory of the elastic properties of rubber. *J. Chem. Phys.* 1943; **11**:455–481.

[176] Beatty MF. An average–stretch full–network model for rubber elasticity. *J. Elasticity* 2003; **70**:65–86.

[177] Miehe C, Göktepe S. A micro-macro approach to rubber-like materials. Part II: The micro-sphere model of finite rubber viscoelasticity. *J. Mech. Phys. Solids* 2005; **53**:2231–2258.

[178] Mathur AB, Collinsworth AM, Reichert WM, Krauss WE, Truskey GA. Endothelial, cardiac muscle and skeletal muscle exhibit different viscous and elastic properties as determined by atomic force microscopy. *J. Biomech.* 2001; **34**:1545–1553.

[179] Zhou E, Quek S, Lim C. Power-law rheology analysis of cells undergoing micropipette aspiration. *Biomech. Model. Mechanobiol.* 2010; **9**:563–572.

[180] MATLAB. R2010b, The Math Works, Inc., USA.

[181] Mezger TG. *The Rheology Handbook*. second edn., Vincentz Network: Hannover, 2006.

[182] Holzapfel GA, Gasser TC. A viscoelastic model for fiber-reinforced composites at finite strains: Continuum basis, computational aspects and applications. *Comput. Meth. Appl. Mech. Eng.* 2001; **190**:4379–4403.

[183] Payne AR. The dynamic properties of carbon black-loaded natural rubber vulcanizates. Part I. *J. Appl. Polymer Science* 1962; **6**:57–63.

[184] Lieleg O, RBausch A. Cross-linker unbinding and self-similarity in bundled cytoskeletal networks. *Phys. Rev. Lett.* 2007; **99**:158 105.

[185] Lieleg O, Schmoller KM, Claessens MMAE, Bausch AR. Cytoskeletal polymer networks: viscoelastic properties are determined by the microscopic interaction potential of cross-links. *Biophys. J.* 2009; **96**:4725–4732.

[186] Taylor RL. Feap — A Finite Element Analysis Program. Version 8.2, University of California at Berkeley, USA. 2008.

[187] Discher DE, Boal DH, Boey SK. Simulations of the erythrocyte cytoskeleton at large deformation. II. micropipette aspiration. *Biophys. J.* 1998; **75**:1584–1597.

[188] Baaijens FPT, Trickey WR, Laursen TA, Guilak F. Large deformation finite element analysis of micropipette aspiration to determine the mechanical properties of the chondrocyte. *Ann. Biomed. Eng.* 2005; **33**:494–501.

[189] Monteiro E, Yvonnet J, He QC, Cardoso O, Asnacios A. Analyzing the interplay between single cell rheology and force generation through large deformation finite element models. *Biomech. Model. Mechanobiol.* 2011; **10**:813–830.

[190] CUBIT. Version 12.1, Sandia Corp., USA.

[191] Alastrué V, Martinez MA, Doblaré M, Menzel A. Anisotropic micro–sphere–based finite elasticity applied to blood vessel modelling. *J. Mech. Phys. Solids* 2009; **57**:178–203.

[192] Federico S, Gasser TC. Nonlinear elasticity of biological tissues with statistical fibre orientation. *J. R. Soc. Interface* 2010; **7**:955–966.

[193] Simo JC. On a fully three-dimensional finite-strain viscoelastic damage model: Formulation and computational aspects. *Comput. Meth. Appl. Mech. Eng.* 1987; **60**:153–173.

[194] Holzapfel GA, Gasser TC, Ogden RW. A new constitutive framework for arterial wall mechanics and a comparative study of material models. *J. Elasticity* 2000; **61**:1–48.

[195] Ogden RW. *Non-linear Elastic Deformations*. Dover: New York, 1997.

[196] Taylor RL. *FEAP – A Finite Element Analysis Program, Version 8.2 User Manual*. University of California at Berkeley, Berkeley, California, 2008.

[197] Macosko CW. *Rheology: Principles, Measurements, and Applications*. Wiley-VCH: New York, 1994.

[198] Rivlin RS. Large elastic deformations of isotropic materials. III. Some simple problems in cylindrical polar co-ordinates. *Philos. T. Roy. Soc. A* 1948; **240**:509–525.

[199] Yeoh OH. Characterization of elastic properties of carbon-black-filled rubber vulcanizates. *Rubber Chem. Technol.* 1990; **63**:792–805.

[200] Rivlin RS. Large elastic deformations of isotropic materials IV. Further developments of the general theory. *Philos. T. Roy. Soc. A* 1948; **241**:379–397.

[201] Rivlin RS. A note on the torsion of an incompressible highly-elastic cylinder. *Math. Proc. Cambridge Philos. Soc.* 1948; **45**:485–487.

[202] Rivlin RS. Large elastic deformations of isotropic materials VI. Further results in the theory of torsion, shear and flexure. *Philos. T. Roy. Soc. A* 1949; **242**:173–195.

[203] Zienkiewicz OC, Taylor RL. *The Finite Element Method. The Basis*, vol. 1. 5th edn., Butterworth Heinemann: Oxford, 2000.

Monographic Series TU Graz

Computation in Engineering and Science

Vol. 1 Steffen Alvermann

Effective Viscoelastic Behaviour of Cellular Auxetic Materials
2008
ISBN 978-3-902465-92-4

Vol. 2 Sendy Fransiscus Tantono

The Mechanical Behaviour of a Soilbag under Vertical Compression
2008
ISBN 978-3-902465-97-9

Vol. 3 Thomas Rüberg

Non-conforming FEM/BEM Coupling in Time Domain
2008
ISBN 978-3-902465-98-6

Vol. 4 Dimitrios E. Kiousis

Biomechanical and Computational Modeling of Atherosclerotic Arteries
2008
ISBN 978-3-85125-023-7

Vol. 5 Lars Kielhorn

A Time-Domain Symmetric Galerkin BEM for Viscoelastodynamics
2009
ISBN 978-3-85125-042-8

Vol. 6 Gerhard Unger

Analysis of Boundary Element Methods for Laplacian Eigenvalue Problems
2009
ISBN 978-3-85125-081-7

Monographic Series TU Graz

Computation in Engineering and Science

Vol. 7 Gerhard Sommer

Mechanical Properties of Healthy and Diseased Human Arteries
2010
ISBN 978-3-85125-111-1

Vol. 8 Mathias Nenning

Infinite Elements for Elasto- and Poroelastodynamics
2010
ISBN 978-3-85125-130-2

Vol. 9 Thanh Xuan Phan

Boundary Element Methods for Boundary Control Problems
2011
ISBN 978-3-85125-149-4

Vol. 10 Loris Nagler

Simulation of Sound Transmission through Poroelastic Plate-like Structures
2011
ISBN 978-3-85125-153-1

Vol. 11 Markus Windisch

Boundary Element Tearing and Interconnecting Methods for Acoustic and Electromagnetic Scattering
2011
ISBN: 978-3-85125-152-4

Monographic Series TU Graz

Computation in Engineering and Science

Vol. 12 Christian Walchshofer

Analysis of the Dynamics at the Base of a Lifted Strongly Buoyant Jet Flame Using Direct Numerical Simulation
2011
ISBN 978-3-85125-185-2

Vol. 13 Matthias Messner

Fast Boundary Element Methods in Acoustics
2012
ISBN 978-3-85125-202-6

Vol. 14 Peter Urthaler

Analysis of Boundary Element Methods for Wave Propagation in Porous Media
2012
ISBN 978-3-85125-216-3

Vol. 15 Peng Li

Boundary Element Method for Wave Propagation in Partially Saturated Poroelastic Continua
2012
ISBN 978-3-85125-236-1

Vol. 16 Andreas J. Schriefl

Quantification of Collagen Fiber Morphologies in Human Arterial Walls
2012
ISBN 978-3-85125-238-5

Vol. 17 Thomas S. E. Eriksson

Cardiovascular Mechanics
2013
ISBN 978-3-85125-277-4

Monographic Series TU Graz

Computation in Engineering and Science

Vol. 18 Jianhua Tong

Biomechanics of Abdominal Aortic Aneurysms
2013
ISBN 978-3-85125-279-8

Vol. 19 Jonathan Rohleder

Titchmarsh–Weyl Theory and Inverse Problems for Elliptic Differential Operators
2013
ISBN 978-3-85125-283-5

Vol. 20 Martin Neumüller

Space-Time Methods
2013
ISBN 978-3-85125-290-3

Vol. 21 Michael J. Unterberger

Microstructurally-Motivated Constitutive Modeling of Cross-Linked Filamentous Actin Networks
2013
ISBN 978-3-85125-303-0